Title

Dynamics and Methods of Manipulating Ferroic Order in BiFeO3 and Related Materials

Author

Parsonnet, Eric Kenneth

Publication Date

2022

Peer reviewed|Thesis/dissertation

Dynamics and Methods of Manipulating Ferroic Order in $BiFeO_3$ and Related Materials

by

Eric Kenneth Parsonnet

A dissertation submitted in partial satisfaction of the

requirements for the degree of

Doctor of Philosophy

in

Physics

in the

Graduate Division

of the

University of California, Berkeley

Committee in charge:

Professor Ramamoorthy Ramesh, Chair
Professor Lane Martin
Professor Zi Qiu

Spring 2022

Dynamics and Methods of Manipulating Ferroic Order in $BiFeO_3$ and Related Materials

Abstract

Dynamics and Methods of Manipulating Ferroic Order in $BiFeO_3$ and Related Materials

by

Eric Kenneth Parsonnet

Doctor of Philosophy in Physics

University of California, Berkeley

Professor Ramamoorthy Ramesh, Chair

This dissertation details methods of manipulating and dynamic studies of ferroic order in the multiferroic material, $BiFeO_3$, and related material systems. The primary advances made as a result of the work described herein are understanding of intrinsic and extrinsic limits on ferroelectric switching (in particular free- and bound-charge dynamics, the role of, and pathways to manipulate the Landau free energy landscape and lattice dynamics) and implications for switching of magnetic order, mechanisms and factors impacting depolarization in ferroelectric materials, and a novel manifestation of magnetoelectric coupling enabling nonvolatile electric field control of magnon spin transport.

To my parents and brother.

Contents

List of Figures

List of Tables

Acknowledgments

First and foremost, I would like to thank my parents, Wanda and Brian. Throughout my entire life, you have been so incredibly supportive that it is difficult to put into words. Thank you for always challenging me to do my best, but only for things I am excited about. Ever since I was little, you have always told me that I could "do anything I put my mind to." The respect you gave me, and the drive you instilled in me as a kid is essential to the person I am today. You are the best role models I could ask for and this degree, nor any major accomplishment I have ever achieved would have been possible without your support and guidance. I am so thankful to be your son.

To my brother Nicholas, you have quite literally planned my entire life for me. I have consistently followed in your footsteps every step of the way. I am happy to say that you haven't let me down with my life planning. Thank you for being there when I needed someone to talk to about the inevitable slogs of the Ph.D., and maintaining reason when I could not. You are, and always will be an amazing role model, and I hope to someday be as cool as you.

To my partner Emma, thank you for being so incredibly supportive. You are always interested in hearing about my research and ideas, and know when to tell me its time to take a break. There is no one else I would have rather (nor could have) spent 6 months quarantining with (and a dog) in a 500 square foot apartment. Thanks for keeping life outside of lab endlessly fun.

To my new friends from graduate school, especially Paul Corbae and Abel Fernandez, thank you for keeping me sane and engaging my interests in everything from stocks to rock climbing to amorphous materials. I can't wait till our startup takes off.

To my lifelong friends, especially Gordon Olsen, Huntley Chamberlain, Daniel Angell, Patrick Weibe, and Ivan Aguilar, your friendship means the world to me.

I would like to thank Intel Corporation for their funding and intellectual support of my research. In particular, I must thank Tanay Gosavi, Ian Young, Dmitri Nikonov and Chia-Ching Lin. I have loved our Friday talks and hope to work together again in the future.

To Lucas Caretta, you have been instrumental in my Ph.D. both as a colleague and friend. You've been an incredible mentor with so much knowledge, passion, and skill. I hope to be as eloquent, innovative, and well-versed as you someday. I can't wait to see the research you achieve in your career.

To Lane Martin, you have, in many ways, been like a second PI for me. Thanks for pushing me to be the best scientist I can be and engaging with me on new ideas and directions for research. Your attention to detail and yet ability to do so many things at once is remarkable.

Last, but certainly not least, I would like to thank Professor Ramesh. I'll never forget our first meeting, and the email chain that followed, where I said I would love to work in your lab and you responded "very strong resonance on my end." From that moment forward, I have never for a moment doubted that you were on my team and were willing to do whatever it took to support me. Your excitement is wildly contagious, so much so that

when I get an interesting result, I know I can send you an email to discuss at any time, whether that's 9 at night or 6 in the morning. Your knowledge-base is seemingly endless and your dedication to the field, and more generally, dedication to simply doing good science is something to be revered. Thank you for pushing me, both scientifically, but equally importantly, professionally. You've taught me how to do great research, present effectively, tirelessly problem solve, and argue in a professional way. These are lifelong skills that I will take with me forever. You've been an incredible mentor and I can't thank you enough for the learning and experience I have gained working in your lab.

Chapter 1

Introduction and Motivation

In condensed matter systems, correlations can exist between and within charge, spin, orbital, and lattice degrees of freedom. The associated energy scales and form of such couplings dictate the properties of a material. Ferromagnets, for example, possess strong spin-spin coupling through the exchange interaction, while so-called "magnetostrictive" effects are usually measured in parts per million, and spin-lattice coupling can often be neglected, or treated as a small correction. The same is not true of ferroelectrics, where strains associated with charge ordering (and strong electric dipole-dipole interactions) induced at the onset of ferroelectricity are frequently of essential importance at 1% or larger [1]. In order to study the coupling strength and mechanisms between the various degrees of freedom, one often employs equilibrium studies. For example, one may use epitaxial growth to modify strain in a ferroelectric material, with subsequent measurements of the ferroelectric order providing insight into coupling between lattice and charge degrees of freedom. Dynamic studies, *i.e.*, studying the time evolution of ferroic order under external stimuli or quasi-particle excitations subject to non-equilibrium conditions, open up new possibilities for deeper understanding of coupling between degrees of freedom. Coupling strength, stability, and mechanisms, as examples, can be addressed via dynamic studies. One can think of equilibrium studies as measuring the properties of the ground state, whereas dynamic measurements probe excited states. Though one can learn a significant amount by studying the ground state alone, in order to gain a comprehensive picture, excited states must also be understood. Such research is not only of fundamental, but also applied interest, as materials possessing (multiple types of) ferroic order are increasingly considered for next-generation computing technology [2, 3].

In this chapter I will provide key background for the main topics and themes discussed frequently in my thesis. The central aim of the work presented in this dissertation is to study dynamics, and establish novel manifestations of multiferroic coupling in condensed matter systems. The work presented herein focuses specifically on coupling between charge, lattice, and magnetic degrees of freedom, coupling, which has piqued both fundamental and applied interest in recent decades. What follows is an introduction to ferroelectric and multiferroic materials, with special emphasis on dynamic coupling between order parameters. This chapter ends with an outline for the remainder of the thesis as well as a brief summary

for each forthcoming chapter.

1.1 Ferroelectrics and Multiferroics - Fundamental Background

A ferroelectric material is an insulating system, which lacks inversion symmetry, and hosts at least two discrete states of non-zero "spontaneous" electric polarization, which can be switched between with an applied electric field[4]. The switchable nature of the polarization can be observed in a ferroelectric hysteresis loop (Fig. 1.1e) where the polarization possesses two stable orientations at zero applied field. Ferroelectric order is one of several ferroic order parameters observed in condensed matter systems, including ferromagnetism, ferroelasticity, and ferrotoroidicity[5]. Materials that exhibit multiple ferroic orderings, referred to as multiferroic materials, or multiferroics[6, 7], have gained significant attention over the last several decades as rich systems for studying fundamental physics as well as promising candidates for technological applications[2]. Today, the term "multiferroic" most commonly refers to magnetoelectric multiferroic materials, which exhibit simultaneous magnetic (antiferromagnetic and/or ferromagnetic) and ferroelectric ordering. Traditionally, "magnetoelectric coupling" refers to the linear magnetoelectric (ME) effect, whereby an applied electric (magnetic) field induces a linearly dependent magnetization (electric polarization)[8], however more recently, ME coupling in magnetoelectric multiferroics has become synonymous with manipulating one ferroic order parameter through the other. In these systems, the coexistence of magnetic and ferroelectric ordering can lead to coupling between them[5], the most common manifestation of which being reversal or switching of magnetic ordering through electric-field switching of the ferroelectric order[9, 10]. It is remarkable that magnetic switching can be induced by electric-field switching of ferroelectric, most obviously, because magnetic switching requires a breaking of time-reversal symmetry, which electric fields do not. I will address this point in detail in sections 1.1.3 and 1.1.4.

While robust magnetoelectric coupling has been demonstrated in the magnetoelectric multiferroic $BiFeO_3$ (BFO), there exist a number of outstanding questions of both fundamental and applied interest. In particular, the dynamics of order in ferroelectric and magnetoelectric systems, *i.e.*, the time-scales, mechanisms, limits, and implications of dynamic order parameter evolution, remain active subjects of intense investigation. To explore the dynamics, one must first understand the different types of order parameters, their couplings, and manifestations in material systems.

1.1.1 Ferroelectricity

A ferroelectric phase change is a structural phase transition, which occurs at a critical (called the Curie, T_c) temperature, and is characterized by the appearance of a spontaneous electric polarization. The spontaneous polarization, $\vec{P}$, characterizes the density and magnitude of

electric dipoles[1], which originate from the physical displacement between the centers of positive and negative charge relative to one another within the unit cell (Fig. 1.1a,b). Above T_c, the phase is referred to as the paraelectric or "high-symmetry" phase, consistent with the fact that the ferroelectric phase lacks inversion symmetry, and has strictly lower symmetry than its high temperature relative. Below T_c, with no externally applied electric field, there exist at least two directions along which the spontaneous polarization can develop. In part, to minimize depolarization fields, which exist for a polarized, finite crystal, ferroelectrics form regions in space which spontaneously polarize along different allowed polarization directions[1]. These regions are called domains[2].

Ferroelectric phase transitions have historically been categorized as either displacive (where the parent, paraelectric phase is microscopically non-polar) or order-disorder (where the paraelectric phase is only macroscopically non-polar, resulting from thermal averaging of polar entities). Displacive transitions are second-order while order-disorder transitions, which involve latent heat, are first order. Displacive transitions are often associated with the freezing of a so-called "soft" phonon mode near the Brillouin-zone center. Soft modes of lattice motion are collective excitations that reduce the symmetry of the system and whose frequency lowers as the temperature is decreased[1]. Soft transverse optical phonon modes, which describe ionic displacement within a unit cell, for example, have lower frequency owing to a competition between the local restoring force and the long range dipole interaction[12]. Eventually as the temperature of the system is lowered, the frequency of oscillation approaches zero, the ionic displacement is frozen in, symmetry is reduced, and the ferroelectric phase is realized (Fig. 1.1a,b). Structural transitions which are governed by condensation of zone-center modes are generally referred to as "ferrodistortive" transitions. While most proper ferroelectrics result from ferrodistortive transitions[1], other mode condensation processes also appear in ferroelectrics and related materials. When condensation occurs away from the Brillouin-zone center, the transition is referred to as "antiferrodistortive". Antiferrodistortive transitions such as freezing of oxygen octahedral tilts, important for magnetic ordering in $BiFeO_3$, will be discussed throughout this thesis. As previously mentioned, not *all* paraelectric-ferroelectric phase transitions are believed to be soft-mode driven. Notably, in Raman studies of $BiFeO_3$, the transition appears to not be accompanied by a soft-mode[13], and has been shown to exhibit both displacive and order-disorder characteristics[14]. Regardless of the precise behavior of polar order near the phase transition, lattice dynamics (phonons), and the couplings between polar and other polar/non-polar modes play a significant role in dictating the characteristics of ferroelectric materials.

Generally, the coupling between polar and acoustic modes is termed the piezoelectric interaction, and as all ferroelectrics are piezoelectrics, it is not surprising that a spontaneous

[1]As with any charge distribution, higher mulitpole expansions are, in principle, allowed. These higher order terms can be important, especially in more complex polar orderings such as polar vortices[11].

[2]Interestingly, the existence of domains means that ferroelectrics can have no *net* response, and it is this reason that many believe explains why ferroelectricity (formally discovered in 1920[1]) was discovered so long after ferromagnetism (discovered > 2000 years ago). Ferroelectricity even got its name, "ferro" from its magnetic analog. "Ferro" comes from iron, with chemical symbol "Fe", which is ferromagnetic.

strain often is a characteristic of ferroelectric materials[1]. This strain may be switched by application of an external stress, and analogous to how ferroelectric order can be switched by external electric fields, "ferroelastic" materials host two or more strain states which can be switched between by external mechanical stress. Ferroelastic transitions are associated with condensation of long wavelength acoustic modes and we often observe the emergence of ferroelastic domains in ferroelectric materials (Fig. 1.1c), whose equilibrium ground state structure can be modified by choice of substrate[15, 16]. Finally, magnetic degrees of freedom can also impact characteristics of ferroelectric materials. While this will be discussed at length in Section 1.1.3, it suffices here to say that in order to build a holistic theory of ferroelectricity (or any ferroic material) one must properly consider all degrees of freedom and associated energies. To do so, one often frames the problem in the context of Landau theory[17], where one can explicitly account for all relevant degrees of freedom. First, however, I establish a simple model Hamiltonian for ferroelectrics as a basis on which to build complexity.

The essential physics of ferroelectrics can be captured in a simple model, which considers local coordinates in the unit cell associated with the ferroelectric phase transition (for example the Bi^{3+} ion displacement in $BiFeO_3$). I begin with a general Hamiltonian describing a solid:

$$H = H(\text{ion}) + H(\text{electron}) + H(\text{electron-ion}) \tag{1.1}$$

where H(ion) describes a collection of n ions interacting in a potential, which is a function of ionic positions ($\vec{R}_i, i \in [0, n]$), H(electron) describes the valence electrons, and H(electron-ion) describes the interactions between the valence electrons and ion cores[1]. To simplify Eq.1.1, I make the assumption that (see Ref. [1]) electrons respond instantaneously to the ion motion, thereby allowing us to treat H(electron-ion) as an additional contribution to the ionic Hamiltonian, and that the contribution is independent of electron configuration and temperature. This allows us to rewrite Eq. 1.1 as an effective Hamiltonian for the ionic motion alone

$$H_{\text{eff}}(\text{ion}) = \sum_i \frac{p_i^2}{2m_i} + V(..., \vec{R}_i, ...) \tag{1.2}$$

where $V(..., \vec{R}_i, ...)$ is a potential accounting for both ion-electron and ion-ion contributions. Following the adiabatic principle[18], I can treat the electronic and ionic energies independently, thereby allowing us to focus on Eq. 1.2 (*i.e.* ignoring H(electron) in Eq. 1.1) in search of any lattice driven instabilities that are responsible for structural phase transitions. For ferroelectric phase transitions, I are often interested in specific 'local modes' (which need not necessarily by soft modes) of lattice motion that describe the phase transition. I can significantly simplify the Hamiltonian further by accounting for only the local modes relevant to the phase transition. To do so I can define canonically conjugate momentum ($\vec{\pi}_{\alpha l}$) and displacement ($\vec{\xi}_{\alpha l}$) co-ordinates for each unit cell, where α indexes the local mode and

l indexes the unit cell[1]. Considering here, for simplicity, only a single local mode of ionic motion (so I can drop the α index), I can write

$$H_{\text{eff}}(\text{ion}) = \sum_l \frac{\vec{\pi}_l^2}{2} + V(\xi_1, \xi_2, ...) \tag{1.3}$$

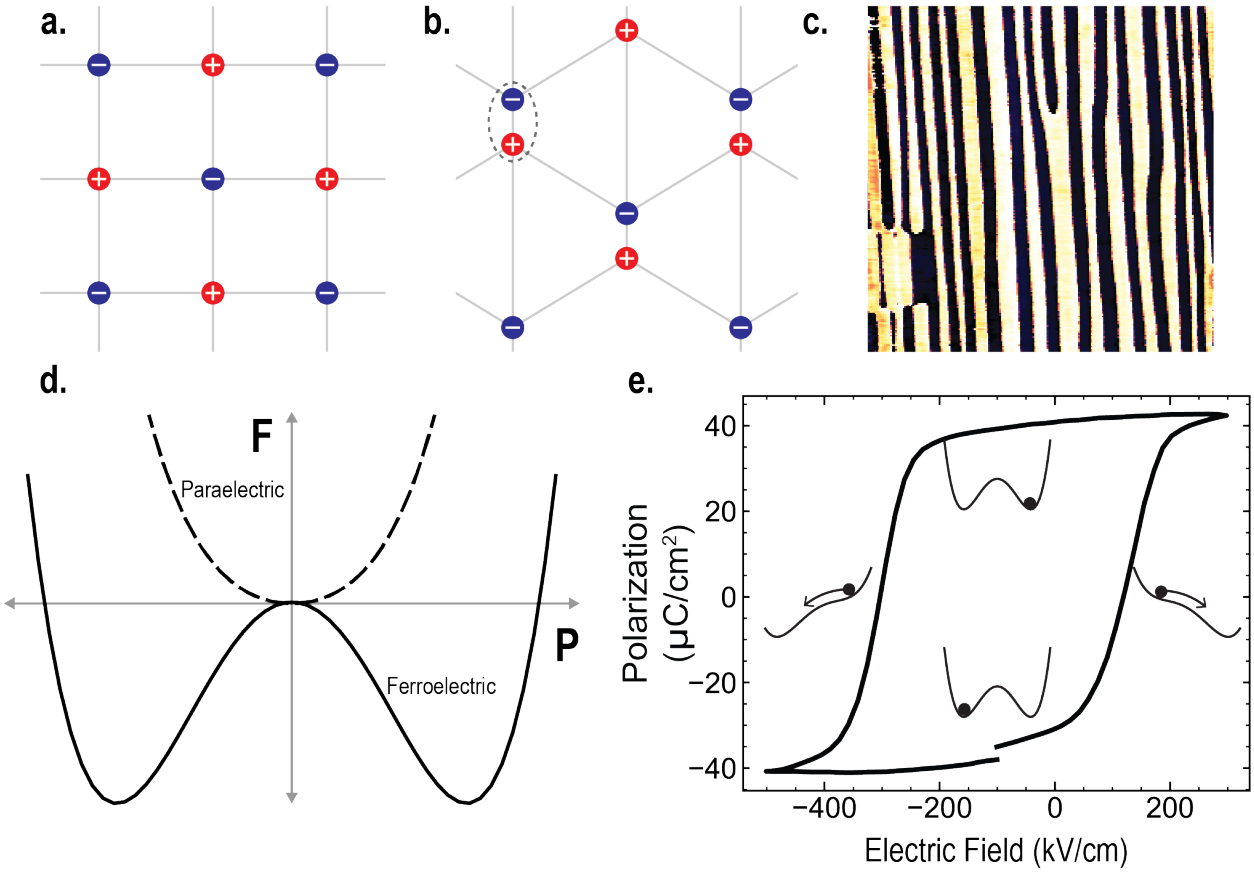

Figure 1.1: Ferroelectric Overview. **a.** and **b.** show a 2D lattice of charged ions in the paraelectric and ferroelectric phase respectively. **c.** shows a piezoresponse force microscope (out-of-plane) image of stripe domains in $BiFeO_3$ grown on a $DyScO_3$ substrate. **d.** shows the prototypical, "double-well potential", free energy vs. polarization (ferroelectric order parameter) for the paraelectric and ferroelectric phases. **e.** shows a polarization-electric-field (PE) ferroelectric hystersis loop for the $BiFeO_3$ and schematic of switching using the double well.

I make the final simplification by noting that $V(\xi_1, \xi_2, ...)$ can be decomposed into single cell contributions ($V(\xi_l)$) and inter-cell contributions, the latter of which I write as a sum of

bi-linear two-body interactions[3] to arrive at the final Hamiltonian:

$$H_{\text{eff}}(\text{ion}) = \sum_{l} \left[\frac{\vec{\pi}_l^2}{2} - V(\xi_l) \right] + \sum_{l,l'} v_{ll'} \xi_l \xi_{l'} \tag{1.4}$$

Eq. 1.4 is a remarkable achievement, and surprisingly general in no small part because the interaction potential ($v_{ll'}$) can encompass both short and long range order, and can describe polar and non-polar displacive as well as order-disorder transitions.

Owing to improvements in computational power, the microscopic formalism has recently been employed for theoretical studies of ferroelectric dynamics. In ref [19] the authors perform molecular dynamics simulations using an first-principles based effective Hamiltonian for $BiFeO_3$ which includes coupling between magnetic, lattice and charge degrees of freedom and demonstrate ultrafast polarization reversal as well as dynamic changes in the antiferrodistortive (oxygen octahedral tilts) vectors. The authors in ref [20] use molecular dynamics to study the microscopic properties of $BaTiO_3$. Such studies are computationally intensive and are only as good as the effective Hamiltonian used. As such, it is vital that experimental work is performed in an effort to verify results and iteratively improve upon the Hamiltonian used.

While the microscopic description of ferroelectricity presented above forms a solid basis for understanding, and recent theoretical work has begun to address dynamics, there exists an alternative approach, namely Landau theory, which uses macroscopic quantities, the thermodynamic free energy of the system and symmetry considerations in lieu of a precise microscopic description. Landau theory has the benefit of relatively low computational complexity, and can therefore be used to describe ferroelectric behavior on significantly longer length scales. Phase-field simulations[16, 21, 22], for example can reproduce domain structures observed in experiment on the micron length scale, whereas first principle calculations deal with low numbers of unit cells. Landau theories have the additional benefit of producing "easy-to-digest" free energy functionals and an intuitive understanding of some of the key properties of ferroelectics.

Landau theory, based symmetry considerations, has been highly effective in describing macroscopic equilibrium phenomena in ferroic materials which possess long range ordering[4]. Landau theories deal with phase transitions, like ferroelectric phase transitions, where one phase has higher symmetry than the other as characterized by an order parameter that is zero in the high symmetry phase, and non-zero in the low symmetry (ordered) phase [17]. The theory proceeds by expanding the thermodynamic free energy of the system in a power series of the order parameter, keeping only symmetry allowed terms. As an example, I consider the simple case of a single component ferroelectric polarization. In this case, the free energy must obey the symmetry $F(P, E) = F(-P, -E)$ where, F is the thermodynamic free energy and E is an external electric field. This symmetry states that upon spatial inversion, the free

[3]More complex forms are allowed though simple bi-linear formalism is sufficient for ferroelectric phase transitions. See [1]

energy remains unchanged. Immediately, this symmetry prohibits inclusion of odd powers of P, and as such the free energy is often written as:

$$F(P) = \alpha_1(T - T_c)P^2 + \alpha_2 P^4 + \alpha_2 P^6 + O(P^8) - EP \tag{1.5}$$

where α_i are fitting parameters determined from experiment or theory and the influence of the externally applied electric field appears as a linear coupling term with the polarization ($-EP$). T and T_c are temperature and Curie temperature, respectively. For brevity, I have included only sixth order in P, though all symmetry allowed terms can be included. Upon cooling through the Curie Temperature from above, one observes the emergence of the so-called "double-well" potential (Fig. 1.1d), a feature critical to the understanding of ferroic materials, where minima in the free energy correspond precisely to the to stable non-zero values of the spontaneous polarization, as described above. By minimizing the free energy with respect to the order parameter, one can achieve an expression for the order parameter at equilibrium. I must re-emphasize that Landau theory is a macroscopic theory and cannot describe the microscopic physics (*i.e.*, atomic displacements like the effective local mode Hamiltonian as before), though holds remarkable power in addressing coupled degrees of freedom an a computationally manageable manor. There exist different complexity levels for Landau theories, and Table 1.1 displays common forms and their differences. Landau theory will prove to be a vital tool in the interpretation of the results presented in this thesis.

Name	Included Terms/Boundary Conditions	Ferroelectric System
Landau-Devonshire	P	Bulk
Landau-Ginzburg	P, ∇P, Finite BC	Bulk/Thin-film w/ domains

Table 1.1: Different named Landau theories considering only the ferroelectric order parameter P.

Landau theory also helps one gain an intuitive (albeit overly simplified) understanding of ferroelectric switching. As can be seen from the form of Eq. 1.5, an externally applied electric field will preferentially favor one polarization state over the other. If the externally applied electric field points opposite the polarization and is sufficiently high, then the ferroelectric will undergo switching, where the macroscopic ferroelectric polarization reverses. One can think of this process as a "tilting" of the double well potential causing the polarization to switch. This intuitive picture, and the association with the ferroelectric hysteresis loop is shown in Fig. 1.1e. One naturally is inclined to write an equation of motion for the macroscopic polarization as (often referred to as the time-dependent Ginzburg Landau equation or TDGL)

$$\gamma \frac{\partial P}{\partial t} = -\frac{\partial F}{\partial P} \tag{1.6}$$

with γ serving as a viscosity coefficient[23] characterizing the timescales of switching. While such analysis can prove fruitful in describing the energetics and dynamics of the switching, as well as interesting properties such as so-called "negative capacitance"[23] (which arises from the negative curvature of the free energy landscape near $\vec{P} = 0$), one must be careful as Landau theory describes the macroscopic polarization and does not take into account essential microscopic physics of, for example, nucleation and growth of domains[4][24, 25, 26] which have been shown play a key role in ferroelectric switching. Still, time-resolved phase field simulations[16] provide a powerful tool for interpreting and predicting ferroelectric dynamics. A detailed discussion of these issues and methods of studying ferroelectric switching dynamics is presented in Chapters 2 and 3.

1.1.2 (Anti-)Ferromagnetism

A material is said to be a "ferromagnet" when there is long range, parallel alignment its constituent magnetic moments, or spins (electron spins) (Fig. 1.2). Similar to ferroelectric materials, which possess a spontaneous polarization, ferromagnets possess a spontaneous magnetization ($\vec{M}$) which can be switched by an applied magnetic field. Where the polarization-electric field hysteresis loop was a characteristic of ferroelectrics, the magnetization-magnetic field (MH) loop is characteristic of ferromagnets. Above the Curie temperature, T_c, like ferroelectrics, ferromagnets undergo a phase transition and become paramagnetic, where the net magnetization is zero. Unlike ferroelectricity which constitutes a structural phase change and there exists a separation of the centers of positive and negative charge in the unit cell mitigated by local modes of lattice motion, ferromagnetism comes from an inherently quantum effect called "exchange". Fundamentally, exchange comes from the Pauli exclusion principle, where electrons, (fermions) cannot occupy the same state. Since the wave function contains both spin and spatial degrees of freedom, it can be energetically favorable for two electrons to have different spatial components (lower Coulomb repulsion when not overlapping in space) while possessing the same spin state. Here I give a cursory introduction to the key elements required for studying (anti-)ferromagnetic properties relevant to this thesis with an emphasis on the dynamics of magnetic order, including switching and quasi-particle (magnon) excitations.

An antiferromagnet (Fig. 1.2) is the most common class of magnetic material and possesses anti-parallel alignment of its constituent spins, below their transition temperature, the so-called Néel temperature, T_N. Where ferromagnets react strongly (high magnetic susceptibility) to an applied magnetic field (exhibiting hysteresis, for example) antiferromagnets, with no net magnetization, are said to be robust to externally applied fields, and typically have low magnetic susceptibilities. The ferromagnetic order parameter is the magnetization, $\vec{M}$. Though there exist cases (importantly $BiFeO_3$) where both antiferromagnetic and ferromagnetic ordering appear, a *pure* antiferromagnet has no net magnetization, so I require a

[4]Some authors claim that the viscosity coefficient can be used as a fitting parameter for domain-wall motion, though the energies predicted by Landau theories often significantly overestimate the energies observed in switching, a shortcoming of the macroscopic approach.

different order parameter. To do so, I describe the system as having two sublattices, A and B, with magnetization $\vec{M}_A$ and $\vec{M}_B$, respectively (Fig. 1.2). The Néel vector, defined as the difference $\vec{L} \equiv \vec{M}_A - \vec{M}_B$ then serves as the relevant order parameter.

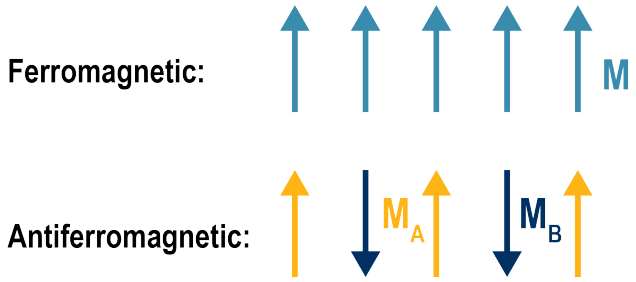

Figure 1.2: Ferromagnetic and antiferromagnetic ordering in a 1D spin chain.

A simple Hamiltonian is capable of capturing the basic concepts of both ferromagnetism and antiferromagnetism. For a 1D spin chain, the Hamiltonian,

$$H = -J \sum_{\langle i,j \rangle} \vec{S}_i \cdot \vec{S}_j \tag{1.7}$$

where the first summation is performed over nearest neighbors, J is a quantity, called the exchange integral, that characterizes the strength and type of ordering and $\vec{S}_i$ is the spin operator for the i^{th} spin. When J is positive, the ordering is ferromagnetic (energetically favorable for the spins of nearest neighbors to align), and when J is negative, the ordering is antiferromagnetic. This type of interaction, which favors either parallel or anti-parallel alignment of spins is termed symmetric Heisenberg exchange.

There exists another type of exchange interaction, namely the anti-symmetric, or the Dzaloshinskii–Moriya (DM) interaction[27, 28], which favors a canting of the neighboring spins. The DM interaction can be obtained by treating spin-orbit coupling as a perturbation in the superexchange[29] formalism[5] for antiferromagnetic ordering[27]. The DM Hamiltonian is given by,

$$H_{DMI} = \vec{D}_{ij} \cdot \left(\vec{S}_i \times \vec{S}_j \right) \tag{1.8}$$

where $\vec{D}_{ij}$ is the so-called Dzaloshinskii–Moriya vector. The DM interaction and canting of spins can thus introduce a (typically weak) net magnetic moment in an otherwise antiferromagnetically ordered system. To account for the canting of the spins, it is convenient to

[5]The intuitive explanation for superexchange in $Fe^{3+} - O_2 -]Fe^{3+}$ linkages is as follows: The Fe^{3+} ions have 5 d electrons, meaning that each of the 5 d orbitals is filled by exactly one electron, which are aligned. To minimize the Coulombic energy, it is preferred to delocalize the wavefunction. If there is an O_2 intermediate between two Fe^{3+}, owing to the Pauli exclusion principle, the electron wavefunction is most delocalized if the two Fe^{3+} have net opposite spin. See the book *Magnetic Materials, Fundamentals and Applications* by Nicola A. Spaldin Chapter 8 (second Ed.) for more.

now define two vectors of interest: the Néel vector, described above, and the magnetization $\vec{M} = \vec{M}_A + \vec{M}_B$. The DM interaction is often mediated by a non-magnetic (often oxygen) atom (Fig. 1.3a) and is strongly dependent on the symmetry of the system. If, for example, there exists a center of inversion symmetry at the point bisecting two spins (Fig. 1.3b), the DM vector must be zero[28]. Since we know that ferroelectric materials lack inversion symmetry this example is of particular interest here, illustrating how structural distortions (from a ferrodistortive or antiferrodistortive phase transition, perhaps) can play a role in setting the magnetic properties of a material. In this way, one can see a pathway for coupling between charge, lattice, and magnetic degrees of freedom[30].

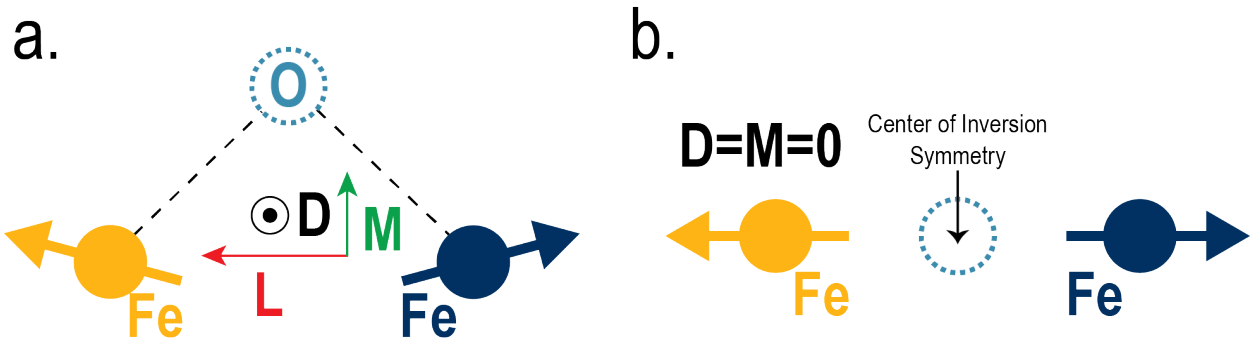

Figure 1.3: Dzaloshinskii–Moriya Interaction. Antisymmetric exchange favors the canting of neighboring spins. **a.** shows canting of adjacent iron spins. **b.** illustrates an example of how the DM interaction is strongly dependent on symmetry.

When it comes to dynamics of magnetic order, one must account for a key difference between from ferroelectric order, in that magnetic systems carry angular momentum. In a magnetic field, and without damping, an isolated spin undergoes precession. From the Hamiltonian $H = -\frac{g\mu_B}{\hbar}\vec{S}\cdot\vec{B}$ ($g, \mu_B, \hbar, \vec{B}$ gyromagnetic ratio, Bohr magneton, reduced Planck's constant, and applied magnetic field, respectively), and the Schrödinger equation, one can show that spin equation of motion is given by[31],

$$\frac{d\vec{S}(t)}{dt} = -\gamma_0 \left[\vec{S}(t) \times \vec{H}\right] \tag{1.9}$$

($\gamma_0 = g\mu_0\mu_B/\hbar, \vec{B} = \mu_0\vec{H}$, and μ_0 is the permeability of free space) meaning that the spin will never align with the applied field. We know this is not the case, and that ferromagnetic materials align with externally applied fields, so to incorporate this experimental fact, one introduces a "damping" term (and performs a suitable re-scaling of t as in [31]):

$$\frac{d\vec{S}}{dt} = \left(\vec{S} \times \vec{H}(t)\right) + \lambda\vec{S} \times \left[\vec{S} \times \vec{H}(t)\right] \tag{1.10}$$

where λ is a damping parameter and we now allow the applied field to vary in time. Eq. 1.10 is referred to as the Landau-Lifshitz-Gilbert (LLG) equation in its most simple form. The LLG can be extended to study both ferromagnets and antiferromagnets and is fundamental to the study of dynamics in magnetic materials[31, 32, 33]. One can readily see key differences in the dynamics for polar vs. magnetic vs. lattice degrees of freedom (see Eq. 1.6 and Eq. 1.10) and that their coexistence can create a rich environment for exploration, discussed more in Section 1.1.3.

Up to now, "dynamics" of the various ferroic orders has largely been framed in the context of switching from one stable state to another. In this thesis, I will also address dynamics of ferroic order which does not constitute switching, but rather collective excitations of said order. Predominantly, I will be concerned with the physics of magnons, *i.e.*, collective, spinful excitations of magnetic order, and how one can manipulate them through coupled degrees of freedom. Here, to lay the fundamental groundwork, I will describe the essential theory behind such excitations.

Given the ferromagnetic Hamiltonian for a 1D spin chain (J positive in Eq. 1.7), it is straightforward to see that the ground state (lowest energy) is for all spins to align. Any spin flip (Fig. 1.4) will result in a higher energy (excited) state. Assuming a spin of 1/2, spin flips also constitute reduce the net spin of the lattice is reduced by 1. In this way, one can think of a single spin flip as spin 1 excitation of the ground state. While a single spin flip, as that depicted in Fig. 1.4 is an intuitive form of an excited state, it is easy to show that it is not an eigenstate of the Hamiltonian. To do this, I write the Hamiltonian in terms of ladder operators, $S_i^{\pm} = S_i^x \pm iS_i^j$ [34] (one should think of $S_i^{\pm}$ as flipping a spin either up (+) or down (−))

$$H = -J \sum_{\langle i,j \rangle} (\frac{1}{2} S_i^+ S_j^- + \frac{1}{2} S_i^- S_j^+ + S_i^z S_j^z) \tag{1.11}$$

which, indeed, has the eigenstate depicted in Fig. 1.4a. However, if I operate on the presumed "excited state" of Fig. 1.4b, I find:

$$H \left|... \uparrow\downarrow\uparrow ...\right\rangle = \alpha_1 \left|... \uparrow\uparrow\downarrow ...\right\rangle + \alpha_1 \left|... \downarrow\uparrow\uparrow ...\right\rangle + \alpha_2 \left|... \uparrow\uparrow\downarrow ...\right\rangle \tag{1.12}$$

where α_1, α_2 are constants. Clearly, the state with a single spin flip is not an eigenstate, and therefore not the correct form of the excited states of this system. In fact from the form of Eq. 1.11, I can already "guess" a good eigenstate. Clearly, the excitation itself (the spin flip) must be delocalized, since the Hamiltonian includes "hoppping" terms such as $S_i^+ S_j^-$. Somehow, the magnetic order itself must collectively account for the excitation. This is achieved in the "spin wave" state depicted in Fig. 1.4c., where the ferromagnetically aligned spins collectively precess with a precessional phase dictated by the spins' location in the chain[34]. The correct eigenstates are indexed by quantum number k[6] (subject to periodic boundary conditions[34]) and are given by:

[6] k is the wavevector, and describes, essentially, the phase between adjacent spins. For example, for $k = 0$ modes, all spins precess together.

$$|\psi_k\rangle = \frac{1}{\sqrt{N}} \sum_j e^{ikja} |\phi_j\rangle \tag{1.13}$$

where $|\phi_j\rangle \equiv |... \uparrow_{j-1} \downarrow_j \uparrow_{j+1} ...\rangle$, *i.e.*, the single spin flip occurring at site j. Such spin waves are quantized, and each carry spin 1 (a single spin flip). These excitations are bosons, carry spin information, and are called "magnons". In ferromagnetic systems, there exists only one (right-circular[7]) polarization of spin wave allowed (carrying angular momentum -1 relative to the ground state magnetic order). In antiferromagnets, where two sublattices of spins exist, the system permits both right and left circular polarized (with energies $\omega_\alpha, \omega_\beta$) spin waves[34, 35]. For the simplest case of an easy-axis antiferromagnet the energy of the two ($k = 0$) modes is given by:

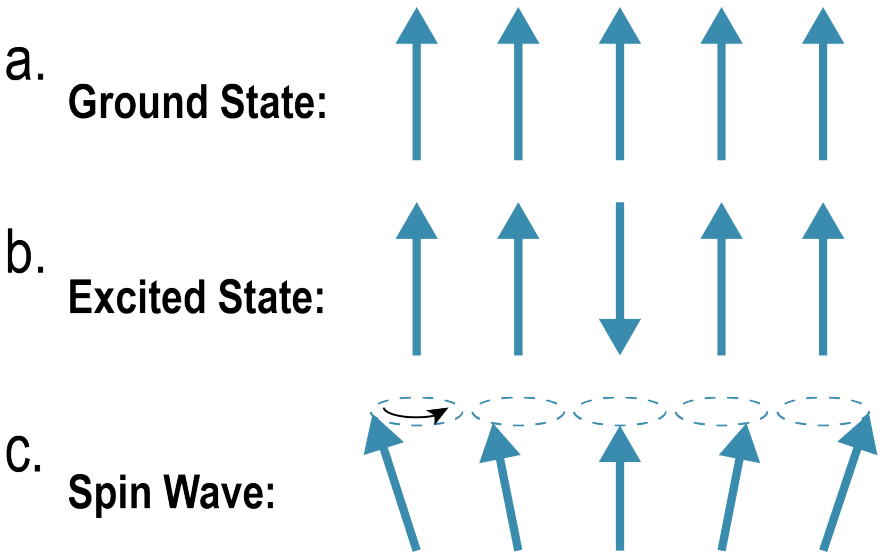

Figure 1.4: Ferromagnetic Spin Waves. **a.** Ground state. **b.** An "intuitive" (though incorrect) excited state showing a single, localized spin flip. **c.** Spin wave: a collective spin 1 excitation of the magnetic ordering.

$$\omega_{\alpha,\beta} = \gamma(H_c \pm H_0) \tag{1.14}$$

[35] where $\gamma = g\mu_0\mu_B/\hbar$, H_c contains exchange and anisotropy contributions to the energy of the system and H_0 is an applied field along the direction of anisotropy[35]. As the applied magnetic field is increased, the two modes split in frequency (Fig. 1.5a.), until $H = H_{\text{spin-flop}}$, at which point, the "magnon-gap", *i.e.*, the energy offset from zero, is said to "close". Here, the system undergoes the so-called spin-flop transition (Fig. 1.5b.) and the spins reorient

[7]Why only right circular? Because of the right hand rule, and the way in which cross products are defined.

orthogonal to the applied field direction. In the spin-flop phase the we observe only a single magnon mode. Importantly, above the spin-flop field, the system has a small canting of the antiferromagnetically aligned spins along the field direction (Fig. 1.5b.), resulting in a net magnetic moment, $\vec{M}$, and by rotating the direction of the applied field, one can rotate both the Néel and magnetization vector.

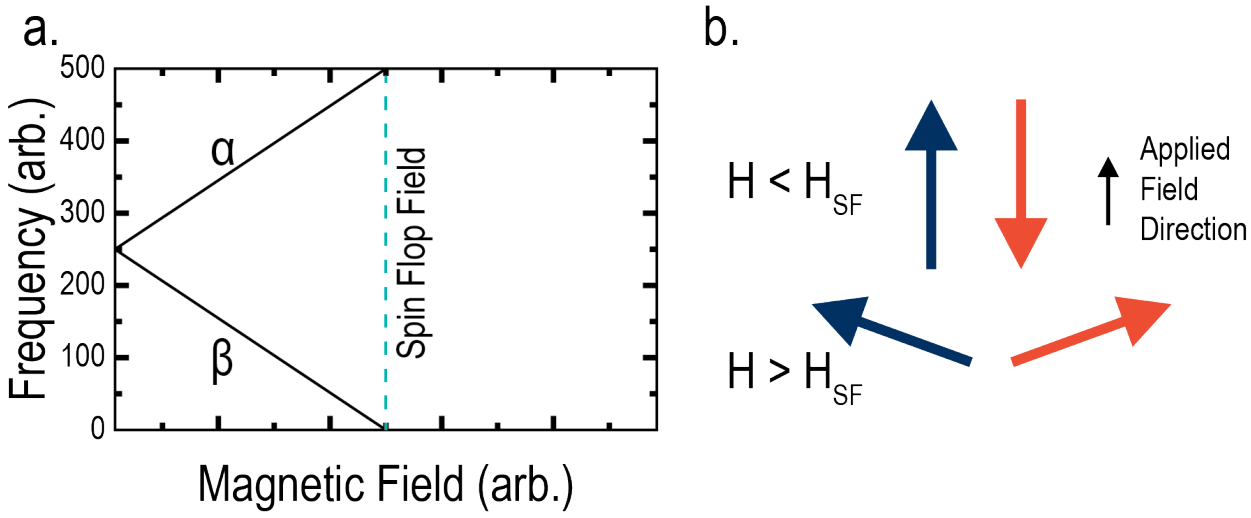

Figure 1.5: **a.** Schematic of α and β magnon frequences as a function of applied magnetic field. The closing of the magnon gap (*i.e.*, $\omega_\beta = 0$), and spin-flop transition occurs at the "spin flop field". **b.** Spin configurations in the antiferromagnetic and spin-flop phases with an external field applied along the easy axis. For additional details, see ref [35], Figures 1 and 3.

In Chapter 5, I will present detailed studies of magnons, with particular emphasis on how multiferroic materials such as $BiFeO_3$ offer an exciting platform for which to study dynamic excitations of magnetic order.

1.1.3 Coupled Order and Multiferroics

A magnetoelectric is a material which is both magnetically and electrically polarizable. A multiferroic is a material which possesses multiple ferroic (or spontaneous) order parameters. As you might guess, a magnetoelectric multiferroic is a system which possesses both magnetic order and ferroelectric order, and importantly, the two are coupled – if I modify one I modify the other. In section 1.1.1, I discussed the strong coupling between charge and lattice degrees of freedom, though I have not yet addressed coupling to magnetic degrees of freedom in detail. Before continuing, it is important to pause and answer a fundamental question: *why study multiferroic materials?* I will provide two answers, the first takes a fundamental viewpoint and the second from an applied one.

From a more fundamental viewpoint, there exists unique physics to be studied in multiferroics. Spin and charge degrees of freedom are in many ways very different from one another. Spins carry angular momentum, where as charge does not. Ordered electric dipoles (ferroelectricity) necessarily coincide with structural phase transitions, and very strong lattice coupling, while magnetic ordering does not. The coexistence of ferroelectric and magnetic ordering in a single phase is, in fact, remarkable. While the equilibrium physics has been studied extensively and is becoming increasingly well understood, even more exciting are dynamic processes of multiferroic order. For example, during reversal of order parameters in a multiferroic, charge must redistribute (potentially through multiple states), the lattice must dynamically adapt, and magnetic order must switch (a process which includes precessional motion as governed by the LLG equation). We know from quasi-static and equilibrium studies that these processes occur, but little is known about the what happens *during* switching. Each of these processes is independently complex and the role of intrinsic coupling between order parameters adds an additional layer of complexity (and intrigue). What role does the lattice play in dictating the timescales of ferroelectric switching? Does the requirement of switching the spin degree of freedom slow the switching of other order parameters? Is there dynamic decoupling on fast timescales? These are all questions that address the physics of magnetoelectric multiferroics in ways not studied before, and can only be addressed through dynamic studies. Finally, not only can we study dynamic processes of order parameter reversal, but also of low energy excitations. Multiferroicity allows one the unique ability to study quasi-particle excitations of order in ways that are not accessible without magnetoelectric coupling, for example, studying magnons in the absence of an applied magnetic field.

Computing efficiency has made exponential gains over the past 5 decades, and has been governed by two, seemingly, unflappable rules[8]: Moore's law, which states that the number of transistors on integrated circuits approximately doubles every two years, and Dennard's scaling, which states that the power density of circuits stays roughly the same as transistors get smaller[2]. To continue these trends, it is necessary to introduce non-traditional materials as well as beyond-CMOS (complimentary metal oxide semiconductor) logic devices[2, 36, 37, 38]. One proposal to make significant improvements in energy efficiency and speed of integrated circuits is to use a "collective switch" of a material's order parameter in lieu of an electronic current[2, 3]. By using a ferroic order parameter as the state variable, one automatically has a non-volatile system, stable to thermal fluctuations and a well-defined (at least) two state system. Multiferroic materials, enabling one to use voltage instead of current to manipulate the magnetic state, can, in principle operate at 1aJ per switch[2], a significant improvement over current technology. Energy is not the only important metric, and dynamic studies of these systems provides vital insight into timescales of switching (and limits thereof), holding vital insight for computation rates and processing speeds. Multiferroics may also open doors to new paradigms in computing, enabling spin-wave-based computing, for example, which would require power-costly magnetic fields in other materials.

[8]These are not "rules" in the strict sense of the word, but rather observations of reliable trends in the semiconductor industry.

With both the fundamental and applied motivations in mind, I now turn to a discussion of multiferroicity in real systems. As it turns out, systems with intrinsic multiferroicity, *i.e.*, coexisting magnetic and ferroelectric ordering, and specifically the ability to manipulate one order parameter with the other, are quite rare. To understand why, I consider symmetry, electrical properties, and chemistry, as in [39].

Symmetry: There are a finite number of crystal structures, corresponding to 122 so-called Shubnikov point groups. 31 points groups can accommodate a spontaneous ferroelectric polarization (lack inversion symmetry) and 31 allow for spontaneous magnetization. There are only 13 point groups which allow for both ferroelectricity and ferromagnetism to exist in the same phase.

Electrical Properties: Ferroelectrics are insulators. Though it is not always the case, ferromagnets are typically metals. This is because ferromagnetism often arises from a high density of states at the Fermi level, which also makes the system metallic.

Chemistry: Perhaps the most important contribution (or at least the most cited) is the fact that ferromagnetism is often driven by electrons in partially filled d shells. In contrast, the common perovskite oxide ferroelectrics have a formal charge corresponding to d^0, and there is a tendency for empty d shells to be associated with ferroelectricity. These two "rules" are at odds with one another.

As is clear from this discussion, single phase multiferroic materials are hard to come by. While there exist composite materials[5], which offer an engineering pathway to creating multiferroic behavior, for this thesis I am predominantly interested in single phase multiferroics, of which, only one is known (to exist at room temperature), $BiFeO_3$.

1.1.4 $BiFeO_3$

$BiFeO_3$ (BFO) is the only known room temperature magnetoelectric multiferroic[9] with a Curie temperature $T_c \approx 1100$K and Néel temperature $T_N \approx 650$K. BFO is in the space group $R3c$ (rhombohedrally distorted perovskite), which arises from the freezing of two normal modes: the polar displacement of the Bi^{3+} ions along $\langle 111 \rangle$, and the antiferrodistortive rotation of the oxygen octahedra (Fig. 1.6). Via super exchange, the iron spins in BFO exhibit G-Type antiferromagnetic ordering (where each iron spin is aligned opposite to its nearest 6 neighboring iron spins). Owing to the DM interaction, the antiferrodistortive rotation of the oxygen octahedra permit the canting of the otherwise antiferromagnetically aligned iron spins in the $\langle 111 \rangle$ plane (Fig. 1.6b.)[40, 41, 42].

Ferroelectricity in BFO predominantly comes from the stereochemically active (affecting the geometry) A-site bismuth $6s^2$ electrons, the so-called "lone-pair"[41, 43]. This effect is nicely summarized in the following excerpt from ref [44], "The 'lone pair' in bismuth-or lead-based oxides is believed to form due to the hybridization of $6s$ and $6p$ atomic orbitals with $6s^2$ electrons filling one of the resulting orbitals in bismuth or lead in their oxides. The

[9]There are other magnetoelectric multiferroics, notably $YMnO_3$ ($T_c \in (570\text{K}, 990\text{K})$ and $T_N \in (70\text{K}, 130\text{K})$) and $BiMnO_3$ ($T_c \approx 450$K and $T_N \approx 100$K)[40]

lone pair is then considered to be chemically inactive, not taking part in the formation of bonds but sterically active. The hybridization causes the lone pair to lose its spherical symmetry and is projected out on one side of the cation, resulting in an asymmetry of the metal coordination and distorted crystal structures." This is in contrast to other prototypical ferroelectrics, such as $BaTiO_3$, where the B-site distortion (titanium) predominantly contributes. The magnetic ordering in BFO, on the other hand, comes from Fe^{3+}, which has 5 d electrons. It is remarkable that BFO naturally has achieved a solution to the aforementioned chemistry problem [5] causing sparsity of magnetoelectric multiferroics (see section 1.1.3). While both magnetic and ferroelectric ordering exist in the same phase in BFO, we also require that they are coupled, *i.e.*, switching one will result in switching of the other. In early work on this topic, Ederer and Spaldin [42] argued that although magnetization reversal in BFO following ferroelectric switching was unlikely due to symmetry considerations, it was in principle possible. In that work, the authors demonstrated how the rotation of the oxygen octahedra play a key role (through the DM interaction) of setting the magnetization orientation. With regard to magnetization reversal however, the authors considered 180° switching, meaning the switching pathway passes through no intermediate (meta-stable) states, which is in part why they concluded magnetization reversal following ferroelectric reversal was unlikely. Subsequent work (explained next), considered alternative switching pathways and was able to show switching of magnetic order by manipulating the ferroelectric state.

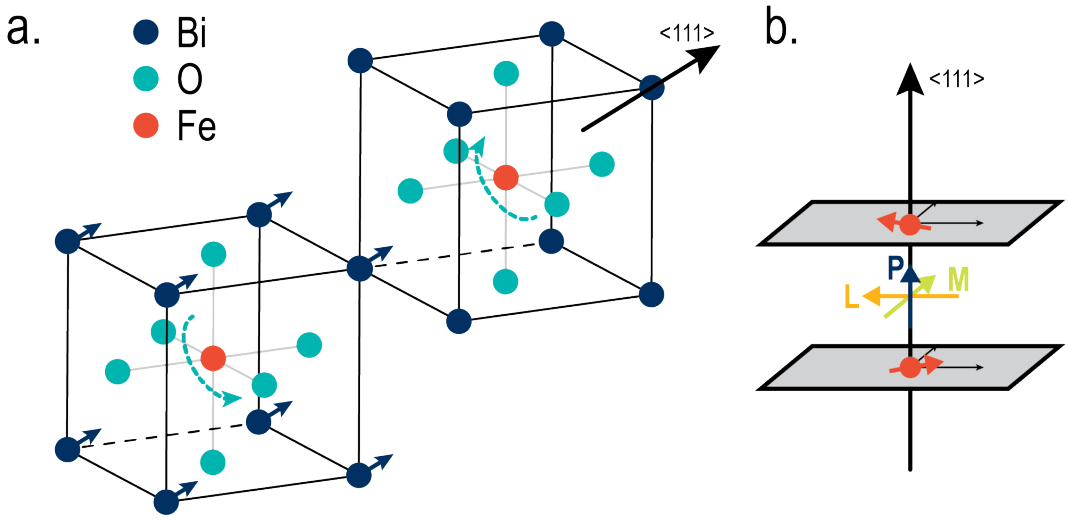

Figure 1.6: **a.** Schematic view of the $R3c$ structure of BFO, comprised of two cubic perovskite unit cells. The cations are displaced along $\langle 111 \rangle$ (arrows indicating Bi^{3+} polar distortion) relative to the anions, and the oxygen octahedra rotate (alternately) about the $\langle 111 \rangle$ axis. **b.** Schematic of Fe^{3+} antiferromagnetically aligned in the $\langle 111 \rangle$ plane with a small canting of the spins producing a net magnetization.

BFO exhibits a stripe domain structure (Fig. 1.1b). As ferroelectricity is the dominant order parameter in BFO, and FE order results from strong coupling between charge and lattice degrees of freedom, the domain structure in BFO is dependent on both electrostatic and elastic boundary conditions. By choice of substrate and/or bottom electrode we can modify the domain structure from 2-variant stripe, 4-variant stripe, to mosaic, to even single domain[16, 45, 46]. For example, we can tune the domain structure from consisting of 109° domains to 71° domains simply by growing a bottom electrode and modifying the electrostatic boundary conditions. Such control of domain structure via epitaxy is a important tool that we as researchers can use.

Three seminal experimental papers laid the foundation for so-called "electric field control of magnetism" in BFO. The first, ref [47], showed that electric field poling, using a piezoresponse force microscope (PFM), of BFO resulted in reversal of the antiferromagnetic order. The ferroelectric and antiferromagnetic (AFM) domains were imaged before and after poling. Ferroelectricity was imaged using PFM. To study the antiferromagnetic order, the authors used photoemission electron microscopy (PEEM) based on X-ray linear dichroism (XLD). XLD-PEEM is sensitive to antiferromagnetic order via a process called the "search-light" effect. In the antiferromagnetic state, spin-orbit coupling leads to a change in the charge density in the unit cell. An intuitive way of understanding the search-light effect is the following: electric field can be absorbed wherever charge exists. In the extreme case where the charge in the system points only along a single axis, if the incident electric field (from linearly polarized incident photons) is orthogonal to this axis, there can be no absorption. The "dichroism" in XLD means that one takes the difference between observed signals (photo-emitted electrons) for orthogonally polarized incident light, allowing one to "see" the antiferromagnetic state (more precisely the resulting charge density) via the search-light effect. XLD-PEEM, is also sensitive to ferroelectricity (which also constitutes a change in charge density in the unit cell), but via temperature dependent studies[47], the authors show that the XLD signal predominantly comes from the antiferromagnetic order in BFO.

The results of PFM and XLD-PEEM are shown in Fig. 1.7a. As can be observed, there is a one-to-one mapping between ferroelectric domains and AFM domains, and importantly, the two are coupled before and after switching, offering some of the first indications of robust magnetoelectric coupling in BFO. In 2011, there was another substantial breakthrough, this time, related to ferromagnetism (as arising from canting and the DM interaction).

In ref [10], the authors again used a combination of PFM and photoemission electron microscopy, though in this case looking at X-ray magnetic circular dichroism (XMCD). XMCD-PEEM, where one subtracts the signals resulting from opposite chiralities of incident light (right vs. left circularly polarized) is sensitive to ferromagnetic ordering. By growing a heterostructure consisting of ferromagnetic CoFe and BFO (*i.e.*, CoFe(2.5nm)/BFO) layers, the authors found a remarkable coupling one-to-one coupling between ferromagnetic domains in the CoFe and ferroelectric domains in the BFO (Fig. 1.7b.). Even more exciting was the finding that the sign of the anisotropic magnetoresistance (AMR) of the CoFe layer reversed upon electric field poling of the BFO. AMR measures the resistance of a ferromagnetic metal under the influence of a rotating externally applied magnetic field, where the relative

orientation between the magnetization of the ferromagnetic and the applied field dictates whether the system is in a high or low resistance state[48]. AMR is typically small, and contributes only a fractional change in resistance. The fact that electric field switching of the BFO resulted in sign reversal of the AMR signal in the CoFe overlayer indicated that the reversal of the BFO in turn reversed the preferred orientation of the magnetization in the CoFe[10]. These findings are explained by the canted moment in the BFO. The net magnetization (canted moment) of the BFO points along $\langle 11-2 \rangle$, which projects parallel to the polarization on the (001) surface, and is exchange coupled to the CoFe layer, explaining the 1-1 correspondence between ferromagnetic and ferroelectric domains. The switching of the ferroelectric order is accompanied by switching of the canted moment, thereby applying an effective field to CoFe, modifying its preferred magnetization orientation and resulting in the sign reversal observed in the AMR data.

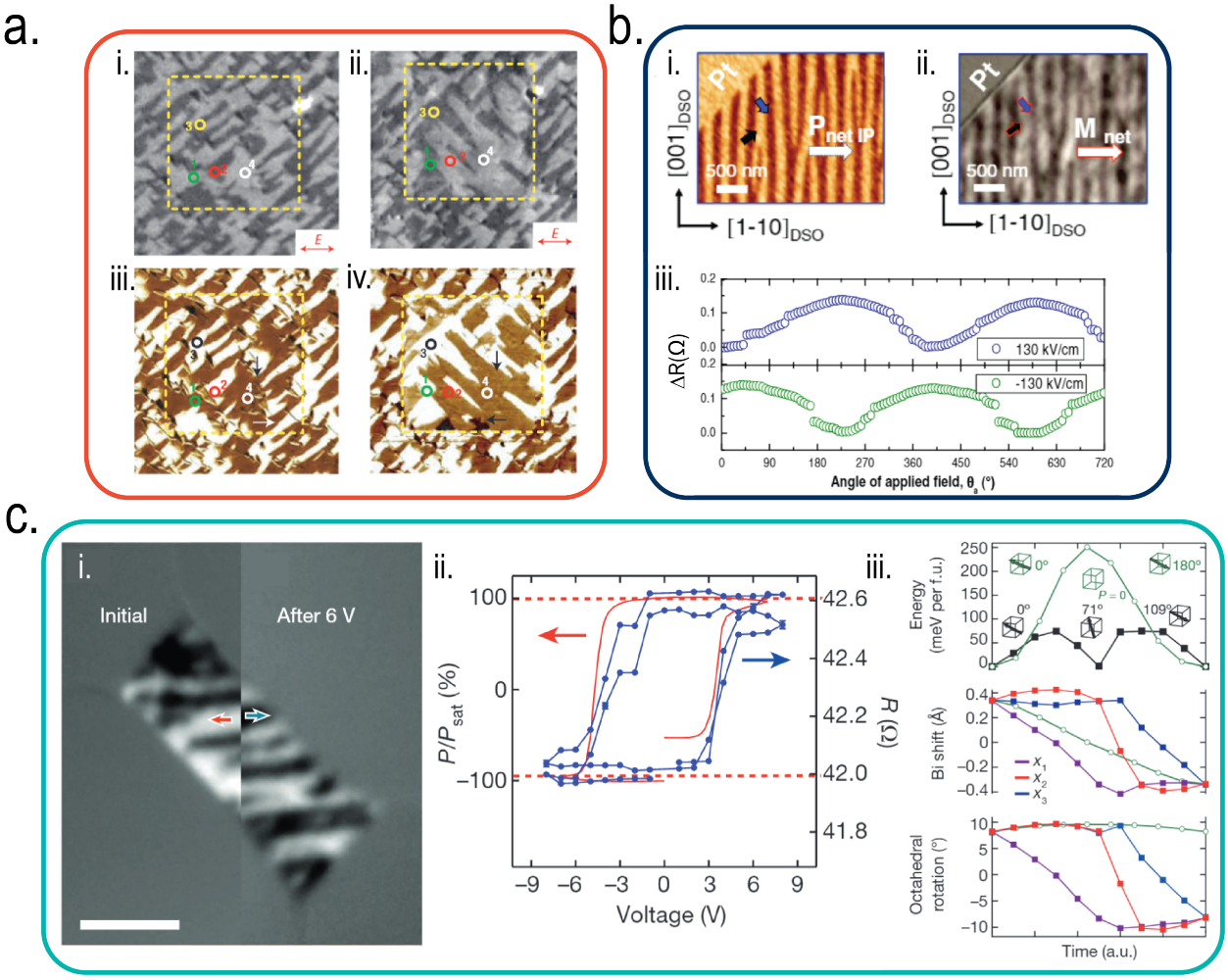

Figure 1.7 *(previous page)*: Figures used with permission from [9, 10, 47]. Electric field control of magnetism in $BiFeO_3$. **a.** From [47], i. and ii. show XLD-PEEM images of BFO before and after electric field poling of a region (dotted yellow box). iii. and iv. show identical location imaged via PFM. Results reveal electric field switching of antiferromagnetic order. **b.** From [10], CoFe/BFO heterostructure. i. shows PFM image of stripe domain structures in BFO. ii. shows XMCD-PEEM images of CoFe ferromagnetic domains at the same spatial location which one-to-one correspondence with the ferroelectric domains. iii. shows sign reversal of AMR upon electric field switching of the BFO. **c.** From [9], i. shows XMCD-PEEM images of CoFe/BFO heteroscructure before and after electric field poling. ii. shows hysteretic GMR signal of CoFe/Cu/CoFe/BFO heterostructure mapping to the ferroelectric hysteresis loop. iii. shows the 2-step switching pathway of BFO polarization reversal. Top panel shows that 2-step switching pathway is energetically preferred over 180° switching, middle and lower panels shows bismuth ion shift (analog for ferroelectricity) and octahedral rotation (essential for magnetic ordering) reversal for three Cartesian coordinates.

In 2014, Heron, *et. al.* [9] presented a robust demonstration magnetoelectric coupling in BFO, resulting in "deterministic switching of ferromagnetism at room temperature using an electric field". There, the authors once again used XMCD-PEEM to study CoFe/BFO heterostructures, but, as an important extension to earlier work, were able to image the ferromagnetic domain structure before and after electric field switching of the BFO (Fig. 1.7c.i.), thereby definitively showing that the switching of the canted moment in the BFO resulted in switching of the exchange coupled ferromagnetic magnetization in the CoFe. In the same work, the authors introduced an additional read-out mechanism for magnetoelectric coupling in the form of giant magnetoresistance (GMR)[49, 50], which makes use of a CoFe/Cu/CoFe (so-called "spin-valve") trilayer heterostructure. For a given relative orientation between the magnetization in the top and bottom CoFe layer, the resistance is either low (magnetizations aligned) or high (magnetizations antiparallel). In a CoFe/Cu/CoFe/BFO heterostructure, the CoFe adjacent to the BFO can be switched by electric field switching of the BFO, meaning that one can switch between high and low resistive states using an electric field. Indeed, such a result was observed, and by comparing a voltage-driven GMR hysteresis loop to the ferroelectric hysteresis loop (Fig. 1.7b.ii.) it is evident that the two ferroic orders are indeed coupled. The GMR technique has become a standard for measuring magnetoelectric coupling in BFO as a simple transport-based alternative to measurements done at a synchrotron[51, 52]. Finally, Heron *et. al.* also addressed the switching pathway in BFO which is crucial to our current understanding of how magnetization reversal occurs in the system. Rather than switch as a single (180°) step, first principle calculations and time-resolved PFM revealed that the polarization reversal occurs in two steps (Fig. 1.8); a 71° followed by a 109°[10] switch, or vice versa. These types of switches are often referred to as "ferroelastic"

[10]Why is it called 109°? It refers to the angle between intitial and final polarization state. *e.g.* switching

switching pathways as there must be significant transient lattice distortion during switching. In so doing, the oxygen octahedral tilts, which are key to setting the magnetization of the system (recall the DM interaction and the off centering of the mediating oxygen atom in super exchange, Fig. 1.3), also reverse (Fig. 1.7c.iii.). This remarkable coupling between lattice, charge, and magnetic degrees of freedom is what allows for magnetization reversal to occur!

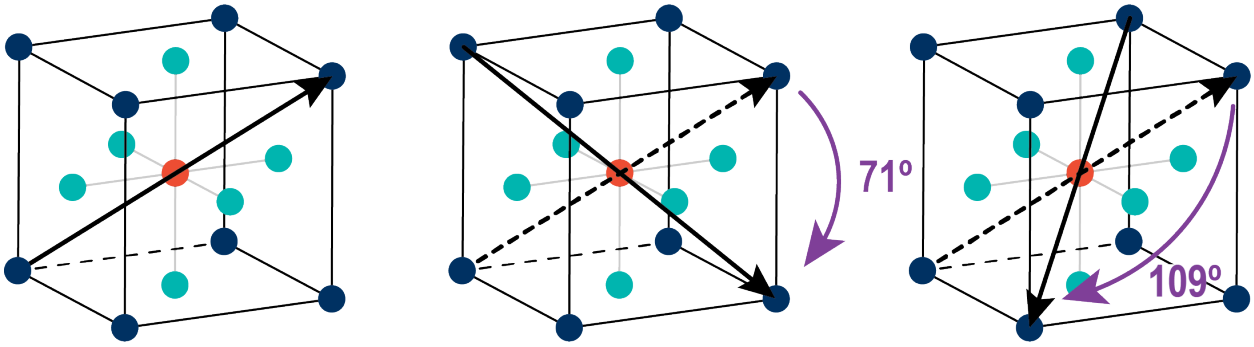

Figure 1.8: Ferroelastic switching pathways in BFO.

As I hope is clear from the discussion above, BFO provides a fruitful playground for studying both fundamental and applied physics. Most intriguing is the correlated behavior of ferroic order parameters and coupling between degrees of freedom that intricately combine to allow for electric field control of magnetism. The remainder of this thesis will be dedicated to dynamics of ferroic order as a means of gaining a deeper insight into multiferroic coupling, both in terms of mechanisms, and implications.

1.2 Dynamics of ferroic order

Multiferroic magnetoelectrics, and specifically BFO, provide a unique platform to study dynamics of ferroic order. As described above, the equilibrium and DC-coupling between charge, lattice and magnetic degrees of freedom has been established and studied though experiments designed to study dynamics (and their implications) of ferroic order in these systems is largely in its infancy. For the remainder of this dissertation, I will focus on dynamic studies both of switching and low-energy excitations, the unique manifestations of mulitferroicity, and the implications of my findings. To assist in contextualizing my findings, I will often discuss application to computing technology and ways in which my progress can be used to improve and/or discover new paradigms in computing. Throughout, I will be guided by a central question, outlined below.

from $\langle 111 \rangle$ to $\langle 1-1-1 \rangle$ corresponds to an angle $\theta = \arccos \frac{(111)\cdot(1-1-1)}{\sqrt{3}\sqrt{3}} = 109.5°$

1.2.1 Central Question

What are the manifestations, mechanisms, and implications of dynamic evolution of (coupled) ferroic order in multiferroic and related materials?

1.2.2 Organization of Dissertation

This dissertation consists of 6 chapters and 3 appendices. With the exception of chapters 1 and 6, each chapter consists of essential background and motivation, including a literature review and technique overview, followed by a detailed account of my results and analysis, and finally a summary, which typically includes extensions and on-going research.

Chapter 1 introduces key concepts and lays the framework for the rest of this dissertation. Chapter 2 introduces high-speed ferroelectric switching dynamics studies, and addresses how a number of factors, both intrinsic and extrinsic, impact switching of ferroelectric order. In Chapter 3, I consider the role of charge-lattice coupling in setting the energetics and dynamics of ferroelectric switching. Importantly, I also establish the role of antiferrodistortive (oxygen octahedral tilt) order in dictating ferroelectric switching in BFO. Implications for switching of magnetic order are discussed. Chapter 4 is dedicated to ferroelectric depolarization, where the stability of the polar state is addressed and the mechanisms/implications of depolarization in ultra-low coercivity thin films is established. Chapter 5 shifts gears slightly, and is dedicated to dynamic low energy excitations of magnetic order (magnons) in BFO. In a novel demonstration of magnetoelectric coupling in BFO, I demonstrate non-volatile electric field control of thermal magnons, and their hysteretic nature. The mechanism of bi-stable states of magnon current is established. I discuss pathways for novel computing applications and ways in which nonlocal spin transport can be utilized. In Chapter 6, I summarize my findings, including summaries of each chapter, and discuss the conclusions and extensions of this work.

Chapter 2

Electric-field Driven Ferroelectric Switching Dynamics

2.1 Essential background and motivation

A defining characteristic of a ferroelectric material is the ability to switch between polarization states with an externally applied electric field. The most straightforward way to measure ferroelectricity in a material is by switching the polarization, which constitutes a destructive readout (*i.e.*, the state is modified when it is measured). This can be done by fabricating a metal/ferroelectric/metal (so-called "ferroelectric capacitor") heterostructure, as in Fig. 2.1, and inserting the FE capacitor into a so-called "Sawyer–Tower" circuit. FE capacitors are typically fabricated by first growing a tri-layer (metal/ferroelectric/metal) and subsequently ion milling, or otherwise etching, a lithographically defined circular top electrode (for additional details see Appendix B). A Sawyer-Tower circuit is a simple circuit consisting of a voltage source and a FE capacitor in series with a dielectric capacitor with well characterized capacitance. Since two capacitors in series have the same charge[4], by monitoring the voltage across the dielectric capacitor and using the relation $Q = CV$, one can measure the charge (and therefore polarization *i.e.*, $P = Q/A$, with A the area of the capacitor) across the ferroelectric capacitor as a function of applied voltage. In this way, by applying a voltage, one can measure the ferroelectric hysteresis loop (Fig. 1.1e). While the Sawyer-Tower circuit is effective in establishing ferroelectricity, it is not well suited to measure dynamic switching on fast time scales. The intuitive reason as to why this is, is because the dielectric capacitor, which ideally has a very large capacitance[1], limits the speed at which one can measure the charge. In order to measure the charge, which results from the switched (or switching) ferroelectric order, the dielectric capacitor itself must charge, the timescale of which is set by the RC-time of the complete circuit. Therefore in the interest of improving the time resolution observable, it is preferred to remove the dielectric capacitor entirely, leaving the ferroelectric capacitor (which you cannot remove) as the dominant source of capacitance

[1] to minimize the voltage drop across it and maximize the voltage drop across the FE capacitor[4]

in the measurement circuit. In this scenario, one no longer measures the voltage across a dielectric capacitor, but instead measures the displacement current through the ferroelectric capacitor as a function of time. To measure the current, one can use a low impedance circuit element designed for broadband signals (such as a high speed oscilloscope). To obtain only the ferroelectric switching contribution to the measured current, one must properly account for other sources of current, most notably dielectric charging of the ferroelectric capacitor. Regardless of how the charge is measured, whether in a Sawyer-Tower circuit or by integrating the measured displacement current less currents from sources other than ferroelectric switching, the polarization-voltage or polarization-electric field (in thin film FE, the electric field is given by $E = V/t$, where t is the film thickness) loop can be obtained by plotting charge versus applied voltage.

Armed with a method of measuring ferroelectric order, I now turn to a discussion of the mechanism of ferroelectric switching. While the origins of ferroelectric order can be understood on the length scale of unit cells, in typical measurements, one measures the macroscopic polarization, which results in averaging over much longer length scales ($\sim$ μm). The mechanism of switching is also understood to take place on scales longer than the unit-cell scale, and generally to require the growth and shrinking of domains through the motion of domain walls[4]. In 1954, Merz [53] described the process of ferroelectric switching to occur via two processes. 1. The formation of new domains when the electric field is reversed, called nucleation, and 2. the growth of these small domains at the expense of domains anti-aligned with the applied electric field. These two processes together are referred to as nucleation and growth. These concepts have been formalized in the years following Merz' seminal work [24, 25, 54], and have been successful in describing ferroelectric switching kinetics. First-principles molecular dynamics simulations [55] have been shown to agree with the nucleation and growth mechanism of ferroelectric polarization reversal and have successfully related the bulk polarization energy and domain wall energy to the rate of polarization reversal. As such, measurements of switching, and specifically switching time, offer a means of quantifiably measuring changes not only the dynamic process by which switching occurs, but also the associated energetics.

Intrinsic vs. Extrinsic Limits: Ferroelectric switching is dependent on a variety of factors, both intrinsic to the material, and extrinsic *e.g.*, dependent on the measurement circuit. Note that my usage of "intrinsic" and "extrinsic" is slightly different from other commonly used meanings in the ferroelectrics community, namely that of the response within a single domain versus movement of domain walls, respectively. On the unit cell level, the details of the rearrangement of charge during switching is not universally agreed upon, and can be dependent on the material system under study. Some authors argue that ferroelectric switching occurs by traversing through the high symmetry phase (which, unlike ferromagnetic switching, is allowed), while others argue that polarization rotation, or ferroelastic switching is preferred[56, 57]. One way of framing the desire to understand "intrinsic" switching is to endeavor to experimentally reveal the unit cell-scale physics of switching and timescales thereof. On a more mesoscopic scale, since ferroelectricity constitutes a structural phase transition, incoherent nucleation and growth of reverse polarized domains is believed to be

fundamentally limited by the group velocity of acoustic phonons in the system. Intuitively, this makes sense, as the growing domains cannot travel faster than the lattice permits. In experiment however, these timescales are rarely observed [58]. To understand why, in this chapter, I provide a detailed description of how free-charge dynamics act as an extrinsic limit on ferroelectric switching and discuss pathways to studying intrinsic switching, both on the unit-cell and mesoscopic scale, alone.

2.1.1 High-speed experimental studies of ferroelectric switching

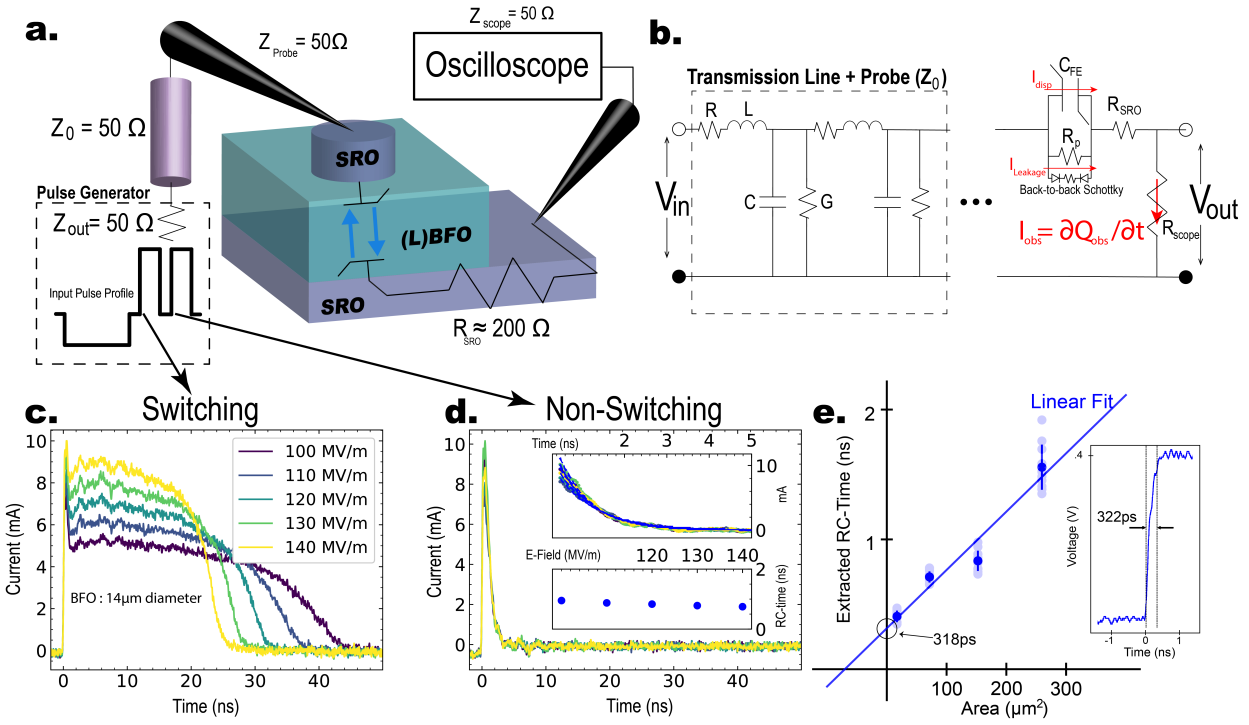

Figure 2.1: From [26]. **a.** shows a schematic of the measurement setup and input pulse profile, with effective circuit shown in **b**. I show Switching and Non-Switching current responses for BFO capacitors in **c.** and **d.** respectively. The RC-curve fits shown in the inset of **d.** indicate the RC-time of the measurement circuit is independent of voltage. In **e.** I observe linear scaling of measurement circuit RC-time with ferroelectric device area. The inset in **e.** shows the rising edge of an input pulse through the identical circuit with ferroelectric capacitor removed.

Pulsed measurements of ferroelectric switching offer an alternative means to hysteresis measurements, and allow one to explore an expanded space of parameters influencing switching. Here, I will outline the details of pulsed measurements with particular emphasis on accessing

fast timescales ($\leq$ 1ns). At its core, any transport measurement of ferroelectric switching is a measurement of displacement current through the ferroelectric. One typically studies ferroelectric switching in capacitor device geometries (Fig. 2.1a.). In a pure dielectric capacitor, (without ferroelectric order) there is a displacement current (RC-charging) that occurs when a voltage is applied. As will be described in great detail below, application of a voltage pulse across a ferroelectric capacitor can cause the polarization (bound-charge) to reverse. This reorientation of bound-charge yields an additional displacement current (in addition to the "normal" RC-charging), which can be detected by the external circuit. I am interested in studying *only* the displacement current coming from ferroelectric switching, *i.e.*, bound-charge reversal.

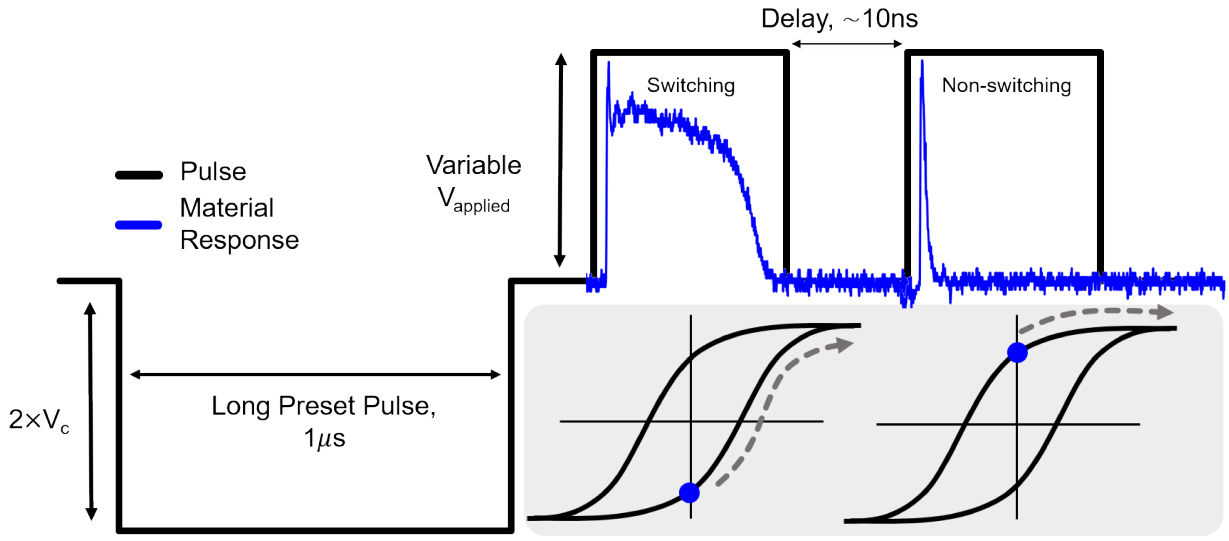

Figure 2.2: From [26]. Pulse train and material response. Via a long preset pulse I initialize the FE into a well-defined polarization state. Then, via two sequential, identical pulses separated by a short time delay, I are able to ascertain the switching transient. As shown in the schematic diagramming the relation to the quasi-static hysteresis loop below the pulse profile, the first pulse induces a switching event, while the second, non-switching pulse, shows only a dielectric response. A typical (here 14µm capacitor BFO) material response is shown in blue along with the effective voltage across the capacitor during the two measurement pulses. It is clear that I must account for the transient voltage during the switching event.

In Fig. 2.2, I show a schematic of a typical 3-pulse voltage pulse train which is used in ferroelectric switching experiments. If the two up pulses are followed by two identical down pulses (giving a total of 5 pulses in the pulse train), the measurement is referred to as a "PUND"[2] measurement. Returning to the 3-pulses of Fig. 2.2, I will refer to the pulses,

[2]My understanding is that PUND stands for Positive Up Negative Down.

sequentially, as P_0, P_1, and P_2[3]. I will use I_1 and I_2 to notate the current observed as a result of applying a voltage pulse. For example, P_1 induces observed current I_1. To understand why this set of pulses is used, I will describe each in detail. Since the state of a ferroelectric is dependent on its history (hysteretic), one must initialize the polarization into a well defined reference state before measuring its switching response. P_0 achieves this goal by serving as a preset pulse which poles the system (solid circle in Fig. 2.2). P_1 and P_2 measure the "switching current" and "non-switching current", respectively. By subtracting the non-switching transient (I_2) from the switching transient (I_1), I determine the contribution to measured current arising from switching of the ferroelectric polarization alone.[58, 59, 60, 61] The schematic arrows adjacent to the hysteresis loops in Fig. 2.2 indicate how the second pulse does not contain a ferroelectric switching contribution.[4] Any contribution to currents arising from dielectric charging, leakage, interfacial Schottky barriers and non-linear dielectric effects (present in all ferroelectric capacitors [62, 63, 64, 65, 66]) is subtracted out when we analyze the difference between the switching and non-switching current transients.

2.1.2 Experimental details

In this thesis, and specifically this chapter, I am particularly interested in accessing switching dynamics on fast timescales (∼ns). Driven dynamics, like that of ferroelectric switching, cannot occur faster than the stimulus which is applied, and so it behooves one to design an experiment with very fast rise-time pulses. Early work [58], fabricated a ferroelectric capacitor directly on a photoconductive switch in order to access sub-ns timescales. However, the fabrication process is difficult and time-consuming, making such an approach not amenable to high throughput experimentation. Instead, I am interested in using a probe tip based approach, which presents additional challenges. A typical DC-probe (Fig. 2.3a.) consists of a single, fine (100s of nm) tip to which you can make electrical connection, and can maneuver using a "micromanipulator" in three directions. The conductor which carries the signal is exposed, allowing for one to contact a sample. At GHz frequencies, like those required here for fast rise-time pulses, impedance matching and proper shielding becomes of the utmost importance. Coaxial cables were invented, in part to be well suited for broadband operation, and when using probes to measure RF components, RF engineers typically use "ground-signal-ground" (GSG) probes where the probe tip contacting the sample is not a single lone tip, but rather a set of 3 tips. There are two ground tips directly adjacent to the signal tip, effectively creating a coaxial cable all the way down to the point of contact between the probe tip and the sample. To use GSG probes, one requires special device geometries (you must now design for 3 probes instead of just 1), and typically, GSG probe are more difficult to use, especially when landing on very small (∼ 5µm in diameter) capacitors. For these reasons, it is desirable to modify DC probes, with fine point tips and high maneuverability,

[3]Others like to call P_1 and P_2 "P*" and "P^", though I find it very confusing to recall which is which, so I just stick with numeric indexing.

[4]As we will see in Chapter 4, this is not always the case, and only holds for perfectly remnant systems

which are able to operate at relatively high frequencies. I developed a scheme to do just that.

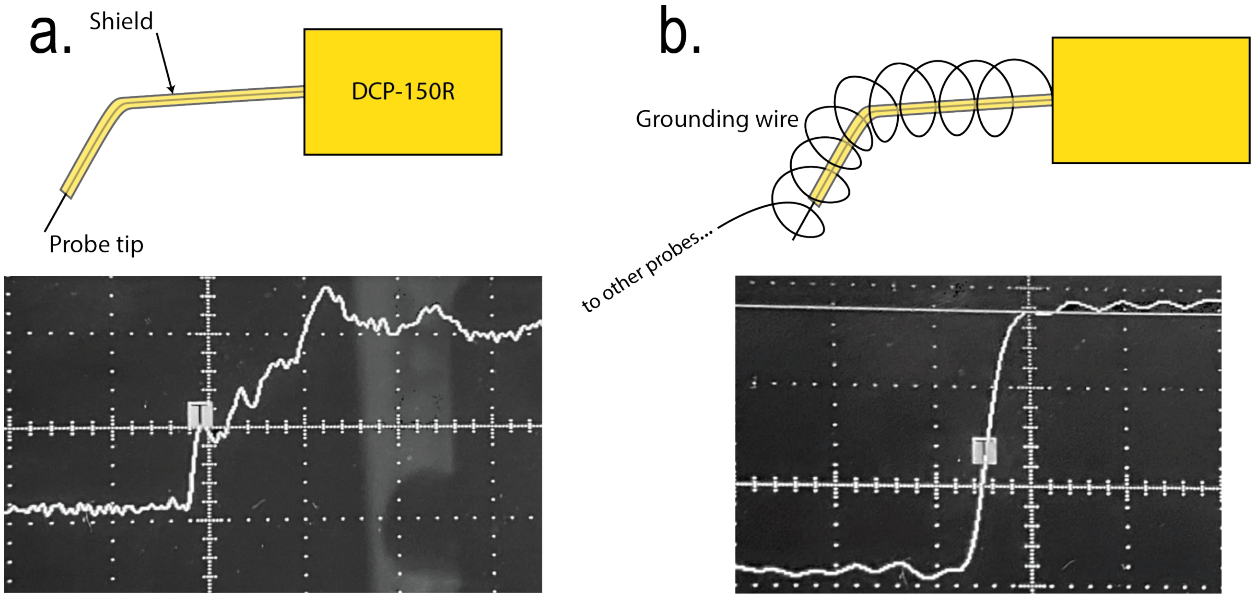

Figure 2.3: Grounding wire influence on pulse profile. **a.** shows schematic of probe without additional grounding wire and resulting (noisy) pulse profile. **b.** shows a schematic of wrapping with grounding wire (Copper) and the resulting clean pulse profile.

In order to generate the fast pulses, I use a Berkeley Nucleonics 765 fast rise-time pulse generator, which has a nominal capability of 70ps rise time. In order to measure the displacement current, I use a Tektronix TDS6604 oscilloscope capable of 20GS/s. Motivated by the shielding role of the "ground" in the GSG probes, I decided to introduce a nearby ground to the DC probe tip, by carefully wrapping the probe tip in a grounded wire. The same ground wire was used for both drive and return probe tips. A schematic of this process and the results of doing so are shown in Fig. 2.3, which shows that the rise time and noise on the voltage pulse is significantly improved. In Fig. 2.1e, I demonstrate that such careful mitigation of parasitics enables us to achieve $\sim$ 300ps rise-times through DC probes, a significant achievement (recall nominal rise-time is 70ps).

Next, I describe how to generate the pulse train required for the switching experiment. I developed two schemes for achieving the desired 3 pulse pulse-train, while working within the constraints of the Berkeley Nucleonics 765. The instrument is capable of uni-polar fast voltage pulses. One can switch the polarity, but the process takes several hundred milliseconds. The two schemes developed are shown in Fig. 2.4. Since I require high time resolution ($\sim$ 100ps) on the oscilloscope, and my pulses can be spaced by up to 100ms, it is impossible to collect all of the data in a single shot (one trial alone would be 125MB of data, beyond the capabilities of the scope). Instead, in Scheme 1, I send the identical pulse

train 3 times, and use Ch2 of the pulse generator to trigger the oscilloscope to collect each pulse (*i.e.*, I_0 is collected the first time the pulse train is applied, I_1 the second time, and so on). In the second scheme, I use an RF power splitter (ZFRSC-183-S+) and both output channels on the pulse generator timed appropriately (Ch1 with negative polarity, Ch2 with positive polarity) to create the pulse-train without the need for switching the polarity of the pulse generator. A second pulse generator (Tektronix AFG3252) is used to trigger the scope and the fast pulse generator. In Scheme 2, the power splitter results in a voltage reduction by half, so the full range (5V) of the Berkeley Nucleonics pulse generator cannot be accessed in this scheme. The advantage of Scheme 2, however is that there is no need to reverse the polarity and I now have precise control over the the delay time between P_0 and P_1. In both schemes, I have precise control over the delay between P_1 and P_2. This pulse train is crucial for ferroelectric switching studies, and the ability to achieve very fast timescales in a probe-based setup allows us to study the mechanisms and factors impacting ferroelectric switching, as described next and throughout this thesis.

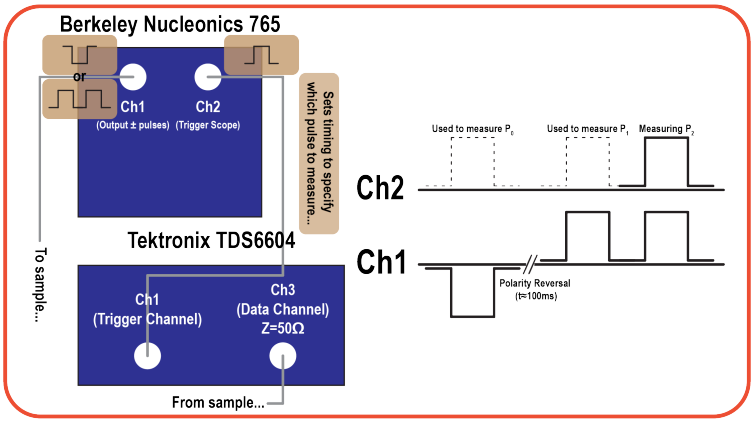

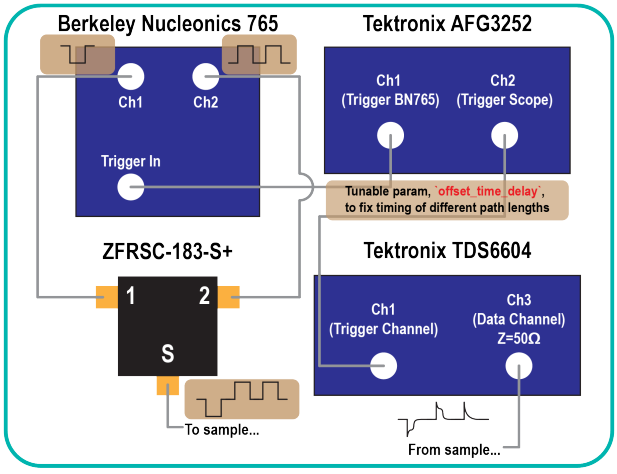

Figure 2.4 *(previous page)*: Two schemes for generating 3-pulse ferroelectric switching experiment pulse-train. The top box (scheme 1) shows connections between the pulse generator and oscilloscope as well as timing (Ch2, pulse generator) used to trigger the scope for data collection. The bottom box shows a schematic for scheme 2, which uses an additional (timing) pulse generator and a power splitter to allow for more precise control of P_0-P_1 delay.

2.2 Toward Intrinsic Ferroelectric Switching in $BiFeO_3$

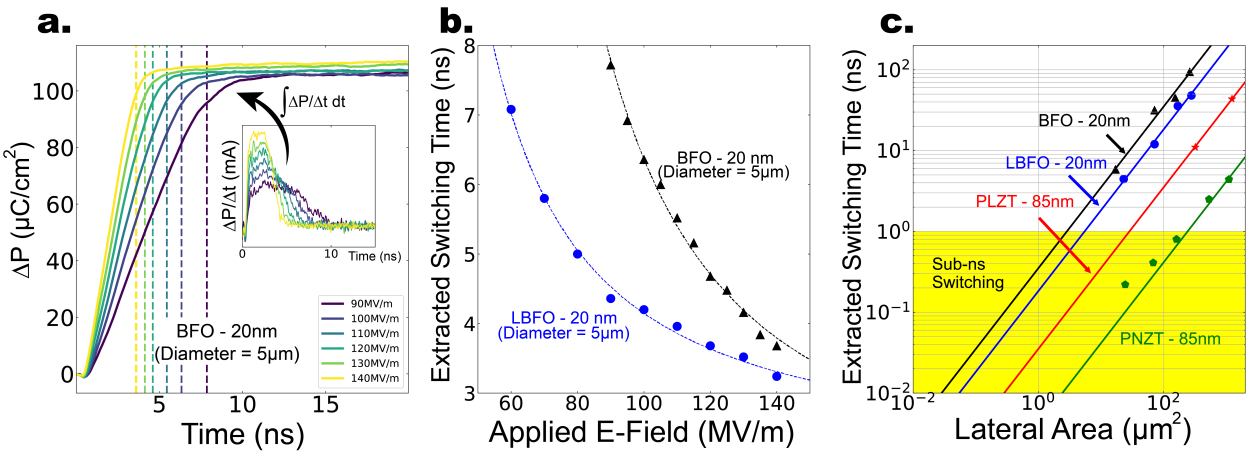

Figure 2.5: From [26]. **a.** shows the polarization transient, determined by integrating the difference between the switching and non-switching current response in the system (inset). Dashed vertical lines show extracted switching time, defined as the time when polarization reached 90% of saturation. **b.** shows experimentally observed switching times for 20 nm-thick $BiFeO_3$ (BFO) and 20 nm-thick $Bi_{0.85}La_{0.15}FeO_3$ (LBFO) as a function of applied field. The data reveals low-ns switching (dashed lines provide a guide to the eye). **c.** shows switching time as a function of area for the following samples: 20 nm $BiFeO_3$ (BFO), 20 nm $Bi_{0.85}La_{0.15}FeO_3$ (LBFO), 85 nm $Pb_{.9}La_{.1}[Zr_{.2}Ti_{.8}]O_3$ (PLZT) and 85 nm $Pb[Nb_{.04}Zr_{.29}Ti_{.67}]O_3$ (PNZT). Solid lines are linear best fits. The data shown is at an applied field of 95MV/m, 95MV/m, 26MV/m, and 60MV/m for BFO, LBFO, PLZT, and PNZT, respectively. I include similar data for all samples and applied fields in this study (Fig. 2.6).

Using pulsed ferroelectric measurements, I probe switching dynamics in multiferroic BFO, revealing low-ns switching times and a clear pathway to sub-ns switching. My data is well described by a nucleation and growth model, which accounts for the various timescales

in the switching process, namely 1) the ferroelectric polarization switching (bound-charge) dynamics and 2) the RC-limited movement of free-charge in the circuit. My model shows good agreement with observed data and begins to bridge the gap between experiment and theory, indicating pathways to study ferroelectric switching on intrinsic timescales.

While there has been extensive work on quasi-static magnetoelectric coupling in BFO, and electric-field control of magnetization has been experimentally demonstrated,[9, 67] the dynamics, fundamental speed limits, and mechanisms of ferroelectric and magnetoelectric switching on intrinsic timescales are largely unexplored. One theoretical study using a first-principles-based effective Hamiltonian within molecular-dynamics simulations predicted ultrafast (∼ps) switching of both ferroelectric and magnetic order in BFO[19] and various theoretical works have predicted ferroelectric switching times on the order of tens of ps.[55, 68] In proper ferroelectrics, it has often been speculated that the limit on switching speed is imposed by an acoustic-phonon mode (approximately the velocity of sound) which sets a limit on domain-wall propagation speed. The ferroelectric phase transition is a structural transition, so, in order to reverse the ferroelectric order parameter, the lattice must also reorient. The speed at which this process can occur is thus limited by the ability of the lattice to respond, or the speed at which "knowledge" of the switching event can traverse the system. The rate at which structural distortion information is transmitted in a material is precisely the speed of sound. Additionally, condensation of long-wavelength acoustic phonon modes are largely responsible for correlated behavior (*i.e.*, domains) in ferroelectrics at equilibrium[1], and reversal of any such structures must be mitigated by the same acoustic phonon modes.

To contextualize this intrinsic limit on ferroelectric switching with an example, one would expect that switching 100 nm of a prototypical ferroelectric such as $PbZr_{1-x}Ti_xO_3$ (velocity of sound ≈ 2500 m/s [58]), would take ≈ 40 ps. There have been numerous experimental studies of switching kinetics in ferroelectrics, both in bulk and thin films;[53, 69, 70, 71, 72, 73, 74, 75] however, these experiments detail a wide range of switching times, and generally report times considerably longer than those predicted by theory. To date, experimental observations of ultrafast switching have been limited, with only a few works approaching the low-ns time scale, [59, 60, 61] and only one reporting a switching time of hundreds of ps.[58] Importantly, and almost ubiquitously in the literature, switching studies claim convolution between the switching time of the ferroelectric and RC-effects from the measurement circuit. Using an electrical test setup that is capable of accessing timescales on the order of hundreds of ps, I measure the switching dynamics of thin-film $Bi_{0.85}La_{0.15}FeO_3$ (LBFO) and BFO. My data show a pathway to sub-ns switching, which is a key milestone for device applications.[2] I developed a model for switching which accounts for free-charge dynamics in the measurement circuit (*i.e.*, RC-effects and parasitics) and demonstrate that such a model accurately describes switching in (L)BFO capacitors as well as a variety of other thin-film ferroelectrics. Finally, the model sheds light on the large disparities in experimentally observed switching times, and provides motivation to study switching on intrinsic timescales.

I performed pulsed measurements of ferroelectric polarization switching (Fig. 2.2, 2.1). A sequence of 3 pulses (Fig. 2.1a), each with nominal rise time of 70 ps (applied using a Berkeley

Nucleonics BN765 fast rise time pulse generator), is used to first preset the ferroelectric capacitor, second measure the switching current transient (Fig. 2.1c), and third measure the non-switching current transient (Fig. 2.1d) of the circuit. Current transients are detected via a Tektronix TDS 6604 Digital Storage Oscilloscope (6GHz, 20GS/s). By subtracting the non-switching transient from the switching transient, I determine the contribution to measured current arising from switching of the ferroelectric polarization alone.[58, 59, 60, 61] Any contribution to currents arising from leakage, interfacial Schottky barriers and non-linear dielectric effects (present in all ferroelectric capacitors [62, 63, 64, 65, 66]) is subtracted out when I analyze the difference between the switching and non-switching current transients.

Pulsed measurements of ferroelectric capacitors are, by necessity, performed within the context of a measurement circuit which imposes additional constraints. As highlighted (Fig. 2.1a,b), careful consideration of the complete circuit is required to understand ferroelectric switching in such configurations. The transmission line delivering and collecting the signal is impedance matched from the pulse generator to the probe tip (DCP-150R coaxial probes: characteristic impedance of 50Ω) and from the probe tip to the oscilloscope. To quantitatively measure the parasitics in the circuit, I extract, via fitting of the non-switching pulse current response to an RC-curve, the RC-time of the measurement circuit and find that it is independent of applied voltage (Fig. 2.1d, insets) and scales linearly with the area of the ferroelectric capacitor being studied (Fig 2.1e). The latter observation indicates that the measurement circuit capacitance is dominated by the ferroelectric device under study. Via extrapolation of the extracted RC-time dependence on device area, I are able to determine the effective time-scale of the parasitics of the circuit to be ≈ 318ps (Fig 2.1e), which matches well with the observed rise time of a pulse through the identical circuit with the ferroelectric capacitor removed (Fig. 2.1e).

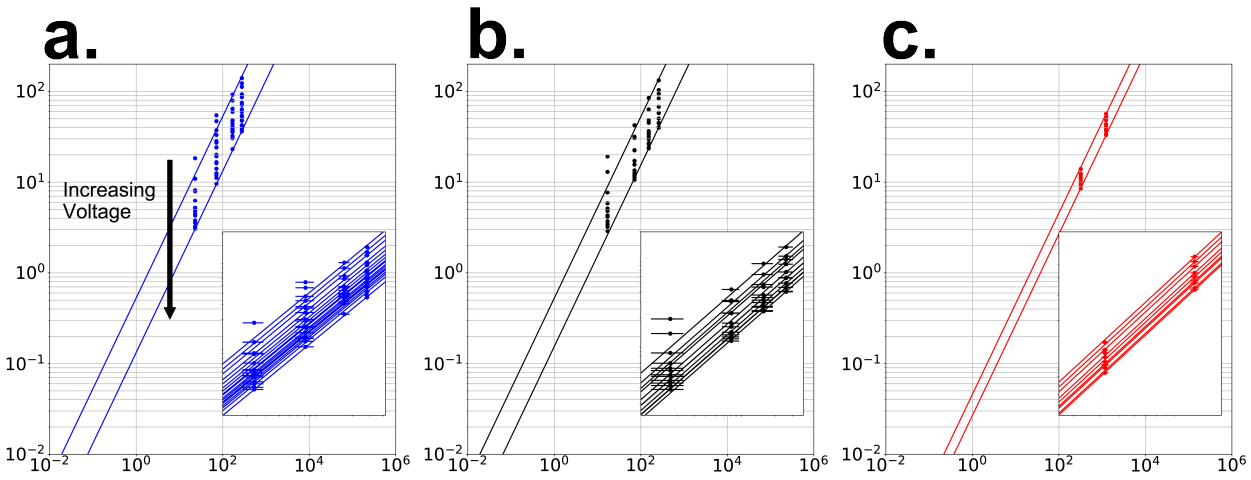

Figure 2.6 *(previous page)*: From [26]. Universality of area scaling. Shown is data for a variety of samples (LBFO, BFO, PLZT in panels **a**., **b**.,**c**., respectively) and voltages, all exhibiting linear area scaling of switching times. The bands in each panel show the range of linear best fits (for different applied fields) of switching time as a function of area. The inset in each panel shows data (error bar in area from fabrication) and linear best fits for all applied fields in the study. As indicated by the arrow in the first panel, higher applied fields induce faster switches.

2.2.1 Role of Landau Free Energy

To better understand the mechanisms and limits on ferroelectric switching I use high quality epitaxial (Fig. 2.8) ferroelectric thin films with systematically tuned spontaneous polarization and study switching under a range of applied electric fields and device sizes. All samples have symmetric top and bottom $SrRuO_3$ (SRO) electrodes. By integrating the difference between the switching and non-switching response current, I obtain the polarization transient (Fig. 2.5a, 2.9) and extract the switching time, defined as the time when the switched polarization reaches 90% of its saturation value (vertical lines in Fig. 2.5a). I show extracted switching time as a function of applied field for 20-nm-thick BFO and LBFO films (Fig. 2.5b). As observed, the LBFO consistently switches faster than its BFO counterpart.

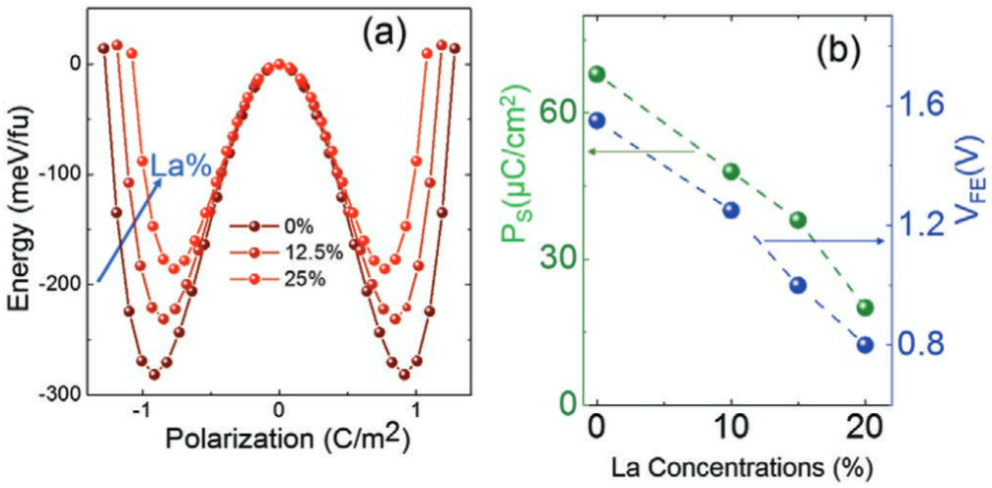

Figure 2.7: Used with permission from [51]. Effect of La substitution in the BFO system. **a**. Theoretical modeling data, obtained from first-principles calculations, showing the evolution of the free energy of BFO with varying La doping. **b**. Variation of saturation polarization (P_S) and ferroelectric switching voltage (V_{FE}) with La concentration of 100 nm thin films.

Within the BFO system, it has been shown experimentally that lanthanum substitution (Fig. 2.7) reduces the rhombohedral distortion thereby lowering the magnitude of the remnant polarization and the coercive field (Fig. 2.8). Similarly, density-functional-theory calculations show that lanthanum substitution reduces both the potential-energy barrier between, and magnitude of, the degenerate ground states of polarization.[76, 51, 52] This systematic change in the free-energy landscape manifests itself as a lowering of the activation energy for switching. Similar dependence on the spontaneous polarization (or, conversely, the spontaneous structural distortion) is also observed in other ferroelectrics (Fig. 2.10a). For example, a $Pb_{0.9}La_{0.1}[Zr_{0.2}Ti_{0.8}]O_3$ (PLZT) sample, with a switchable polarization of $\approx 15\mu C/cm^2$ switches much faster than the (L)BFO, with a switchable polarization $\approx (80)100\mu C/cm^2$. I show switching times as a function of lateral device area for LBFO, BFO, PLZT, and $Pb[Nb_{0.04}Zr_{0.29}Ti_{0.67}]O_3$ (PNZT) (extracted from [77]) (Fig. 2.5c) for single applied fields and include extended results for LBFO, BFO, and PLZT for several applied fields (Fig. 2.9). In all cases, a similar trend is observed, wherein there is a linear scaling with capacitor area. As such, the data presented provide a pathway to sub-ns switching for capacitor areas of $\leq 5\ \mu m^2$ for LBFO.

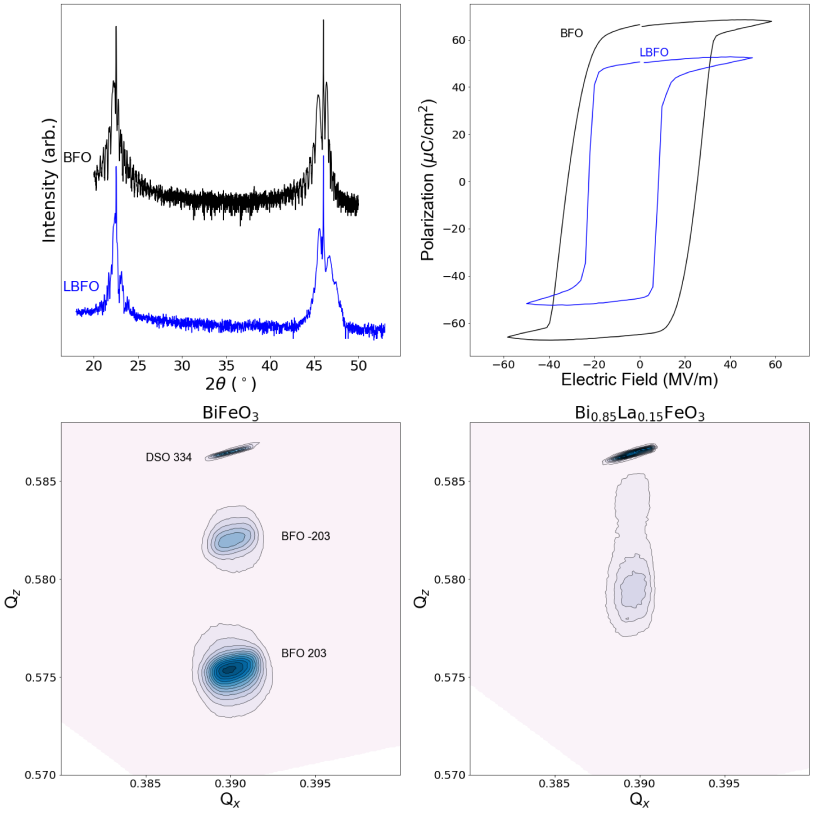

Figure 2.8 *(previous page)*: From [26]. **a**. XRD Theta-2 theta scans of $BiFeO_3$ and $Bi_{0.85}La_{0.15}FeO_3$ films deposited on single-crystal substrate DSO $(110)_O$. **b**. P-E hysteresis loops for $BiFeO_3$ and $Bi_{0.85}La_{0.15}FeO_3$ films. Recipical sapce mappings for **c**. $BiFeO_3$ and **d**. $Bi_{0.85}La_{0.15}FeO_3$ films thin films in the (203)pc diffraction condition. From the XRD data, the LBFO and BFO do not show a clear difference in terms of crystallinity.

I developed a scheme to compare switching times across materials and device sizes. By re-scaling the extracted switching time (90% of switched polarization saturation) as: $t_s \rightarrow t_s \times t_{\mathrm{FE}}/(AR)$ where t_{FE}, A, and R are the thickness of the ferroelectric, device area, and external resistance, respectively, (Fig. 2.1a) I can map switching-time data onto families of curves (plotted as switching time vs. applied electric field), which depend only on the ferroelectric material (Fig. 2.10). Since the capacitance of the circuit is dominated by ferroelectric capacitor (Fig. 2.1e) the ratio RA/t_{FE} enters directly into the calculation for the RC-time of the circuit. I note that in performing the re-scaling (Fig. 2.10), I account for the extrinsic factors impacting the RC-time of the measurement circuit, revealing dynamics dependent on material alone. The success of such re-scaling illustrates an effective way to compare switching speeds across samples and materials where the free-energy landscape differs.

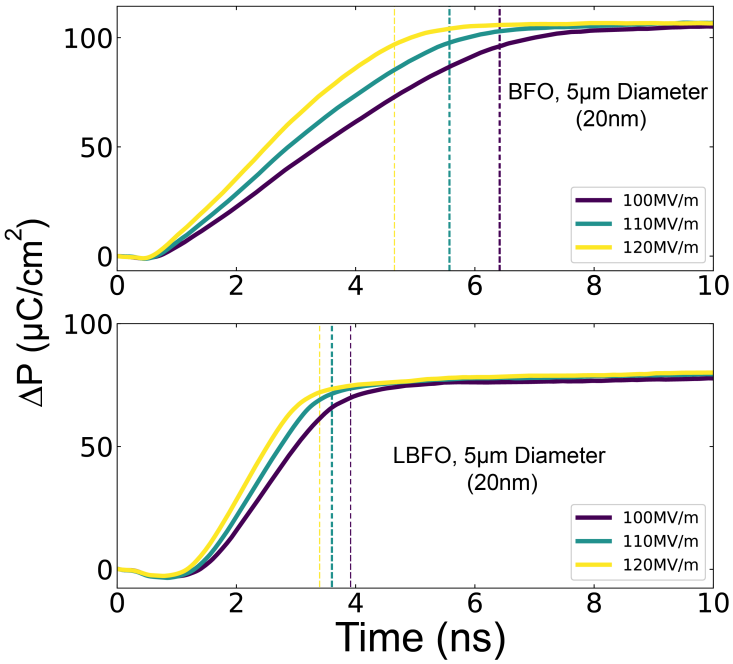

Figure 2.9: From [26]. Polarization switching transients for (L)BFO capacitors for various applied fields. Vertical dashed lines show extracted switching time.

2.2.2 Bound- vs. Free-charge Dynamics

When studying ferroelectric switching, I must account for the charge dynamics of the entire system, including the measurement circuit and parasitics inside and outside the ferroelectric capacitor (*e.g.* leakage current, nonlinear dielectric response, external resistance and capacitance, and electrode-ferroelectric interfacial Schottky barriers). The total observed current (I_{obs}) is comprised of the sum of displacement and leakage (I_{L}) currents. Displacement current has three contributions; ferroelectric switching (I_{FE}), linear dielectric response (I_{LD}), and non-linear dielectric response (I_{NLD}).

$$I_{\text{obs}} = I_{\text{L}} + I_{\text{FE}} + I_{\text{LD}} + I_{\text{NLD}} \tag{2.1}$$

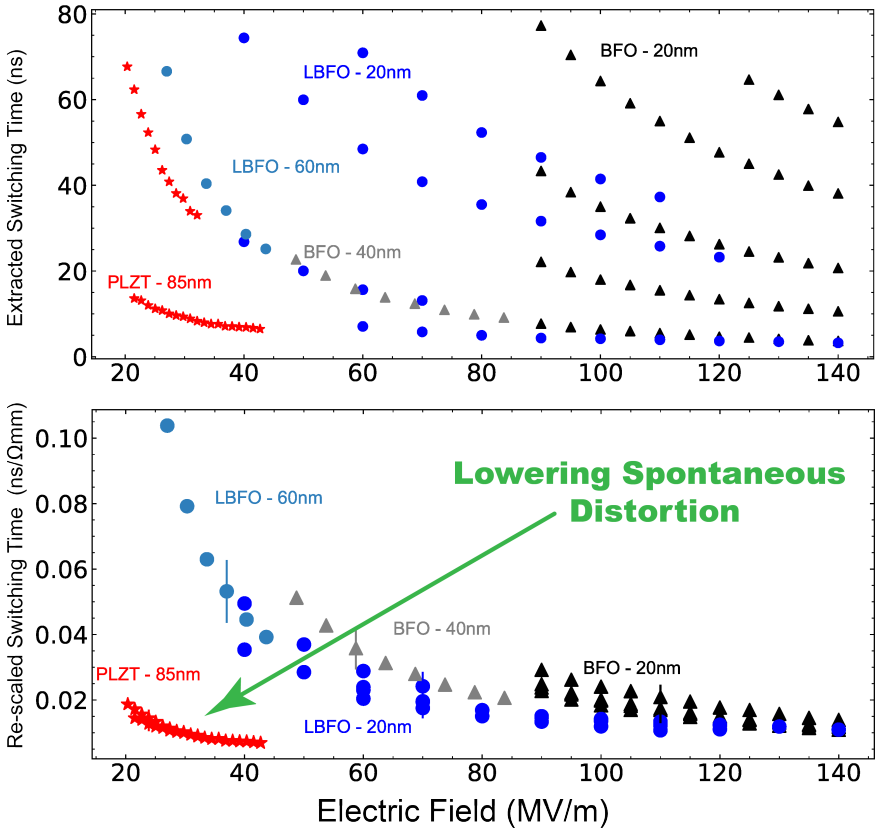

Figure 2.10: From [26]. The top panel shows switching time data for a variety of measurements as a function of applied field. I vary composition, thickness and lateral capacitor size and find a broad spread in data. Decreasing capacitor size correlates with faster switching time. In the bottom panel I re-scale switching time as $t_s \rightarrow t_s \times t_{\text{FE}}/(AR)$ and collapse all data points of a single composition onto a single curve, providing a protocol for comparing switching times across materials and samples.

The observed current ($I_{\rm obs}$), the displacement current ($I_{\rm disp} = I_{\rm FE} + I_{\rm LD} + I_{\rm NLD}$), and the (leakage) current ($I_{\rm L}$) arising from Schottky barriers [62, 78, 63, 64, 65, 66, 79] at the metal/ferroelectric interfaces and resistive leakage in the ferroelectric (Fig. 2.1b) are given by:

$$I_{\rm obs} = \frac{V_{\rm in} - V_{\rm FE}}{R} \tag{2.2}$$

$$I_{\rm disp} = \frac{V_{\rm in} - V_{\rm FE}}{R} - I_{\rm L} \tag{2.3}$$

$$I_{\rm L} = A\frac{2J_{S1}J_{S2}\sinh\frac{qV_{\rm FE}}{2kT}}{J_{S1}\exp\left[-\frac{qV_{\rm FE}}{2kT}\right] + J_{S2}\exp\left[\frac{qV_{\rm FE}}{2kT}\right]} + V_{\rm FE}/R_{\rm P} \tag{2.4}$$

where R, $V_{\rm in}$, $V_{\rm FE}$, $I_{\rm L}$, A, q, T, and k are the external resistance, applied voltage, voltage across the ferroelectric, current through the back-to-back Schottky diodes with a series resistance (Fig. 2.1b) [80, 81] and parallel resistor ($R_{\rm P}$), device area, elementary charge, temperature, and Boltzmann constant, respectively. $J_{S1,S2} \equiv A^*T^2\exp\left[-\frac{-q\Phi_{\rm b1,\ b2}}{kT}\right]$, where A^* is the Richardson constant, and $\Phi_{\rm b1,\ b2}$ is the Schottky barrier at the interfaces[80, 81]. The simulated (Fig. 2.12) maximum leakage current is $\approx$ 10µA, similar to the observed steady state leakage current (Fig. 2.1d) of $\approx$ 4µA. For a complete list of parameters used herein, Table 2.1. The charge on the ferroelectric capacitor ($Q_{\rm cap}$) is given by:

$$Q_{\rm cap} = A(\epsilon_0\epsilon_r E_{\rm FE} + P) \tag{2.5}$$

where $E_{\rm FE}$, ϵ_0, ϵ_r, and P, are the electric field across the ferroelectric, vacuum dielectric constant, relative permittivity, and average ferroelectric polarization, respectively.

Combining Eqs. 2.2 - 2.5, I find:

$$\frac{dQ_{\rm obs}}{dt} = \frac{1}{R}\left[V_{\rm in} - \frac{t_{\rm FE}\left(Q_{\rm cap}/A - P\right)}{\epsilon_0\epsilon_r}\right] \tag{2.6}$$

$$\frac{dQ_{\rm cap}}{dt} = \frac{1}{R}\left[V_{\rm in} - \frac{t_{\rm FE}\left(Q_{\rm cap}/A - P\right)}{\epsilon_0\epsilon_r}\right] - I_{\rm L} \tag{2.7}$$

In the limit $I_{\rm L} \to 0$, Eq. 2.6, 2.7 reduce to Eq. 4 of [23].

Polarization reversal in ferroelectrics has been successfully described by a nucleation and growth model [82, 83, 24, 55] where domain-wall motion determines switching speed. Thus, domain-wall velocity is of the utmost importance in this process. In his seminal work on polarization reversal, Merz found the domain-wall velocity (u) to be empirically described by [53, 69]:

$$u = u_0 e^{-\alpha/E_{\rm FE}} \tag{2.8}$$

where u_0, α, $E_{\rm FE}$, are the domain-wall velocity at infinite applied field, the activation field (related to the double-well structure of the Landau free-energy landscape), and the electric-field across the ferroelectric, respectively. Merz' law has been used since its conception, and it is commonly found that the activation field is $\approx 10E_c$ where E_c is the coercive field [84].

Merz' law provides a framework to describe the average polarization dynamics of the film. I assume nucleation and growth of cylindrical domains (Fig. 2.12a), yielding the rate of change of polarization:

$$\frac{dP}{dt}(t) = 2\pi n r(t) u(t) P_{\mathrm{sw}} = 2\pi n u(t) P_{\mathrm{sw}} \int_0^t u(t')dt' \tag{2.9}$$

where n, $r(t) = \int_0^t u(t')dt'$, $u(t)$, P_{sw} are the areal density of nucleated domains, instantaneous domain radius, instantaneous domain-wall velocity, and switchable polarization, respectively. Eqs. 2.6-2.9 define a system of equations which are simultaneously solved numerically, yielding polarization, observed current, domain-wall velocity, and voltage across the ferroelectric as a function of time. I approximate the relative permittivity as constant [76] for the present simulations. Increased leakage current will slow polarization reversal as the voltage across the ferroelectric will be reduced. Here, the observed leakage current is ≥ 4 orders of magnitude smaller than displacement current (Fig. 2.1), and thus contributes only a small ($\sim$ mV) change in voltage. I compare (Fig. 2.11) resistive versus Schottky emission leakage current and show that even for reduced parallel resistances the effect on switching polarization is minimal in macroscopic device structures.

The model reveals a transient voltage profile across the ferroelectric (Fig. 2.12b) where the voltage across the device *reduces* during switching. This effect has been observed before, is known to stem from the negative curvature of the double well potential near the zero of polarization, and is sometimes referred to in the literature as "transient negative-capacitance", where, during switching, the voltage across the ferroelectric transiently decreases despite an increase in current (recall $dQ/dt = CdV/dt$, so $C < 0$) [23, 85, 86, 87]. Here, I further explore the origins of such a temporal voltage profile and discuss the implications for ferroelectric switching. The physical origin of the time-dependent voltage and domain-wall velocity profile (Fig. 2.12b) can be explained as a competition between free- and bound-charge dynamics.

Two dynamical timescales play an essential role in ferroelectric switching of capacitor structures. The first is the polarization (bound-charge) dynamics (here modeled as nucleation and growth within the context of Merz' law), while the second is RC-limited movement of free-charge in the measurement circuit.

The key equation linking free-charge on the ferroelectric capacitor, voltage across the ferroelectric and average ferroelectric polarization is given by Eq. 2.5 (for simplicity I ignore leakage current at present). The rate of change of charge on the ferroelectric capacitor is described by Eq. 2.7

$$\frac{dQ_{\mathrm{cap}}}{dt} = \frac{1}{R}\left[V_{\mathrm{in}} - t_{\mathrm{FE}} E_{\mathrm{FE}}\right] \tag{2.10}$$

which precisely describes free charge dynamics in a normal RC-circuit. The rate of change of the average polarization of the ferroelectric is given by:

$$\frac{dP}{dt}(t) = 2\pi n r(t) u(t) P_{\mathrm{sw}} = Kru \tag{2.11}$$

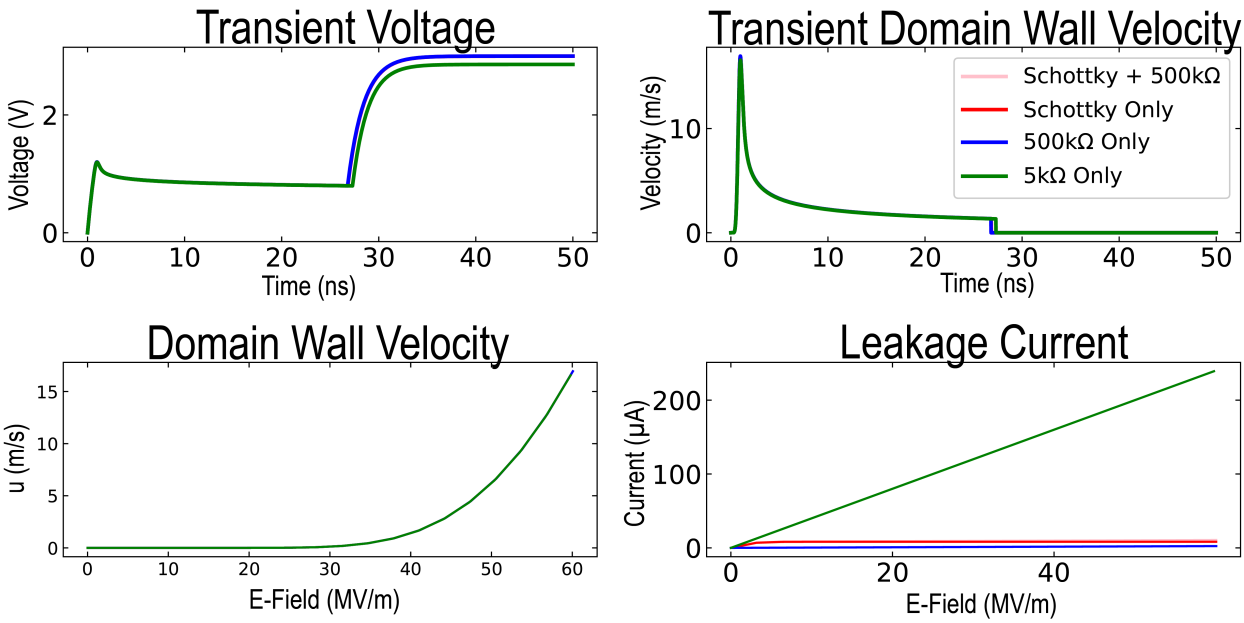

Figure 2.11: From [26]. Effect of leakage current. Top panels show transient voltage (Left) and domain wall velocity (Right) as a function of time for various leakage mechanisms and values. As observed, differences in leakage mechanism have little effect on switching. Bottom panels show domain wall velocity (Left) and leakage current (Right) as a function of electric field across the ferroelectric during switching for the same leakage mechanisms. Even with dramatic reduction of parallel resistance (5kΩ) resulting in a dramatic increase in leakage current (Bottom Right Panel), switching time is not dramatically effected (as observed in the top panels, Green). Importantly, leakage current will more dramatically affect switching dynamics at smaller device sizes, higher applied field and lower spontaneous distortions.

which describes growth of cylindrical reverse polarized domains. I have defined a new constant, $K \equiv 2\pi n P_{\mathrm{sw}}$. Substituting Eq. 2.10 and Eq. 2.11 in to Eq. 2.7 yields

$$\frac{dE_{\mathrm{FE}}}{dt} = \frac{1}{\epsilon_0 \epsilon_r}\left[\frac{1}{RA}(V_{\mathrm{in}} - t_{\mathrm{FE}}E_{\mathrm{FE}}) - Kru\right] \tag{2.12}$$

Eq. 2.12 now describes the electric field across the capacitor and includes contributions from free- and bound-charge. Upon examination of Eq. 5, I find a competition between the free-charge dynamics ($\frac{1}{RA}(V_{\mathrm{in}} - t_{\mathrm{FE}}E_{\mathrm{FE}})$) and the bound-charge dynamics (Kru), which, together, determine the rate of change of the electric field. Since domain wall velocity is a function of electric field (Merz' law), this competition also feeds back into the process of polarization switching itself. Initially, when the external switching voltage (V_{in}) is turned on, $E_{\mathrm{FE}}(t=0) = u(t=0) = 0$. Which means that at $t = 0$,

$$\frac{dE_{\mathrm{FE}}}{dt} = \frac{V_{\mathrm{in}}}{\epsilon_0 \epsilon_r RA} > 0 \tag{2.13}$$

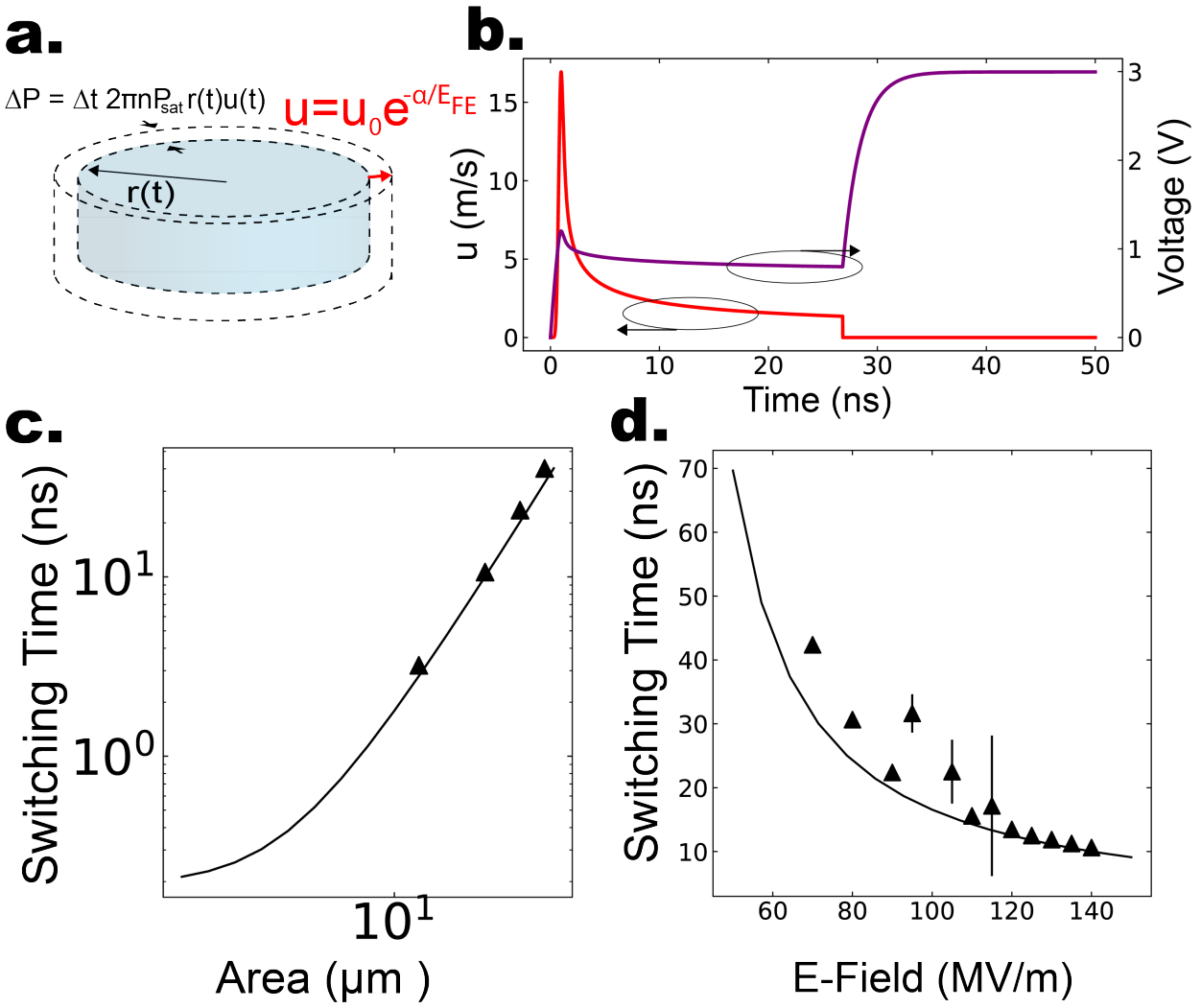

Figure 2.12: From [26]. **a.** shows a schematic of a single growing (radially) cylindrical domain with instantaneous radius $r(t)$ and domain-wall velocity $u(t)$ given by Merz' law. The change in polarization for many domains, with density n, ΔP, is given for an infinitesimal time-step Δt. In **b.** I show simulated voltage and domain-wall velocity transient profiles during ferroelectric switching. **c.** shows measured switching time for 140MV/m applied field in 20nm-thick BFO (points) and simulated switching time (solid line) as a function of area. The asymptote is that of the "domain growth limit." **d.** shows switching time for 14μm diameter 20nm-thick BFO capacitors (points) and simulated switching time (solid line) as a function applied field. For a full list of parameters used in the simulation see Table 2.1.

implying voltage across the ferroelectric begins to rise at time $t = 0$. As voltage across the ferroelectric builds, domain wall velocity increases and domains grow. If the domain radius (r) and domain wall velocity (u) satisfy $Kru = \frac{1}{R}[V_{\text{in}} - t_{\text{FE}}E_{\text{FE}}]$ at some time t_{critical} the

Parameter	Meaning	Value
P_{sw}	Switchable Polarization	$100\mu C/cm^2$
T	Temperature	300K
t_{FE}	Ferroelectric Film Thickness	20nm
$\Phi_{\text{b1,b2}}$	Schottky Barrier Height	.75eV[62, 78]
R	External Resistance	250Ω
ϵ_r	Relative Permittivity	100
α	Activation Field	2.5×10^8V/m[84]
u_0	Maximum Domain Wall Velocity	2500m/s
n	Density of Nucleated Domains	1×10^{14} m^{-2}

Table 2.1: From [26]. List of Parameters used for simulated data.

voltage across the ferroelectric (and domain wall velocity) reach a maximum. Then ($t > t_{\text{critical}}$), the voltage across the ferroelectric (and therefore domain wall velocity) decreases monotonically until switching completes. To see this explicitly, I search for extrema of $E_{\text{FE}}(t)$ by setting its first time derivative to zero:

$$\frac{dE_{\text{FE}}}{dt} = \frac{1}{\epsilon_0 \epsilon_r}\left[\frac{1}{RA}(V_{\text{in}} - t_{\text{FE}}E_{\text{FE}}) - Kru\right] = 0 \tag{2.14}$$

which gives the condition for a extremum:

$$Kru = \frac{1}{RA}\left[V_{\text{in}} - t_{\text{FE}}E_{\text{FE}}\right] \tag{2.15}$$

relating the free- and bound-charge dynamics. Recalling that domain wall velocity (Merz' law) is given by Eq. 2.8, taking the derivative, I find:

$$\frac{du}{dt} = u_0 e^{-\alpha/E_{\text{FE}}}\frac{\alpha}{E_{\text{FE}}^2}\frac{dE_{\text{FE}}}{dt} = u\frac{\alpha}{E_{\text{FE}}^2}\frac{dE_{\text{FE}}}{dt} \tag{2.16}$$

thus, in search of extrema, when the rate of change of the electric field ($\frac{dE_{\text{FE}}}{dt}$) is zero, so is the acceleration ($\frac{du}{dt}$) of the domain wall.

$$\frac{dE_{\text{FE}}}{dt} = 0 \implies \frac{du}{dt} = 0 \tag{2.17}$$

Peak in domain wall velocity during switching: To determine whether extrema are maxima or minima, I examine the second time derivative (when $\frac{dE_{\text{FE}}}{dt} = 0$)

$$\frac{d^2E_{\text{FE}}}{dt^2} = \frac{1}{\epsilon_0\epsilon_r}\left[-\frac{t_{\text{FE}}}{RA}\cancel{\frac{dE_{\text{FE}}}{dt}} - K\left(u^2 + r\cancel{\frac{du}{dt}}\right)\right] = -\frac{K}{\epsilon_0\epsilon_r}u^2 \leq 0 \tag{2.18}$$

which means that any extrema must be a maximum (second time derivative is < 0), or $u = 0$. In the case that $u = 0$ and $\frac{dE_{\rm FE}}{dt} = 0$ this is a trivial solution with no dynamics. Notably, at $t = 0$, $u = 0$ but $\frac{dE_{\rm FE}}{dt}(t = 0) \neq 0$, producing non-trivial evolution. Since extrema in electric field (domain wall velocity) can only be maxima, once a maximum is reached, the electric field (domain wall velocity) will decrease monotonically until switching stalls or completes (Fig. 2.12b). Physically, a peak in electric field (domain wall velocity) can occur only once, because after such a peak, the radii of growing domains are sufficiently large that any change in free-charge, which would otherwise transiently increase the voltage across the ferroelectric, will coincide with a sufficiently high change in polarization which will negate the voltage increase. When switching completes as in Fig. 2.12b, the domain wall velocity drops to zero, and the voltage across the capacitor follows a transient RC-curve charging to $V_{\rm in}$ (assuming no leakage current). In Fig. 2.13, I show the effect of reducing the switchable polarization ($P_{\rm sw}$) on the transient voltage ($E_{\rm FE}t_{\rm FE}$) and domain wall velocity (u) profile. As observed, a low switchable polarization results in little deviation in voltage from a normal RC-curve. This is contrast to a large switchable polarization which dramatically deforms the transient voltage profile. These observations can be understood within the context of a negative feedback loop, where, during the polarization switching process, rapidly growing domains (switching bound-charge) act to lower the voltage across the device. This lower voltage across the ferroelectric results in slower domain wall velocities and extends switching time.

As seen in Fig. 2.13, electric field (and domain wall velocity) does not have to reach a maximum during switching if complete switching occurs rapidly with minimal deviation in electric field from an RC-curve. I explore this scenario quantitatively. In order for no transient peak in electric field (domain wall velocity) to occur, I require that $\frac{dE_{\rm FE}}{dt} > 0$ for all time during switching. This is satisfied if

$$Kru < \frac{1}{RA}\left[V_{\rm in} - t_{\rm FE}E_{\rm FE}\right] \tag{2.19}$$

The radii of growing domains, the domain wall velocity and the electric field are all time dependent and coupled, so there is not an analytical solution to this inequality. However, I can explore an important limiting case. The radius of growing domains can be no larger than one half of the distance between adjacent nucleation sites (otherwise switching would be complete): $r_{max} = 1/(2\sqrt{n})$ so, $Kru \leq Kr_{max}u$ and, substituting in the definition of K, $\implies Kru \leq \pi\sqrt{n}P_{\rm sw}u$. Thus in order for no maximum to occur in electric field (domain wall velocity) during ferroelectric switching, a sufficient condition is:

$$Kru \leq \pi\sqrt{n}P_{\rm sw}u < \frac{1}{RA}\left[V_{\rm in} - t_{\rm FE}E_{\rm FE}\right] \implies u < \frac{V_{\rm in} - t_{\rm FE}E_{\rm FE}}{RA\pi P_{\rm sw}\sqrt{n}} \tag{2.20}$$

substituting in Merz' law for the domain wall velocity, I find the condition:

$$u_0 e^{-\alpha/E_{\rm FE}} < \frac{V_{\rm in} - t_{\rm FE}E_{\rm FE}}{RA\pi P_{\rm sw}\sqrt{n}} \tag{2.21}$$

I plot Eq. 2.21 in Fig. 2.14 and observe two regions. If, during the course of the ferroelectric switching event, the electric field across the capacitor stays in region I, there will be no maximum in electric field (domain wall velocity) in time domain. However, if, during the switching event, the electric field increases sufficiently to cross from region I into region II, I will observe a maximum in electric field (domain wall velocity) and then subsequent monotonic reduction in electric field (domain wall velocity) at times after which the maximum occurred. As can be observed upon examination of Eq. 2.21, one way to extend region I to higher electric fields is by decreasing the switchable polarization, and indeed as shown in Fig. 2.13, upon lowering the switchable polarization, I are able to get rid of the peak in voltage across the ferroelectric (domain wall velocity) during switching.

Role of switchable polarization magnitude: This model further explains (in addition to the lowering of the activation energy, as described in Section 2.2.1) the decrease in switching time observed with decreased spontaneous distortion (Fig. 2.10). As voltage across the ferroelectric, polarization, and domain wall velocity are all intimately linked by Eq. 1, a lower switchable polarization will result in smaller deviations from normal dielectric capacitive charging and correspondingly, less significant reductions in domain wall velocity, i.e. faster switching.

As a final illustrative example, consider a 14µm diameter BFO capacitor with assumed switchable polarization of 100µC/cm^2, which yields approximately 150pC of bound-charge. If I assume such a device (ignoring momentarily the ferroelectric nature) has a capacitance of 20pF, an applied voltage of 5V produces only 100pC of free charge on the metallic electrodes. Since the free- and bound-charges have similar magnitudes, a change in the polarization can dramatically effect the voltage across the device.

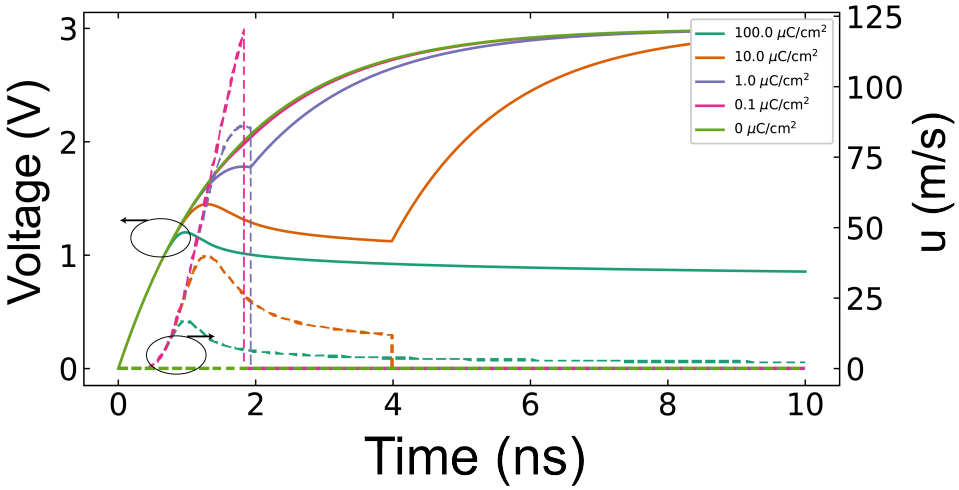

Figure 2.13 *(previous page)*: From [26]. Simulation: effect of lowering switchable polarization on voltage (solid lines, left y-axis) and domain wall velocity (dashed lines, right y-axis) transient profiles. Once switching completes, velocity drops abruptly to zero and voltage follows an RC-charging curve. For higher switchable polarizations the voltage profile exhibits larger deviations from an RC-curve during switching. At low switchable polarizations, the voltage curve (Solid Pink) shows little deviation from a true RC-curve (Light Green) and I observe no peak in domain wall velocity during switching. Notably, the peak observed occurs when switching completes.

2.2.3 Intrinsic vs. Extrinsic Limits

Based on my model, I can extract the area and field dependence of the switching time (Fig. 2.12c, d). For fixed capacitor dimensions, this model is in close agreement with the experimental data of the field dependence of the switching time (Fig. 2.12d). The areal scaling is consistent with the experimental data (Fig. 2.12c, Fig. 2.5c); however for smaller device sizes, I begin to observe asymptotic behavior (similar to the PNZT data Fig. 2.5c). A likely origin of the asymptote in areal scaling is the rise time of the measurement circuit (which includes parasitics) and the device under study. This sets an "extrinsic" limit to switching speed whereby the switching cannot occur faster than the stimulus. When the parasitics of the circuit do not limit switching, the asymptotic behavior can arise due to an intrinsic "domain-growth limit", defined as the time it takes for adjacent growing domains to coalesce at maximum velocity (*i.e.*, $\sim u_0/\sqrt{n}$). A final possibility is "intrinsic" switching whereby nucleation and growth is no longer the switching mechanism. This would occur at very small thicknesses or lateral device sizes, likely on the order of the critical nucleus size [55] or in systems in which nucleation and growth can be sufficiently suppressed.

PNZT data deviation from Linear: The PNZT data was obtained on a fully integrated, chip mounted device, driven with a photoconductive switch for pulse application[58]. This significantly reduces the parasitics which set the "extrinsic" dynamical timescales in conventional probe-based setups. One explanation for the deviation observed is an approach toward intrinsic "domain growth limit" switching, where I are seeing the beginnings of asymptotic behavior. As detailed above, this is likely to occur as the spontaneous distortion of the PNZT sample is sufficiently small that the voltage across the ferroelectric deviates only slightly from the normal (RC-) charging curve, resulting in very high domain wall velocities.

As a final demonstration of an approach to intrinsic switching, I used free energy landscape engineering, in combination with improved film quality and area scaling to achieve sub-ns switching in LBFO, as observed in Fig. 2.15. The measurable charge decreases with capacitor area, making measurement of ever smaller capacitors (a requirement for further reductions in free-charge dynamical timescales) increasingly difficult. Nonetheless, this result indicates that I have a viable pathway to observing switching at least on the time-scale of the rise time of the pulse generator. The most straightforward way to go beyond that limit,

and, hopefully, approach limits set by the intrinsic physics of the ferroelectric, may be to use ultra-low coercivity ferroelectrics and "over-drive" the system *i.e.*, apply an exceptionally large voltage pulse[5] such that the time to reach an appreciable fraction of the activation energy is in fact lower than the rise time of the circuit. It will be, of course, difficult to definitively say that any asymptotic behavior observed in such an experiment is the result of intrinsic physics, unless the observed switching time is *unequivocally lower* than the rise time of the pulse. The implications of this work are significant for computing applications. In order to compete with current CMOS technology, any ferroelectric-based technology must be capable of operating at timescales below 1ns[2], a feat which I have already demonstrated here.

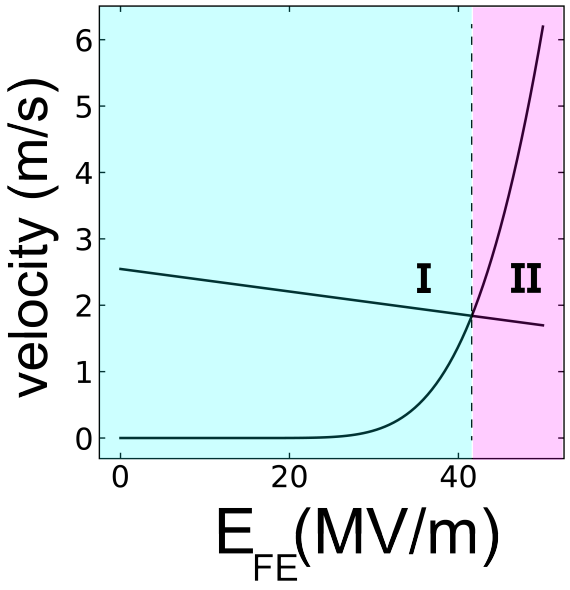

Figure 2.14: From [26]. Determining whether or not a peak in voltage across the ferroelectric (domain wall velocity) will occur during ferroelectric switching. If the electric field during switching stays in region I, no peak will occur, if the electric field crosses into region II, a peak will occur.

In summary, I present direct measurements of the polarization switching dynamics in the (L)BFO model system. My experimental measurements show a clear pathway to studying ferroelectric switching on timescales approaching that set by the intrinsic physics of the material. My model accurately predicts the scaling observed experimentally and presents an possible avenue to explain the wide disparity in switching times reported in the literature. Intrinsic ferroelectric switching, and mechanisms pertaining to that process, are convoluted

[5]By using ultra-low coercivity films, "exceptionally large" may be only a few volts

in current switching experiments by the competition between free- and bound-charge dynamical timescales. Careful consideration of the free- and bound-charge dynamics within the framework of the measurement circuit might explain why different measurements have yielded dramatically different results. While device scaling offers a viable pathway to sub-ns switching, it remains an important question to address the limits of such scaling, which will provide vital insight into intrinsic ferroelectric switching speeds and mechanisms.

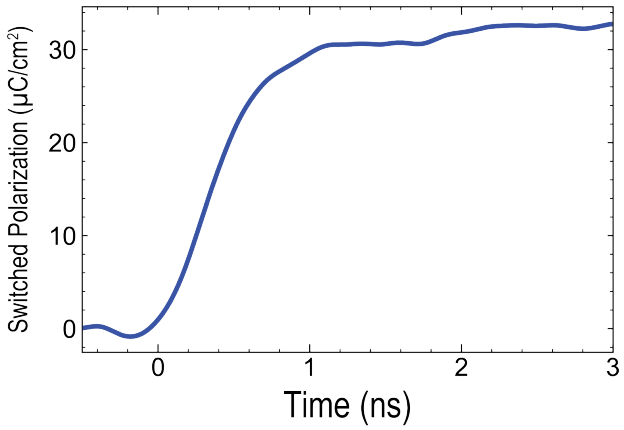

Figure 2.15: Sub-ns switching in LBFO 4μm diameter capacitor.

2.3 Ultra-low coercivity $BaTiO_3$

In this section, I turn to $BaTiO_3$ (BTO) as a means of further probing the limits on switching of ferroelectric capacitors and extending my results to a well-studied system which yields additional tunability in the free energy landscape. BTO is a prototype ferroelectric, and in its single-crystal form ferroelectric switching can be accomplished with small fields (coercive field $\approx$ 1kV/cm) and energy densities ($\sim$ 0.1J/cm^3), while maintaining a relatively large remanent polarization ($\approx$ 26μC/cm^2)[88]. It is also a chemically simple, environmentally benign, and robust ferroelectric which must be in the conversation as a candidate material for novel low-voltage, non-volatile, ferroelectric-based devices. BTO, unlike BFO, is not a magnetoelectric multiferroic, and, in the context of this dissertation, serves as an import reference material, helping to build a holistic picture of ferroelectric switching dynamics. The ferroelectric properties of BTO thin films have exhibited large variations and deviations from the values measured in single crystals, including: larger coercive fields [88, 89, 90, 91, 92, 93], increased switching energies and diminished remanent polarization [94, 95, 96, 97, 98].

Here, we synthesize high-quality, epitaxial BTO films[99] via pulsed-laser deposition and demonstrate ferroelectric properties that approach those of BTO single crystals. Structural, chemical, and device fabrication requirements reveal important metrics (see [99] for complete

details) that inform researchers how to achieve this "idealized" performance with the production of structurally ideal films having a direct and strong correlation to the best performance. Subsequent thickness-scaling studies produce films (<50nm in thickness) which exhibit the desired coercive voltages (<100mV) and fields (<10 kV cm^{-1}) sought for future applications [3]. While further reducing the film thickness reduces the coercive voltage, it does so at the expense of the remanent polarization. The important role of depolarization fields is evident in these model films (a topic discussed in detail in Chapter 4). The depolarization fields, however, have the fortunate consequence that they suppress the coercive field, thereby lower switching energy and enhancing switching speed. I observe switching times as short as ≈2 ns observed in 25-nm thick films with 5-μm-diameter capacitors and lateral scaling studies reveal a route to sub-nanosecond switching in devices as large as 10 μm^2.

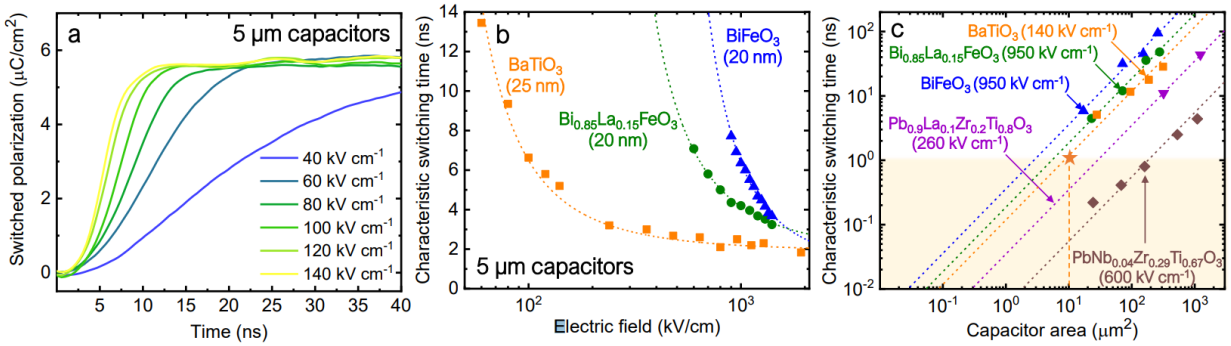

Figure 2.16: Used with permission from [99]. Switching dynamics studies on $BaTiO_3$ thin films grown at 60mTorr. **a.** Polarization transient curves as a function of applied field, measured on 5-μm-diameter circular capacitors. **b.** Extracted characteristic switching time as a function of applied electric field on 5-μm-diameter circular capacitors for 25nm-thick BTO, 20-nm-thick BFO, and 20-nm-thick $Bi_{0.85}La_{0.15}FeO_3$ films. The dashed curves are fits to Merz' law. **c.** Comparison of characteristic switching time between 25-nm-thick BTO films and other common ferroelectric thin films, as in Fig. 2.5. The dashed lines are linear fits to the data. The orange star is the projected capacitor area at which sub-ns switching time can be achieved with these BTO films.

As observed in Fig. 2.16, these near-bulk-like BTO films exhibit exceptional switching properties. The essential physics is captured in Fig. 2.16b,c (which can be compared to, and includes data from, Fig. 2.5 for BFO). I see the emergence of a family of curves (both as a function of electric field and area) for switching times, where a single curve corresponds to a single combination of spontaneous polarization and free energy landscape. Further, the BTO data shows the broad applicability of the area scaling and interplay between free- and bound-charge, discussed above. From a plot of switching time versus area, one can derive a meaningful comparison across material systems. From an applied, device design viewpoint, the same plot allows one to estimate the geometry required to reach a desired timescale (for

a given applied field). Finally, deviation from linear scaling allows one to study the ultimate limits on switching (both intrinsic and extrinsic).

2.4 On-going work

There are a number of on-going/future work projects that aim to study ferroelectric switching. One approach is to further manipulate the free-energy landscape, and/or switching mechanism. I will discuss one such pathway, *i.e.*, tuning mechanical boundary conditions, in Chapter 3. Other projects include further area scaling, by fabricating devices below 1μm in diameter. The signal to noise ratio is expected to decrease, where smaller areas result in smaller ferroelectric displacement currents. In order to increase the signal, we have considered using arrays of small capacitors, though this will introduce additional capacitance to the measurement circuit (slowing down the measurement speed). An alternative is to use an amplifying circuit, though such an amplifier must be capable of accessing timescales significantly faster than 1ns. This can be a challenge, though one option is to use an avalanche diode. Improved pulse generation, with faster rise times ($\leq$ 50ps), will also assist in accessing switching near intrinsic limits. I will discuss such experiments in greater detail in Chapter 6, Section 6.2

Other on-going work is predicated on observing, in real-time, the ferroelastic switching pathway (Fig. 1.8) in BFO. Such a measurement would enable studies of factors impacting the switching pathway (*i.e.*, strain), and have important implications for the switching of magnetic order (Fig. 1.7). I provide preliminary results for such an experiment, using time-resolved second-harmonic-generation, in Chapter 6, Section 6.2.1.2.

Chapter 3

The Role of Lattice Dynamics in Ferroelectric Switching

In Chapter 2, I discussed the interplay between free- and bound-charge dynamics and revealed a pathway to studying ferroelectric switching dynamics on intrinsic timescales. Even in macroscopic device structures, where free charge in the measurement circuit can convolute absolute switching times, I showed how fair comparisons can be made across material systems, specifically how tuning the free energy landscape with chemical substitution (or by choice of material, *i.e.*, BFO versus BTO) can lower the activation energy of polarization switching, and how this is measured in switching studies. The coupling between charge and lattice degrees of freedom is a key feature of ferroelectricity. The nucleation and growth mechanism of polarization reversal is widely believed to be intrinsically limited by acoustic phonons, which mitigate domain wall motion. For films grown epitaxially on a substrate, the substrate will undoubtedly modify the phonons of the thin-film, altering their energetics and dispersion characteristics. These considerations are especially pertinent to thin film geometries where the film is a fraction of the thickness of the substrate on which it is grown. The requirement of lattice deformation accompanying ferroelectric switching, and the continuity of such deformation at the ferroelectric/substrate interface means that the substrate can impose mechanical boundary conditions that act to inhibit, or otherwise alter ferroelectric switching by "clamping" the film, and resisting structural deformation associated with ferroelectric switching. This can be a dynamic process, whereby the lattice dynamics of the substrate can influence, or in fact, dictate, the ferroelectric switching dynamics of the film. Additionally, consider BFO, which undergoes both ferroelectric and antiferrodistortive (oxygen-octahedral tilts) structural phase transitions. A perovskite substrate that does not contain any oxygen-octahedral tilts will probably soften (and reduce the equilibrium amplitude of) the O_6 tilts of a BFO film, which will in turn impact ferroelectric switching via coupling between antiferrodistortive and ferroelectric order parameters through the lattice. In contrast, a perovskite substrate presenting rigid oxygen octahedral tilts may harden the corresponding phonons of the film, and may act as a "built-in field" of sorts for the BFO tilts; this will most likely result in slower switching, and potentially even modify the switching

pathway. In this chapter I discuss charge-lattice coupling at length and reveal how dynamic coupling between order parameters in multiferroic BFO and ferroelectric BTO manifests both energetically and dynamically. Notably, I address dynamic coupling between ferroelectric and antiferrodistortive order in BFO, which has strong implications (see Chapter 1) for switching of magnetic order in the system.

Even if we restrict ourselves to simple considerations – ignoring subtle effects related to phonon dynamics and their interplay with polarization and strains – it is clear that this is an exceedingly difficult problem. As such, I devise a tractable set of theoretical calculations and experiments that aims to answer a question that addresses how lattice dynamics influence polarization reversal, namely, what is the role of the substrate in influencing ferroelectric switching? I begin by considering the clamping effect, or resistance to structural deformation, which imposes an additional energy barrier that must be overcome to induce switching in films constrained to a substrate. Such an enhanced energy barrier can be understood as a coupling between the dynamic lattice strain and the primary order parameters in the system, which manifests itself both in the energy required to switch the state (coercive field) as well as in the switching time (both nucleation and growth regimes of polarization reversal). Indeed, previous work combining phase-field modeling with in-situ biasing transmission electron microscopy to study mechanical and electrical loading of relaxor ferroelectrics has demonstrated the importance of such mechanical constraints in establishing ferroelastic switching energies [100, 101]. Here, I present a detailed theoretical and experimental analysis of the role of substrate clamping in influencing ferroelectric switching in the proper ferroelectric/multiferroic, BFO. It is found that by removing the constraints imposed by mechanical clamping from the substrate I can realize a $\sim$40% reduction of the switching voltage and a consequent $\sim$60% improvement in switching speed. Our findings highlight the importance of a dynamic clamping process occurring during switching, which impacts strain, ferroelectric, and antiferrodistortive order parameters and plays a critical role in setting the energetics and dynamics of ferroelectric switching. In this chapter, I reveal the fundamental importance of considering all coupled order parameters in the BFO system, and introduce the notion of "strain + tilt clamping".

While all thin-film ferroelectrics are subject to clamping constraints from the substrate, it can play a larger role in inhibiting ferroelastic switching pathways [102, 103]. BFO, which follows a two-step polarization switching pathway, (consisting of out-of-plane (109°) and in-plane (71°) steps (Fig 3.1c.), with its antiferrodistortive oxygen octahedral tilts following the ferroelectric polarization [9, 104]) is therefore an ideal candidate for studying the role of clamping in impacting the switching of coupled primary order parameters. Previous theoretical works have developed highly successful theories for the equilibrium energetics of the BFO system, including effects from oxygen octahedral tilting [105, 106], though they have not addressed how substrate clamping influences such energetics (or dynamics) of the switching process. I theoretically study varying degrees of clamping, and introduce the notion of "strain + tilt clamping" where the substrate influences not only the ferroelectric and strain order parameters, but also, importantly, the oxygen octahedral tilts. I show that "strain clamping" alone (ignoring the role of the substrate in clamping the antiferrodistortive

order) is insufficient to explain the changes to the energetics and dynamics of switching in freestanding vs clamped BFO films, which I observe in our experiments. Interestingly, phase field calculations reveal that the rotation of the antiferrodistortive order slows the switching by almost an order of magnitude in comparison to the case where oxygen octahedral tilts are ignored. Our findings are further complemented by similar measurements in the literature [107] on thin films of ferroelectric BTO, a prototypical tetragonal ferroelectric, a finding which highlights how substrate clamping impacts a variety of ferroelectric materials. In the case of BTO [107] and in the present study, the data reveal a clear impact on the switching voltage (a measure of the barrier energy) as well as the switching dynamics (as manifested by changes in the switching time). These observations indicate that the effects from mechanical clamping by the substrate are broadly applicable to all displacive ferroelectrics. Such an understanding is essential, as the 100mV switching voltage goal remains a grand challenge for the field[3, 108].

3.1 Essential background and motivation

A key question is how to quantify the role of the substrate in dictating the switching process and whether switching can be studied experimentally without the influence of the substrate. Freestanding ferroelectric membranes have recently emerged as an exciting platform to study the role of mechanical constraints in ferroelectric systems[109], and here, I attempt to quantitatively address the effect of mechanical clamping by using a combination of thermodynamic calculations, phase-field simulations, piezoresponse force microscopy, and quasi-static and dynamic switching measurements on epitaxial, substrate-attached and freestanding versions of the same thin films (Fig 3.1a.).

3.1.1 Thermodynamic calculations (Landau free energy)

To quantitatively understand the switching-energy landscape with and without substrate clamping in BFO (Fig. 3.1b.), we modeled the thermodynamic free-energy within the context of the Landau theory for ferroelectrics [22, 110, 111], using a potential of the form:

$$f = \alpha_{ij}p_ip_j + \alpha_{ijkl}p_ip_jp_kp_l + \beta_{ij}\theta_i\theta_j + \beta_{ijkl}\theta_i\theta_j\theta_k\theta_l + t_{ijkl}p_ip_j\theta_k\theta_l + \frac{1}{2}C_{ijkl}\left(\epsilon_{ij} - \epsilon^0_{ij}\right)\left(\epsilon_{kl} - \epsilon^0_{kl}\right) \tag{3.1}$$

[112]where p_i,θ_i,and ϵ_{ij} refer to the ferroelectric polarization, ferrodistoritve rotation of the oxygen octahedra, and strain, respectively, while $\epsilon^0_{ij} = \lambda_{ijkl}\theta_k\theta_l + Q_{ijkl}p_kp_l$. We use two sets of parameters for this Landau potential: a first set directly fitted to first-principles results (nominally at 0K) and a second one corresponding to the room-temperature Ginzburg-Landau potential for BFO previously introduced in [112], the latter of which is the same model used for the phase-field simulations of ferroelectric switching discussed below. The set of Landau coefficients used presently is summarized in Table 3.1. Guided by previous

literature[9, 113], we know that upon the application of an out-of-plane electric field, BFO typically undergoes 180° switching via a two-step process (Fig. 3.1c): a 109° switch (where the out-of-plane polarization component reverses together with one in-plane component) followed by a 71° switch (where the remaining in-plane component reverses), or vice versa. In our thermodynamic analyses, we calculate the free-energy profile associated with the two switching steps while considering different levels of clamping.

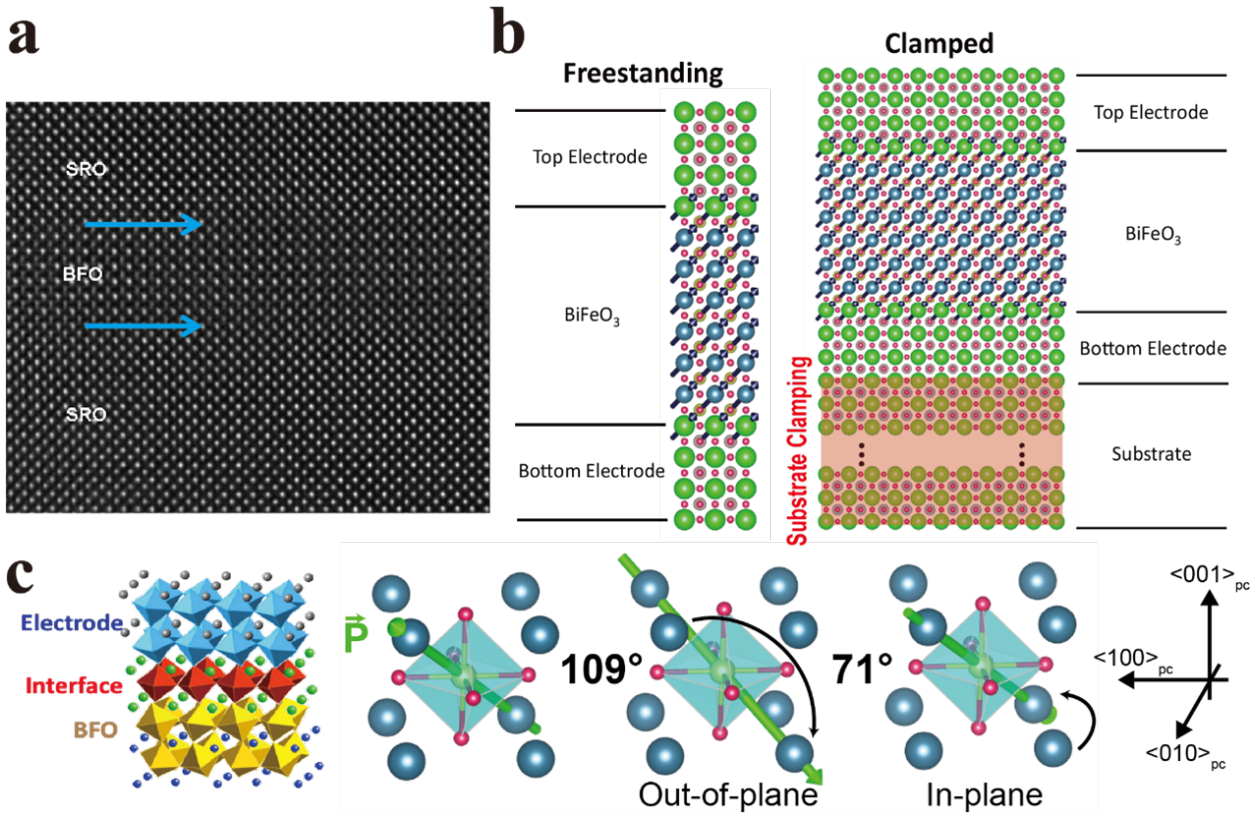

Figure 3.1: From [16]. Role of Clamping. **a.** Transmission electron microscope (TEM) image of SRO / BFO / SRO heterostructure. **b.** Schematic highlighting significant mechanical constraints imposed by the substrate compared with the freestanding film. **c.** SRO/BFO interface schematic showing ferrodistortive oxygen octahedra rotations and switching pathway (109° out-of-plane followed by 71° in-plane) for BFO films.

The calculations of free-energy profiles are performed by solving the system of equations $\frac{\partial \phi_i}{\partial t} = -L_\phi \frac{\partial f}{\partial \phi_i}$[114], where f is defined by Eq. 3.1, ϕ_i is the order parameter of interest and L_ϕ is the kinetic coefficient describing the rate at which ϕ approaches its equilibrium value. Since, in these simulations, we are only interested in the equilibrium values of the order parameters and not the trajectory by which it is reached, we let the system evolve to

Parameter	**Phase Field**	**DFT**	**Unit**
α_1	$(4 \times 10^5)(T - 1193)$	-2.98×10^9	$\mathrm{Jm/C^2}$
α_{11}	3×10^8	1.38×10^9	$\mathrm{Jm^5/C^4}$
α_{12}	1.188×10^8	2.06×10^9	$\mathrm{Jm^5/C^4}$
β_1	$(6 \times 10^6)(T - 1198)$	-4.78×10^{10}	$\mathrm{J/m^3/rad^2}$
β_{11}	3.44×10^{10}	3.89×10^{11}	$\mathrm{J/m^3/rad^4}$
β_{12}	6.799×10^{10}	5.25×10^{11}	$\mathrm{J/m^3/rad^4}$
λ_{11}	0.288	0.261	$\mathrm{rad^{-2}}$
λ_{12}	-0.097	-0.125	$\mathrm{rad^{-2}}$
λ_{44}	0.206	-0.825	$\mathrm{rad^{-2}}$
t_{11}	4.532×10^9	3.96×10^{10}	$\mathrm{Jm/(C^2rad^2)}$
t_{12}	2.266×10^9	6.40×10^{10}	$\mathrm{Jm/(C^2rad^2)}$
t_{44}	-4.84×10^9	-1.16×10^{11}	$\mathrm{Jm/(C^2rad^2)}$
C_{11}	2.95×10^{11}	3.12×10^11	Pa
C_{12}	1.18×10^{11}	1.24×10^{11}	Pa
C_{44}	0.74×10^{11}	0.78×10^{11}	Pa
Q_{11}	0.0603	0.0572	$\mathrm{m^4/C^2}$
Q_{21}	-0.0111	-0.0143	$\mathrm{m^4/C^2}$
Q_{44}	0.0176	0.0703	$\mathrm{m^4/C^2}$

Table 3.1: From [16]. BFO Landau potential coefficients.

equilibrium for each set of conditions before obtaining the relevant order parameter values and energies.

We perform the calculations of the free-energy profiles for the polarization switching path in which 109° out-of-plane switch (P_y and P_z polarization components are reversed) is followed by the 71° in-plane switch (P_x component is reversed). This path is chosen based on PFM experiments on BFO/SRO heterostructures previously reported [9], in which the initial polarization switching event follows the aforementioned step sequence. In the following description of the simulation details, I will only discuss the 109° out-of-plane switch, though the same considerations can be applied to 71° in-plane switch.

For the freestanding $BiFeO_3$ membrane we assume that during the polarization switching process all order parameters can freely evolve and adapt to the instantaneous values of the switching polarization components. For example, for 109° out-of-plane switch, at each value of P_y=-P_z between -0.7 and 0.7 $\mathrm{C/m^2}$, we allow P_x as well as of all the components of θ and the strain tensor, to evolve to their preferred values as dictated by $\frac{\partial \phi_i}{\partial t} = -L_\phi \frac{\partial f}{\partial \phi_i}$. Then, we use the relaxed values of P, θ and strain to compute the energy of the system, at each step of the switch. The evolution of all order parameters with varied P_y is shown in Fig. 3.2.

In the simulations of the films clamped by the substrate, we consider three possible clamping effects. First, we assume that the substrate clamps only $\epsilon_{11}, \epsilon_{22},$ and ϵ_{12} compo-

nents of the strain tensor ("strain clamping" case). To reflect this in our simulations, we fix $\epsilon_{11}, \epsilon_{22},$ and ϵ_{12} to their equilibrium values corresponding to the initial direction of the polarization and to the considered set of model parameters (either DFT or phase-field). Then, for 109° out-of-plane switch we vary P_y=-P_z components of the polarization between -0.7 and 0.7 C/m^2 and for each P_y value we optimize P_x, $\theta_x, \theta_y, \theta_z$ as well as the unclamped components of the strain tensor. The evolution of the order parameters with varying P_y is presented in Fig. 3.2 together with that of freestanding case, where the system has no such constraints and is free to evolve.

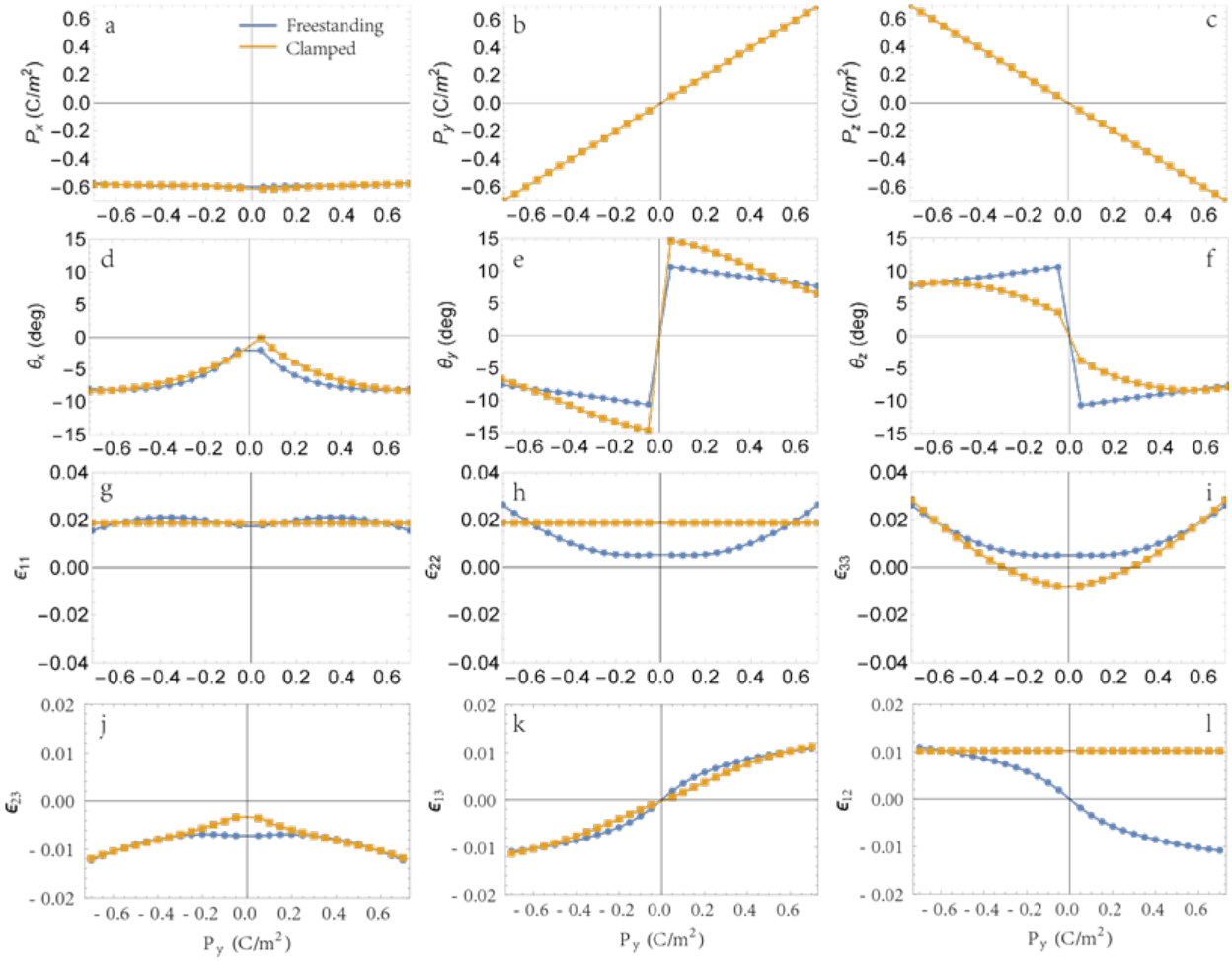

Figure 3.2: From [16]. Evolution of the polarization, octahedral tilts and strain tensor components during the 109° polarization switching. The curves denoted as "clamped" correspond to the strain clamping case ($\epsilon_{11}, \epsilon_{22},$ and ϵ_{12}) are fixed to their equilibrium values corresponding to the initial direction of the polarization while all the other order parameters are allowed to relax.)

Next, we consider the possibility that the presence of the substrate can have an additional clamping effect on other order parameters, such as O_6 octahedral tilts ("strain + tilt clamping"). In particular, we study two cases, to which we refer in the following as "weak strain+tilt clamping" and "strong strain + tilt clamping". In the case of weak strain+tilt clamping, in addition to $\epsilon_{11}, \epsilon_{22},$ and ϵ_{12}, we fix the non-switching components of polarization and tilts (*e.g.*, P_x and θ_x for 109° out-of-plane switch) to their initial equilibrium values. Then, we vary P_y=-P_z components and for each considered P_y value we optimize θ_y, θ_z as well as the remaining components of the strain tensor $\epsilon_{33}, \epsilon_{13},$ and ϵ_{23}. The evolution of all order parameters with P_y is presented in Fig. 3.3. To simulate the case of strong strain+tilt clamping, we first identify the equilibrium values of all order parameters for both sets of the Landau potential coefficients (DFT and phase-field). Then, we vary P_y=-P_z and $\theta_y = -\theta_z$ between their equilibrium values corresponding to up and down polarization directions while we keep P_x, θ_x, as well as$\epsilon_{11}, \epsilon_{22},$ and ϵ_{12} fixed to their initial values. For each value of P_y and θ_y we relax the unclamped components of the strain tensor $\epsilon_{33}, \epsilon_{13},$ and ϵ_{23}. The evolution of the order parameters is shown in Fig. 3.3.

The results of this effort are effective double well potentials for ferroelectric switching in BFO, which account for varied mechanical boundary conditions imposed by the substrate. This provides a good intuitive picture that summarizes the dynamic coupling between charge and lattice order parameters in a digestable (energy-based) way for comparison with experiment.

3.1.2 Experimental realization (Freestanding membranes)

To experimentally study the effect of clamping imposed by the substrate, we employ recent advances in chemically assisted lift-off techniques to produce freestanding BFO (and later, BTO) layers. Such techniques are rapidly emerging as an approach for tuning the lattice distortion and strain in ferroelectrics[107, 115, 116, 117, 118, 119]. Several sacrificial layers have been developed, such as water soluble $Sr_3Al_2O_6$[117], acid solution soluble $La_{0.67}Sr_{0.33}MnO_3$ (LSMO)[107], and graphene for mechanical exfoliation[118], leading to freestanding ferroelectric films down to the monolayer limit[109], as well as integration of single-crystalline membranes[118], and flexible layers with super-elasticity[119]. We demonstrate that quantitatively different features are obtained in freestanding BFO membranes versus their clamped counterparts, both in quasistatic measurements of the energetics (coercive field from hysteresis measurements) and dynamical measurements (pulsed switching studies) of the switching process.

Two types of samples were employed for this study. The first type, henceforth referred to as "clamped", is a Pt (20 nm)/$SrRuO_3$ (SRO 30 nm)/BFO(x nm)/SRO(30 nm), (where x ranges from 12.5 nm to 100 nm) heterostructure (Fig. 3.1a.) epitaxially grown via pulsed-laser deposition (PLD) on $SrTiO_3$ (STO)[001] substrates. The second sample type, henceforth referred to as a "membrane", is a Pt/SRO/BFO/SRO/LSMO stack, that has been subsequently released from the STO[001] substrate by etching the LSMO layer (Fig. 3.4a.) [107] to completely lift-off the Pt/SRO/BFO/SRO stack from the STO substrate. A sup-

portive PDMS layer is used to then transfer the stack to a Pt/Si (001) substrate. We use an etch rate of ∼1 nm/hour to dissolve the LSMO layer in order to avoid deformation or damage of the Pt/SRO/BFO/SRO heterostructure during lift-off. To verify a successful transfer, we measured via atomic force microscopy (AFM) the surface roughness of the initial film and that of the transferred freestanding membrane. Typical measurements are shown (Fig. 3.4b,c), yielding a surface roughness of 223 pm and 406 pm, respectively, indicating that the high-quality samples can be maintained during this process.

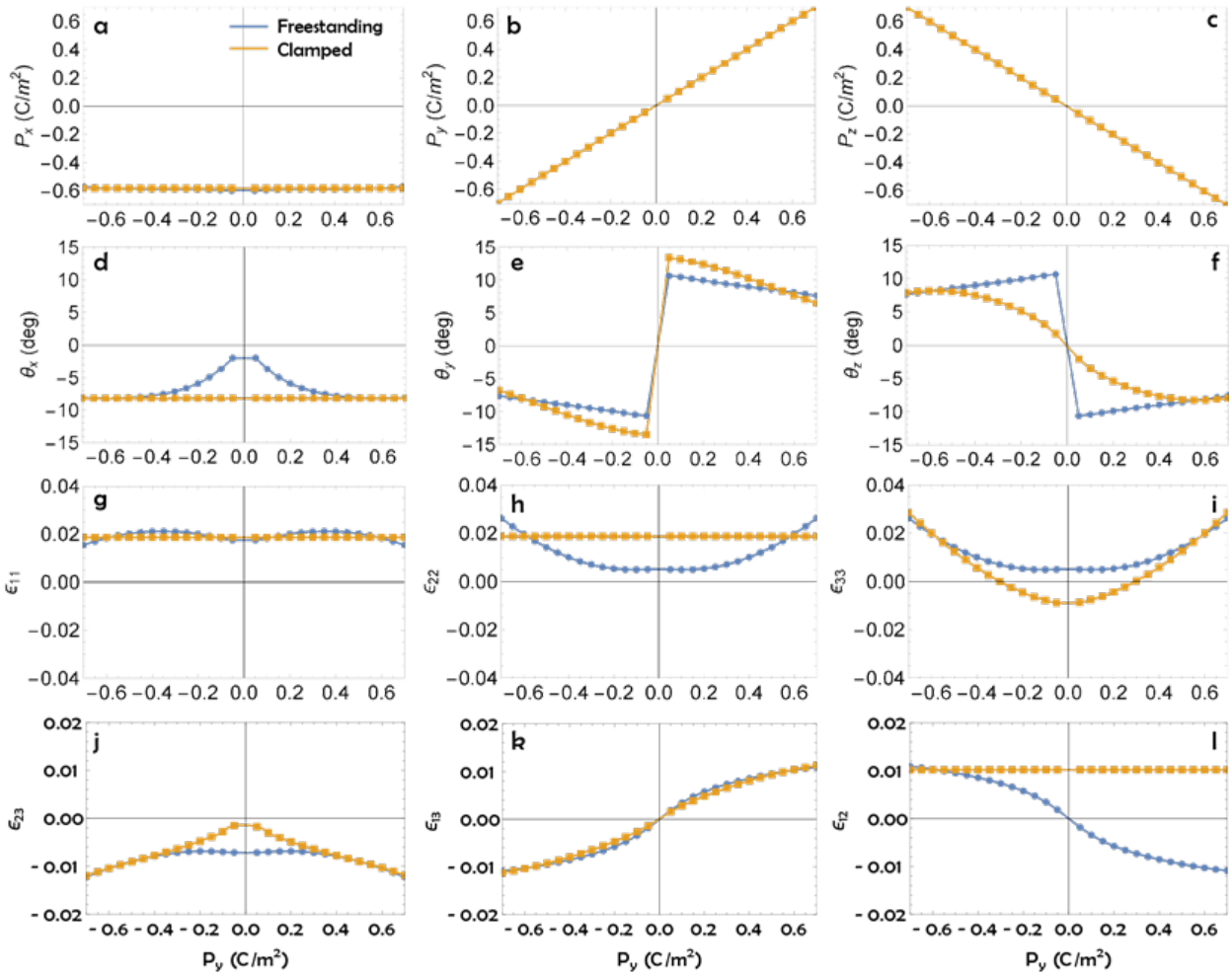

Figure 3.3: From [16]. Evolution of the polarization, octahedral tilts and strain tensor components during the 109° polarization switching. The curves denoted as "clamped" correspond to the "weak strain + tilt clamping" case (non-switching components of polarization and tilts (P_x and θ_x) as well as $\epsilon_{11}, \epsilon_{22},$ and ϵ_{12} components of the strain tensor are fixed to their initial equilibrium values. For each value of P_y only θ_y, θ_z and the unclamped components of strain tensor are allowed to relax).)

Film Growth The oxide heterostructures BFO/SRO/LSMO or SRO/BFO/SRO/LSMO were grown on single-crystalline (001) STO substrate by pulsed laser deposition at 650-720°C with focused laser fluence ∼1.2 J cm^{-2} in 100-160 mTorr oxygen pressure and cooled down to room temperature in 400 Torr oxygen pressure. To protect the film during the lift-off process, a 20-nm Pt layer was deposited on top of the SRO or BFO layer by magnetron sputtering. The top SRO layer was patterned into circular top electrode and the bottom SRO layer served as a bottom electrode for ferroelectric switching testing.

Lift-off process PDMS stamps were cut into 8 mm x 8 mm x 1.5 mm from a commercial specimen (Gelfilm from Gelpal). Then they were stacked tightly onto the film. After floating the PDMS/films in an etching solution (low-concentration HCl solution (0.3 vol %) mixed with 0.1 mol mL-1 potassium iodide) for several hours, the LSMO dissolved to lift the freestanding film off STO substrate, which were subsequently washed with deionized water and dried with N_2 gas. The samples were then transferred onto Si/Pt substrate. The entire stack was annealed at 110°C for 30 min to promote adhesion at the film/new substrate interface. After cooling to 70°C and peeling off the PDMS stamp with tweezers, the transferred membrane on Si/Pt substrate was obtained.

3.1.3 Phase field calculations

The phase-field model used here is an extension to previous models for bulk and epitaxial thin film simulations[22, 112, 21, 120, 121, 122] in which we use the spontaneous polarization $p = (p_1, p_2, p_3)$ and oxygen octahedral tilt $\theta = (\theta_1, \theta_2, \theta_3)$ as the order parameters . A temporal evolution of the order parameters can be obtained by solving the time-dependent Ginzburg-Landau equation [123, 124]:

$$\frac{\partial p_i}{\partial t} = -L_{p_i} \frac{\delta F_{\text{tot}}}{\delta p_i}, i \in [1, 2, 3] \tag{3.2}$$

$$\frac{\partial \theta_i}{\partial t} = -L_{\theta_i} \frac{\delta F_{\text{tot}}}{\delta \theta_i}, i \in [1, 2, 3] \tag{3.3}$$

in which L_p and L_θ are the kinetic coefficients, t is time, F_{tot} is the total free energy of BFO membrane. Owing to the lack of experimental data to which to fit L_p and L_θ (which requires studies on intrinsic timescales), we set both L_p and L_θ to be 1 after normalizing all coefficients to unitless values. By doing this normalization, our "timestep" is meaningless as an absolute time, though comparisons between material systems *i.e.*, between the BFO membrane and clamped film, are valid. The expression for the total free energy is,

$$F_{\text{tot}} = \int \left(f_{\text{Landau}} + f_{\text{grad}} + f_{\text{elec}} + f_{\text{elast}} \right) dV \tag{3.4}$$

where

$$f_{\text{Landau}} = \alpha_{ij} p_i p_j + \alpha_{ijkl} p_i p_j p_k p_l + \beta_{ij} \theta_i \theta_j + \beta_{ijkl} \theta_i \theta_j \theta_k \theta_l + t_{ijkl} p_i p_j \theta_k \theta_l \tag{3.5}$$

represents the local free energy density, which includes the landau energyfor polarization, oxygen octahedral tilt and the coupling terms.

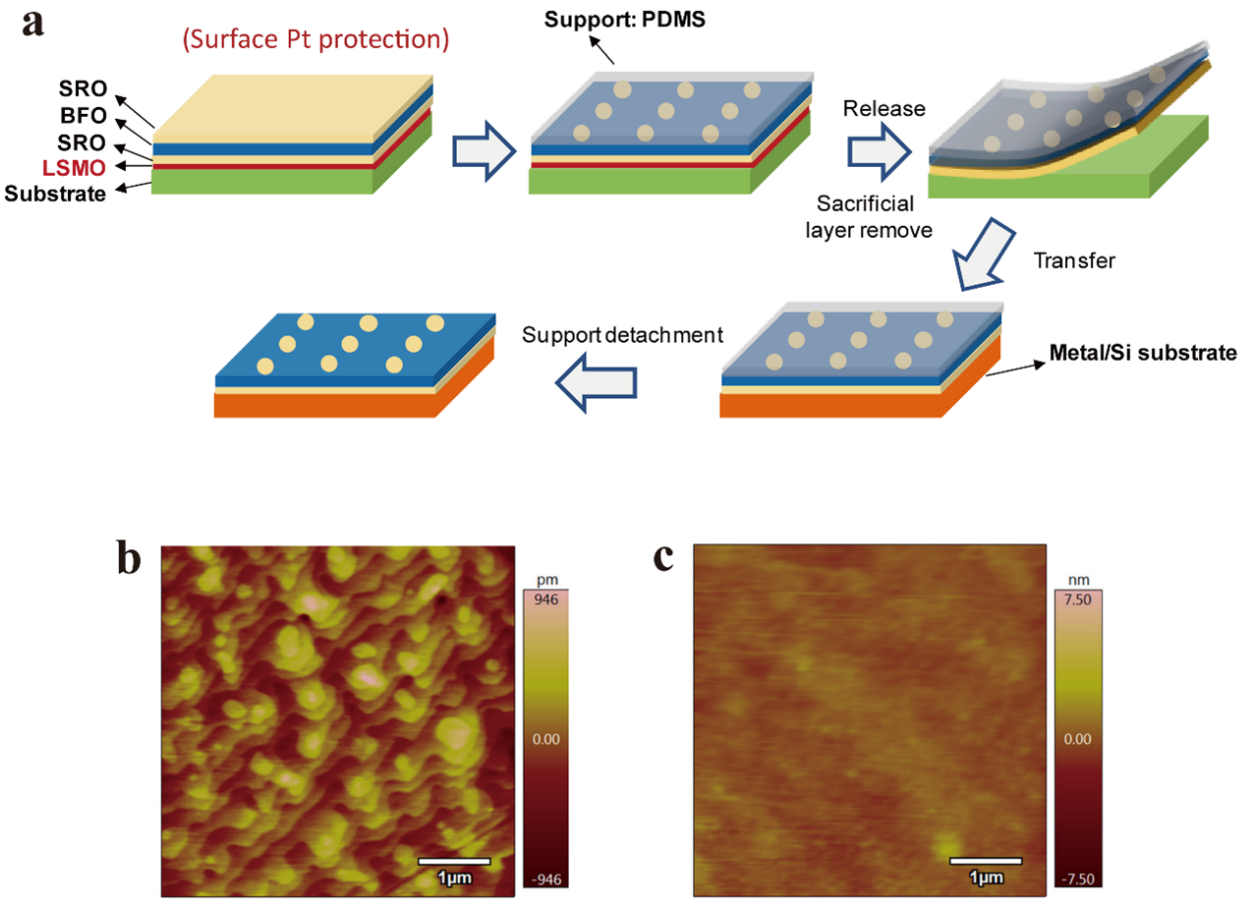

Figure 3.4: From [16]. Growth, transfer, and characterization of freestanding BFO membranes. **a.**, Schematic of the SRO / BFO / SRO / LSMO / STO heterostructure growth, freestanding membrane release and transfer. AFM images of the BFO film (**b.**) and freestanding membrane (**c.**) with thickness of 35nm. The roughness is 223 pm and 406 pm, respectively.

$$f_{\text{grad}} = \frac{1}{2} g_{ijkl} p_{i,j} p_{k,l} + \frac{1}{2} \kappa_{ijkl} \theta_{i,j} \theta_{k,l} \tag{3.6}$$

represents the gradient energy, which includes the gradient energy for both polarization and oxygen octahedral tilt. All equations with repeating subscripts follow the Einstein summation notation, and the comma in subscript means spatial differentiation, *e.g.*, $p_{(i,j)} = \frac{\partial p_i}{\partial x_j}$.

$$f_{\text{elec}} = -\frac{\epsilon_0 \epsilon_{ij}^b}{2} E_i E_j - E_i p_i \tag{3.7}$$

is the electrostatic energy, where ϵ_{ij}^b is the background dielectric constant, E_i is the electric field obtained by solving the electrostatic equilibrium equation

$$\epsilon_0 \left(\epsilon_{11}^b \frac{\partial^2 \phi}{\partial x_1^2} + \epsilon_{22}^b \frac{\partial^2 \phi}{\partial x_2^2} + \epsilon_{33}^b \frac{\partial^2 \phi}{\partial x_3^2} \right) = \frac{\partial p_1}{\partial x_1} + \frac{\partial p_2}{\partial x_2} + \frac{\partial p_3}{\partial x_4} \tag{3.8}$$

ϕ is the electrical potential, and

$$f_{\text{elast}} = \frac{1}{2} C_{ijkl} (\epsilon_{ij} - \epsilon_{ij}^0)(\epsilon_{kl} - \epsilon_{kl}^0) \tag{3.9}$$

is the elastic energy, in which ϵ_{ij} is the total strain distribution obtained by solving the mechanical equilibrium equation $\sigma_{(ij,j)} = 0, \sigma_{ij} = C_{ijkl}(\epsilon_{ij} - \epsilon_{ij}^0)$, and the eigenstrain is connected to the order parameters $\epsilon_{ij}^0 = \lambda_{ijkl}\theta_k\theta_l + Q_{ijkl}p_k p_l$. There are two differences between our free-standing film and our epitaxial thin film model[112], both of which pertain to solving for the mechanical equilibrium state. First, the clamped thin film has a fixed displacement bottom and traction-free top surfaces, while for the free-standing film, both the top and bottom surfaces are set as traction-free boundaries. Second, the in-plane macroscopic strain in clamped thin films is controlled by the misfit of the substrate, while for the free-standing film, the in-plane macroscopic strain is set to be the average eigenstrain (calculated from the current order parameter distribution) since overall the free-standing film is in a stress-free state. Refer to Table 3.1 for a full list of parameters used.

Phase field calculations, as those just described, yield a variety of important results for comparison to experiment. First off, phase field calculations can be used to obtain equilibrium domain structures, which can be directly compared to PFM imaging. Importantly, such calculations allow us to calculate the energy for different switching pathways, as in Section 3.1.1. By breaking down the energy into contributions from various sources (Landau, ferroelastic, *etc.*), we also have unprecendented insight into how each energy term contributes *relative to other energy scales.* Finally, we can also evolve the system in time and see how each energy scale contributes, not only in equilibrium, but in time domain. In these ways, phase-field simulations offer an excellent means of interrogating the physical origin behind the observed (experimental) data.

3.2 Results

3.2.1 Strain and Strain + Tilt clamping

First, we calculate the case of no clamping, or the "membrane" case. The energy profiles labeled "membrane" (blue curves in Fig. 3.5) are obtained by continuously varying the transformed polarization components (P_2 and P_3 for the 109° step, P_1 for the 71° switch)

while allowing all other variables (remaining polarization components, tilts and strains) to adapt to this change. We observe, as expected[9, 102, 104, 113], that the tilts reverse together with the polarization. This yields the lowest-energy switching paths corresponding to the experimental case of a free-standing membrane.

Next, we consider the case of the so-called "strain clamping". In order to separate clamping effects from the effects of epitaxial misfit strain, we assume the film is thick enough so that it is fully relaxed to its rhombohedral ground state. The fully relaxed nature of the film does not, however, mean that it is free to deform; on the contrary, it is still clamped and, as dictated by the substrate, energetically favors maintaining its original state. To obtain the free energy profiles labeled "clamped" in Fig. 3.5a(b), 3.5e(f) we vary P_2 and P_3 for 109° switch (P_1 component for 71° switch) while keeping the strains $\epsilon_{11}, \epsilon_{22},$ and ϵ_{12} fixed to their equilibrium values corresponding to the initial polarization direction (before the initial 109° out-of-plane switch). All the other order parameters are allowed to relax following the polarization switching process (Section 3.1.1). One can see that strain clamping leads to slightly increased energy barriers compared to the freestanding case, about 6% for the 109° step and 20% for the 71° step. Notably, the results obtained for the first-principles Landau potential (Fig. 3.5a and 3.5b) and the phenomenological model (Fig. 3.5e and 3.5f) are essentially equivalent with regards to the change in activation energy barriers, highlighting the consistency of both methods. Additional free-energy calculations for the prototypical ferroelectrics PTO and BTO are presented for clamped and membrane cases (Fig. 3.6). These calculations, consistent with previous experimental work [107], show a similar reduction in switching energy for freestanding membranes compared to clamped films suggesting a broad applicability of the role of strain clamping effects in ferroelectric switching.

There exist other ways in which the substrate can impact switching, namely by clamping additional order parameters (such as octahedral tilts) beyond strain. This can arise, for example, by a mismatch in roto-strictive coefficients between the film, electrode, and substrate. To quantify this effect, we introduce "strain + tilt clamping" (and varying degrees, *i.e.*, weak vs strong, thereof) and compute the free-energy profiles while imposing additional constraints on some order parameters in our simulations. In the limiting case of "strong strain + tilt clamping" (Fig. 3.5g, 3.5h) we fix all non-switching polarization and tilt components (as well as $\epsilon_{11}, \epsilon_{22},$ and ϵ_{12}) to their equilibrium values corresponding to the initial polarization direction. Moreover, we do not fully relax the switching tilt components, but interpolate them between the values corresponding to the minima of the free energy curves. Only strains $\epsilon_{33}, \epsilon_{13},$ and ϵ_{23} are allowed to relax following the variation of the other order parameters. One can see that clamping of other degrees of freedom immediately results in a greater difference between the membrane and clamped cases (about 64% for both the 109° and 71° steps for the phase-field parameter set). We expect the true clamping effects to lie between "strain clamped" and "strong strain + tilt clamped" cases, which serve as limiting cases of clamping effects. To quantify such an intermediary degree of clamping, we consider a third type of clamping termed "weak strain + tilt clamping." In this case, (Fig. 3.5b, 3.5c, 3.5g, 3.5h) we fix the non-switching tilt components, but allow switching tilt components

to adapt freely to the change in polarization. In this case we see a smaller reduction in the energy barrier upon releasing the film from the substrate, which more accurately describes our experimental data, discussed below.

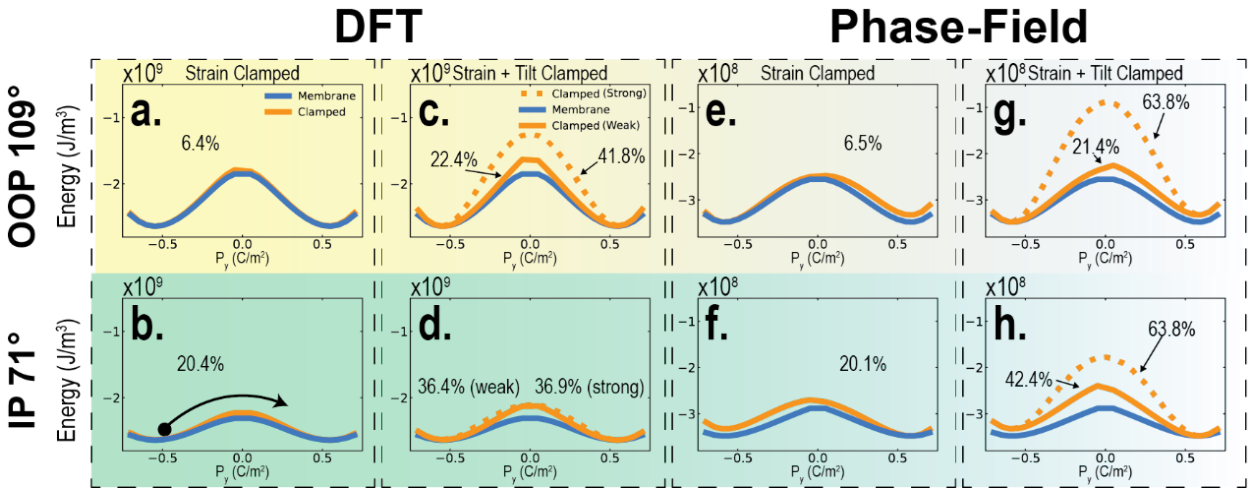

Figure 3.5: From [16]. Thermodynamic calculation of switching free energy for BFO. **a.** (**e.**) and **b.** (**f.**) show 109°, out-of-plane, and 71°, in-plane, switching energy landscapes, respectively, calculated using Landau coefficients obtained from DFT (used in the phase-field model) for the strain-clamped and membrane cases. **c.** (**g.**) and **d.** (**h.**) show 109° and 71° double well potentials, respectively, calculated using the Landau potential from DFT (from the phase-field model) for strain + tilt clamped and membrane cases. In all panels, the "membrane" curves (blue) correspond to a film free of constraints, *i.e.*, all order parameters are free to adapt to the switching polarization. To obtain the "clamped" (solid orange curves) results in panels **a.**, **b.**, **e.**, and **f.**, the in-plane strains are held fixed, modeling the effect of strain clamping from the substrate. "Clamped (Weak)" (solid orange) curves in **c.**, and **d.**, (**g.**, and **h.**) represent switching potentials derived from DFT parameters (phase-field parameters), but subject to so-called "weak strain + tilt clamping" constraints, where, additionally, all non-switching polarization and tilt components are held fixed. "Clamped (Strong)" (dashed orange) curves in **c.**, and **d.**, (**g.**, and **h.**) show switching potentials derived from DFT parameters (phase-field parameters), but subject to so-called "strong strain + tilt clamping" constraints, where, all the non-switching polarization and ferrodistortive components are held fixed and the switching components of tilts are linearly interpolated between the values corresponding to the minima of the free-energy curves. Percentages listed are reductions in maximum energy barrier for membrane vs. clamped films in each scenario. Calculations correspond experimentally to the thickest, fully relaxed, films.

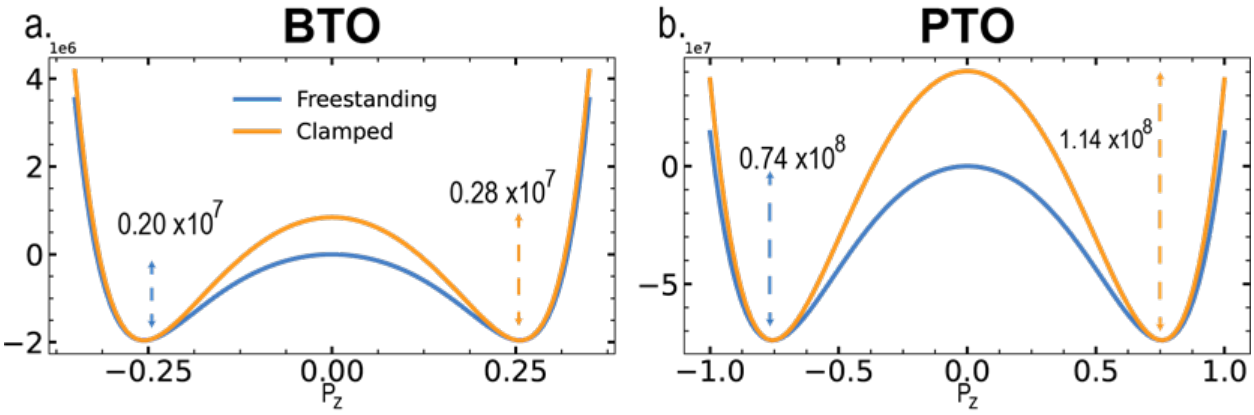

Figure 3.6: From [16]. Clamped vs. Membrane Switching Energy Landscapes for BTO and PTO. **a.** and **b.** show calculated switching energy landscapes for prototypical ferroelectrics BTO and PTO, respectively, showing energy barrier height reductions of ∼30% in BTO and ∼35% in PTO. Calculations are performed by clamping non-switching order parameters.

3.2.2 Energetics: PFM imaging and ferroelectric hysteresis

As described in Section 3.1.2, we fabricated both clamped and freestanding BFO membranes for study. The impact of mechanical constraints from the substrate can be observed directly in PFM imaging of the ferroelectric domain structure before and after release from the substrate. In-plane and out-of-plane PFM amplitude images for both the clamped BFO and freestanding membrane (Fig. 3.7b,c, and Fig. 3.8a,b), reveal dramatic differences. The well-ordered 71° stripe domain pattern of BFO in the clamped film evolves into a "blocky" 180° domain pattern with a larger domain size in the freestanding membrane. These changes are also observed in the corresponding in-plane and out-of-plane PFM phase (Fig. 3.8c-f) images for the clamped film and membrane. Kittel's law[125] for ferroelectric domains states that the domain width scales as:

$$w = \sqrt{\frac{\sigma t}{U}} \tag{3.10}$$

where $\sigma, t,$ and U are the domain-wall energy, film thickness, and domain energy, respectively. The domain-wall energy is given by

$$U = U_{dip} + U_x + U_e \tag{3.11}$$

where U_{dip}, U_x, U_e are the energy contributions from dipolar interactions (correlation energy), elastic energy, and depolarization energy, respectively[1]. By releasing the film from the substrate, we significantly reduce the elastic energy (correspondingly leading to an increase in the domain width), and therefore the electrostatic energy becomes the dominant energy scale. In order to minimize electrostatic energy, ferroelectric domains typically adopt

configurations such that $\nabla \cdot P \approx 0$ at domain-wall boundaries, and such a condition is satisfied with 180° domains in perovskite ferroelectrics[1]. We directly observe this effect here, highlighting the dominance of electrostatic energy after removal of elastic constraints from the substrate. It is important to note that the changes in domain structure observed (Fig. 3.7) can be unequivocally attributed to the role of substrate clamping. In both the clamped and freestanding cases, the SRO layer is the same thickness (30nm), so, while the SRO layer may play a small role in epitaxially constraining the BFO, its effect is present in both the clamped and freestanding cases. Therefore, any differences we observe between these two cases can be attributed to the substrate clamping alone, and not to the SRO layer.

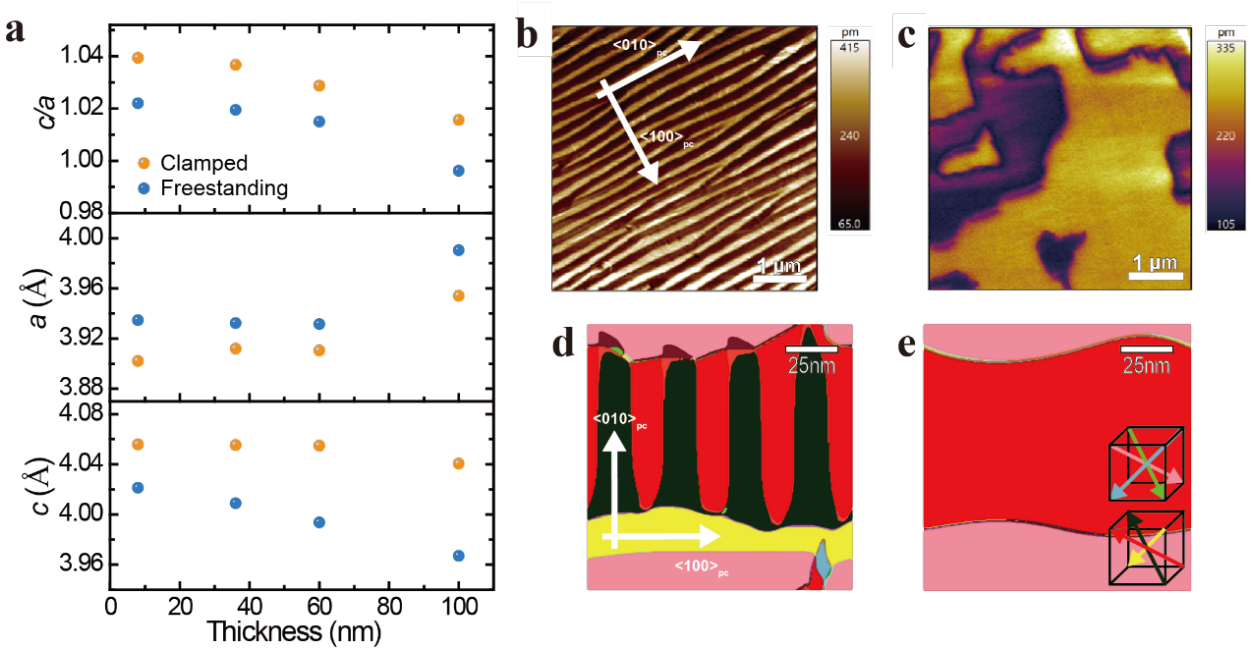

Figure 3.7: From [16]. Lattice parameters and domain structure of the BFO clamped films and freestanding membranes. **a.** **c** and a lattice parameters and their ratio c/a for the BFO films and membranes as a function of thickness. The freestanding BFO membranes exhibit decreased c, increased a, and decreased c/a ratio. **b.**, **c.**, In-plane PFM amplitude image of 100-nm BFO film (**b.**) and freestanding membrane (**c.**). **d.**, **e.**, Phase-field simulation of BFO layer before (**d.**) and after lift-off (**e.**).

Our experimental PFM results are in good agreement with the mesoscale domain structure predicted by phase-field simulations, calculated using the same Ginzburg-Landau potential [112] as that used to calculate free-energy switching landscapes (Fig. 3.6) and including gradient terms (see Section 3.1.3) to allow for determination of the domain configuration. As observed in our simulations, by releasing the film from the substrate, the lateral width of the domain indeed increases dramatically, and 180° domain walls emerge in the freestanding

membranes (Fig. 3.7d,e). There are two important considerations in understanding the observed domain structure evolution: misfit strain and the clamping effect from the substrate. To disentangle the two effects, and specifically elucidate the role of clamping in the system, we turn to experimental measurements of the energetics and dynamics.

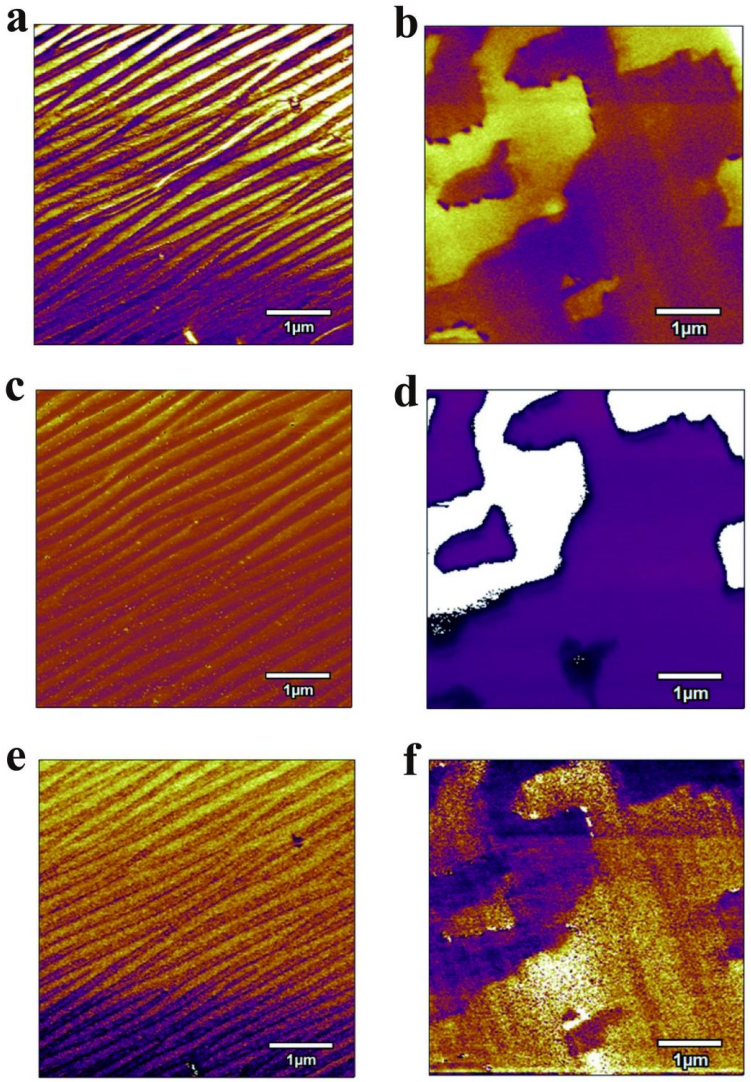

Figure 3.8: From [16]. Domain patterns of the 100-nm BFO film and free-standing membrane. Out-of-plane PFM amplitude images of film (**a.**) and free-standing membrane (**b.**). In-plane PFM phase images of film (**c.**) and free-standing membrane (**d.**). Out-of-plane PFM phase images of film (**e.**) and free-standing membrane (**f.**). The free-standing membrane features larger domain size and an exclusively 180° domain pattern.

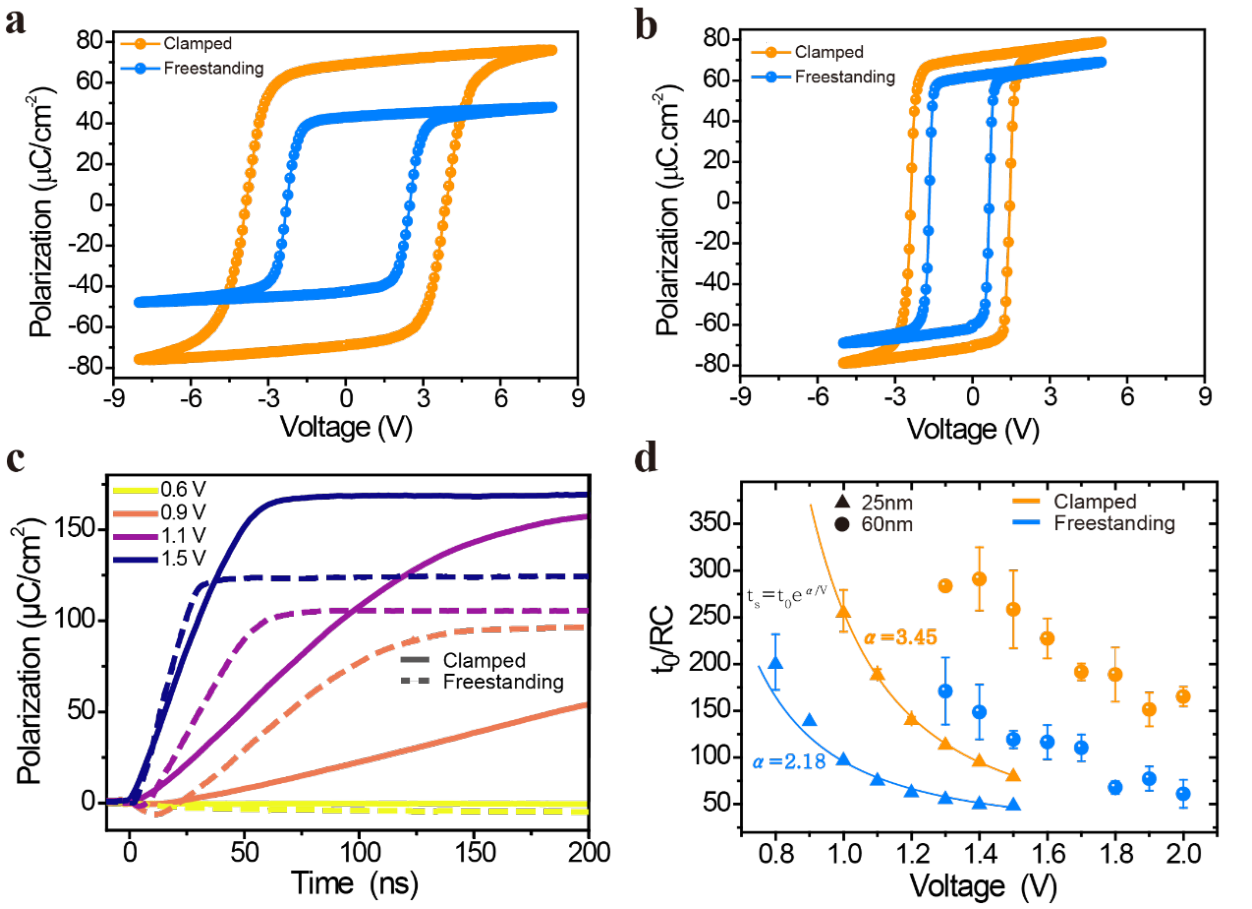

Figure 3.9: From [16]. Ferroelectric switching voltage and switching dynamics of BFO films and membranes. Ferroelectric polarization versus voltage (P-V loops) of 100nm (**a.**) and 35nm (**b.**) clamped films and membranes measured at 10 kHz. **c.** Switching dynamics as a function of applied voltage for the clamped and free-standing 25nm films. **d.**, Comparison of the extracted switching time (normalized by the RC-time constant) of the samples before (clamped) and after lift-off (freestanding), with BFO thicknesses of 25nm and 60nm. Solid lines and activation voltages (α) are shown for fits to the Merz' law for the 25nm films. These findings show a $\sim$40% reduction in switching energy stemming from substrate clamping effects.

The measurements of polarization versus applied voltage (P-V) hysteresis loops on both the clamped films and freestanding membranes were carried out at low temperature (100 K) to minimize the effects of leakage. We compare P-V hysteresis loops measured at 10 kHz for 100-nm and 35-nm BFO clamped films (orange) and membranes (blue) (Fig. 3.9a,b). The data demonstrate that the coercive voltage, defined as the voltage at which the average polarization is zero, measurably decreases upon lift-off. The free-standing membranes also

have a lower remnant polarization, consistent with the observed decrease in c/a ratio (Fig 3.7a). Both 100-nm and 35-nm BFO samples show a significant decrease (∼40%) in the coercive voltage after the lift-off process. It is important to note that, while the 100-nm-thick clamped film is known to be almost fully relaxed (c/a ratio matches that of bulk, Fig 3.7a), reductions in switching energy persist even at this film thickness, indicating that clamping, and resistance to structural distortion during switching, plays a dominant role in setting the switching energetics over effects from misfit strain. In other words, I am able to conclude that a dynamic process (and not static misfit strain), which serves to inhibit switching as it progresses, is imposed by the charge-lattice coupling in BFO. The coercive voltage is a measure of the energy required to switch the polarization, and our observed coercive voltage ratio (∼40%) between free-standing and clamped films indicate that the clamping effect lies somewhere between the limiting cases of strain clamping and strong strain + tilt clamping, and is most accurately described by weak strain + tilt clamping (Fig. 3.5). This is an important finding, and deserves special attention. Strain clamping alone, where the mechanical effect of the substrate only inhibits switching via the strain order parameter, is insufficient in explaining the dramatic reduction in energy observed experimentally. The substrate clamping plays an additional role, namely that the mechanical constraints imposed also inhibit variation of oxygen octahedral tilting. Only when both effects are considered, can we explain the significant reduction in switching energy observed. Furthermore, the extreme case of strong strain + tilt clamping predicts a reduction in energy larger than that observed. This indicates that while clamping effects during switching inhibit changes in octahedral tilting, they do not completely prevent these changes from occurring.

3.2.3 Dynamics: ferroelectric switching

Having established the role of clamping on switching energetics, we now turn to the dynamics of the switching process. Polarization reversal in ferroelectric thin films is known to proceed via nucleation and growth of reverse polarized domains[71, 26, 55, 53] and we used pulsed ferroelectric measurements[26] to directly measure the ferroelectric polarization evolution during switching. We show polarization transients for various applied voltages for a 25-nm-thick clamped film and freestanding membrane (Fig. 3.9c, Fig. 3.10a, b show corresponding observed ferroelectric switching displacement current). It is known that the dynamical timescale of free-charge in the measurement circuit, namely RC (resistance×capacitance) time, plays a significant role in the ferroelectric switching times observed in macroscopic device structures at these timescales (Chapter 2, [26]) because the RC-time of the measurement circuit imposes limits on how fast one can deliver charge to facilitate polarization switching. In order to account for any such effects, we normalized all measured switching times to the measured RC-time for each device (Fig. 3.9d)[107], thereby enabling us to make meaningful comparisons across material systems (*e.g.*, freestanding vs clamped films). Clear decreases in switching time persist even after such normalization, verifying that the observed changes are from the mechanical clamping and not changes to extrinsic-circuit parameters. The normalized switching time, defined as the time when the switched polarization reaches

90% of its saturation value, normalized by the non-switching RC-time of the measurement circuit, was extracted for the samples with thicknesses of 25 nm and 60 nm (Fig. 3.9d) with capacitors of the same area. The freestanding membranes show a significant decrease in the switching time compared to the clamped films. Particularly, the 60-nm-thick sample presents a ∼63% decrease in the switching time after lift-off. To quantitatively determine the role of clamping from the switching dynamics measurements, we employ Merz' law[53] to extract the ratio of the activation voltage for the clamped and freestanding films, taking care to account for RC effects in the measurement circuit. Our findings (Fig. 3.9d) shows that the activation voltage for the 25-nm-thick clamped film is 3.45 V while the 25-nm-thick membrane film has an activation voltage of 2.18 V, indicating that the removal of clamping effects results in a ≈37% reduction in switching energy. This finding is consistent with the considerable decrease observed in coercive voltage in the hysteresis loops (Fig 3.9a,b) and energy barrier in our thermodynamic calculations (Fig. 3.5), showing best agreement with "weak strain + tilt" clamping scenario.

Finally, we performed time-resolved phase-field simulations (Section 3.1.3) to further investigate the relevant energy scales and the effects of clamping during switching. We simulated the same applied voltage (13V)[1] for both the clamped and membrane cases, and the evolution of elastic, electric, and Landau energy during the switching process (2000 time steps) were computed (Fig. 3.11). All simulations start from an equilibrium domain state with polarization pointing downwards. A voltage is then applied to switch the polarization upwards. Changes in the various energy values correspond to changes in the polarization distribution within the simulation, with the most dramatic changes occurring as domains are switched. We can clearly see that the time for a freestanding membrane to switch (∼200 timesteps) is significantly shorter than that for the clamped film to switch (∼800 timesteps). Corroborating the true dynamic nature (opposed to quasi-static) of the experiment is the remarkable agreement between reductions in switching time predicted (∼63% for the 60nm film, and ∼75% as predicted by simulation).

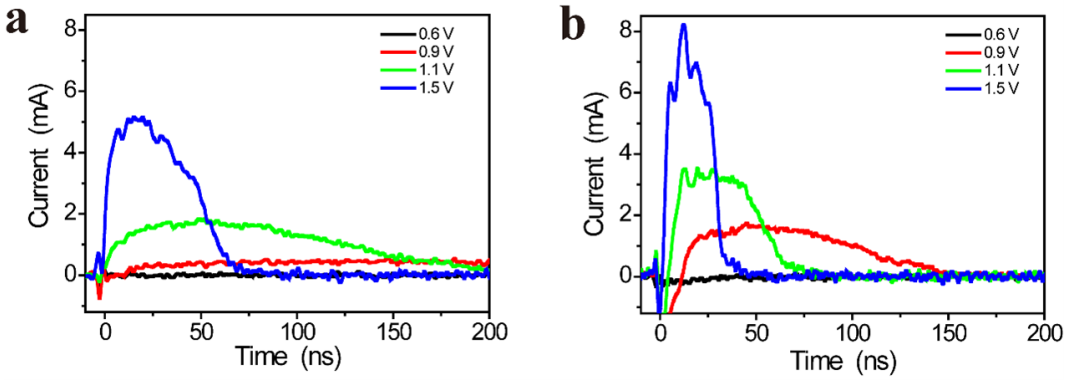

[1]Phase field simulations are known to overestimate the applied voltage required to induce switching

Figure 3.10 *(previous page)*: From [16]. Switching transients (displacement current) in the SRO/BFO/SRO capacitors samples before and after lift-off. **a**, **b**, The switching current responses for the samples with BFO thickness of 25 nm, before and after lift-off, respectively.

Returning now to the fundamental aim of this study, by examining the time-resolved evolution of the elastic, electric, and Landau energies individually (Fig. 3.11a-c), we can use our simulations to directly interrogate the role of substrate clamping during switching in a relative sense, *i.e.*, how does each energy contribution compare relative to the others? As expected, the elastic energy of the membrane (Fig. 3.11a) is essentially negligible throughout the ferroelectric switching process, except for small local stresses imposed by adjacent domains. The time-resolved elastic energy of the clamped film, on the other hand, remains high, and locally peaks just before switching is completed. These results demonstrate that dynamic evolution of the polar state and accompanying structural distortions transiently modify the energy landscape. The peak at close to them moment where switching occurs, indicates how switching transiently creates an energetically unfavorable state. Since both nucleation and growth of reverse polarized domains are activated processes[53] and both have exponential dependence on the activation energy, such transient changes (even moderate) in the energy landscape can have a dramatic effect on switching time. Other energy terms (Landau and electric) are also impacted by mechanical constraints, where the high elastic energy slows the evolution of the polarization so that the higher energy state persists for a longer period of time. Finally, we address the role of oxygen octahedral tilting. The data presented (Fig. 3.11) includes dynamical evolution of the oxygen octahedral tilts, and as such, an associated energy increase (Eq. 3.1). Informed by our earlier findings that the switching energy barrier lies somewhere between strain clamping and strong strain + tilt clamping (*i.e.*, weak strain + tilt clamping), and to extract the effect on switching from the octahedral tilts, we simulate the same polarization switching (Fig. 3.12) without consideration of the oxygen octahedral tilts. There is a stark contrast between these two cases, with the oxygen octahedral tilts accounting for a $\sim$10x increase in switching time over the case where oxygen octahedral tilts are removed from the simulations. This is an important finding, and the dramatic increase in switching time highlights the importance of proper consideration of all coupled order parameters in setting the dynamics and energetics of switching in BFO.

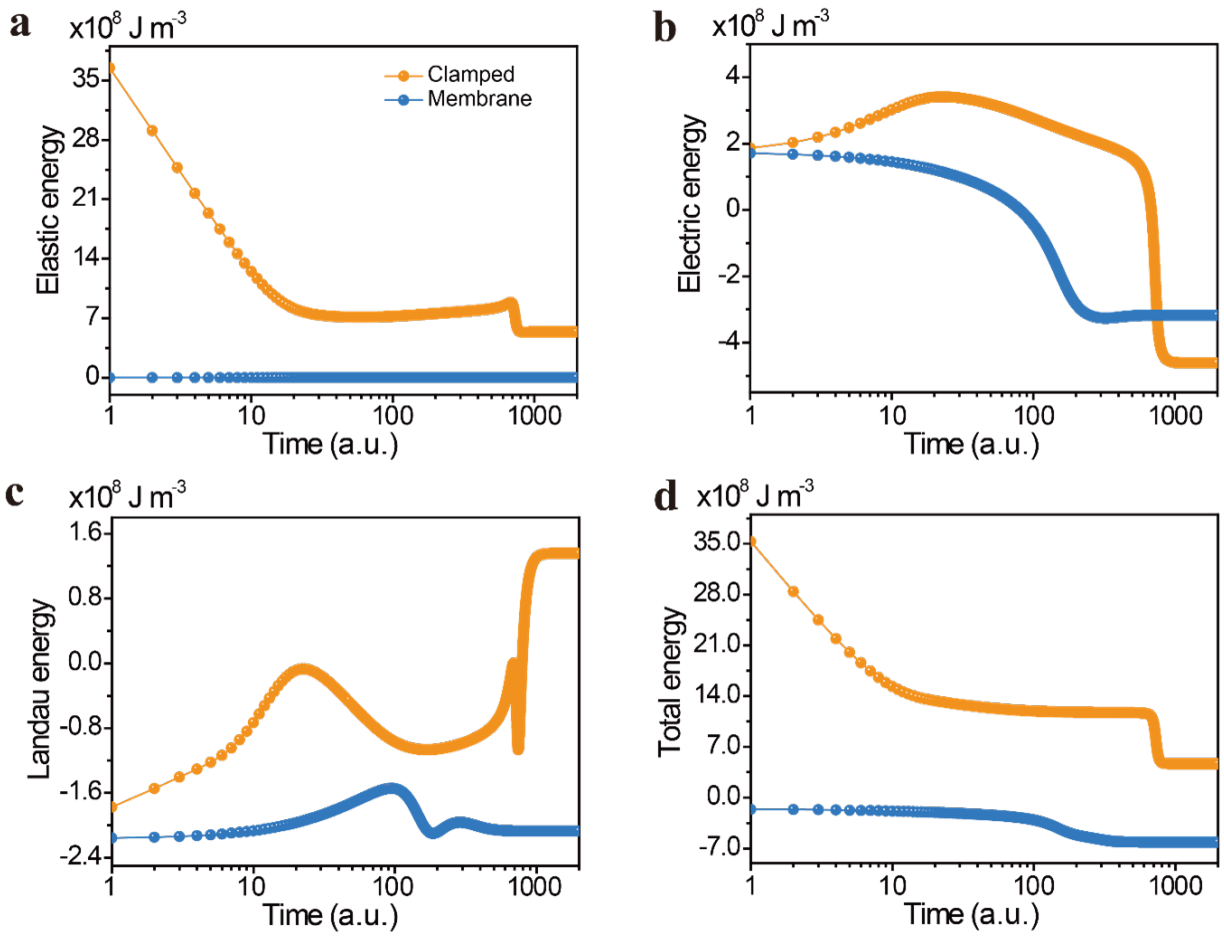

Figure 3.11: From [16]. Free energy evolution during the switching process under an externally applied voltage for clamped film and membrane cases. Horizontal axis is time (a.u.) and vertical axis is the average energy for various contributions to the total energy. **a.** Elastic energy. **b.** Electrostatic energy. **c.** Landau energy. **d.** Total free energy which is the summation of the elastic, electrostatic, and Landau energy. For the clamped film case, 0.4% compressive mismatch strain is considered.

This work reveals the fundamental role of substrate mechanical constraints, and more generally charge-lattice coupling, in dictating ferroelectric switching energetics and dynamics in BFO. With the grand challenge of achieving sub-100mV switching in ferroelectrics, clamping effects and the relative contribution to switching energetics and dynamics of all coupled order parameters must be understood. We employ a Landau free energy formalism to conduct thermodynamic calculations modeling varying degrees of clamping effects from the substrate, both using *ab-initio* and phenomenological models. We experimentally demonstrate a method of mitigating clamping effects by lifting-off SRO/BFO/SRO trilayers from an STO substrate. Other methods, for example, by tuning device aspect ratio[120] may

provide additional pathways to mitigate clamping. Here, we observe a marked evolution of crystal and domain structure, consistent with changes in elastic constraints, and show that the energetics and dynamics of the system drastically change after lift-off. We observe a significant reduction in switching voltage and improved switching speeds for freestanding membranes relative to clamped films. The origins of the changes observed are better understood with the help of phase-field simulations, where the dynamic elastic energy and oxygen octahedral tilts play a predominant role in slowing polarization reversal. In the following sections, I expand upon the significance of our findings surrounding strain + tilt clamping, with particular emphasis on implications for dynamic coupling between charge, lattice and magnetic degrees of freedom. Finally, I discuss the broad applicability of our findings, and the significance of charge-lattice coupling, by presenting studies on the prototypical ferroelectric $BaTiO_3$.

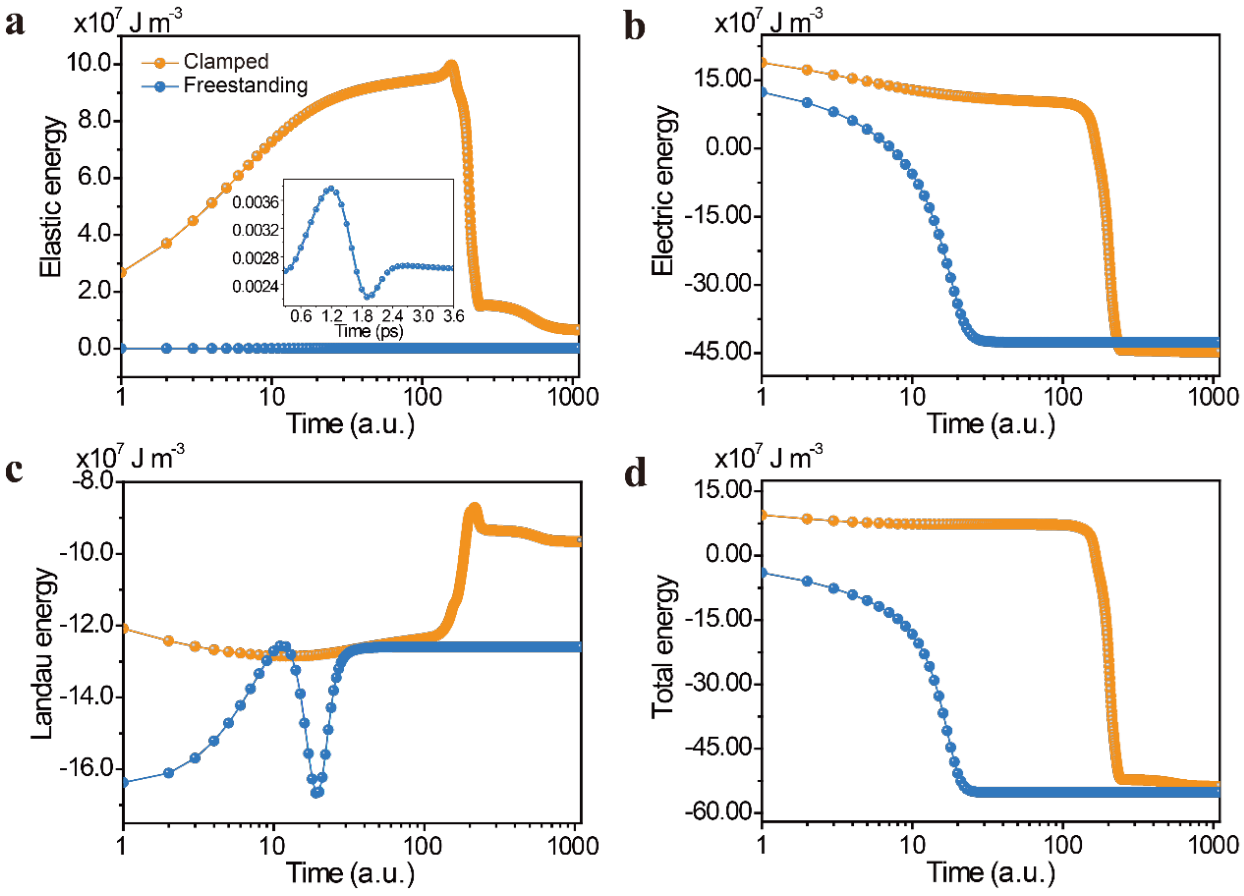

Figure 3.12 *(previous page)*: From [16]. Free energy evolution during the switching process under an externally applied voltage for clamped film and membrane cases **without oxygen octahedral tilts**. Horizontal axis is time (a.u.) and vertical axis is the average energy for various contributions to the total energy. **a.** Elastic energy. **b.** Electrostatic energy. **c.** Landau energy. **d.** Total free energy which is the summation of the elastic, electrostatic, and Landau energy. For the clamped film case, 0.4% compressive mismatch strain is considered.

3.2.4 Implications for switching of magnetic order

There are two important observations from our findings that the deserve additional attention. The first is that our results are most consistent with "weak strain + tilt clamping" (Fig. 3.5) This means that the oxygen octahedral tilts are vital in setting the energetics of the switching process in BFO. The second observation (Fig. 3.11,3.12) is that by including the oxygen octahedral tilts in the phase field simulation, the switching time of ferroelectric order is observed to increase dramatically. We know that the oxygen octahedral tilts are key in setting the magnetization (and dynamics thereof) orientation through the DM interaction [9, 42]. What this means is that the required coupling between charge and lattice order parameters inhibits ferroelectric switching, and more importantly, the magnetic order, which in some sense is a slave to the lattice degree of freedom, induces slower switching dynamics. Notably, this finding does not come from the spinful nature (recall the LLG equation in section 1.1.2) of magnetization, which can induce additionally complex dynamics. Yet, even in the case where we consider just charge-lattice coupling, the implications for dynamics of all couple order parameters in BFO is significant. On-going/future work (Appendix 6.2.1.3) aims to address the spinful nature of magnetization directly.

3.3 $BaTiO_3$

Next, I turn to the broad applicability of our findings on charge-lattice coupling by examining another material system, namely the prototypical ferroelectric $BaTiO_3$. Here, using the ferroelectric BTO, production of precisely strain-engineered, substrate released nanoscale membranes is demonstrated via an epitaxial lift-off process (the same as for BFO, Fig. 3.4) that allows the high crystalline quality of films grown on substrates to be replicated. Similar to the case of the BFO, releasing the substrate clamping is shown to dramatically impact ferroelectric switching and domain dynamics (including reducing coercive fields to $<$10 kV/cm and improving switching times to $<$5 ns for a 20 μm diameter capacitor in a 100-nm-thick film).

Mechanical separation of a film from the substrate is expected to facilitate polarization switching processes, either by enabling ferroelastic events limited by substrate constraint,[120] or by reducing domain-wall pinning at the substrate/film interface.[126] Struc-

tural inhomogeneities emerging in unclamped membranes, however, can mask the impact of the substrate release on the switching kinetics.[115] Therefore, preserving high crystal quality in the ferroelectric membranes after the release is important to identify intrinsic changes in switching mechanisms and domain-wall mobilities with the aim of lowering switching times, as is sought after for ultra-high-speed, non-volatile memories,[127] memristors,[128] and neuromorphic networks.[129]

Though pulsed measurements of ferroelectric switching have to date accessed the fastest timescales observed, researchers also employ frequency dependent polarization-electric field hysteresis loops to extract information about domain wall dynamics. The idea is that by tuning the drive frequency of the (typically) triangular voltage waveform, and studying the change in the observed "coercive field"[2], one can extract meaningful information about how fast the domain walls move. As with any transport-based measurement of ferroelectrics, if one properly accounts for free-charge dynamics, fair comparisons can be made across material systems, even if absolute dynamics are difficult ascertain. As such, we use frequency dependent measurements of the coercive field in BTO to study the impact of mechanical constraints imposed by the substrate. From a log-log plot (Fig. 3.13c) we identify a linear dependence of the observed coercive field as a function of stimulus frequency that allows us to fit our data to the Ishibashi and Orihara model for domain-growth-limited switching,[25] where $E_c \propto f^{\beta}$. The fitting reveals a decrease by a factor of 2 and 4 in the scaling exponent (β) for films with bottom electrode chemistry $SrRuO_3$ and $Ba_{0.5}Sr_{0.5}O_3$, respectively. (The introduction of Ba into the SRO modifies tunes the strain on the ferroelectric, BTO [107].) Lower β values indicate lower frequency dispersion of coercive fields which implies higher domain-wall mobility[130]. Faster dynamics under ac fields can be obtained by reducing the inhomogeneities cause by structural defect so or surface roughness[131]; however, these membranes show comparable structural quality and surface morphology to the epitaxial films, implying that the change of dynamics is directly related to the substrate release.

To provide further insight into domain-wall dynamics and the switching kinetics of the films, I performed pulsed-electric-field switching measurements (as in Chapter 2) on epitaxial BTO films and freestanding membranes. From the polarization transients from the on-substrate films (Fig. 3.13d) as well as the membrane (Fig. 3.13e)on silicon substrates, I extract the characteristic switching times for the polarization reversal, t_0 (Fig. 3.13f). The on-substrate BTO film shows $t_0 = 17$ns, where as the the released membrane exhibits a $t_0 = 5$ns and a similar value of switched polarization. While different circuit RC time constants for the clamped and freestanding film can contribute to differences in measured switching times, I find that after re-scaling by RC, the membranes on silicon still show faster switching times (Fig. 3.13f), indicating that the switching times are not solely dominated by RC effects, but rather the influence of the substrate. These results agree with the domain dynamics under ac fields, as described above.

[2]Here, one defines the coercive field as the applied voltage at the time when the average polarization of the film is zero.

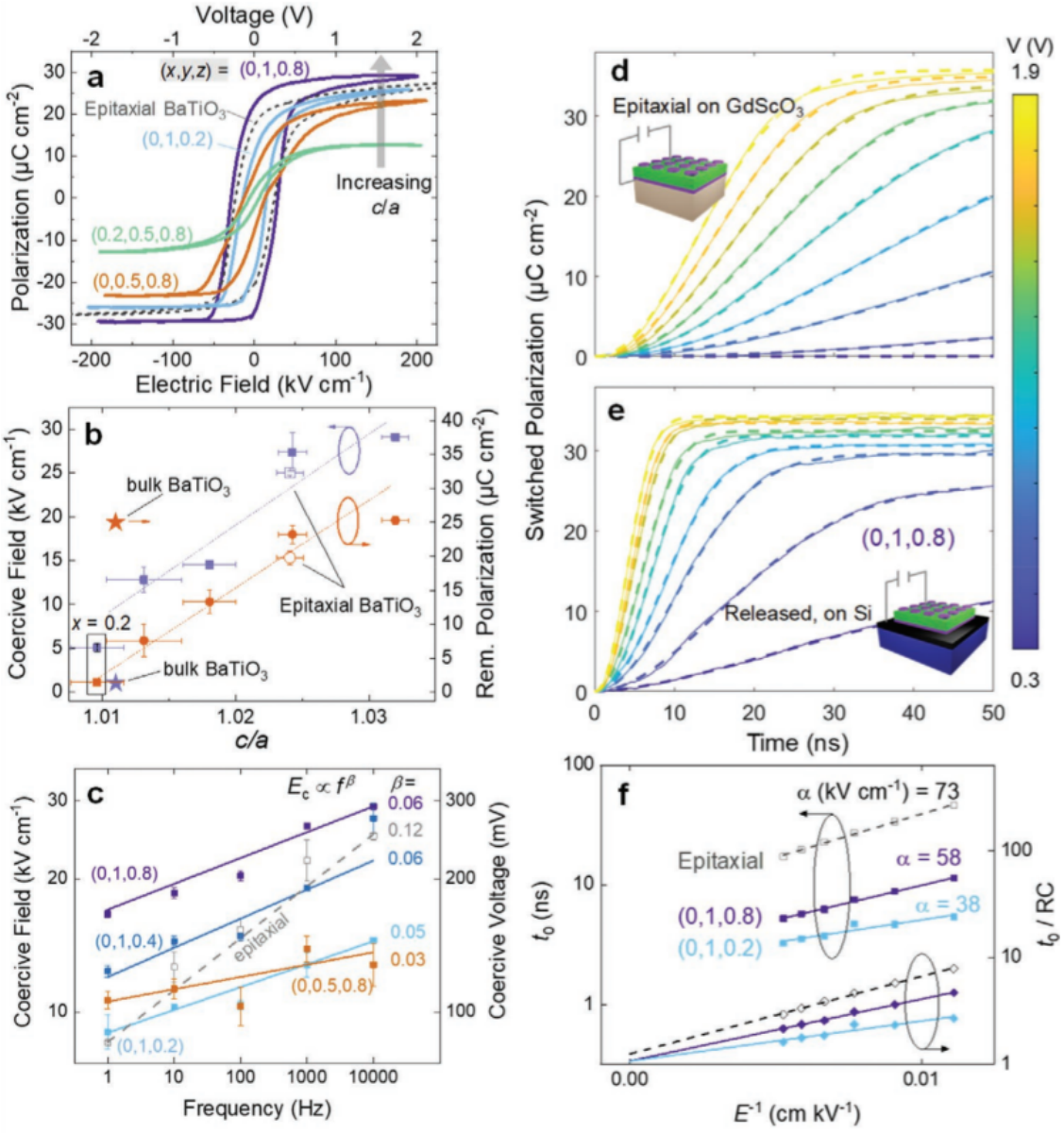
a
Voltage (V)
(x,y,z) = (0,1,0.8)
Epitaxial BaTiO3
(0,1,0.2)
Increasing c/a
(0.2,0.5,0.8)
(0,0.5,0.8)
Polarization (μC cm-2)
Electric Field (kV cm-1)
b
bulk BaTiO3
Epitaxial BaTiO3
x = 0.2
bulk BaTiO3
Coercive Field (kV cm-1)
Rem. Polarization (μC cm-2)
c/a
c
Ec ∝ f β
β=
0.06
0.12
0.06
0.05
0.03
(0,1,0.8)
(0,1,0.4)
epitaxial
(0,0.5,0.8)
(0,1,0.2)
Coercive Field (kV cm-1)
Coercive Voltage (mV)
Frequency (Hz)
d
Epitaxial on GdScO3
V (V)
1.9
0.3
Switched Polarization (μC cm-2)
e
(0,1,0.8)
Released, on Si
Time (ns)
f
α (kV cm-1) = 73
Epitaxial
α = 58
(0,1,0.8)
α = 38
(0,1,0.2)
t0 (ns)
t0 / RC
E-1 (cm kV-1)

Figure 3.13 *(previous page)*: Used with permission from [107]. Controlling polarization and switching dynamics of $Ba_{1-x}Sr_xTiO_3$ membranes on silicon at room temperature. **a.** Room-temperature ferroelectric polarization hysteresis loops measured at a frequency of 10kHz on capacitor devices of various (x, y, z) heterostructure types transferred onto silicon substrates. x denotes the chemistry of the ferroelectric layer ($Ba_{1-x}Sr_xTiO_3$), y denotes the chemistry of the electrode layer ($Ba_{1-y}Sr_yTiO_3$), and z denotes the ratio of the electrode thickness to ferroelectric thickness, ($2t_E/t_{FE}$). Data for an epitaxial BaTiO3 sample with $SrRuO_3$ electrodes are also shown (dashed). Ferroelectric hysteresis loops are corrected for bias imprint and permittivity contributions at high field. **b.** Coercive field (left axis) and remanent polarization (right axis) obtained from polarization hysteresis loops, as a function of lattice parameter ratio, c/a. Data for epitaxial samples on $GdScO_3$ substrates are shown as empty symbols and bulk $BaTiO_3$ data[88] are shown as star symbols. Lines are guides to the eye. **c.** Frequency dependence of the coercive field (log–log plot) obtained for all $BaTiO_3$ membranes (filled symbols) and epitaxial films (open symbols). Lines are fit to the Ishibashi and Orihara model. **d,e** Switched polarization obtained from the integration of the current transient after a switching voltage pulse of varying amplitude, for an as-grown $BaTiO_3$ epitaxial film (with 10nm $SrRuO_3$ electrodes) on: **d.** GdScO3, and **e.**) a $BaTiO_3$ membrane on silicon with $SrRuO_3$ electrodes of thickness 40nm. **f.** Polarization switching times as a function of the inverse of electric field pulse amplitude for three $BaTiO_3$ films, before (left axis) and after (right axis) rescaling with the circuit RC time. Lines are fit to Merz's law.

Further I consider the eneregetics of the switching process: from the switching time dependence on the pulse amplitude, I obtain the activation field (α) from Merz' law[53] (Eq. 2.8), which results in values that are nearly 20% lower for the freestanding membrane (Fig. 3.13f); implying that the domain walls require less energy to move after release from the substrate. This observation, together with the evidence of modified domain dynamics, points to a lower energy switching pathway upon removal of the mechanical constraint of the growth substrate. Calculations show that the energy to create 90° domain boundaries is significantly lower than that of their 180° counterparts[56], making it more favorable to realize the polarization reversal via two successive ferroelastic switching steps with creation of 90° domain walls, as observed experimentally in single crystals[]. In epitaxial films, however, substrate clamping prevents the formation and propagation of these 90° domain walls during switching due to the large elastic energy cost. The removal of this constraint in the membranes-which are only weakly bonded to the silicon substrate-likely permits the local strains generated by 90° domain walls to be readily accommodated thus facilitating a lower-energy switching process. These findings are perfectly in line with those observed in BFO, where the charge-lattice coupling introduces additional energy terms that must be overcome during the switching process. What is interesting is that BFO is known to switch via a two-step ferroelastic switching pathway, where BTO was believed to switch via one, 180°

switch. From our BTO data, it turns out that a ferroelastic switching pathway (two 90° steps) is actually preferred, but the coupling between charge and lattice degrees of freedom can inhibit such switching pathways, increasing the energy and slowing the process.

Chapter 4

Relaxation Mechanisms of Polar Order

4.1 Essential background and motivation

Applications of ferroelectric materials make use of the collective nature of ferroelectric order to enable low energy switching and make use of inherent non-volatility. As ferroelectrics progress toward increasingly low voltage operation (a necessity for device applications), issues pertaining to polarization stability must be addressed. Recent progress has demonstrated ultra-low voltage operation of thin film ferroelectrics [51, 52, 99] approaching the 100mV goal [2, 3] and continues to show the potential of these materials to revolutionize computing hardware [2, 3, 132, 133, 134]. In efforts to reduce the switching voltage further, researchers have employed doping[51, 52] electrode interface engineering [99, 135] and thickness scaling [136] as well as a variety of other methods including using freestanding films [16, 107], which are free from mechanical constraints imposed by the substrate (Chapter 3). While reduction of the switching energy and time has seen significant improvement[26, 52, 58, 107, 137], an increasingly important metric to consider is the stability of the polar state. In the prototypical metal/ferroelectric/metal trilayer configuration, one must carefully consider the role of depolarizing fields in impacting the stability of the ferroelectric polarization. If sufficient depolarization persists in the ferroelectric, the utility of the remnant state is significantly reduced or completely destroyed. I aim to better understand the mechanisms and factors impacting depolarization in an effort to make more robust the ferroelectric order parameter. Such studies are important in the BFO system as ferroelectricity sets the dominant energy scale of the coupled order, so, depending the mechanism (*e.g.*, reduction in polar displacement on the unit-cell level or nucleation and growth of domains), depolarization can result in decoupling or suppression of all order parameters, or domain formation modifying the macroscopic length scale and/or timescale over which magnetoelectric coupling is useful. This work is also broadly applicable, holding important insight for other ferroelectric systems and applications thereof.

Here, using high-speed, time-resolved, pulsed ferroelectric measurements, I study dynamic evolution of the ferroelectric order parameter in ultra-low coercivity $BaTiO_3$ (BTO). I choose BTO as it is a prototype ferroelectric (not multiferroic) and allows me to isolate ferroelectric order and study the impact of a number of factors on, and mechanisms of, depolarization. Via thickness and temperature dependent studies, I interrogate the interaction between depolarization fields and the energy barrier between adjacent polarization states. A comparison is made with the prototypical relaxor ferroelectric, $0.68Pb(Mg_{1/3},Nb_{2/3})O_3$ - $0.32PbTiO_3$ (PMN-PT), which, as expected, does not follow the same mechanism of depolarization. My thickness and temperature dependent studies are understood within the framework of the Landau free energy and my results show how mitigating depolarization fields and/or modifying the energy barrier between adjacent polarization states can significantly increase polarization stability. Finally, I contextualize my findings within the framework of computing applications.

4.1.1 Background

Previous first-principles work predicts a lower bound on film thickness for stabilization of ferroelectric order of ∼24 Angstroms[138]. Beyond such a "critical thickness" electrostatic depolarization fields, arising from incomplete screening of the polarization by the adjacent top and bottom electrode fully suppress ferroelectric ordering[1]. The dominant role of electrostatics is confirmed by implementing a simple model for the polarization, which self consistently accounts for atomic displacements and electronic polarization. The simplified model reproduces the results from first-principles calculations, indicating that the chemistry of the interface (including in the first-principles calculation, but not in the simple model) does not play a significant role, and electrostatics dominate the suppression of ferroelectric order [138]. More recent work, however, has addressed depolarization as it results from pinned dipoles at the ferroelectric/metal interface. In particular, in ref [135], the authors demonstrate that by inserting a thin layer of $SrTiO_3$ at the $SrRuO_3/BaTiO_3$ interface, they can favorably modify the termination sequence and remove pinned dipoles, thereby enhancing the stability of the ferroelectric order of the BTO. Remarkably, recent progress in $HfZrO_2$ (HZO) has stabilized FE order down to the single nanometer limit[139], while other work has shown a significant impact of depolarization fields at thicknesses at least an order of magnitude larger than that predicted by Ghosez, *et. al.*[140] and even up to 4μm film thicknesses[141]. Depolarization fields are known to increase with decreasing film thickness[140, 141], and as the community moves toward thinner films with lower coercivities (as necessitated by applications), the issues arising from depolarization fields will only become increasingly acute.

Here I study depolarization in the classical ferroelectric material $BaTiO_3$. BTO has received significant attention over the past several decades prototypical, tetragonal ferroelectric, and provides a parallel ferroelectric system to BFO. Much of the early work on

[1]This is understood as a suppression of the polar displacement itself, not the macroscopic polarization, which can exhibit depolarization through domain formation

switching of the ferroelectric order was performed on BTO [69] and depolarization has been extensively studied theoretically [138, 141] and experimentally [140, 135], adding context and background to my studies. Unlike BFO, BTO does not contain magnetic ordering, and importantly has a much lower Curie temperature. The high Curie temperature of BFO ($\approx$ 1100K [41]) means (as detailed in Sections 4.1.2 and 4.3.2) that the ferroelectric order is relatively stable. Depolarization in BFO, while not significant at the thicknesses typically studied here (> 10nm), is predicted to become increasingly important as progress is made toward thinner and thinner films in the sub-5nm range. Using BTO as a test system, therefore, allows me to study the mechanisms and effects of depolarization in a well-characterized ferroelectric system, without the need for exceptionally thin films.

4.1.2 Depolarization Fields

Here, I detail the role of electro-statics in producing depolarization fields, and interpret them within the context of the thermodynamic free energy landscape. The Landau free energy of a classical ferroelectric, up to 4^{th} order, can be written:

$$F = \alpha_1(T - T_c)P^2 + \alpha_2 P^4 - EP + O(P^6) \tag{4.1}$$

where α_i (i=1,2) are coefficients determined via experiment or first principles calculations, P, is the polarization order parameter, E is an external electric field, and T,T_c are the temperature and Curie temperature, respectively. For brevity, I write only the out-of-plane (z-component) of the polarization here, though the full free-energy functional includes in-plane components as well [142, 143]. Below the Curie temperature, and in the absence of an external field, there are two degenerate ground states, corresponding to minima of the so-call "double well potential", where, in principle, the uniformly polarized state is a stable energy minimum. As observed from Eq. 4.1, the presence of an electric field modifies the free energy such that one polarization state is energetically preferred over the other. Under the influence of such an electric field, it is known that ferroelectrics undergo an activated process of domain nucleation and growth to form domains of different polarization states and minimize the free energy [69, 25, 54, 55]. Taken in isolation, a finite ferroelectric with polarization P will experience a depolarization field independent of thickness:

$$E = -\frac{P}{\epsilon_f} \tag{4.2}$$

where ϵ_f is the relative dielectric constant of the material [144, 145]. To see this, consider a uniformly polarized insulating ferroelectric (finite in $\hat{z}$, but infinite in $\hat{x}$ and $\hat{y}$, *i.e.* a thin-film) with polarization

$$\vec{P} = P\hat{z} \tag{4.3}$$

In the absence of external free charge, the resulting volume and surface charge densities are:

$$\rho \equiv \nabla \cdot \vec{P} = 0,\ \sigma \equiv \vec{P} \cdot \hat{n} = P \tag{4.4}$$

assuming the ferroelectric has dielectric constant ϵ_f, the relation for the electric field (E) within the material can be obtained using the equation for the parallel plate capacitor, $Q = CV = \frac{\epsilon_f A}{d} Ed$, and using the charge density $Q/A = P$ from the surface charge, one arrives at the electric field of Eq. 4.2, which points opposite the polarization. The origin of this "depolarization field" is the presence of uncompensated charges at the edge of the ferroelectric, which produce an electric field.

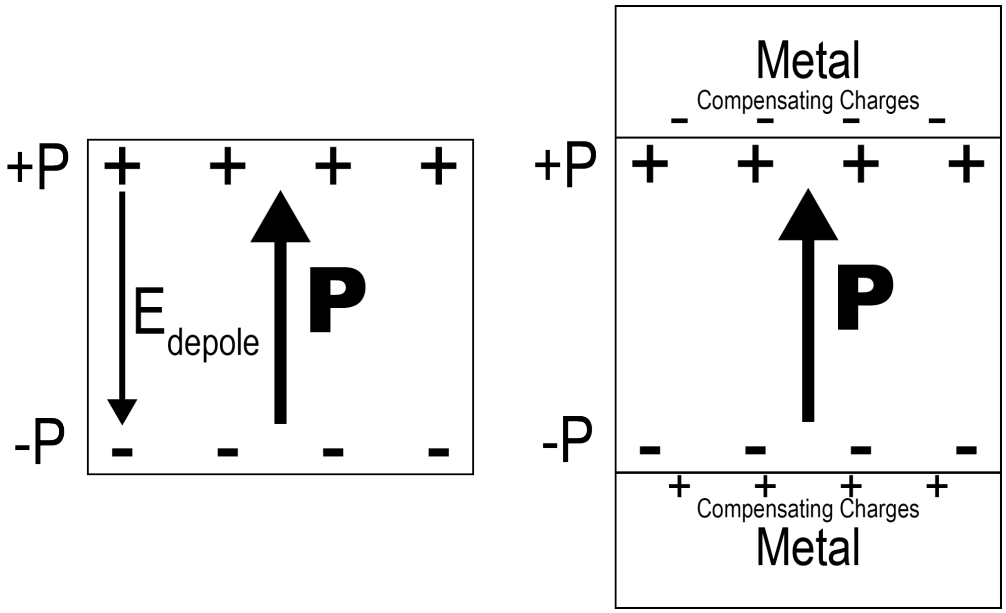

Figure 4.1: Depolarization fields in an isolated ferroelectric vs in a metal/ferroelectric/metal trilayer configuration with compensating (screening) charges.

In a metal/ferroelectric/metal trilayer heterostructure (Fig. 4.1), such as that studied here, however, the polarization of the ferroelectric, $\vec{P}$, induces compensating charges in the metal electrodes. The depolarization field in this case can be calculated by solving Poisson's equation subject to appropriate boundary conditions (here I use a short circuit boundary conditions) and carrier statistics in the adjacent electrodes. In such a configuration the depolarization field is found to be thickness dependent and is given by:

$$E = -\frac{P}{\epsilon_f}\left(\frac{2\epsilon_f/d}{2\epsilon_f/d + \epsilon_e/\lambda}\right) \tag{4.5}$$

where d, ϵ_e, λ are the film thickness, dielectric constant of the electrode, and screening length (related to carrier density, effective carrier mass and dielectric constant) of the electrode, respectively[141]. If such depolarization fields are sufficiently strong, they can

drive nucleation and growth of domains in the ferroelectric, which will dynamically evolve to minimize its energy. In this case, depending on the relative strength between depolarization energy ($P \cdot E_{depole}$) and the "activation energy"[69] (related to the depth of the double well), the uniformly polarized state may no longer be an energy minimum. Using a relative dielectric constant for the BTO (SRO) layer of 360 (10) [99], a screening length $\lambda = 0.5$Å, a film thickness of 100nm and a polarization value of $25\mu C/cm^2$, I obtain a depolarization field of ∼27kV/cm. For context, operation of an identical 100nm film at 100mV switching voltage corresponds to an electric-field of only 10kV/cm. This comparison makes clear the significance of depolarization fields in ultra-low coercivity ferroelectrics.

4.2 Experimental observation of polarization relaxation

4.2.1 Experimental protocol

Here, to address both the issues concerning polar instability for practical applications, and the fundamental mechanisms, implications, and timescales of such instability, I study depolarization dynamics of the prototypical classical ferroelectric $BaTiO_3$ (BTO). To do so, I perform high-speed pulsed ferroelectric measurements. Similar pulsed measurements of switching have been used extensively in the study of ferroelectric materials, though typically, such measurements are used to study dynamics under the influence of an externally applied voltage [26, 58, 69]. In standard pulsed switching experiments, a pulse train (Fig. 4.2a), consisting of three pulses is used to 1. Preset the polarization, 2. Drive a ferroelectric switching event and 3. Measure the non-switching response of the measurement circuit. The ferroelectric switching displacement current is then obtained by subtracting the non-switching response from the switching response ($j_1 - j_2$ Fig. 4.2b). These measurements have been used to observe ferroelectric switching at very fast timescales and to study the mechanisms of switching [24, 146, 147]. The technique, however, relies on a key assumption of ferroelectric order, namely non-volatility, *i.e.*, that the polarization does not change during the time (t_d) between the switching and non-switching pulses (P_1 and P_2, respectively in Fig 4.2a). The assumption of non-volatility allows me to disentangle ferroelectric switching displacement current from other sources of charge transport [26] (from resistive leakage, capacitive charging, etc.). However, depolarization mechanisms in classical ferroelectrics, arising from internal fields[138, 140, 141] or imprint from, for example, electrode asymmetry, defects, or composition gradients can cause internal fields and result in a dynamic evolution of the order parameter during the time t_d, when no external field is applied. In the presence of depolarization, as the delay, t_d, becomes longer, the response to pulses P_1 and P_2 will become increasingly similar. To understand this, consider the limiting case of instantaneous depolarization, *i.e.*, after pulsing, the sample immediately returns to a net zero polarization state. In such a scenario, the initial state of the material for any pulse applied will be the same, and I expect to see no difference between what was previously referred to as the

"switching" (j_1) and "non-switching" (j_2) responses. In experiment, depolarization does not occur instantaneously, and my measurement scheme allows me to probe depolarization dynamics and associated timescales by studying the difference between j_1 and j_2 as a function of t_d (Fig. 4.2c).

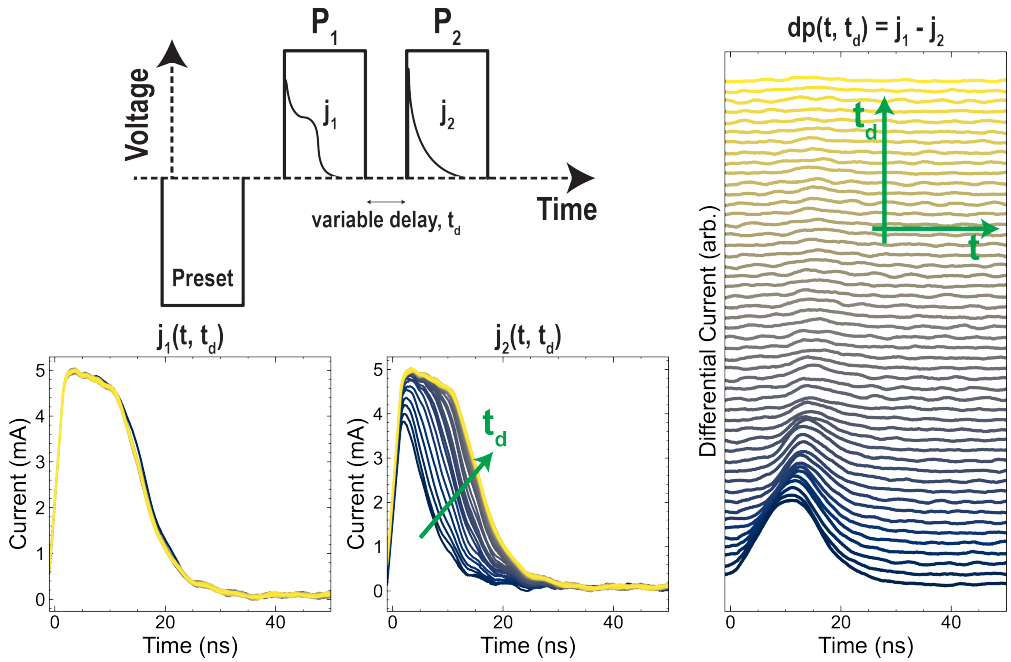

Figure 4.2: Depolarization or ferroelectric relaxation experimental protocol. **a.** Experimental voltage pulse profile. An identical pulse profile is used in two different polarities ('up' or 'positive' refers to P_1 and P_2 corresponding to positive applied voltages, and 'down' or 'negative' refers to P_1 and P_2 corresponding to negative applied voltages). P_1 is the so-called "switching pulse" with P_2 the so-called "non-switching pulse". To probe depolarization dynamics, I tune the time delay (t_d) between pulses P_1 and P_2. **b.** Observed displacement current for a 25nm BTO film during pulses P_1 (j_1) and P_2 (j_2). Data is shown for a nominal 9.5μm-diameter capacitor. As the time delay t_d lengthens, j_2 increasingly resembles j_1 because of depolarization. **c.** Differential current (d_p) and differential switched polarization (DSP) for increasing td. Though I observe a polarization switching transient in the displacement current (j_1, j_2), the DSP tends towards zero as depolarization progresses, since the film's initial state just before application of P_1 and P_2 becomes increasingly similar.

4.2.2 Imprint versus Depolarization

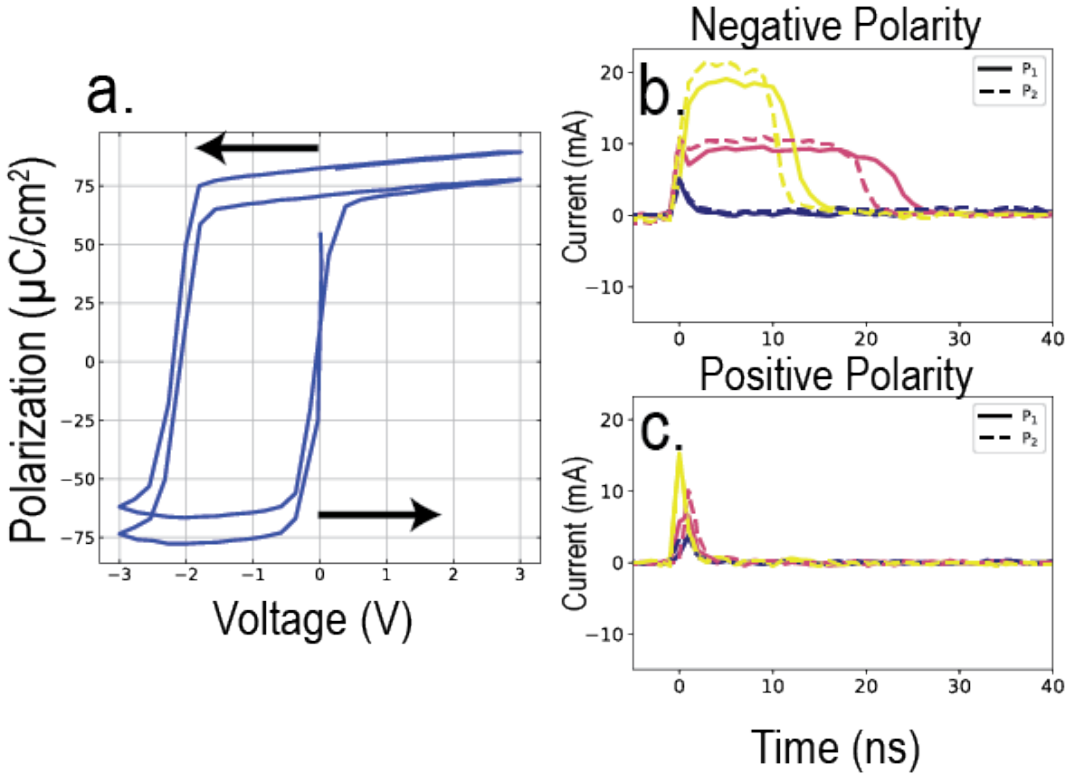

Figure 4.3: Imprinted Polarization Reversal. Owing to internal fields in the ferroelectric (BFO shown here), one polarization state is preferred over the other. This is observed in the PE loop (a.) as well as in bipolar switching transients (b., c.). When poling in the non-switching direction (c.), *i.e.*, towards the already preferred state, only a dielectric response is measured. When poling in the switching direction (b.) pulses P_1 and P_2 more closely resemble one another as the delay time t_d is increased.

First, in order to ensure that the observed decay in DSP does not stem from the effects of imprint (*i.e.*, a hysteresis loop which is not centered at 0V), I perform an identical pulsed measurement with the polarity reversed (preset positive polarity, P_1 and P_2 negative polarity, in Fig. 4.2a.). Depolarization from imprint acts differently than the depolarization effects presented here. Imprinted ferroelectric films have a preferred polarization direction, and in the absence of an applied electric field will tend toward that direction. This creates a scenario where a ferroelectric switching transient is only observed for one pulse train polarity (Fig. 4.3). The BTO films presently studied, however, show essentially an identical DSP decay for both polarities (Fig. 4.4), indicating true depolarization, *i.e.*, the system depolarizes toward net zero macroscopic polarization rather than "back-switching" towards a preferred

direction. This finding agrees with the symmetric nature of the quasi-static hysteresis loops (Fig. 4.5).

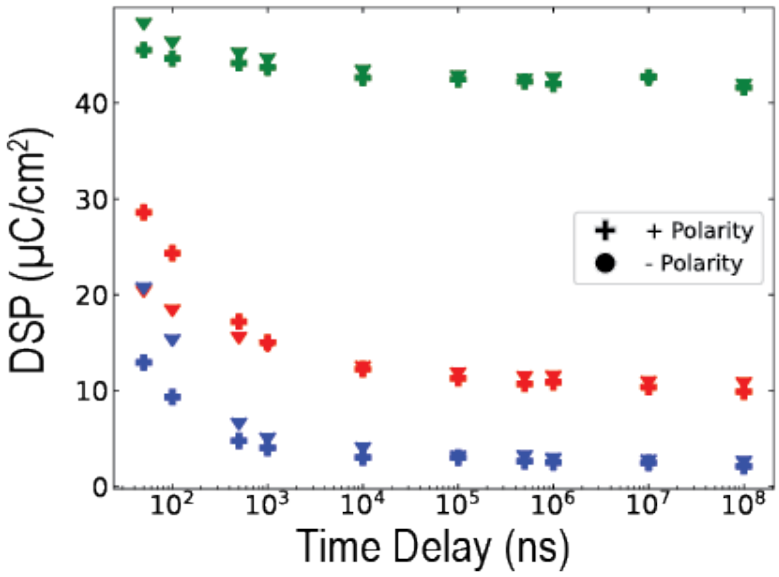

Figure 4.4: Bipolar Polarization Decay. Identical polarization relaxation transients are observed for both negative and positive polarities. This is in contrast to Fig. 4.3 and indicates there is no existing preferred polarization state.

4.3 Depolarization in $BaTiO_3$

To experimentally study depolarization, I turn to the same ultra-low coercivity BTO films studied in Section 2.3. As before, the BTO system offers a parallel universe to BFO, enabling me to study the effects of modifying the free energy landscape on dynamics of ferroelectric order. As will be described in detail in Section 4.3.2, the low (in comparison to BFO) Curie temperature of BTO also offers a means of more easily studying factors impacting depolarization.

4.3.1 Effect of thickness

Motivated by favorable switching voltage scaling upon reductions in film thickness, I begin by studying depolarization in a thickness series of BTO films. High quality $SrRuO_3$(27nm) / $BaTiO_3$(X nm) / $SrRuO_3$(27nm) (X = 25, 50, 100) tri-layer samples are grown via pulsed laser deposition (see ref [99] for complete details) on GdScO3 (110) substrates. Careful growth optimization (idealized structure, chemistry and interfaces) has enabled us to create

ultra-low coercivity BTO films with almost bulk like-properties, and coercive voltages below 100mV (Fig. 4.5), corresponding to quasistatic coercive fields of ∼20kV/cm or lower, resembling bulk-like BTO.

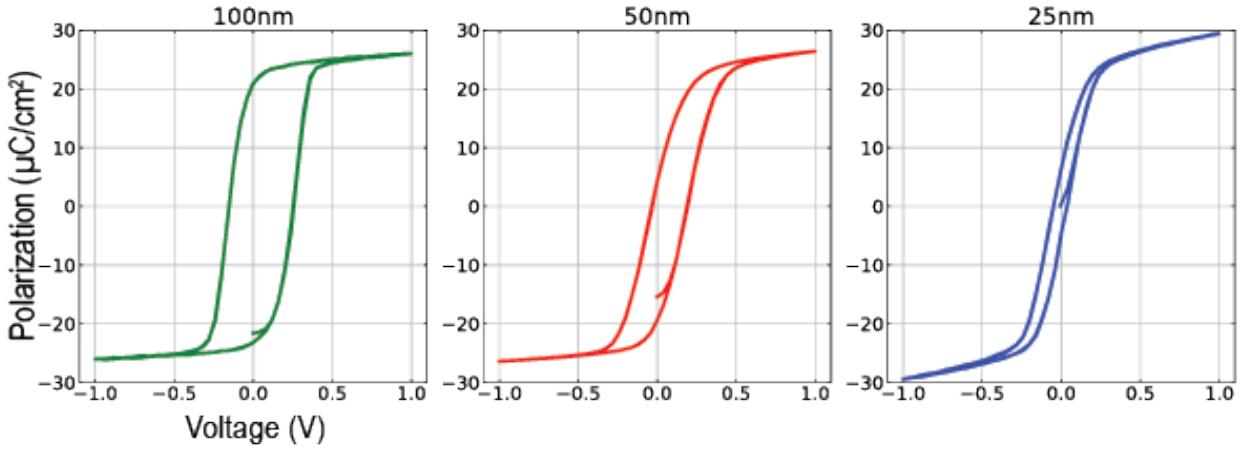

Figure 4.5: Ultra-low coercive field BTO ferroelectric hysteresis loops.

I apply the aforementioned pulse train (Fig. 4.2a) to the sample and study the differential current ($\Delta P = j_1 - j_2$) between responses to pulses P_1 and P_2 as a function of delay time (t_d) for fixed applied electric field (100kV/cm). As seen in the data for a 25nm BTO film (Fig. 4.2b,c), as t_d increases, the differential current tends towards zero. I then integrate the differential current and normalize by the device area to obtain the differential switched polarization (DSP), *i.e.*,

$$\mathrm{DSP}(t_d) = \frac{1}{A}\int_0^{t_p} j_1(t, t_d) - j_2(t, t_d)dt \tag{4.6}$$

where A,t_p are the device area and pulse width time, respectively. In the absence of depolarization for a classical ferroelectric, the DSP is simply twice the remnant polarization, and in the limiting case of instantaneous, complete depolarization, the DSP is zero for all delay times, t_d. I show the DSP(t_d) (Fig. 4.6) for various BTO film thicknesses, shows clear polarization decay as the film is made thinner.

To better understand the mechanisms influencing the observed depolarization, I employ a thickness series of 25nm, 50nm, and 100nm thick films and plot DSP as a function of t_d (Fig 4.6). For all measurements (Fig 4.6), the voltage amplitude was set such that the nominal applied electric field was fixed to 100kV/cm, *e.g.*, 250mV applied for the 25nm sample. Depolarization is significantly more pronounced in thinner samples (25nm and 50nm), with almost no depolarization occurring in the 100nm film. This behavior might be expected from the form of Eq. 4.5, where the depolarization field increases with decreasing thickness; however, the sharp roll-off, where I observe significant decay in the 50nm film and

minimal decay in the 100nm film, is surprising. It has been shown experimentally [99] and theoretically [148, 149] that reducing the film thickness reduces the Curie temperature. The fractional change in Curie temperature can be expressed as:

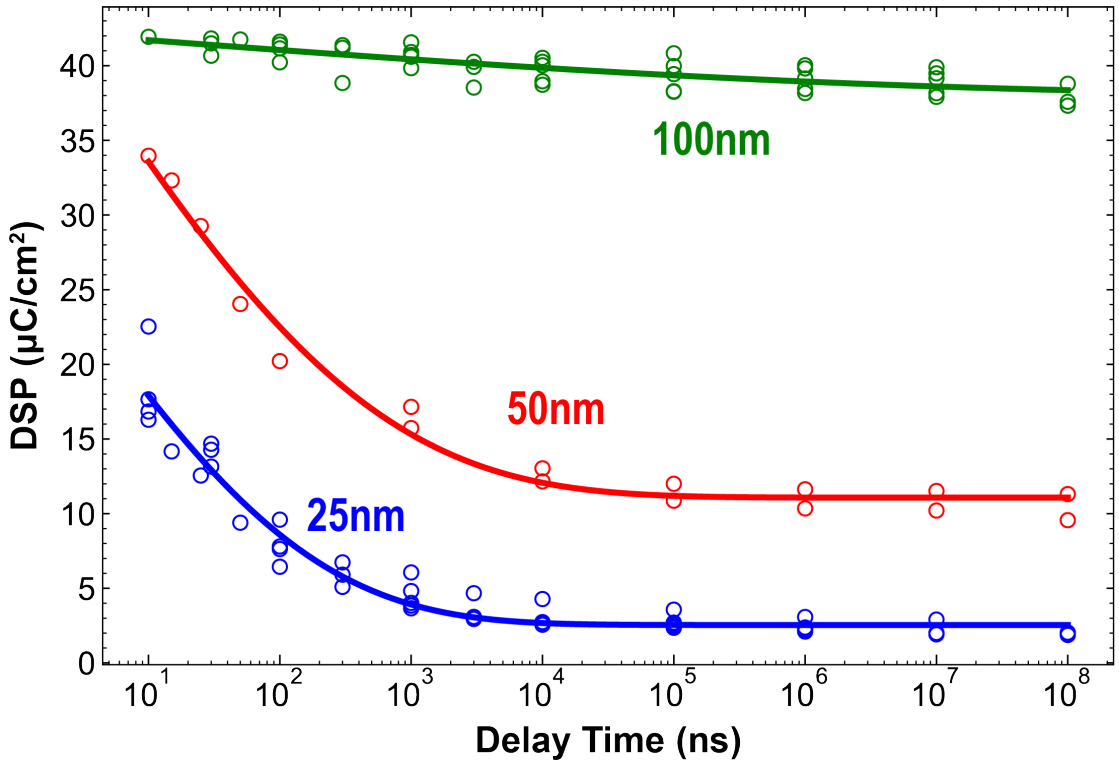

Figure 4.6: Depolarization as a function of time for 100nm, 50nm and 25nm thick BTO films.

$$\Delta T \equiv \frac{T_c(\infty) - T_c(d)}{T_c(\infty)} = \left(\frac{\xi_0}{d}\right)^{\lambda} \tag{4.7}$$

where $T_c(\infty), T_c(d)$ are the Curie temperature of the bulk and film of thickness d, respectively. ξ_0 and λ are physically meaningful parameters corresponding to the correlation length of the order parameter in the bulk and critical exponent of the universality class, which is believed to be that of 3d random ising model for ferroelectrics [149]. As such, as the film thickness is decreased, I get closer to the phase transition, further reducing the energy barrier between adjacent polarization states. By measuring the dielectric constant as a function of temperature, I observe that the Curie temperatures are 190°C 350°C and 390°C for the 25nm, 50nm, and 100nm films, respectively [99]. This means that as I thin the film, I am simultaneously approaching the phase transition (*i.e.*, lowering the energy barrier, and therefore activation energy, between polarization states) and increasing the depolarization

field. These effects combine to produce the sharp depolarization observed (Fig. 4.6) below a thickness of 100nm. In the case of other ferroelectrics, such as BiFeO3 (with a Curie temperature of >1100K)[40, 41], the fractional change in the barrier height is expected to be less significant upon thinning the film since room temperature remains a small fraction of the Curie temperature.

4.3.2 Landau Free Energy and Depolarization

Having gained an understanding of the size effects on ferroelectric depolarization, I now turn to the Landau free energy in detail. Returning to Eq. 4.1, one can solve for the equilibrium values of the polarization (P_{eq}) as well as the energy barrier (G) (related to the activation field for nucleation and growth):

$$P_{eq} = \begin{cases} 0 & \text{Unstable} \\ \pm\sqrt{\frac{\alpha}{2\beta}(T_c - T)} & \text{Stable} \end{cases} \tag{4.8}$$

$$G = \frac{\alpha^2}{4\beta}(T_c - T)^2 \tag{4.9}$$

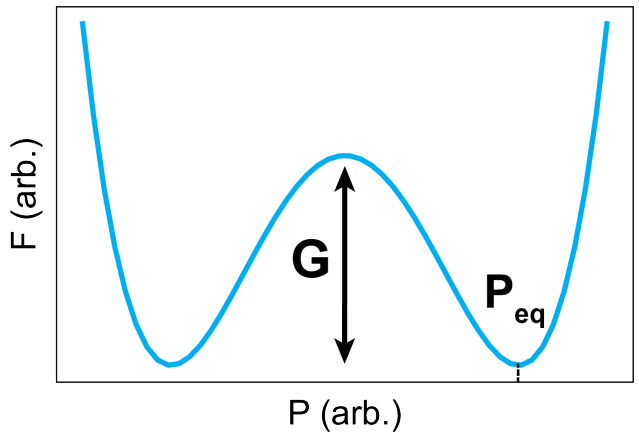

Figure 4.7: Landau double-well potential highlighting equilibrium polarization values (P_{eq}) and the energy barrier (G) between adjacent polarization states.

since electric fields enter into the Landau free energy (at leading order) as $P \cdot E$, to represent the energy barrier (G) as a field, one must divide by the polarization, *i.e.*, the activation field is given by $E_A \propto G/P_{eq}, E_A = C_1 G/P_{eq}$, [2] where C_1 is the constant of proportionality. Given the form of the polarization from the Landau free energy and the depolarization

[2] In principle, the activiation field could be a more complex function of G and P_{eq}, though experimental results [150] show that a simple proportionality is sufficient

field (Eq. 4.5) I can write the resulting depolarization field as $E_{depole} = -C_2 P_{eq}$ where $C_2 = \frac{1}{\epsilon_f}\left(\frac{2\epsilon_f/d}{2\epsilon_f/d+\epsilon_e/\lambda}\right)$. Given the form of Merz' law ($t_s = t_0 e^{E_A/E}$), I are interested in the ratio of the activation field to the applied (in this case internal depolarization) field, E_A/E[3].

$$\left|\frac{E_A}{E}\right| = \frac{C_1 G}{C_2 P_{eq}^2} = C\frac{G}{P_{eq}^2} \tag{4.10}$$

where I have grouped constants into one new constant, C. Combining Eq. 4.9, 4.8, 4.10 into Merz' law, I find an expression for the depolarization time as a function of temperature:

$$t_s(T) = t_0 e^{\frac{C\alpha}{2}(T_c - T)} = Ae^{-BT} \tag{4.11}$$

where $A = t_0 e^{\frac{C\alpha T_c}{2}}$ and $B = \frac{C\alpha}{2}$ are fitting parameters, which can be used to fit temperature dependent data.

In Fig. 4.8a, I show the results of depolarization for 25nm BTO at a variety of temperatures from ranging from room temperature to 83K. The solid lines represent fits to stretched exponential decays. I can define the depolarization time as the time at which n% of the depolarization is completed, *i.e.*, $P(t_{depole}) = \max(P) - \frac{n}{100} \times (\max(P) - \min(P))$, where the depolarization percent, $n \in [0, 100)$. For the present analysis, I use a depolarization percent of 80, though variations (± 10) in this value do not alter my results.

Fig. 4.8b shows the extracted depolarization time as a function of temperature for the 25nm BTO film. The (green) solid line represents a fit to Eq. 4.11, which shows remarkable agreement with the expected temperature dependence. These results can be interpreted as follows: the mechanism of depolarization in ultra-low coercivity ferroelectric thin-films is nucleation and growth of reverse polarized domains. The macroscopic polarization, which is what I measure, is the sum of the contributions from all domains in the device. Though depolarization fields are known to destabilize ferroelectricity directly [138], what I am observing here is quite different. The decay of polarization is not the suppression of the ferroelectric order parameter itself, but rather the formation of domains, each of which has a polarization value equal to that (P_{eq}) given by the Landau free energy. The driving field for this process of nucleation and growth is internal, and is directly proportional to the macroscopic, instantaneous polarization of the complete device. As I cool the sample, the value of P_{eq} increases (thereby increasing the depoling field), but so does the energy barrier, G that must be overcome to drive nucleation and growth of domains. A simple 4^{th} order Landau theory in combination with the nucleation and growth mechanism of macroscopic polarization reversal (as dictated by Merz' law) is able to capture (with remarkable agreement) the essential physics, where the simultaneous increase in $G \propto T^2$ and $P_{eq} \propto \sqrt{T}$ result in an exponential suppression of the depolarization time as a function of temperature. In order to test the validity of this theory, I turn to another material system, namely a relaxor ferroelectric[151],

[3]I am interested in the absolute value of the ratio because I make the assumption that the depoling field drives switching, so I redefine the positive direction as along the depoling field direction

where depolarization is not expected to obey the same mechanism of domain nucleation and growth governed by internal depolarization fields.

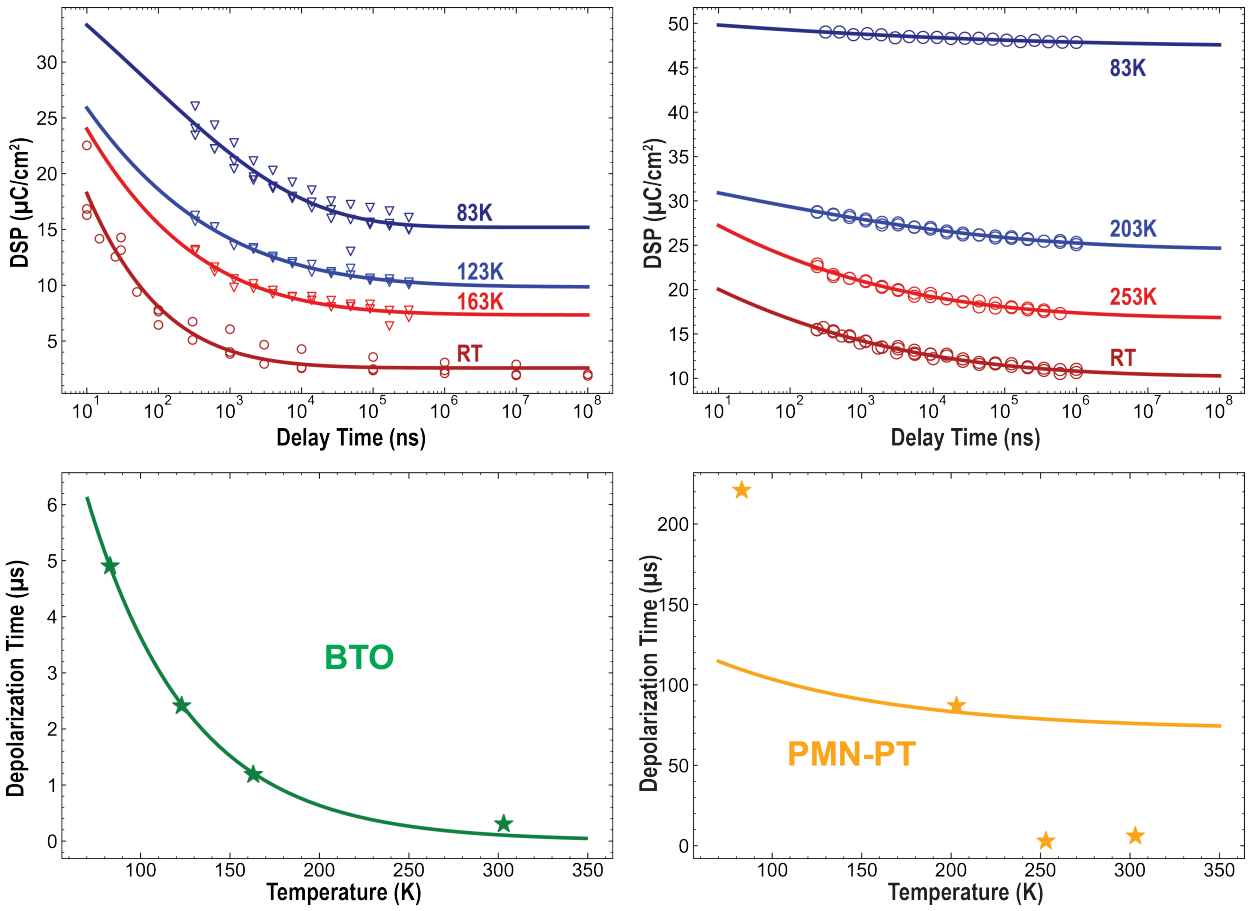

Figure 4.8: Temperature dependent depolarization transients.

The study of relaxor ferroelectrics (often referred to as relaxors) has spanned several decades, with countless PhD theses devoted solely to the subject. I do not attempt to discuss the rich physics of relaxors here, and instead direct the interested reader to several insightful articles[151, 152, 153]. The theses of Abel Fernandez and Jieun Kim, from Lane Martin's group at UC Berkeley, though not yet published at the time of this writing, also serve as excellent resources for relaxor physics. For my purposes of understanding depolarization, it is sufficient to have only a cursory understanding of relaxor ferroelectrics, and explain the essential details in the following.

Relaxor ferroelectrics are characterized by a slim PE loop, with high saturation polarization and low remnant polarization. Relaxors can be used for a variety of applications and host interesting correlated physics between polar units in the material. My work on energy storage[154] and in proposing a novel method of probing correlated behavior [155] in these

systems aim to address both applications and fundamental physics of relaxors. Relaxors have complicated phase diagrams [151] characterized by three temperatures: Burns (T_b), intermediate (T^*) and freezing (T_f), listed in order from high to low. In the high temperature, paraelectric phase, there are no domains. Upon cooling through T_b, the system enters the relaxor phase, with "fluctuating domain formation and domains vary in size" [151]. Cooling through T^* results in the "coexistence of static and dynamic domains". After further cooling, through T_f, the system enters the frozen phase with "static domains with very slow dynamics"[151].

I am interested in the relaxor and frozen phases. The essential physics to understand for depolarization (and a comparison with BTO) is this: in the relaxor phase there exist polar nanodomains which are thermally activated and fluctuating in time. In the absence of an externally applied electric field, these fluctuations cause the macroscopic polarization to average to (close to) zero, *i.e.*, very small remnant polarization. Still, the fact that polar nanodomains exist, means that the relaxor is highly polarizable, with high permittivity, as externally applied electric fields will align the domains. The ground state in the relaxor is to have (close to) net zero polarization, and depolarization from a polarized state will proceed via thermal fluctuations of polar nanodomains, not nucleation and growth of ferroelectric domains, as is the case for BTO. It is this difference in physical mechanism of depolarization that explains my choice of a relaxor as a comparison to ultra-low coercivity BTO. In the frozen phase, the relaxor begins to resemble a ferroelectric, with increasingly remnant polarization. Since the relaxor undergoes a phase change upon cooling (where the ferroelectric does not) I expect to see fundamental differences between depolarization in relaxors and depolarization in classical ferroelectrics.

To that end, I study depolarization transients and temperature dependent depolarization times for the prototypical relaxor ferroelectric, 150nm $0.68Pb(Mg_{1/3},Nb_{2/3})O_3$ - $0.32PbTiO_3$ (PMN-PT). The data is summarized in Fig. 4.8c,d which reveals starkly different behavior to the corresponding BTO data. The solid orange line (Fig. 4.8d) represents a fit to Eq. 4.11 and shows strong disagreement with the model. This is, of course, expected as the mechanism of depolarization in the PMN-PT is not expected to follow the same depolarization field driven nucleation and growth. In the relaxor phase, ($T \sim\geq 250$K) depolarization time is relatively constant with temperature, consistent with the thermally activated, fluctuating, polar nanodomains which collectively average to contribute zero to the net macroscopic polarization. In this phase, one can think of depolarization as stemming from the thermally activated decoherence of the polar nanodomains which are initially aligned by the external electric field. Since this process is not driven by an internal depolarization field, I do not see the exponential dependence on temperature. As I cool the sample into the frozen phase, and the system increasingly resembles a ferroelectric, one might expect depolarization fields to begin playing a significant role, however, at the film thickness of 150nm, given the form of Eq. 4.5, depolarization fields are not expected to play a significant role. This can be seen directly in the depolarization transient data at $T = 83$K, where very little depolarization occurs.

These results can be summarized as follows: In classical ferroelectrics, dynamic polar-

ization reversal occurs via an activated (governed by Merz' law) process of nucleation and growth of domains. The energy cost to initiate and sustain this process can be directly mapped to the energy barrier between adjacent polarization states in the Landau free energy double-well. Methods for reducing the switching energy (and consequently switching time) therefore, which lower the energy barrier between polarization states, will see benefits in driven dynamics, though will also have to deal with an increased tendency for depolarization. Cooling the system far from its Curie temperature will have the effect of stabilizing the polarization only at sufficient temperature where the energy barrier has increased significantly, with respect to the (also increasing) polarization-induced depoling field. Thus, the requirement for achieving minimal depolarization can be written succinctly as:

$$G \gg \frac{P_{eq}^2}{\epsilon_f}\left(\frac{2\epsilon_f/d}{2\epsilon_f/d + \epsilon_e/\lambda}\right) \tag{4.12}$$

The conclusions of this work naturally lead to a catch-22 of sorts where efforts to reduce the switching energy/voltage/time simultaneously contribute *negatively* to depolarization. To make matters worse, an ideal ferroelectric, say, for FeRAM applications possesses low work of switching, but high remnant polarization. From my analysis, it is clear that these two requirements are seemingly at odds with one another. Given these challenges, one naturally is curious of there exists a "sweetspot" amongst tunable parameters which is most optimal. I address this directly in the following section.

4.4 Implications and on-going work

An ideal classical ferroelectric, say, for usage in an FeFET[134], possesses: 1. Fast switching time, 2. Low voltage operation and 3. Robust non-volatility. These three metrics are not mutually exclusive. Decreasing the activation field, for example, will clearly lower both switching time and operation voltage, but may also be a detriment to non-volatility following depolarization effects as seen above. Other factors impacting these three metrics are depolarization field strength, polarization magnitude, strain or mechanical constraints, free-charge dynamics (predominantly capacitance, including area, thickness and dielectric constant), free-energy landscape (from Landau theory), applied field, the screening length of the adjacent metal, and interface-dependent effects (*e.g.* pinned dipoles or Schottky barriers). Many, if not all of these parameters can vary with film thickness. So, to summarize these effects, I introduce two quantities: area-normalized switching time (ANS) and initial polarization fraction at time ($t = 100\mu$s)[4] (IPF). ANS is the switching time, normalized by the area of the device, and refers to external-voltage-driven switching. By normalizing by area, ANS properly accounts for variation in device dimensionality. ANS should be thought of as a metric quantifying how the system responds to external stimuli. An ideal system with

[4]One can, in principle, define the initial polarization fraction at any time throughout the depolarization process. I chose 100μs as it is long enough for applications, *i.e.*, many logic operations can occur within 100μs, but short enough that I am still able to maintain some polarization even for the thinnest films studied.

fast switching and low voltage operation will have a low ANS. IPF refers to the measured DSP at a delay time (t_d) of 100µs normalized by the maximum DSP observed (which is observed at shortest delay times). IPF should be thought of as a metric quantifying internally driven depolarization in the film. An ideal system with robust non-volatility will have an IPF value of 1, with higher values (closer to 1) being better and lower values (closer to 0) being worse. I show results for ANS and inverse IPF (IPF^{-1}) (Fig. 4.9) as a function of film thickness. There is a trade-off observed, where thinning the film improves the driven metric (ANS) but is a detriment for the depolarization metric (IPF). The results presented here clearly indicate the importance of mitigating depolarization and improving the stability of the polar state as the field approaches lower voltage operation of thin-film ferroelectrics.

From Fig 4.9 it indeed appears that there is a trade off. By utilizing films at intermediate thicknesses, I gain low voltage driven operation while maintaining (relatively) long-lived remanence. There exists, however, a new opportunity for polar materials with inherent instability. Recent progress in probabilistic computing, where logical bits populate "on" and "off" states subject to a (electric-field-dependent, for example) probability distribution, has shown promise for a number of use-cases[156, 157, 158]. While implementations so far have been limited to ferromagnetic tunnel junctions, such as in ref [157], work studying a parallel implementation using ferroelectrics with inherent instabilities, such as those presented here, is on-going. The very same mechanisms, of low coercivity and high depoling fields, which contribute to depolarization in my ultra-low coercivity BTO films, for example, can cause dipolar fluctuations whose timescale and probability of occurrence will be strongly influenced by an external DC bias. To study polar fluctuations I have proposed to use noise electrometry with nitrogen-vacancy centers in diamond [155] in addition to using fabricated devices and measuring the electrical noise spectrum. The latter technique would consist of an isolated (including Faraday cage[5]) ferroelectric capacitor which is electrically contacted with a wirebond. If the polarization fluctuates with characteristic time-scales, I can observe such fluctuations in the noise spectrum (as measured with a network or spectrum analyzer) of the current in the circuit. By applying a DC bias, I expect to be able to tune the probability distribution (biasing one state over the other) of the polarization in the film, which will be observed as a change in the noise spectrum.

In summary, I presented depolarization and external-voltage-driven ferroelectric switching dynamics in the prototype ferroelectric, BTO. The results highlight the importance of proper consideration of depolarization fields in thin-ferroelectrics, and hold particular significance in addressing the stability of the polar state as the field progresses towards the goal of ultra-low power operation of ferroelectric materials. Depolarization dynamics in BTO are understood within the context of a nucleation and growth model, where the activation energy decreases, and the depolarization field increases with increasingly thin films. Owing to the local nature of depolarization effects, no lateral area device scaling is observed, in stark contrast to external-voltage-driven polarization dynamics. Depolarization in BTO is compared to the prototype relaxor ferroelectric PMN-PT, where the different mechanisms

[5]One must take care to remove erroneous signals such as WiFi in the building

of depolarization (nucleation and growth versus thermal fluctuation of polar nanodomains) result in starkly different depolarization behavior as a function of temperature.

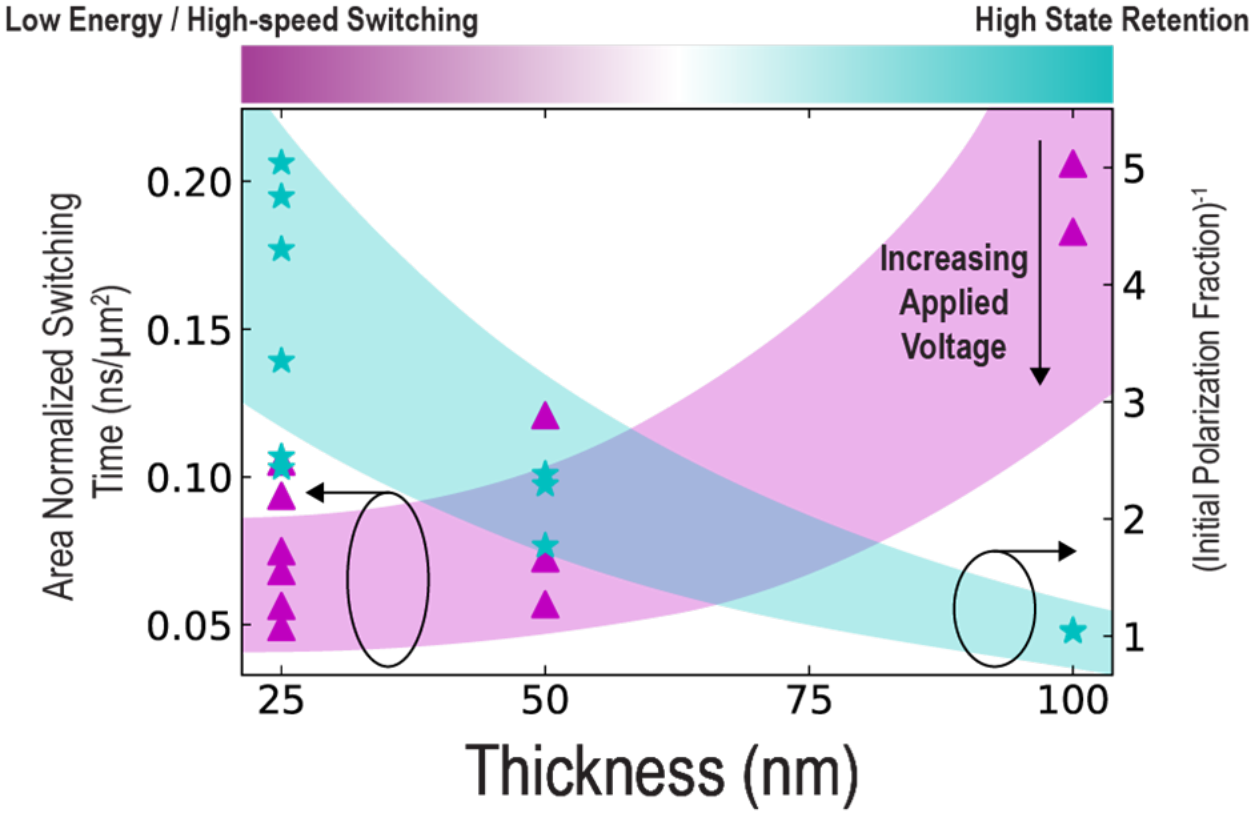

Figure 4.9: Driven and Depolarization Metric. Left axis shows area-normalized switching time (ANS), right axis shows inverse initial polarization fraction (IPR) at a time delay of 100μs, both as a function of film thickness for a fixed, nominal, applied voltage of 500mV. In ultra-low coercivity thin films I observe a trade-off, where thinner films show lower voltage operation and faster switching times, but also lower stability of the polar state.

There are several pathways to mitigating the effects of depolarization fields. A significant reduction in the screening length (λ) is possible by changing electrode material, though growth quality must be maintained. A potential choice is yttrium barium copper oxide (YBCO) which is superconducting at liquid nitrogen temperatures. In the superconducting phase, the YBCO will, in principle have a vanishingly small screening length. In this limit, the depolarization field should also vanish[6]. Another option is to address the reduction in activation energy presently observed. This can be achieved through defect implantation[159] though will also coincide with increased coercivity. In the drive toward 100mV operation of

[6]Studies using superconducting YBCO would have the added benefit of disentangling depolarization from electrostatic effects and other mechanisms such as in ref [135]

ferroelectric materials, one must not lose sight of the stability of the polar state, and must find a delicate balance of effects.

Chapter 5

Probing Magnetic Dynamics Through Spin Transport in $BiFeO_3$

So far, I have discussed "dynamics" in the context of switching, from one (meta-)stable state to another, of ferroic order. In this chapter, I turn to dynamic eigen-excitations of (magnetic) order, specifically magnons, and the ways in which they can be detected, manipulated, and applied. I will discuss how such excitations manifest in multiferroic materials and how I can manipulate them with electric fields and domain walls. The findings presented in this chapter are of both fundamental and applied interest. Fundamentally, transport of angular momentum (spin transport) via magnons (particularly in insulating systems) has received an immense amount of attention in the last decade as researchers seek to understand excitation, detection, and manipulation mechanisms, and my research adds important discoveries to that end. From an applied point of view, much excitement surrounds novel computing architectures built on spin-wave memory and logic (so-called "magnonics")[36, 160, 161, 162], and my work offers a viable pathway toward magnon-based devices that can be integrated into current charge-based computing technology. In this chapter, I will discuss a novel manifestation of magnetoelectric coupling in BFO, to demonstrate how intrinsic multiferroicity in the system allows us to control magnons in a non-volatile fashion, using an applied electric field, instead of an applied magnetic field.

5.1 Essential Background

Magnons are quantized spin waves in magnetic materials (see Section 1.1.2). Historically, magnons have been studied via scattering or resonant means. For example, Raman scattering spectroscopy [163, 164, 165] has been used to study $k = 0$ magnons in BFO [166, 167, 168] and the effect of magnetoelectric coupling[169, 170]. In particular, observation of "electromagnons"[171, 172, 173] and phonon-electric-dipole-magnon coupling has been reported. Ferromagnetic resonance (or antiferromagnetic resonance) [174, 175, 176] can also be used

as a means of measuring magnons resonantly[1]. Recently, there has been a resurgence of interest in the study of magnon physics, for spintronics [177, 178, 179] applications, especially as spin-pumping and spin Hall-based measurements have gained significant traction in the community [180, 181, 182, 183, 184]. Notably, as described in this chapter, the spin Hall effect can be used to incoherently create and detect magnons in a variety of magnetic materials, including insulators. This technique can be sensitive to propagating magnons, with wavevector $k \neq 0$, naturally lending itself to transport of spin information. This discovery has led to a significant body of work studying magnon spin transport in magnetic materials and holds promise for new paradigms in device technology based on magnons. In this chapter, I am interested in a simple question: how can one study magnetic (magnon) dynamics in BFO, and, most importantly, how can one make use of magnetoelectric coupling in BFO to manipulate magnons with an electric field?

In the field of magnonics, spin waves, rather than electrons, form the fundamental operating unit [36, 160, 161, 162]. The field has experienced rapid growth over the last decade as exciting progress has yielded a breadth of interesting physics as well as the potential for low power dissipation in computing [185]. In lieu of an electronic current, insulating magnetic materials can host magnon currents, which carry spin information and avoid Ohmic losses associated with electron transport. Such materials are well-suited for wave-based computing based on magnon logic [186, 187, 188, 189, 190]. Indeed, theoretical work has proposed antiferromagnetic spin wave field-effect transistors [191] and realizations of all-magnon transistors based on magnon-magnon scattering with resonant excitation have already been experimentally demonstrated [189]. There are several ways to create magnons [36, 162, 192, 193, 194], and spin transport via magnon currents have already been reported in a variety of magnetic systems [185, 195, 196, 197, 198]. Though resonant excitations are typically used to study spin waves [199, 200], magnon currents can be excited incoherently by a thermal gradient through the spin Seebeck effect (SSE) [201] or near-DC-frequency spin accumulation mechanisms [192, 202]. Thermal excitation of magnons, however, is better suited to materials with complex domain structure since it does not require long-range magnetic order [203]. Here, I will focus on so-called "non-local" spin transport through insulating magnetic materials, where magnons are excited by thermal gradients or other means and detected via the inverse spin hall effect (ISHE) in a spin orbit metal (typically Pt) some distance away from the source location.

[1]The frequencies of antiferromagnetic resonance are typically much higher than ferromagnetic resonance.

5.1.1 Non-local spin transport

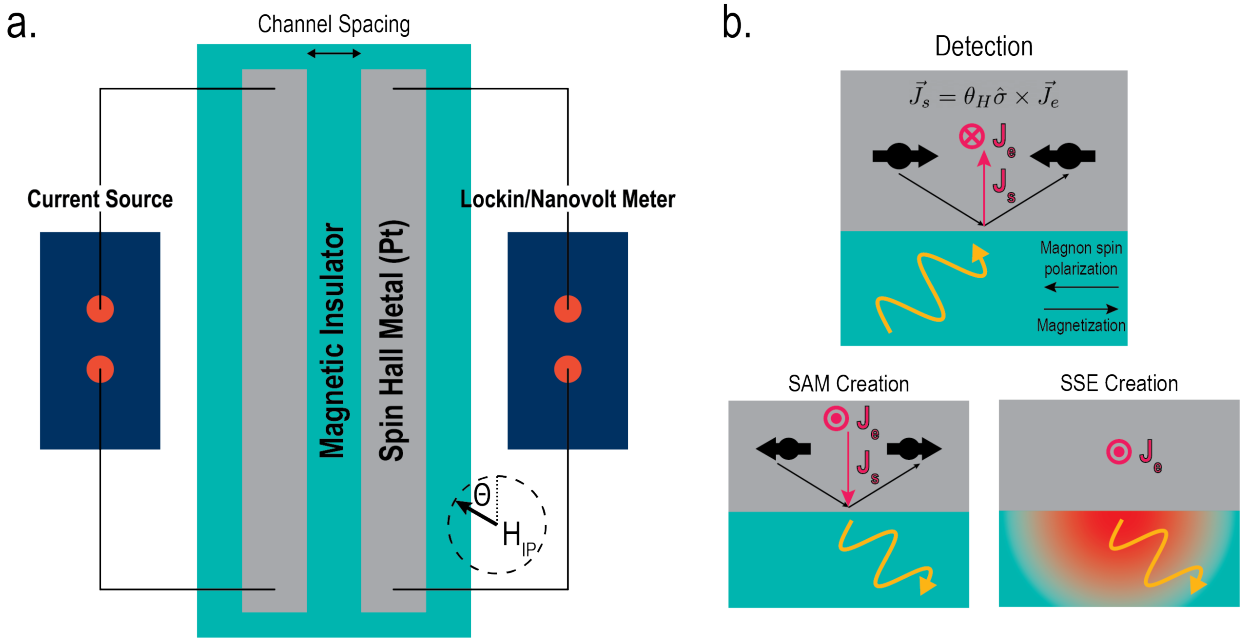

Figure 5.1: Overview of nonlocal spin transport experiment. **a.** shows the experiment configuration. A charge current (AC or low-frequency DC) is driven through an injector wire lithographically defined on top of a magnetic insulator. The magnon current through the magnetic material is sensed by the resulting inverse spin hall voltage in the detector wire, as measured by a lockin amplifier (for AC current) or nanovolt meter (for DC current). **b.** shows the ISHE detection mechanism in addition to spin accumulation (SAM) and spin Seebeck effect (SSE) creation mechanisms.

A schematic of the experimental setup for non-local spin transport is shown in Fig. 5.1. In order to perform the measurement, one lithographically defines two wires, typically both[2] made of a good spin Hall metal. Spin Hall metals, such as Pt, have the unique property that a charge current flowing in the metal will induce a transverse spin current, given by:

$$\vec{J}_s = \theta_H \hat{\sigma} \times \vec{J}_e \tag{5.1}$$

where $\vec{J}_s$ is the spin current, $\hat{\sigma}$ is the spin polarization, and $\vec{J}_e$ is the charge current. θ_H is called the spin Hall angle[3] and characterizes the efficiency of the material in converting

[2]This is not always a requirement, though to detect magnons via the ISHE, at least one wire (the detector) must be made of a good spin hall metal, of which Pt is the standard in the literature.

[3]A substantial amount of effort has been devoted to increasing the spin Hall angle, as a means of increasing the conversion rate between spin and charge (useful for spintronics applications), though typical values are quite low. For example, Pt has a spin Hall angle of just ≈0.07

between spin and charge currents. This phenomenon is (aptly) called the spin Hall effect (SHE)[204].

When a charge current is driven through the "injector" wire (left wire in Fig. 5.1a) magnons are excited in the magnetic insulator. These magnons then traverse the channel and are incident on the "detector" wire (right wire in Fig. 5.1a). This incident magnon can be scattered by a spin in the detector metal (Fig. 5.1b), and in order to conserve angular momentum in the process, induce a spin flip of the incident spin. This is referred to in the literature as the "spin flip scattering mechanism." The net result of such scattering is a spin current in the metal ($\vec{J}_s$). Just as a charge current can induce a spin current via the SHE (Eq. 5.1), the inverse process can also occur, *i.e.*, the inverse spin Hall effect (ISHE), where a spin current induces an orthogonal charge current. In the geometry shown, (Fig. 5.1), spin flip scattering of interfacial spins results in a net spin current, and therefore a charge current along the length of the wire. So, by measuring the differential voltage along the wire, one obtains a measure of the incident magnon current into the wire. This mechanism of detection means that the measurement is sensitive to the incident magnon current *with spin polarization pointing orthogonal* to the length of the wire (*i.e.*, across the channel). If the incident magnons are spin polarized along the length of the wire, the induced ISHE voltage would not be detected in this geometry. As such, this measurement scheme acts as a spin polarization "directional" detector[4]. The detected (non-local) voltages are typically quite small ($\sim$100nV), so one must use a nanovolt meter (if using DC currents in the injector wire), or, as is more common, a lock-in amplifier and a low frequency AC current in the injector wire to provide the reference signal. Having established the detection mechanism, I now to two mechanisms for creation of magnons.

Spin Seebeck effect: The first mechanism of creation is called the spin Seebeck effect (SSE). The SSE is the spin analog of the Seebeck effect, where a thermal gradient in a metal can induce a voltage, $E \propto \nabla T$, resulting in a charge current. Owing to the SSE, a spin current can flow as the result of a thermal gradient in a magnetic material[201]. Importantly, such spin currents can flow, even in magnetic insulators, where magnons , in lieu of electrons, transmit spin. In the non-local geometry as described above, the charge current in the "injector" wire induces a thermal gradient in the magnetic material owing to Joule heating in the wire (Fig. 5.1b). As described in detail below (section 5.2) thermal gradients can persist for long distances, meaning that magnons can be excited via the SSE at the injector, or away from it.

Spin Accumulation: The second mechanism of creation is called the spin accumulation mechanism (SAM), or, as it is often referred to in the literature, the "electronic" mechanism. SAM magnons are excited in the inverse process to which they are detected, *i.e.*, a charge current in the injector wire induces a spin current toward the interface with the magnetic material, and, via spin flip scattering, creates magnons (Fig. 5.1b). Unlike thermal magnons excited via the SSE, SAM magnons can only be excited at the interface between the injector wire and the magnetic material, meaning that they must traverse the channel without damp-

[4]I like to think of it in analogy to an optical linear polarizer

ing, scattering, or other attenuation mechanisms, if I am to detect a magnon current in the detector wire. From Fig. 5.1b and the form of Eq. 5.1, it is clear that the spin polarization of the created magnon is dependent on the spin polarization ($\hat{\sigma}$) of the incident interfacial spin, which is set by the properties of the spin Hall metal and the direction of the applied charge current. If one reverses the direction of the applied spin current, one also reverses the interfacial spin polarization, and therefore the created magnon spin polarization. In section 1.1.2 (Fig. 1.4), I discussed how magnons are (in the simple case of a ferromagnet) delocalized spin flips of single spins. So, if the interfacial incident spin is polarized antiparallel to the magnetization of the magnetic material, magnons *can be* excited. If the incident spin polarization is aligned with the magnetization of the material, no magnons will be excited (see [192] for a nice description). Thermal magnons are excited wherever a thermal gradient exists, and are spin polarized antiparallel to the magnetization of the material.

It is important to note that fundamentally, there is no difference between thermal and SAM magnons (in terms of dispersion relation, *etc.*), except for how (and where) they are created. As we will see, the location and mechanism of creation is very important for interpretation of results. Regardless of how they are excited, magnons are detected in an identical way (ISHE) in the detector wire.

Disentangling contributions: Since the detection mechanism is the same, and thermal and SAM magnons have different creation mechanisms, I seek a method of decomposing the observed non-local voltage into a contribution from the two effects. This can be achieved one of two ways, depending on how the experiment is configured. I will first describe the case of using an AC current (for the injector wire) and a lock-in amplifier (for the detector wire). Since SAM magnons depend on the charge current in the injector wire for excitation, to detect SAM magnons, one should look at the first harmonic, and specifically the in-phase (X) component[205], of the measured voltage on the detector wire. Since thermal magnons are dependent on Joule heating the injector wire, which is dependent on the power dissipated, *i.e.*, $P = I^2R$, one should observe the second harmonic, specifically the out-of-phase (Y) component[205], of the measured voltage on the detector wire. If one chooses to use a DC current source, a similar decomposition can be achieved by running the current in the injector first positively(j_+), then negatively (j_-). Since the thermal magnons are sensitive only to the thermal gradient, reversal of the current should have no effect, with the opposite being true of SAM magnons. The two contributions can thus be obtained as:

$$V_{\text{thermal}} = \frac{V_+ + V_-}{2},\ V_{\text{SAM}} = \frac{V_+ - V_-}{2} \tag{5.2}$$

In order to confirm that the observed non-local voltage indeed stems from magnon current, one typically applies an external magnetic field to modify, in some way, the magnetic order in the magnetic material, and in so doing modulate the observed magnon current. In the following section I describe this in detail.

5.1.2 Modulation via in-plane magnetic field rotation

The most prototypical non-local experiments have been performed on the ferrimagnetic insulator, $Y_3Fe_5O_12$ (YIG). A non-local device geometry is used, and an in-plane magnetic field (Fig. 5.1a) is applied at a variable angle, θ. The magnitude of the applied field should be above the coercive field in the YIG ($\sim$500Oe) such that the magnetization in the YIG follows the direction of the applied magnetic field. Owing to the fact that the detector (and injector, for SAM magnons) is directional, and sensitive only to the spin polarization component of incident magnons oriented orthogonal to the length of the channel, by rotating the magnetization with the applied field, the observed non-local signal is modulated as in (Fig. 5.2). The first harmonic (SAM) and second harmonic (thermal) signals exhibit different angle dependence, where the first harmonic is π-periodic and the second harmonic is 2π-periodic. To understand why, it is easiest to first understand the thermal signal dependence. For an applied field at angle θ, the thermal magnons have spin polarization antiparallel, *i.e.*, at an angle $\alpha \equiv \theta + \pi$. The Pt detector wire is sensitive only to incident spin polarization only along a single direction (without loss of generality, let it be $\hat{x}$). Owing to the spin flip scattering mechanism, the magnitude of the observed voltage is

$$V_{nl} \propto (\cos(\alpha + \pi)\hat{y} + \sin(\alpha + \pi)\hat{x}) \cdot \hat{x} \propto \sin(\alpha) \tag{5.3}$$

[192] explaining the 2π periodicity in the case of the second harmonic. In the second harmonic (thermal) signal, the angle dependence has no meaning on injection (Joule heating), though the same is not true of the first harmonic (SAM) signal. There, the injector acts as a directional injector in an analogous way to the detector, so I observe the product of two 2π-periodic signals. $\sin^2(x) = \frac{1}{2} - \frac{\cos(2x)}{2}$, *i.e.*, a π-periodic signal.

YIG is an ideal candidate for studying non-local spin transport owing to its low coercivity, robust magnetic moment, and insulating nature. Early work, was performed almost exclusively on YIG for these reasons. More recently, however, researchers have begun to explore other classes of materials (most notably antiferromagnets), and used non-local spin transport as a means of studying fundamental magnetic phenomena for example magnetic transitions, such as the Morin transition in α-Fe_2O_3 [206]. In antiferromagnetic systems, researchers have observed similar magnetic field dependencies to YIG, though the magnetic fields required are typically much larger. This is because antiferromagnets are generally robust to externally applied fields and one must apply a field above the so-called "spin-flop" field, where the Néel vector reorients orthogonal to the applied magnetic field[5]. Above the spin-flop field, one also induces a net magnetization stemming from the canting of the spins along the applied field direction (Fig. 1.5).

[5]This happens because it is energetically costly for either sublattice, alone, to orient along the magnetic field direction because the other sublattice is aligned antiparallel. It even more energetically unfavorable for both to align (that would require overcoming the antiferromagnetic exchange energy, typically $\sim$100T), so orthogonal alignment is preferred.

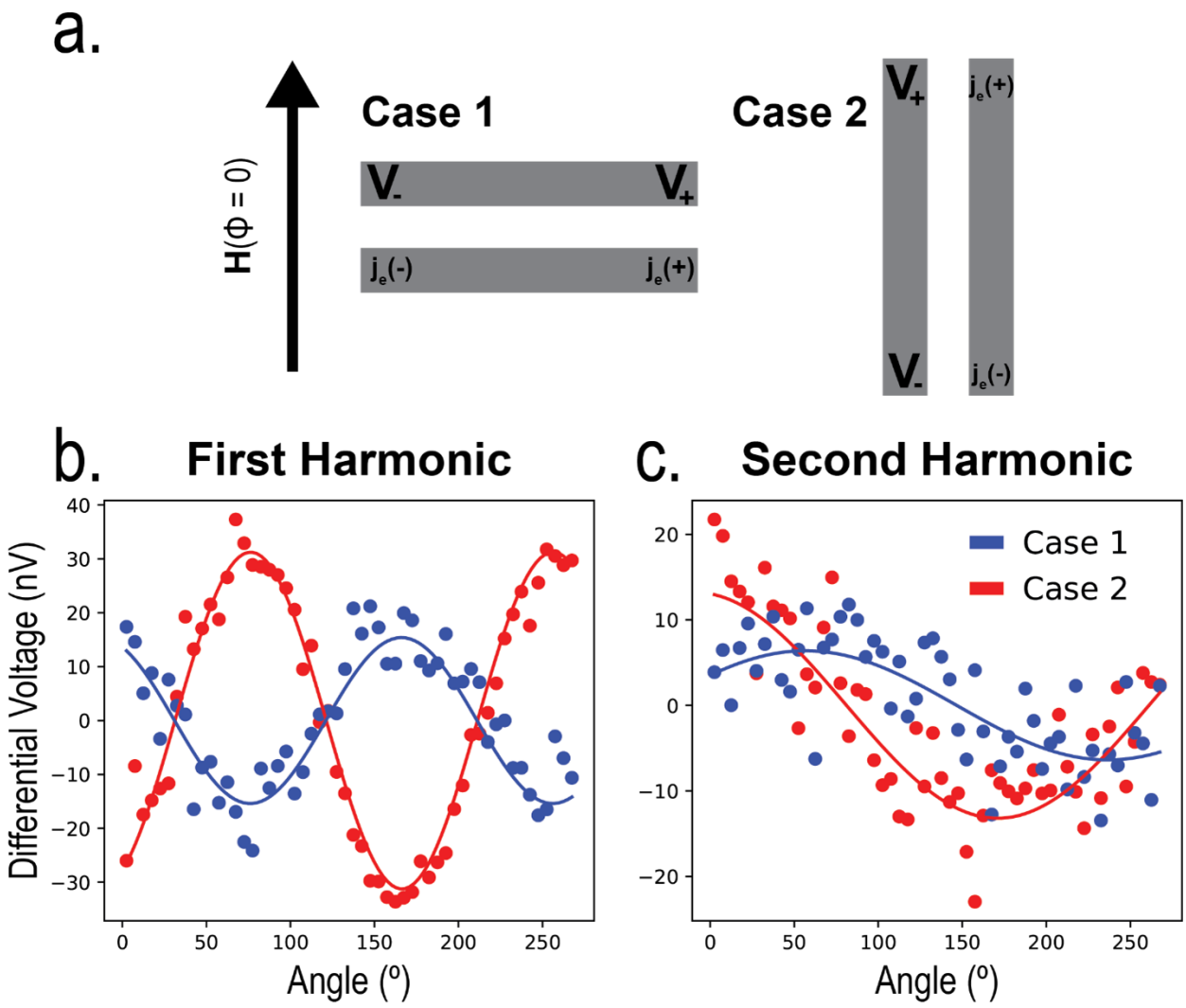

Figure 5.2: Non-local measurement on YIG. **a.** Orientation of devices, relative to zero of magnetic field. A charge current is driven through the injector wire (labeled with $j_e(+)$ and $j_e(-)$) and the nonlocal voltage at the **b.** first harmonic (sensitive to the spin accumulation mechanism) and **c.** second harmonic (sensitive to the spin Seebeck effect) are measured in detector wire (labeled with V_+ and V_-). The charge current amplitude is 500μA. As expected, I observe a 90° phase shift in the observed nonlocal signal for devices (Case 1, 2) oriented orthogonal to each other.

Magnetic field magnitude dependent measurements of nonlocal spin transport in iron oxide (the parent compound of BFO) reveals a peak in the first harmonic nonlocal signal (see Figure 2 of ref [185]). As described in Chapter 1.1.2 (Fig. 1.5) the applied magnetic field modifies the energy of the two magnon modes, with one increasing in energy, and the

other decreasing. At the spin-flop field, the decreasing mode reaches zero energy (referred to as closure of the magnon gap), and, as it costs negligible energy to excite magnons in that mode, the nonlocal voltage, in principle, diverges. This is the origin of the peak in nonlocal voltage observed in ref [185]. Above the spin flop transition, also in iron oxide, where one has deterministic control over the Néel and magnetization vectors, in-plane magnetic field angle dependent studies [198] have revealed similar angle dependence of the first harmonic signal (see Figure 2 of ref [198]) to that of YIG. The authors in [198] argue that SAM magnons exhibit spin transport via the Néel vector[6] (and not the magnetization vector stemming from the canting of the spins in the spin flop phase), though do not show results for second harmonic, *i.e.*, thermal magnons. In [206], the authors argue that SAM magnons are transported along $\vec{L}$ and thermal magnons are transported along $\vec{M}$, consistent with my findings in BFO, presented next.

5.2 Electric Field Control of Thermal Magnons in $BiFeO_3$

Spin transport through magnetic insulators has been demonstrated in a variety of materials and is an emerging pathway for next-generation spin-based computing. To modulate spin transport in these systems, one typically applies a sufficiently strong magnetic field to allow for deterministic control of magnetic order (see section 5.1.2). Here, I make use of the well-known multiferroic magnetoelectric, $BiFeO_3$, to demonstrate non-volatile, hysteretic, electric-field control of thermally excited magnon current in the absence of an applied magnetic field. These findings are an important step toward magnon-based devices, where electric-field-only control is highly desirable.

Previous research has demonstrated non-local spin transport [208] in insulating ferrimagnets [192, 209, 210] and antiferromagnets [185, 197, 198, 196, 211], thermally excited spin-transport over exceptionally long distances [212, 213], and non-volatile magnetic field control [198]. Electric field control of magnon spin transport, however, has been limited to concurrent application of high magnetic fields [203]. For operational devices based on magnon transport, electric field control in the absence of an applied magnetic field could be a crucial advance for the field.

Here, I make use of the well-known multiferroic material, $BiFeO_3$ (BFO), to demonstrate such electric field control of thermal magnons. BFO is a room-temperature magnetoelectric with a large ferroelectric polarization ($\approx$90 $\mu C/cm^2$), G-type antiferromagnetic ordering, and a weak ferromagnetic moment arising from the Dzyaloshinskii-Moriya interaction [40, 47, 9]. The ferroelectric and antiferromagnetic domain structures in BFO exhibit a one-to-

[6]It is known, however, that there may be arbitrary voltage offsets in nonlocal experiments from parasitic capacitance/inductances or other sources [207], and depending on the existence/sign of such an offset in the data of [198], it is not immediately clear whether the "minimum" they claim is actually minimum, or if it is a maximum. This makes interpreting the results of whether the spin transport occurs via $\vec{L}$ or $\vec{M}$ challenging.

one correspondence [47], and deterministic control of magnetic order via manipulation of the ferroelectric state (with applied electric fields) has already been demonstrated [9, 51, 214], making BFO an attractive option for high-speed, low energy computing [52, 2, 3, 26]. Previous work on BFO [169, 173] has revealed broad tunability of the magnon dispersion with applied electric field, and early theoretical work predicted all electrical switching of magnon propagation [170].

In the section, I demonstrate a novel manifestation of magnetoelectric coupling in BFO to manipulate magnon current. Magnons are excited via the SSE and spin transport is detected via the inverse spin Hall effect (ISHE) [204, 215]. I demonstrate non-volatile, hysteretic, bistable states of magnon current and establish a robust means of switching between the two states with an applied electric field. Via piezo-response force microscopy (PFM), I reveal the switching pathway of the ferroelectric order, which is accompanied by the switching of net canted magnetic moment, providing the mechanism for electric field control of magnon current.

5.2.1 Experimental design

We grow BFO samples via pulsed laser deposition and employ a non-local device geometry (Fig. 5.3a) consisting of two lithographically defined (Appendix B) Pt wires separated by a distance d ($\leq$1μm) on the BFO surface. Devices are patterned via UV lithography using a Heidelberg MLA150 Maskless Aligner in the Berkeley Marvell NanoLab at CITRIS, using AZ MiR 701 Photoresist. After patterning, a blanket layer of $\approx$10nm of Pt is deposited via room temperature DC magnetron sputtering at 2 mTorr Ar pressure (base pressure of 10^{-8} Torr). Pt is then lifted off via $\sim$5 hr soak in 1-methyl-2-pyrrolidone (NMP) at 85°C. In the channel between the Pt electrodes, I observe well-ordered 109° ferroelectric domains (Fig. 5.3a). This confirms the high quality of the BFO film and, via the established correspondence between ferroelectric and magnetic order, allows us access to the magnetic domain structure of the device [47, 214, 52]. Each of the four leads (Fig. 5.3a) is wire-bonded for the non-local measurement, described next. In the "measurement configuration," low-frequency AC current, $f = 7$Hz, driven through the injector Pt wire (Fig. 5.3b) creates a thermal gradient in the film via Joule heating of the Pt (heater) wire. This thermal gradient excites magnons via the SSE. The resulting magnon current is detected at the detector Pt wire as a voltage along the length of the wire, originating from ISHE and spin scattering at the Pt/BFO interface [192, 215, 216]. I use the standard lock-in technique to measure the magnon current as a differential voltage along the detector wire, V_{nl}. Since the thermal magnon current scales with the square of the charge current in the injector wire, I measure the second harmonic of the detected voltage, *i.e.*, $V_{nl}(2\omega)$.

In my experiments, the non-local measurements are performed using a Keithley 6221 current source to run current through the heater wire, and two identical Stanford Research Systems Model SR830 Lock-in amplifiers are used to simultaneously measure the first and second harmonic differential voltage along the detector wire. All measurements, unless oth-

erwise stated, are performed at a frequency of 7Hz in the absence of an applied magnetic field.

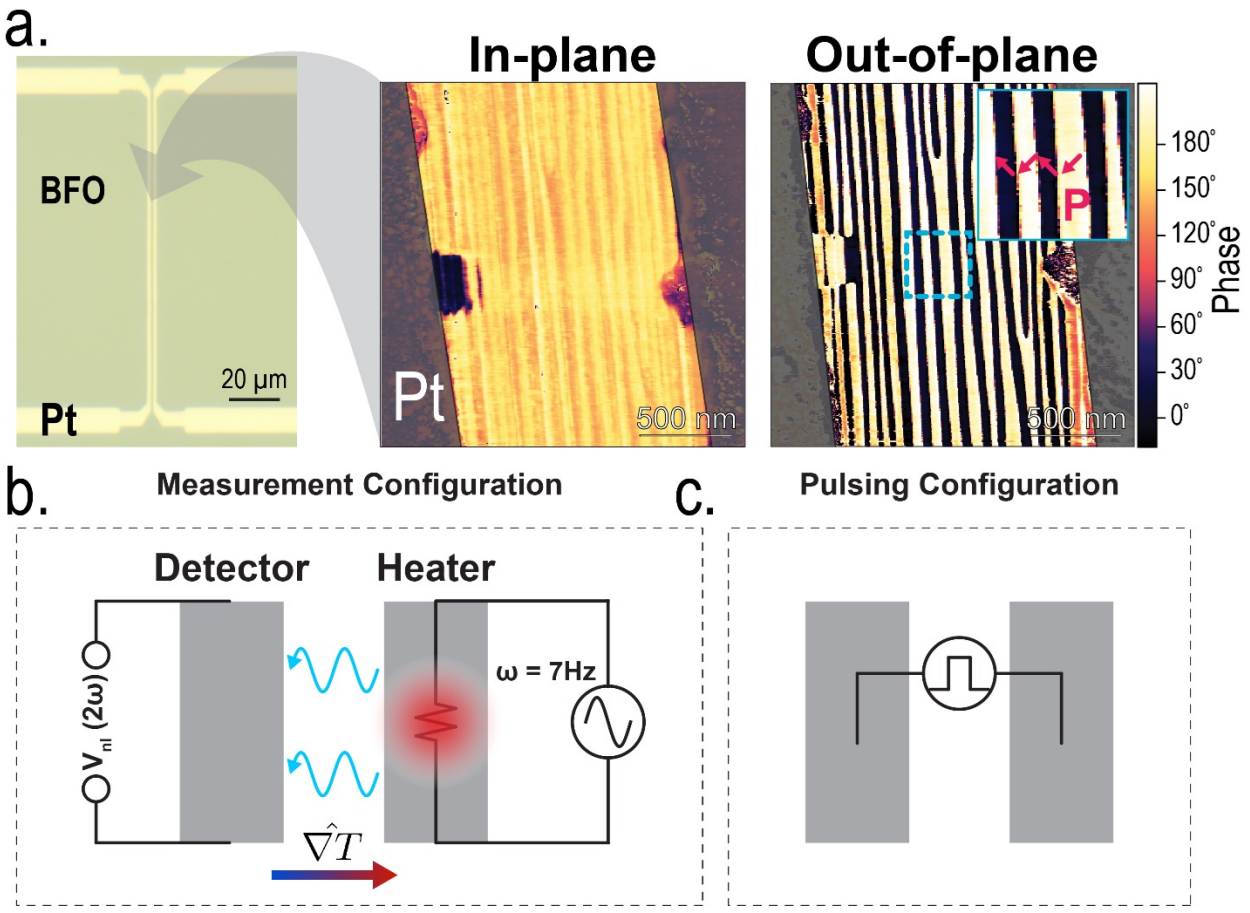

Figure 5.3: Experimental Setup. **a.** Optical and PFM images of non-local device structure. Out-of-plane (OOP) and in-plane (IP) PFM images reveal a well-ordered 109° domain structure. Arrows in inset (OOP) show IP projection of spontaneous polarization, **P**. **b.** Measurement configuration. **c.** Pulsing configuration.

I confirm the efficacy of my device structure and non-local ("measurement configuration", Fig. 5.3a) testing protocol by fabricating identical devices on (YIG) and performing the prototypical in-plane magnetic-field dependent nonlocal measurement (Fig. 5.2), which shows the expected behavior[192]. To modulate the magnon current in BFO in the absence of an applied magnetic field, I perform in-situ electric-field pulsing across the channel ("pulsing configuration", Fig. 5.3c) thereby switching the ferroelectric, and consequently magnetic order parameters.

5.2.2 Non-volatile Control

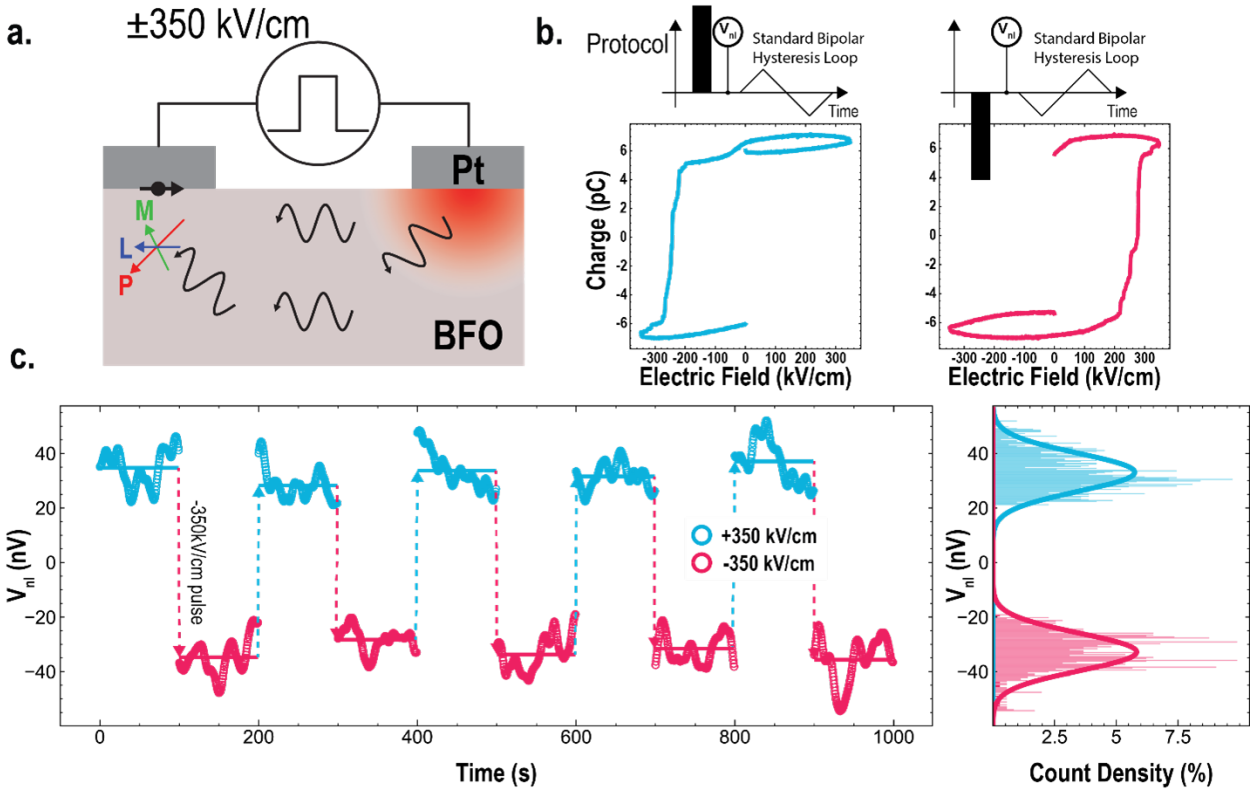

Figure 5.4: Bi-stable states of thermal magnon current. **a.** Cross sectional device schematic. As shown by the interfacial spin (black), the detected voltage along the detector (left) wire is dependent on the magnon spin polarization component orthogonal to the length of the Pt wires. **b.** Experimental protocol and results of "half" hysteresis loops confirming the stability of the ferroelectric state after electric field poling. **c.**Measured lock-in second harmonic voltage, $V_{nl}(2\omega)$, measuring magnon current, as a function of time. 100 seconds of data are collected after each electric-field pulse. Data reflects relative changes upon poling, *i.e.*, a small (≈10s of nV) DC offset is subtracted from both positively and negatively poled signals. Histogram combining results from 10 trials confirms two distinct states of magnon current. Fits are to normal distributions. An 800 μA charge current was used to generate the thermal gradient for SSE.

I follow an experimental protocol (Fig. 5.4b.) designed to both confirm the switching of the ferroelectricity and monitor resulting changes in detected magnon current. Following a unipolar (5ms, 350kV/cm) voltage pulse in the pulsing configuration, I measure the second harmonic voltage on the detector wire, $V_{nl}(2\omega)$, in the measurement configuration. I then confirm the ferroelectric state by measuring a single bipolar ferroelectric hysteresis (PE) loop. As observed, (Fig. 5.4b.), the PE loop shows only one switching event (*e.g.*, only

showing switching in the positive direction, following negative poling) confirming that the ferroelectric state is both switched and remnant. I then switch the pulse polarity and start again. By alternating positive and negative polarity electric field pulses (Fig. 5.4c.) one can clearly observe two non-volatile states of measured magnon current.

Notably, the measured resistance across the channel, *i.e.*, from the heater to detector is >20GΩ. When measured by a Keithley 2400 multimeter, the resistance measures overload. These results hold both before and after electric field poling, and cycling between states. As such, are confident the measured signal does not stem from leakage currents between the electrodes.

Owing to the ISHE detection mechanism, the Pt detector wire acts as a directional detector, sensitive to the component of incident magnon spin polarization orthogonal to the length of the wire (Fig. 5.4a) [185, 192, 198]. The existence of two states of magnon current, therefore, indicates that the electric field induced switching results in changes to the magnon spin polarization pointing across the channel. My results thus indicate that the switching of the ferroelectricity induces switching of the net canted moment (M) adjacent to the detector Pt wire. As a result, the spin polarization of thermally excited magnons along M, also flips, resulting in the observed change in detected non-local voltage. To better understand the mechanism of such switching, I turn to PFM to directly image the ferroic order.

5.2.3 Magnetoelectric Coupling Mechanism

It has been shown previously [47], that there is one-to-one correspondence between ferroelectric domains and antiferromagnetic domains in BFO, so, via PFM I am able to intuit the magnetic domain structure. Within a single domain, the ferroelectric polarization, Nél vector and canted ferromagnetic moment are oriented orthogonal to one another (Fig. 5.5a) with the in-plane projection of the canted moment pointing along the in-plane projection of the ferroelectric polarization [9, 133, 10]. Owing to mechanical and electrostatic boundary conditions [45], adjacent domains' polarization vectors are oriented 109° from each other and aligned head to tail (Fig. 5.5a). The existence of such 109° domains is confirmed via PFM in my films (Fig 5.3a.), and results in a net canted moment (along $\langle 100 \rangle_{\mathrm{pc}}$), which points orthogonal to the directionality (¡010¿pc) of the stripe domains (Fig. 5.5). To study the switching of the ferroic state, I perform PFM imaging after application of ±350kV/cm across the channel. I observe reversal of the in-plane contrast (Fig. 5.5b), indicating in-plane reversal of the ferroelectric polarization. Importantly, while the in-plane component of the polarization reverses, the underlying ferroelastic domain structure is preserved, *i.e.*, switching occurs within each ferroelastic (stripe) domain. The persistence of the ferroelastic domains very likely contributes to the reversibility of the magnonic signal observed upon bipolar electric field pulsing (Fig. 5.4c). The IP PFM results, in combination with out-of-plane (OOP) PFM imaging after switching (Fig. 5.62), which does not show reversal, allow us to conclude that polarization switching proceeds via a 71° IP switch, consistent with previous research [9]. I show, schematically (Fig. 5.5c), the resulting reorientation of the polarization, Néel vector, and canted moment after 71° switching. The ISHE detection

mechanism is sensitive to the magnon spin polarization, and therefore the magnetic order, directly beneath the detector Pt wire. Furthermore, since the Pt wire spans several domains, the detected voltage is a function of the adjacent net magnetic order (i.e. the sum of twin domain contributions). While magnons have been shown to traverse both **M** and **L** [12,15,19], from the schematic (Fig. 5.5c), one can observe that while the net canted moment, M, does reverse, the net Néel vector, **L**, does not reverse following 71° switching. This indicates that my data is sensitive to spin wave excitations carried along (spin polarization antiparallel to) the net canted moment, **M**. Previous literature, [206], has also observed thermal magnons to traverse **M**.

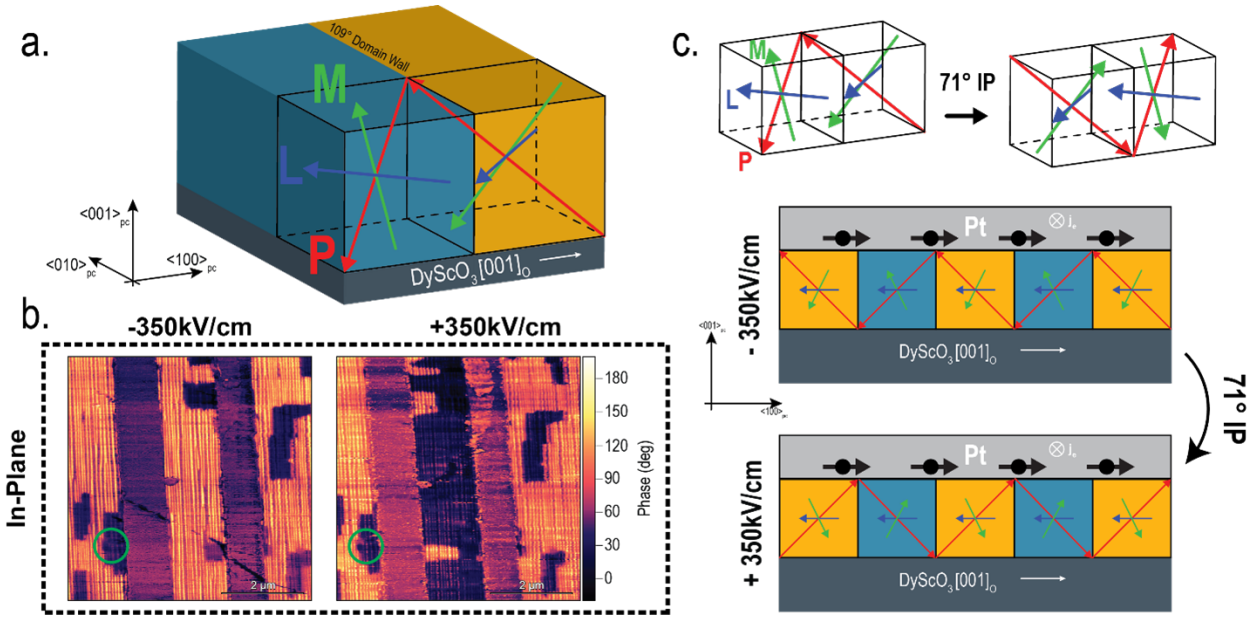

Figure 5.5: Switching Mechanism. **a.** Schematic of twin 109° domains showing ferroelectric polarization vector, **P** (red), Nél vector **L** (blue), and canted magnetization vector **M** (green). **b.** In-plane phase PFM images after +350kV/cm and -350kV/cm applied across the channel. The change in contrast indicates reversal of the net in-plane polarization (and therefore canted magnetization). A (Green) circle marks an external reference domain pattern for comparison. **c.** Schematic of 71°IP switch showing reversal of the both the net ferroelectric polarization, **P**, and net canted moment, **M**.

While I have so far discussed thermal magnons, it is important to address another excitation mechanism, namely the spin accumulation mechanism (SAM) [185, 192, 198, 216] from the spin Hall effect (SHE) in the injector wire. This effect is dependent on the charge current in the injector wire (as opposed to j^2 in SSE) and therefore appears in the first harmonic nonlocal voltage. Electric-field switching of BFO results in no change in the first harmonic signal (Fig. 5.7). It has been shown both experimentally [196] and theoretically [217, 218] that (anti-) ferromagnetic domain walls act as scattering sites for incident magnons. To

observe a first harmonic signal, magnons excited via SAM at the injector must traverse the channel without (or with minimal) scattering. My PFM data reveal many domain walls between the injector and detector, which scatter all SAM excited magnons, and result in no observed first harmonic signal. Thermal magnons however, can be "re-excited" after a domain wall since the thermal gradient, governed by phonon diffusion, for example, persists. As described in detail in section 5.2.4 similar physics can explain the lack of first harmonic signal in multidomain NiO [194], and is corroborated by reports on YIG which study the effects of nonlocal thermal gradients [213] and heat-transparent/spin-opaque interfaces[219].

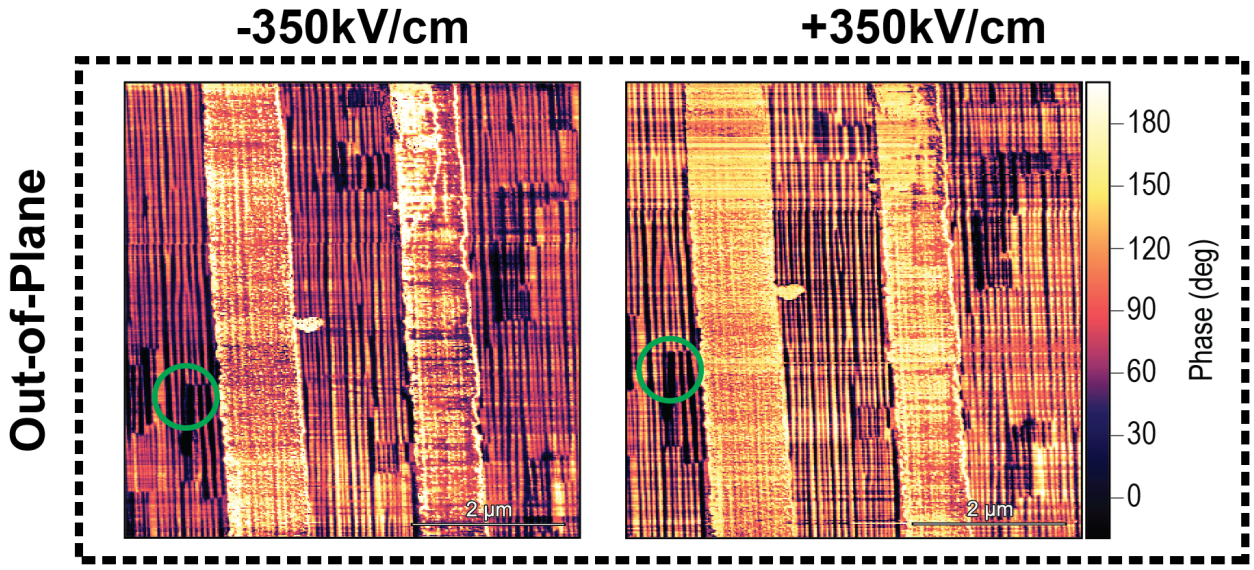

Figure 5.6: Out-of-plane PFM after ±350kV/cm poling. Green circles highlight identical area outside of the channel as a reference state. One can readily observe no out-of-plane switching, evidencing that poling of the channel results in 71 degree switching of domains.

5.2.4 Attenuation mechanisms of first and second harmonic signals

The first harmonic and second harmonic signals, while related, probe slightly different physics. As described in [192], the first harmonic measures spin transport via magnons excited by the spin accumulation mechanism, while the second harmonic probes thermally excited magnons. In systems such as YIG, a ferrimagnetic insulator with low Gilbert damping and long-range magnetic order, the two processes are closely related and indeed, the authors in [192] find similar values of magnon spin diffusion lengths (as measured by varying the channel spacing in the nonlocal device) for both first and second harmonic signals. To measure a first harmonic signal, magnons, which are excited locally at the injector, must diffuse to the detector without scattering or significant attenuation. The authors treat the

thermal excitation similarly, where Joule heating at the injector excites thermal magnons which then diffuse to the injector. However, later work [213] has shown that the picture of local Joule heating at the injector is incomplete, since the thermal gradient persist beyond the local region surrounding the injector, and the heating/spin-current source are delocalized.

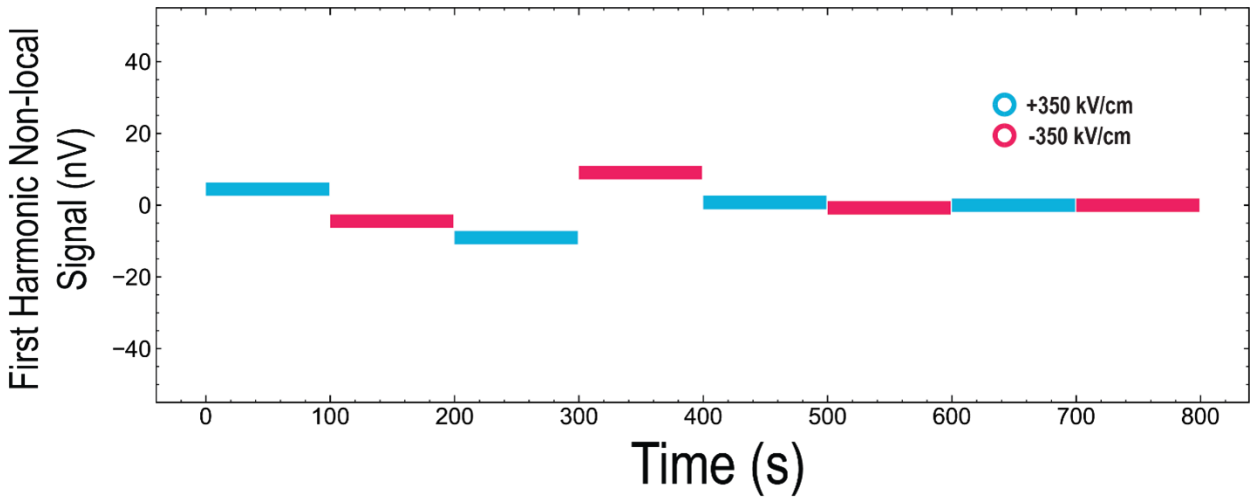

Figure 5.7: First-Harmonic non-local voltage upon Electric-Field pulsing. Average first harmonic signal before and after application of 350kV/cm electric field pulse, measured concurrently with second harmonic voltage (Fig. 5.4). The data reveal no repeatable change in first harmonic signal before and after switching.

Though the first and second harmonic signals exhibit similar length scalings in YIG, more complex systems such as multidomain NiO [194], where the authors observe a thermal signal, but no electrical signal, Cr_2O_3 [197], where researchers observe a thermal, but no electrical signal, or Fe_2O_3[185], where the authors find a spin diffusion length of the electrical signal to be ∼9 microns, but the thermal signal to persist beyond 80 microns, require a more nuanced investigation of the two signals. To understand why I observe similar effects in BFO, I must return to the origin of the two signals.

To observe the first harmonic signal, electrically excited magnons at the injector must diffuse to the detector without damping, scattering or encountering other attenuation mechanisms. It has been shown theoretically that magnetic domain walls act as scattering sites for incident magnons [217, 218]. This has also been shown experimentally, in the same non-local geometry to that is implemented in my experiment, in Fe_2O_3[196], where multidomain films exhibit significantly shorter magnon attenuation lengths, as measured by the spin accumulation mechanism (*i.e.*, first harmonic) signal. As more domains are introduced between the injector and detector the first harmonic signal will decrease owing to scattering of the magnons in the channel between the detector and injector. I see the exact same effect in BFO. In BFO, magnetic domains and ferroelectric domains are known to exhibit a 1-1

correspondence [47, 10], so, by my piezo-response force microscopy imagining (Fig. 5.3 and 5.5), I am able to confirm the existence of many magnetic domain walls (which are pinned in place, owing to multiferroicity in BFO and the dominant ferroelectric and ferroelastic energy scales) that act as scattering sites for incident magnons. As demonstrated in [219], thermal gradients can persist through spin-opaque interfaces, meaning the thermal gradient can persist through a domain wall, even if the magnons are scattered. Wherever a thermal gradient exists, so too does the SSE, so the thermal magnons can then be "re-excited" on the other side of the domain wall. This is starkly different from the electrically excited magnons, which, following scattering cannot be "re-excited." As such, it is not surprising that only second harmonic switching data is observed, and the findings presented here support the conclusions of a growing body of work studying magnon scattering at domain walls.

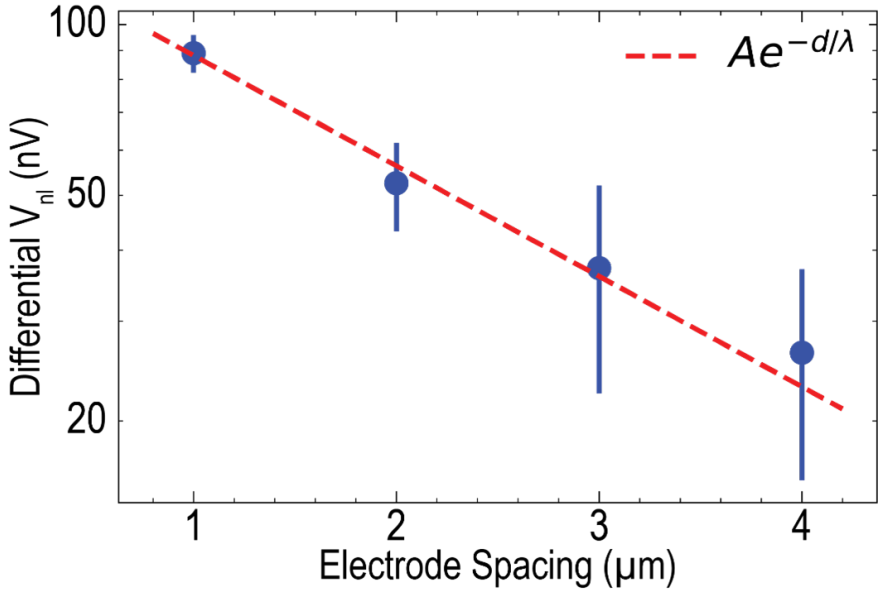

Figure 5.8: Electrode spacing series. Differential V_{nl} as a function of electrode spacing on log-linear scale. Heater current is 800μA for all devices. Error bars represent standard deviation of differential V_{nl} as measured by a lock-in amplifier for 200 seconds. Protocol is identical Fig 5.4. Red dashed line shows fit to $y = Ae^{-d/\lambda}$. The exponential fit is justified by a 1D diffusion model (see section 5.4.2) in the exponential regime [213]. Later (Fig. 5.15), I discuss the implications of such scaling.

In order to probe the attentuation mechanisms in my BFO films, I perform a study measuring the thermal magnon signal as a function of channel spacing.The range of spacings achievable in my experiment differs from that of systems, such as YIG, where the signal is modulated with an applied magnetic field. Owing to the need for electric field control, and the high voltages required to reach the same electric field value at increased electrode spacing, I am limited in the number of spacings achievable. My results (Fig. 5.8) for the differential

nonlocal voltage, $V_{nl} = V_{nl}(\text{positively poled}) - V_{nl}(\text{negatively poled}$ for an electrode spacing series, fits well to an exponential decay function, as would be expected in a 1D spin diffusion model [192].

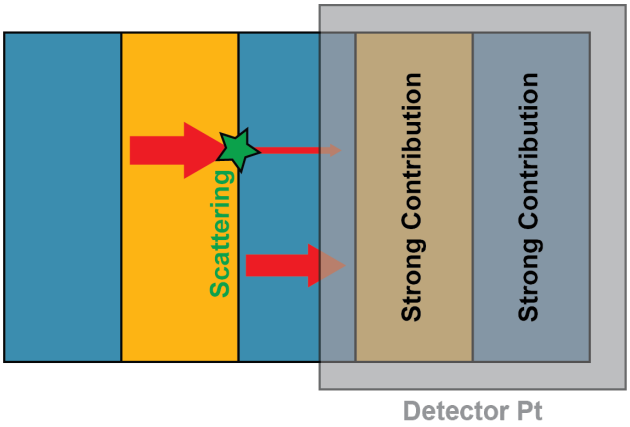

Figure 5.9: Schematic showing thermal magnon signal dominated by domains directly beneath the detector, as well as thermally activated magnons (notated by Red arrows) in nearby domains which are attenuated via scattering, though contribute a nonzero amplitude at the detector.

As noted in [213] the distance dependence can be a function of both the distance dependence of the thermal gradient, $\nabla T(x)$, and magnon relaxation. Further, as in [219], magnon accumulation can occur at interfaces with variable spin opacities, so it is possible that there exists a cascading magnon accumulation at successive domain wall interfaces. These two effects combine to give the net thermal magnon current, observed. Considering a simple model of phonons as heat carriers, I expect diffusive phonon heat transport, and, similar to the model for diffusive magnon transport [192], I expect the resulting thermal gradient (from phonons alone) to exhibit exponential dependence on distance. Therefore, if I consider only the domains directly beneath the Pt detector (and their magnetic state, as dictated by the electric field control) as being relevant to the detected thermal magnon signal, I expect to record the observed exponential dependence. I stress that this is a limiting case where magnons are completely scattered any time they encounter a domain wall, the effects of magnon diffusive transport resulting from magnon accumulation at domain walls are ignored, and phonons are the dominant heat carrier. While it is likely that the contribution to magnon signal from domains directly adjacent to the Pt detector are significant (dominant), as seen in Fig. 5.9 one must also consider magnons thermally excited magnons near the detector, which, although attenuated, do not completely scatter to zero amplitude when traversing a domain wall, or undergo diffusive transport following the magnon accumulation profile. Finally, one must consider that magnons also carry heat. It is possible, then, that the electrode spacing dependence contains two exponential decay terms, one from

the thermal gradient (*i.e.*, phonons) and one from magnon relaxation. Disentangling these two contributions is the subject of ongoing research, as discussed at length in section 5.4.

5.2.5 Hysteretic Thermal Magnon Behavior

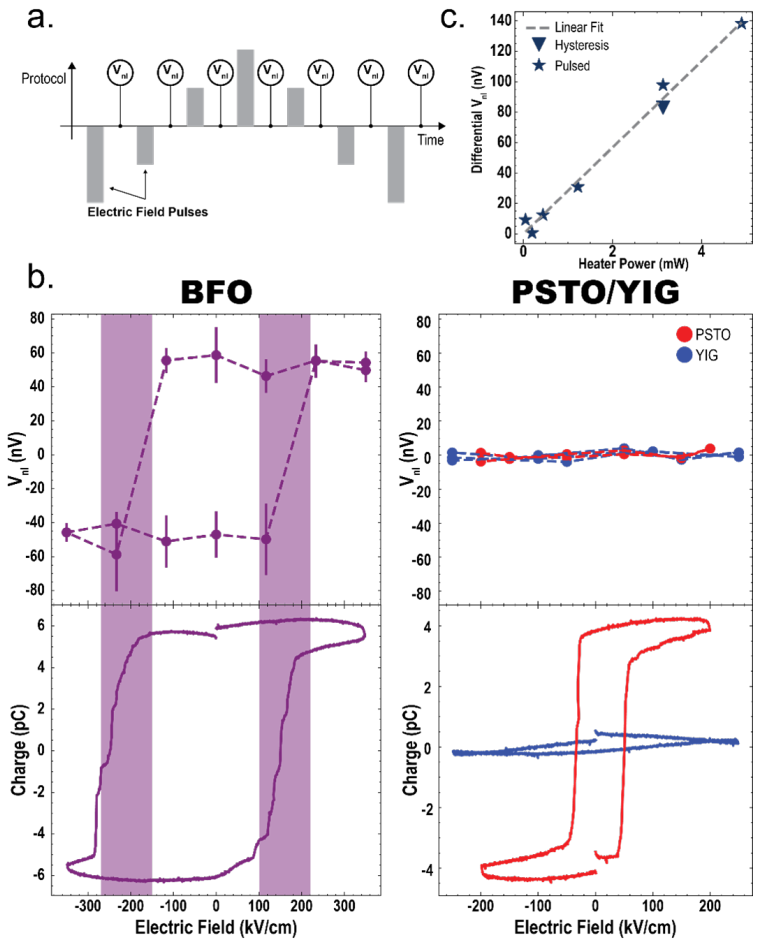

Figure 5.10: Hysteretic Response. **a.** Hysteretic magnon current measurement protocol. **b.** Observation of hysteresis in nonlocal second harmonic signal in BFO showing excellent agreement with the associated ferroelectric hysteresis loop. Identical measurements on PSTO and YIG are also shown. **c.** Magnitude of differential nonlocal voltage as a function of injector (heater) current, as measured through several different means.

Having established the mechanism behind magnetization reversal and the observed magnon current, I now demonstrate its hysteretic nature. I perform a quasi-static measurement (Fig. 5.10a), varying the magnitude of the electric field pulse across the channel from negative to positive and back again, while measuring (over 100 seconds) the non-local signal after each

applied electric field pulse. I observe a hysteretic response in the magnon current (Fig. 5.10b) which closely matches the ferroelectric hysteresis loop of the same device. To confirm that the observed data does not stem from capacitive charging or other extrinsic circuit effects [207], I perform the identical measurement on YIG (Fig. 5.10b). As expected, I observe no ferroelectric hysteresis, and importantly no hysteretic magnon current. Next, to confirm that the signal does not come from the remnant state of the ferroelectric polarization alone, I use a non-magnetic, in-plane ferroelectric $Pb_{0.7}Sr_{0.3}TiO_3$ (PSTO) sample with a similar value of switchable charge and again perform the identical experiment (Fig. 5.10b). Here, I observe a strong ferroelectric hysteresis response, as expected, but do not observe any hysteresis in the nonlocal voltage. The YIG and PSTO control samples together, therefore, allow us to conclude that the BFO signal is magnetic in nature. Finally, as the SSE signal scales with the square of the charge current in the injector wire, I expect a linear dependence on injector (heater) power (I^2 R) in the differential nonlocal voltage, defined as the difference between measured nonlocal second harmonic voltage when poled with a positive vs. negative electric field. I show (Fig. 5.10c) the expected linear dependence as a function of heater power. Finally, I show the repeatable nature of the electric field-switchable thermal magnon current (Fig. A.1), where the bistable states persist beyond ∼100 cycles. Fig. A.2 shows that the thermal magnon signal is does not depend on the lock-in frequency, at least at the relatively low frequencies studied here.

In conclusion, I have demonstrated a novel manifestation of intrinsic magnetoelectric coupling in BFO, establishing electric field control of non-volatile, hysteretic, bi-stable states of magnon current in the absence of an applied magnetic field. This represents a crucial step towards operational magnon-based devices. On-going work focuses on several pathways for increasing the magnitude of the non-local voltage for practical applications [3]. By varying the domain structure with choice of substrate [45], one can vary the number and type of magnon scattering sites present between the injector and detector. Advanced lithography techniques can also be utilized to minimize the injector-detector distance, with previous research indicating highly favorable scaling laws for reduced channel widths [192, 212]. In fact, with improved magnon coherence and/or decreased channel spacing, domain walls can be written using an out-of-plane electric field (rather than in-plane as demonstrated here), thereby enabling a non-volatile three terminal transistor which operates on magnon scattering at domain walls at the gate (see section 5.2.6 for more discussion). Perhaps most importantly, however, is the inclusion of alternate spin-orbit (SO) metals (replacing Pt). The spin Hall angle sets an intrinsic limit on the detected voltage, while the interface between the SO metal and the BFO can limit spin conductance and introduce variability in the fabrication process. Oxide SO metals, such as $SrIrO_3$, have recently shown high spin hall angles [220], and most importantly can be grown epitaxially, *in-situ*, via PLD on BFO, likely allowing for improved spin conductance, higher non-local voltages, and lower operating current, while maintaining BFO quality. The results shown here, offer an initial verification, highlighting an important synergy between multiferroics and magnonic spintronics, and demonstrating a novel pathway toward functional magnonic devices. In the next section, I discuss extensions to this work and the exciting implications/possibilities for computing technology.

5.2.6 Implications for computing applications

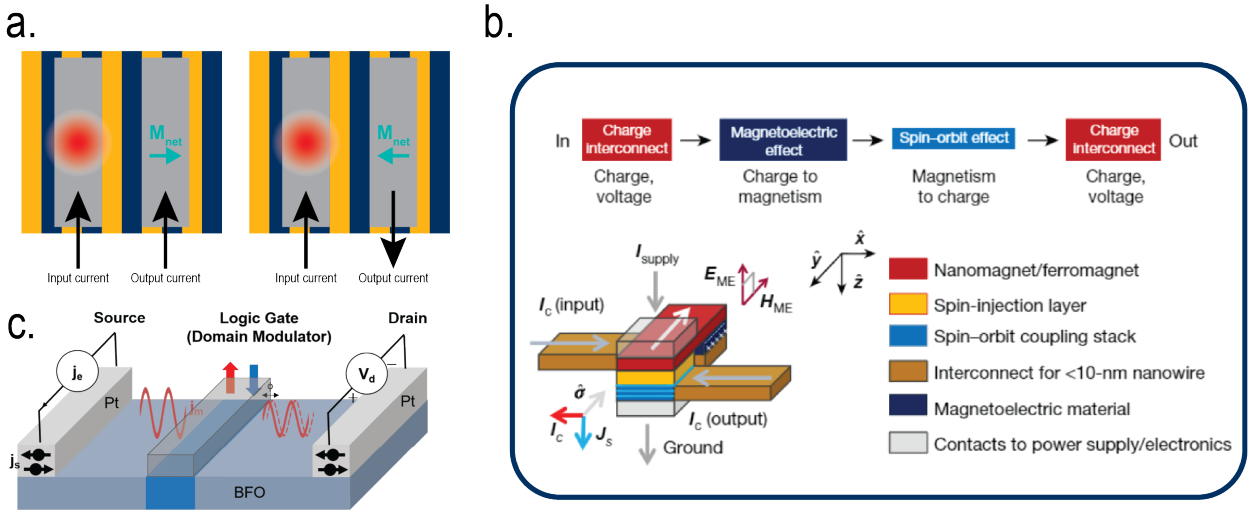

Figure 5.11: **a.** Schematic of an inverter based on thermal magnon spin transport in BFO. By switching the in-plane magnetization of the BFO with an applied electric field (through intrinsic magnetoelectric coupling) the sign of the output current reverses. **b.** Used with permission from ref [3], a schematic of a magnetoelectric spin-orbit logic device. By transitioning to a magnon-based read-out, the device can be simplified by replacing the spin-injection layer, spin-orbit coupling stack, and ferromagnet, with a single SOC metal layer (*e.g.*, Pt or SIO). **c.** Schematic of logic device operating on SAM magnons, instead of thermal magnons. A third terminal (gate) can be used to write magnetic domain walls, causing scattering, attenuation, or even phase shifting (necessary for wave-based computing) of incident magnons.

Previous work on BFO for magnetoelectric spin orbit (MESO) logic devices [2, 3] focused on using the switchable canted moment in BFO coupled to an adjacent ferromagnetic overlayer, thereby allowing one control of the magnetic state of the ferromagnet with an applied electric field. To write the state, an electric field is applied to the BFO/FM heterostructure poled either positively or negatively. In order to read-out the state, a supply current is injected into the device, causing a flow of spin-polarized electrons from the ferromagnet into an adjacent "spin-orbit coupling (SOC) stack". Owing to SOC spin-to-charge transduction (like the SHE), a charge current is generated at the output of the device[3]. Depending on the state of the BFO (and therefore the FM), the output current with be either high or low (positive or negative). This device design shows promise for very-low-power computation (*i.e.*, 10aJ), despite consisting of a large set of modules. For example, in the seminal work on MESO logic, [3], the proposed device consists of a ferromagnet, a spin-injection layer, a spin-orbit coupling stack, two charge interconnects, a magnetoelectric (BFO) material and contacts for power supply, all of which need to work together perfectly to achieve the goals of low

power consumption. Each material, let alone interface must be perfectly engineered so as to not introduce any losses. As such, one is naturally inclined to pursue alternative pathways which simplify the design (number of moving parts) while maintaining the ability to perform ultra-low power computation. Magnons in BFO, offer one such pathway.

The data presented in Fig 5.4, represent a non-destructive read-out the (magnetic) state of the BFO. Unlike sensing the ferroelectric state, as one does by switching the ferroelectric order, using magnonic spin transport through the BFO does not change the state of the BFO. This is highly desirable, as it represents a non-volatile method of doing logic. Perhaps most importantly, suggest a straightforward pathway to making an inverter, which is a key logic element. The reversal of the magnetic order with electric field switching of the BFO allows for inversion of the input charge current (Fig. 5.11). The ISHE detection mechanism acts as a directional detector. Thermal magnons, which carry spin polarization antiparallel to the net magnetization in the BFO will only scatter spins in the SOC detector metal which conserve angular momentum. This means that for well ordered BFO (stripe domains with consistent relationships between $\mathbf{P}$, $\mathbf{L}$ and $\mathbf{M}$) in a given state, the direction of the current in the detector wire is a directly maps to the magnetic state. 180° switching (of the in-plane projection, *i.e.*, a 71° switch of the ferroelectric order) will induce reversal of the charge current in the detector wire, which is precisely the objective of an inverter.

A few remarks are in order here. The inverter presented in Fig 5.11a works only for thermal magnons transmitted along $\mathbf{M}$. If I were instead to use SAM magnons, the same process would not occur upon switching of the BFO. This is because I now must consider the directional nature of the injector in addition to the detector (recall that the angular dependence, in Fig. 5.2, of the first harmonic signal is $\pi-$periodic). There are, however other benefits to using SAM magnons instead of thermal magnons, including the possibility for ballistic magnon transport, and using a gate electrode to write domain walls[7], enabling toggling of, or otherwise manipulating, spin transport without the need for switching the entire volume of the device (Fig. 5.11c). Lowering the required switched volume will have a positive impact on energy consumption.

As I have described, BFO and the intrinsic coupling between magnetic and charge degrees of freedom, makes it a uniquely attractive magnon-based devices. Unlike other magnetic systems which require the application of (high) magnetic fields, BFO can operate at room temperature with no applied magnetic field. As an example of how BFO-based devices operating on electric field control of magnons, consider the MESO device in Fig. 5.11c. The BFO serves as the "magnetoelectric material", and its state is read out in the following manner: 1. a ferromagnetic overlayer is exchange coupled to the BFO, enabling electric field switching of the ferromagnetic magnetization. 2. a current is run through the ferromagnetic layer, then through the spin-injection layer and the spin orbit coupling stack, which converts the state of the ferromagnet into a charge via the SHE. Note that in the geometry of Fig.

[7]This very likely requires large domain sizes or advanced lithography techniques. 110 oriented BFO offers a potential material system with larger domain structures, and e-beam lithography is capable of defining devices which could, in principle, sit with a single stripe domain

5.11c, electric field switching of the ferromagnet (via coupling to the BFO) must result in switching of the entire ferromagnetic magnetization, including the region not directly in contact with the BFO layer. This design, while achievable, is a complicated device structure, and by using magnon-based alternative, one can replace the ferromagnet, spin-injection layer, and spin orbit coupling stack with a single spin-orbit coupled metal (such as Pt). Such a simplification can improve yield, reliability, and energy losses at interfaces. For devices based on magnonic spin transport in BFO to reach maturity, however, a key hurdle is increasing the output voltage (or current) on the detector wire. Currently, I observe $\sim$ 100nV differentials between positive and negative poling, corresponding to only $\approx$20pA of current. When these values are compared to the 100mV and $\sim$60μA currents proposed in the MESO devices [3], it is clear that this is not a small challenge. My on-going efforts, described in more detail in section 5.4, include a multilateral approach to solving this problem, including, but not limited to, channel spacing, epitaxially control of domains, BFO/SOC metal interface engineering, and pursuing alternate SOC metals with higher spin-to-charge conversion (higher spin Hall angle) Before discussing next steps and on-going work, in the next section, I will address my magnetic field dependent studies of nonlocal devices in BFO, and specifically how the high spin-flop field in BFO and the Nernst effect makes the observation of non-local spin transport in such a configuration very difficult.

5.3 Magnetic Field Dependence

Here, I address the question of magnetic-field dependence of the observed nonlocal signal in BFO. In typical nonlocal spin transport experiments (Fig. 5.2, one rotates an applied magnetic field in the plane of the sample, while measuring both the first and second harmonic nonlocal voltages. With a sufficiently high magnetic field, the magnetic order (ferri-, ferro-, or antiferromagnetic) can be rotated along with the field. In-plane rotation of the applied field then results in a sinusoidal modulation of the observed non-local signal[197, 192]. I show the results of in-plane magnetic field angular dependent measurements on BFO (Fig. 5.12), which exhibit π-periodic oscillation (linearly dependent on the applied magnetic field magnitude), which is apparently consistent with the SSE. Upon closer examination, however, it is revealed that this signal is dominated by the Nernst effect in the Pt.

The Nernst effect is the thermal analog of the Hall effect in a metal, where an out-of-plane magnetic field and transverse thermal gradient produce a voltage proportional to the cross product of the two, *i.e.*, $V_{Nernst} \propto H \times \nabla T$. Careful study of the observed sinusoidal oscillation (explained in section 5.3.1), shows that it can be attributed to a small misalignment during mounting creating a $\approx$2.8 degree tilt out-of-plane. This then begs the question: where is the thermal magnon signal in the magnetic field dependence? The non-local SSE signal is very small, since the field is not high enough to have an impact on the magnetic order. Estimates of the spin flop magnetic field in BFO, for example, are as high as 15-20T [221], meaning that at the fields studied ($\leq$6T) the signal from the Nernst effect completely dominates any potential signal from the SSE, which is known to be weak below the spin

flop transition [185]. Furthermore, the Nernst effect signal will scale linearly with the applied magnetic field magnitude, making it difficult to distinguish the magnon signal from the Nernst effect signal. In order to properly do so, one would ideally have multi-axis control of the applied magnetic field direction and could minimize (correct for out-of-plane tilting) the Nernst effect at low field, before ramping above the spin flop field.

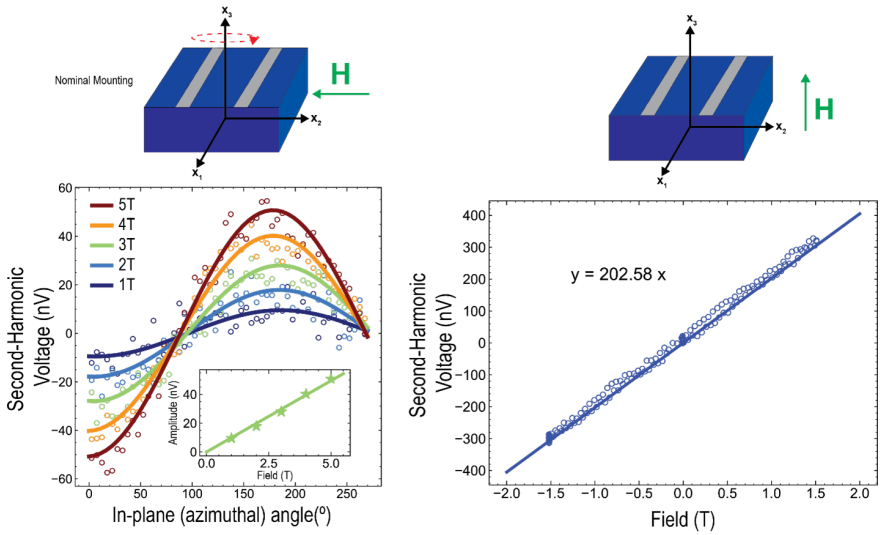

Figure 5.12: Second Harmonic Voltage for nominal in-plane and out-of-plane orientations. Left data shows nominal in-plane mounting of the sample with π-periodic oscillation of second harmonic voltage on the detector wire (consistent with SSE or Nernst effect). Right panel shows out-of-plane mounting and linear dependence of measured second harmonic voltage (consistent with the Nernst effect). Both right and left are measured with the same heater current. These measurements (see section 5.3.1) indicate that just $\approx$2.8 degrees of out-of-plane tilt from mounting the sample "in-plane" can result in the signal observed in the left panel, even in the absence signal stemming from the SSE.

While the magnetic field itself has no measurable effect on the magnonic nonlocal signal, I can still observe electric field control in the magnetic field angular dependent measurements. Upon electric field poling, I can induce an offset in the sinusoidally oscillating Nernst effect signal (Fig. 5.14). The magnitude of this nonlocal voltage offset, after correcting for variability in resistance across different devices (on both the detector and injector Pt wires), matches that predicted by the quadratic scaling nonlocal current on heater power (Fig. 5.10). This is a noteworthy finding, indicating that the *electric field control is not only remnant, but robust to spuriously applied magnetic fields*, a finding that represents another vote of confidence for BFO in terms of device application.

5.3.1 Nernst Effect

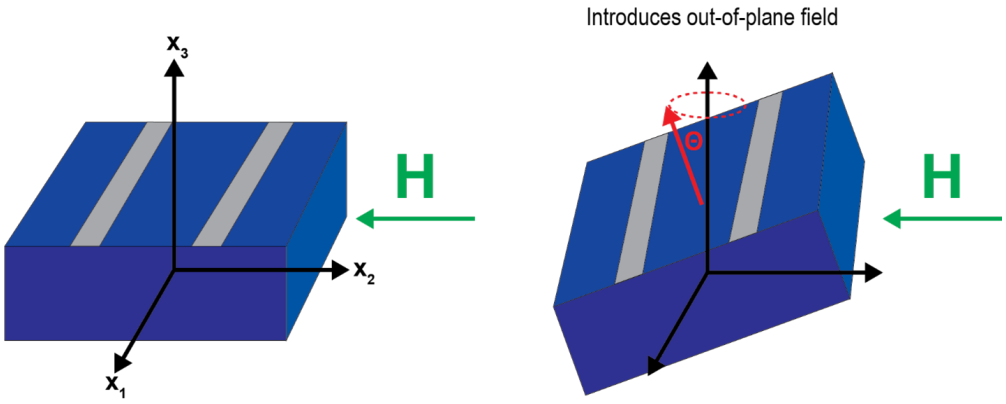

Figure 5.13: Out-of-plane tilt during mounting. (Nernst Effect). A small tilt when mounting the sample can lead to erroneous Nernst effect signals which can qualitatively match the expected non-local signal from the SSE.

The Nernst effect in a solid is the emergence of an electric field, $\vec{E}$, orthogonal to an applied magnetic field, $\vec{H}$ and a temperature dependent gradient, ∇T, in the solid, *i.e.*, $\vec{E_N} \propto \nabla T \times \vec{H}$. A non-local geometry is highly susceptible to erroneous Nernst effect signals, whereby, a material mounted with a slight tilt with respect to an otherwise "in-plane" magnetic field (Fig. 5.13) can display a signal with identical qualitatively identical features to that of a non-local spin Seebeck signal. I will derive this in detail in the following:

Let the applied magnetic field direction be along x_2. I first solve the case of no tilt. x_1', x_2', x_3' describe coordinate axes rotating with the sample (around x_3). The thermal gradient ∇T points across the channel, *i.e.*, $\hat{\nabla T} \propto \hat{x_2'}$. The measurement is sensitive only to electric field (in the form of a voltage) along the wire, *i.e.*, $V \propto E_{x_1'}$. I solve for the electric field from the Nernst effect:

$$\vec{E} \propto \hat{\nabla T} \times \vec{H} \propto \hat{x_2'} \times \hat{x_2} \propto (R_3(\phi)\hat{x_2}) \times \hat{x_2} \tag{5.4}$$

where $R_3(\phi)$ is the rotation matrix for a rotation ϕ around x_3, *i.e.*,

$$R_3 = \begin{pmatrix} \cos\phi & -\sin\phi & 0 \\ \sin\phi & \cos\phi & 0 \\ 0 & 0 & 1 \end{pmatrix} \tag{5.5}$$

$$\implies \vec{E} \propto (-\sin\phi, \cos\phi, 0) \times (0,1,0) = (0,0,-\sin\phi) \tag{5.6}$$

This indicates that there is no detected, erroneous, non-local voltage ($E_{x_1'} = 0$) for the case of no out-of-plane tilt. Next, I solve for the case with a small tilt angle (meaning the sample does not lie perfectly flat in the plane in which the external magnetic field is

applied). Without loss of generality, let this tilt be parameterized by an angle θ and occur via a rotation about x_1, *i.e.*, the tilted sample before rotating about x_3 has coordinate axes:

$$\begin{aligned} \hat{x_1'} &= R_1(\theta)\hat{x_1} \\ \hat{x_2'} &= R_1(\theta)\hat{x_2} \\ \hat{x_3'} &= R_1(\theta)\hat{x_3} \end{aligned} \tag{5.7}$$

where

$$R_3 = \begin{pmatrix} 1 & 0 & 0 \\ 0 & \cos\phi & -\sin\theta \\ 0 & \sin\theta & \cos\theta \end{pmatrix} \tag{5.8}$$

now, upon rotating the sample around x_3, I solve for the induced electric field from the Nernst effect.

$$\vec{E} \propto \hat{\nabla T} \times \vec{H} \propto \hat{x_2'} \times \hat{x_2} = (R_3(\phi)R_1(\theta)\hat{x_2}) \times \hat{x_2} \tag{5.9}$$

$$= (-\cos\theta\sin\phi, \cos\theta\sin\phi, \sin\theta) \times (0,1,0) = (-\sin\theta, 0, -\cos\theta\sin\phi) \tag{5.10}$$

and the measured voltage along the detector wire is then

$$V \propto \vec{E} \cdot \hat{x_1'} = -\sin\theta\cos\phi \tag{5.11}$$

which shows π-periodic dependence on the azimuthal (in-plane) angle, ϕ, precisely the same dependence one would expect from the nonlocal (SSE) voltage. Furthermore, the thermal gradient scales with the square of the applied current, meaning that Nernst signals and non-local SSE signals show qualitatively the same current and angle dependence. There are, however, a few key signatures of Nernst signals as opposed to true SSE signals.

1. Linear dependence on applied magnetic field. While this may come from lack of saturation of the magnetic order in the material (especially the case in antiferromagnets), linear dependence of applied field is consistent with the Nernst effect.

2. Variability in phase and or amplitude of the signal when remounting the sample. Each time one remounts the sample, in principle one introduces a random tilt, which will result in a random amplitude (random θ) and random phase (as I tilts can occur from rotations along either x_1 or x_2.

3. Devices fabricated orthogonal to each other give the same angle dependence

To ensure that a measured signal is not from the Nernst effect, one should mount the sample normal to the applied magnetic field, and measure a field dependence of the measured voltage on the detector wire for fixed current on the heater wire. In this case, the measured Nernst voltage is linearly dependent on field and given by:

$$V = \alpha H j^2 \tag{5.12}$$

where H is the applied magnetic field amplitude, j is the heater current amplitude, and α is a fitting parameter, which is fit to the experimentally obtained data. Returning now to the "in-plane" angular dependence, given the amplitude of the sinusoidally varying signal, A, one can calculate the required erroneous out-of-plane tilt angle to produce such a signal as:

$$\theta_{\text{tilt}} = \arcsin(A/j^2 \alpha H) \tag{5.13}$$

using the α measured in the OOP configuration.

When applied to my data (Fig. 5.12), this analysis performed on my BFO sample revealed a required tilt of just ≈2.8 degrees. As a rule of thumb, mounting of the sample introduces <5 degree out-of-plane tilt. If the required tilt is very large (to fit ones OOP data), then it is unlikely that your signal stems solely from the Nernst effect.

This analysis ignores that one will undoubtedly introduce a small tilt in the out-of-plane mounting as well. If one so desires, the sample can be mounted several times in order to obtain several values for α. The researcher should then use the maximum value of α obtained across remount trials.

If one has access to multi-axis alignment, it behooves one to rotate in-plane to a maximum of the π-periodic signal, and minimize the measured voltage using other axes of alignment. This will help correct for out-of-plane tilts.

5.3.2 Nernst effect, comparison with YIG

I also performed an identical analysis on my YIG sample, mounting the sample out of plane and measuring the Nernst effect, as in Fig. 5.12. The YIG data showed a slope of ≈ 50, which is approximately a quarter of the slope observed for the BFO (≈ 200). The thermal gradient (and therefore Nernst signal) at the Pt detector is a function of the thermal conductivity of the material (either YIG or BFO), with higher thermal conductivity resulting lower thermal gradients. My results, thus suggest that BFO has a thermal conductivity ≈ 1/4 of that of YIG. This finding is corroborated by the literature, where $\kappa_{\text{YIG}} \approx 6.6$W/mK[222] and $\kappa_{\text{BFO}} \approx 1.5$W/mK[223]. This also finding also has implications for the true SSE signal (Fig. 5.4), where, owing to the (relatively) low thermal conductivity, BFO is expected to produce high thermal gradients and therefore high thermal magnon signals. BFO is, however susceptible to erroneous signals *in the presence of applied magnetic fields*, further motivating my method of electric field control of the thermal magnon signal.

The reason that measurements on YIG are not dominated by Nernst effect signals is two fold. First, the thermal conductivity is higher, meaning the thermal gradients are lower. Secondly, YIG has a low coercive (magnetic) field. Since the Nernst effect signal scales linearly with the applied magnetic field amplitude (Eq. 5.4), at low field, SSE dominates.

5.3.3 Persistence of electric-field signal in BFO under applied magnetic field

Here, I reiterate the finding that in spite of the Nernst signal dominating the angular dependence, the effects of electric field poling (and switching) of the BFO order are robust to externally applied magnetic fields. As observed in Fig. 5.14, in-plane angle dependent studies reveal that the sinusoidal (Nernst) signal has a variable offset for a device poled positively and negatively with an electric field, which precisely matches the differential nonlocal voltage in absence of an applied magnetic field (Fig. 5.4). This confirms that the electric field controllable thermal magnon signal is, in fact, robust to external magnetic fields, consistent with the fact that ferroelectricity sets the dominant energy scale in the system, and a positive result for device applications.

Having now completed my discussion of the nonlocal voltages observed in BFO (both erroneous and as a result of thermal magnon transport), I will return to a discussion of on-going and future work.

5.4 On-going Work

There exist a number of open questions and extensions concerning my magnon work in BFO. In this section, I will classify two sets of directions that I believe could be fruitful pathways. The first class addresses fundamental questions pertaining to spin transport and the ways I believe BFO provides a unique opportunity to gain new understanding both of spin transport, and of BFO. The second class (as discussed in section 5.2.6) concerns applications to computing technology and pathways to creating viable magnon-based technology.

5.4.1 Fundamental

In the iron oxide (a parent compound of BFO) literature there exists a discrepancy between SAM and thermal magnons, where SAM magnons are believed to traverse the Néel vector, $\vec{L}$, while thermal magnons are believed to be transmitted along $\vec{M}$[185, 198], which is consistent with my findings (Fig. 5.4, 5.5). Of course, $\vec{M}$ and $\vec{L}$ are conventions that I have adopted to succinctly summarize the magnetic order in a material, and, as such, can overly simplify the picture of magnon spin transport in the system. A proper treatment of magnonic spin transport (see [35, 194, 224]) must consider the dispersion relation of the system which consists of many modes with different magnon spin polarizations[8]. I direct the interested reader to Dr. Hoogeboom's doctoral dissertation[224], Chapter 2, Figure 2.18, which shows the many different types of possible magnon modes in antiferromagnetic NiO (also see the final paragraph of Chapter 2). The population of each of these modes (via thermal excitation

[8]In some sense, it does not even make sense to say that spin is "transported along $\vec{M}$" (except in a ferromagnet, where this is exactly true), since the spin is transported by the collective excitations of magnetic order in the system, which of course, has no knowledge of whether it is $\vec{M}$ of $\vec{L}$.

or other means), as well as the magnon-spin polarization relative to the interfacial spin in the detector SOC metal ultimately determines the non-local voltage observed. In an effort to better understand magnon mode occupation and experimentally verify spin polarization of different modes, it would be useful to be able to use the geometry of the system to your advantage. As a simple illustration of this point, consider, as a thought experiment, an out-of-plane ferromagnet. Non-local spin transport as I have described in this chapter (in-plane), would be insensitive to changes in the magnetic order in the out-of-plane direction. However, if I were to take the system and force the magnetization in-plane, I would now be able to measure a nonlocal signal. BFO offers a unique system to do just this type of study, albeit with significantly more complex magnetic structure than a simple ferromagnet. Via expitaxy, electrostatic boundary conditions (recall that ferroelectricity sets the dominant energy scale) and device geometry, I can build out a toolbox for experimentally probing magnon occupation and spin polarization.

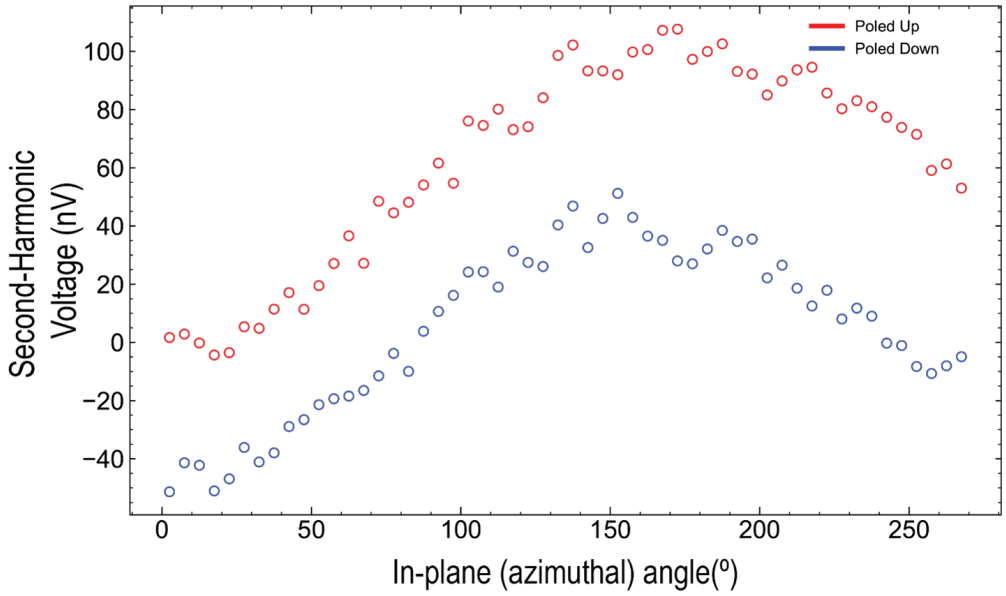

Figure 5.14: Non-volatility of Electric-field control; robust to applied magnetic fields. Nernst effect (angle dependent) signal before and after electric field poling. The data reveal that while the Nernst effect dominates the angular dependence with applied magnetic field, electric field poling induces non-volatile changes to the magnetic order which are robust to externally applied magnetic fields (consistent with the exceptionally high spin flop field in $BiFeO_3$). Data shown is at 5T applied magnetic field.

The detection mechanism, via the ISHE, acts as a directional detector, only sensitive to magnon spin polarization orthogonal to the length of the channel. In the case of the first harmonic signal, the injector also acts directionally. By tuning the orientation of the BFO film, by growing on $DyScO_3$, $SrTiO_{3(111)}$, or $SrTiO_{3(110)}$ oriented substrates, for example, I

can modify the relative orientation between the detector/injector directionality and relevant magnon modes in the BFO with different spin polarization. As an example, in $\langle 111 \rangle$ oriented BFO the polarization points purely OOP, while the magnetic order lies in the plane of the sample. This control via epitaxy potentially allows us to interrogate specific eigen modes.[9] Importantly, however, by modifying the film orientation, one will also modify the domain structure [45], and must take care to properly account for this (perhaps by using e-beam lithography to always operate within a single domain). Future measurements can be supplemented by first-principles calculations, or micromagnetic simulations, to better understand the excitation and detection mechanisms as well as provide a holistic (experimentally verifiable) map of the magnon dispersion in BFO, which includes sensitivity to mode-specific magnon spin polarization.

Finally, non-local spin transport also allows us access to additional information about the nature of magnetic ordering in BFO itself. My results are consistent with the canted moment pointing along $\langle 11-2 \rangle$ (Fig. 5.5), consistent with that reported in much of the thin-film literature on BFO[10, 9, 133]. In bulk BFO, however, the magnetic ordering is known to exhibit the so-call spin cycloid [226, 227, 228] where the magnetic Néel vector and canted moment rotate with a propagation vector along one of three directions, $[-211], [1-21], [11-2]$. The spin cycloid is typically thought to be destroyed in thin-films, owing to expitaxial constraints [229], though recent work using nitrogen-vacancy (NV) centers in diamond as sensitive magnetometers has suggested that the spin cycloid can persist even in thin films [214, 230]. If this is the case, the spin cycloid's existence[10] will certainly modify the magnon modes and dispersion in BFO, something that will hopefully be studied by a combination of NV magnetometry and non-local spin transport in the future.

5.4.2 Applied

As discussed in section 5.2.6, my work on magnons in BFO has laid a strong foundation for using magnon-based technology for computing applications. Here I will discuss on-going

[9] I have performed such measurements on [110] oriented BFO, and found that, while the sample exhibits a remnant, switchable in-plane polarization (as measured via in-plane PFM and "half" hysteresis loops, similar to Fig. 5.4), it does not appear to exhibit bi-stable states of thermal magnon current. This can be explained by careful analysis of the magnon modes and their spin polarization in [110] BFO (known to have interesting magnetic structure [225]) and is consistent with PEEM data indicating that in such an orientation, the canted moment does not project onto the in-plane direction to which the non-local measurement is sensitive.

[10] The existence of the spin cycloid in thin-film BFO challenges some of the existing literature, particularly works which discuss coupling between BFO and an adjacent ferromagnetic overlayer, where the canted moment (which averages to zero in the case of the spin cycloid) is crucial to current understanding of the coupling mechanism. One possible explanation is that the ferromagnet instead couples to a spin cycloid propagation vector, rather than a net canted moment. Notably, all works agree that the magnetic order (whether that is $\vec{M}$, $\vec{L}$ or the spin cycloid propagation vector) changes upon electric field poling [9, 230, 52, 51, 214]. Even in the case of the cycloid propagation vector persisting in my thin films, electric field poling, and consequent manipulation of the cycloid would still be consistent with my observed magnon data. This is an exciting time, and my magnon findings presented in this chapter could prove to be an important tool for future studies of magnetic ordering in BFO.

work aimed at maturing such technology. A key barrier to using magnon-based BFO devices is the low, 100s of nV, voltages measured on the detector wire. In Table 5.1, I outline several characteristics that determine the magnitude of the detected voltage, intrinsic and extrinsic factors which impact these characteristics, and outline potential pathways for improving each.

Characteristic	Factors Impacting	Pathway for improvement
Magnon amplitude	Domain wall scattering	Epitaxy
	Damping	Channel spacing
	Diffusion length	Device geometry
Spin conductance	SOC metal/BFO interface	Epitaxial SOC metal growth
Spin-to-charge conversion	Spin hall angle	Alternative SOC metals
	Magnon mode spin polarization	New geometries
		Improved eigen-mode excitation

Table 5.1: Factors impacting nonlocal voltage, and pathways for improvement.

Spin transport in magnetic insulators has been shown to follow a 1D spin diffusion model[192], where the nonlocal voltage is given by:

$$V_{nl} = \frac{C}{\lambda} \frac{e^{x/\lambda}}{1 - e^{2x/\lambda}} \tag{5.14}$$

with x the channel spacing, λ the characteristic diffusion length, and C a fitting parameter including the diffusion coefficient, spin conductance and spin-charge conversion efficiency. As observed in Fig. 5.15a., my data (although additional data is required to confirm such scaling) can be fit to Eq. 5.14, allowing us to *roughly* estimate the voltage scaling I can expect by going to smaller channel spacings, as in [185]. Owing to the mechanism of magnon scattering at domain walls, I am interested in using domain engineering via epitaxy, in conjunction with channel spacing series, to ideally reveal a family of curves (in addition to that presented in Fig. 5.15a). The emergence of such a family of curves may be possible, if, for example, one is able to tune the average domain size (reducing scattering per length), transition to ballistic transport, or manipulate which magnon modes are occupied as different modes may have different scattering characteristics.

The results presented here offer a pathway for improving the measured nonlocal voltage by decreasing the channel spacing. However, even more importantly, by moving to an alternate (out-of-plane) device geometry, as in Fig. 5.15b, I expect to see dramatic improvements in the measured voltage as well as the emergence of the first harmonic signal. In an OOP geometry, I can get the benefits of exceptionally thin propagation distances, where PLD grown thin-films can reliably be made less than 10nm thick. Eq. 5.14 scales as $1/x$ to leading order, meaning that as the magnon propagation length is made ever smaller, I expect to see a larger signal. Additionally, in the OOP configuration, I expect minimal scattering at domain walls

(Fig. 5.15, likely resulting in significantly higher signals, and the appearance a first harmonic (SAM) signal. The OOP geometry in BFO is made possible by the fact that BFO can be grown epitaxially on $SrIrO_3$ (SIO), which is already known to have a high spin Hall angle (good spin-to charge conversion) [220]. The SIO/BFO epitaxial interface will also help with improved spin conductance. By using a combination of epitaxy, device geometry, thickness scaling, and alternative SOC metals, I believe nonlocal voltages of at least 100s of μV are obtainable.

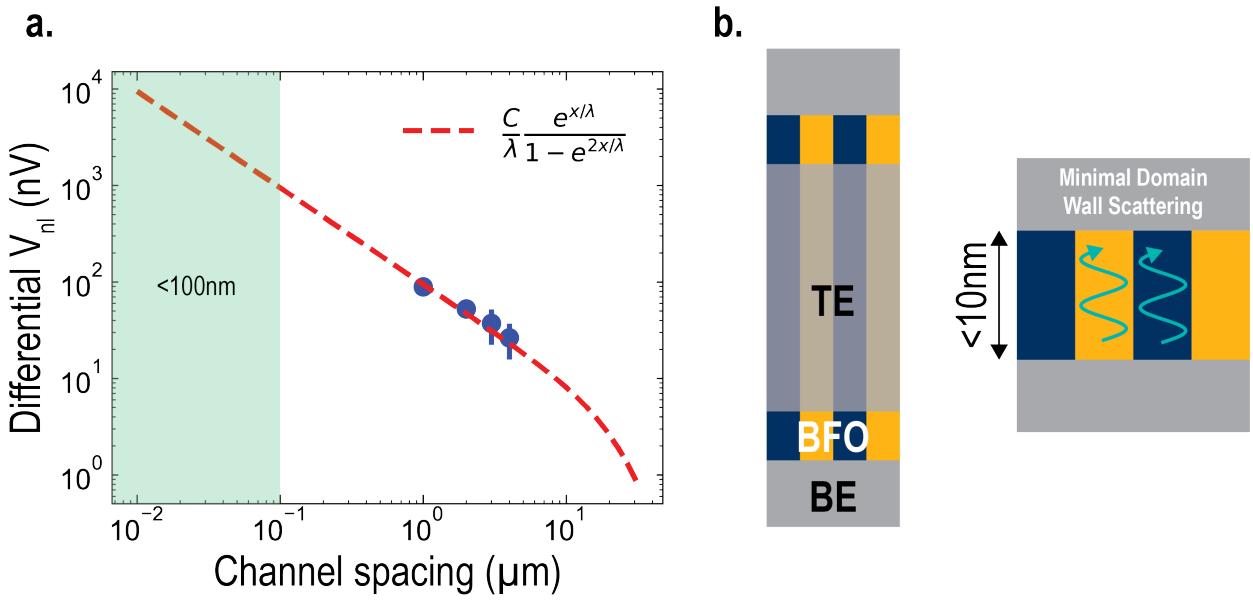

Figure 5.15: Pathways to increasing nonlocal voltage. **a.** shows channel spacing scaling and fit to 1D spin diffusion model (as in [192]). The emergence of a family of curves is possible via domain engineering. **b.** shows top view and cross sectional view of proposed out-of-plane device enabling exceptionally short "channel" spacings, and mitigation of attenuation mechanisms (*i.e.*, scattering at domain walls.)

Chapter 6

Summary and future work

6.1 Chapter Summaries

6.1.1 Chapter 1

Chapter 1 served as an introduction to the key concepts and themes of this thesis. I discussed theoretical background for ferroelectrics, ferromagnets, antiferromagnets and multiferroic materials. $BiFeO_3$, the main material focus of this thesis, was introduced and described. Key questions concerning dynamics of ferroic order, specifically switching and low energy eigen-excitations, were detailed within the context of both fundamental and applied physics.

6.1.2 Chapter 2

Chapter 2 detailed electric-field driven dynamics of ferroelectric switching. I began by introducing a measurement technique, focused on mitigating circuit effects when measuring ferroelectric switching. This lead to interesting discoveries concerning an approach to intrinsic timescales and model of how the interplay between free- and bound-charge dynamics influence the observed dynamical timescales. By tuning the free energy landscape (double-well potential) through chemical substitution within the BFO system, I show that the nucleation and growth mechanism of switching, and specifically the "activation" energy required to switch and grown reverse polarized domains, can be modified, and how this manifests in ferroelectric switching experiments. Via comparison with alternate material systems, most notably the prototype ferroelectric BTO, I further show that spontaneous polarization and free energy landscape are essential for understanding ferroelectric switching dynamics. Through area-dependent switching studies, I show how extrinsic factors impact switching, and ways to mitigate such effects. The work presented in Chapter 2 lays the foundation for Chapter 3, where I explore alternate means of tuning the free energy landscape through modification of mechanical boundary conditions, and provides vital context for Chapter 4, exploring depolarization dynamics.

6.1.3 Chapter 3

Chapter 3 expands upon the findings of Chapter 2, and addresses a vital question in ferroelectric switching, which to date has not been studied exhaustively: given the robust coupling between charge and lattice degrees of freedom in ferroelectric materials, what role do lattice dynamics have in influencing ferroelectric switching dynamics? In order to study this in a tractable fashion, I make use of recent progress in freestanding ferroelectric membranes and phase field calculations to explore changes in switching energetics and dynamics upon removal of the epitaxial constraint imposed by the substrate. To undergo switching, the ferroelectric thin film, which accounts for only a small volume fraction of the substrate/ferroelectric stack, must structurally deform, thereby requiring the substrate lattice to dynamically evolve in time. My findings show that the resistance to structural deformation imposed by the substrate results in significantly higher energy of switching, and slower switching dynamics. This can be understood as a hardening of the free-energy landscape, as modified by changes in lattice dynamics for freestanding and epitaxial films. I introduce the notion of "strain+tilt" clamping, whereby the substrate can impose mechanical constraints on both strain and antiferrodistortive order parameters in the BFO system, and address the implications for magnetoelectric coupling. Finally, I show how similar results can be obtained in BTO, indicating a universality of the role of the substrate, and lattice dynamics, in dictating ferroelectric switching dynamics.

6.1.4 Chapter 4

In Chapters 2 and 3, I focused on driven switching dynamics, and ways in which one can tune (both intrinsically and extrinsically) the energetics and dynamics of ferroelectric switching. Chapter 4 represents a transition, where I now turn to a study of internally driven, depolarization, dynamics, and the implications (possibly detrimental) of significant reductions in driven switching energy and time. Here, I predominantly study BTO, as it offers a prototypical ferroelectric response and exceptionally low work of switching (and consequently exhibits significant depolarization). I reveal the critical role of film thickness and electrode screening length in dictating depolarization dynamics. Via temperature dependent studies, I develop a simple model based on Landau theory and show how depolarization in BTO is consistent with nucleation and growth. This finding is contrasted with results on the prototypical relaxor ferroelectric (PMN-PT), which, as expected, does not exhibit the same temperature dependence. Finally, I analyze the implications of depolarization in ultra-low coercivity ferroelectric thin films within the context of device applications. I consider a "sweet-spot" in film thickness, where driven dynamics remain fast and require low energy, but depolarization is small and the polar state remains stable.

6.1.5 Chapter 5

In Chapter 5, I shift gears from switching dynamics to dynamic eigen excitations of magnetic order, specifically magnons, in BFO. I show show results that demonstrate electric field control of thermal magnons in the system, a novel manifestation of magnetoelectric coupling and multiferroicity. I demonstrate bi-stable, non-volatile states of magnon current as measured via the ISHE in an adjacent Pt wire. Via PFM studies, I show that the device geometry used in my experiment is sensitive to magnons with spin polarization anti-parallel to the canted moment of the BFO. By using YIG and PSTO control samples, I ensure the obtained signal is spinful, and not ferroelectric in nature, though can be mapped one-to-one to the ferroelectric hysteresis loop, thereby demonstrating the origin in multiferroicity. I address the role of domain walls in dictating the observed magnon signal, and offer pathways to mitigate such effects. Erroneous Nernst effect signals are discussed.

The work on magnon transport in BFO is perhaps the most exciting work presented in this thesis, not only because it represents the first demonstration of electric field control of magnon propagation in the absence of an applied magnetic field, but because of the promise it holds for potential new paradigms in magnon-based logic and memory devices. Future work on device scaling, domain engineering, BFO orientation and alternate SOC metals offer pathways to improved voltages required for device applications. Finally, I believe my progress studying thermal versus SAM magnons represents important learning for the entire field of magnonics. Now, I am most interested in out-of-plane devices (to minimize domain wall scattering), and using the directionality of the detection (and creation) mechanism in conjunction with film orientation to create a 3-dimensional map of magnon wave vector and spin polarization in BFO.

6.2 Future work

6.2.1 Switching Dynamics

6.2.1.1 Fast ferroelectric switching

There are a number of on-going/future work projects that aim to study ferroelectric switching. One approach is to further manipulate the free-energy landscape, and/or switching mechanism, for example, by tuning mechanical boundary conditions as in Chapter 3. Other projects include further area scaling, by fabricating devices below 1μm in diameter. The signal to noise ratio is expected to decrease, where smaller areas result in smaller ferroelectric displacement currents (current $\propto P \times A$). In order to increase the signal, we have considered using arrays of small capacitors, though one must take care to not introduce additional capacitances in doing so. An alternative is to use an amplifying circuit to increase the signal to noise ratio. Such an amplifier must be capable of accessing timescales significantly faster than 1ns. This can be a challenge, though one option may be to use an avalanche diode. Improved pulse generation, with faster rise times ($\leq$ 50ps), will also assist in ac-

cessing switching near intrinsic limits. This can be achieved by fabricating the ferroelectric capacitor on CMOS, or by using a photoconductive switch, as in [58].

Much of the difficulty in accessing switching timescales ∼ps, comes from the metallic electrodes and the interplay between free and bound charge. Alternatively, if one is able to forgo the need for such electrodes, and had another means of applying the electric field, the timescales accessible may be significantly improved. One such option is to use THz radiation as a means of creating a propagating electric field. Ideally, one would have unipolar THz pulses, something that is typically not observed in tabletop THz setups, though may be able to be achieved by making use of a half cycle unipolar THz field at an accelerator such as SLAC (at Stanford University). If one is to use THz electric fields, one also requires a sufficiently high-speed probe of switching, something that can be achieved using optical second harmonic generation, as in [231], or perhaps by using the THz spectroscopic characteristics of the ferroelectric itself[1]. I will discuss early work on using second harmonic generation as a probe of ferroelectric switching below, as well as in section 6.2.1.2.

6.2.1.2 Real-time observation of switching pathway

Other on-going work is predicated on observing, in real-time, the ferroelastic switching pathway (Fig. 1.8) in BFO. Such a measurement would enable studies of factors impacting the switching pathway (*i.e.*, strain), and have important implications for the switching of magnetic order (Fig. 1.7). As described in Chapter 2, there exist outstanding questions as to the fundamental limits on ferroelectric switching, and I am interested in techniques to further study these dynamics on the timescales at which they occur. Owing to the convolution of free and bound charge dynamics, it may be preferred to use alternative means (*e.g.*, optical) to probe switching, and already, researchers have used optical techniques to observe ultrafast ferroelectric switching [231] in the ferroelectric $LiNbO_3$. In this section, I outline on-going/future work which aims to use an optical probe (namely, second harmonic generation) enabling time-resolved measurements, which are sensitive to both in-plane (*i.e.*, 71°) and out-of-plane (109°) switching events. Such a technique allows for real-time observation of switching pathways in BFO that are essential for switching of magnetic order in the system.

Ferroelectric switching experiments on ferroelectric capacitors fabricated in the out-of-plane orientation (Fig. 2.1) are only sensitive to the projection of the polarization in the OOP direction. This is why, for example, the measured switchable ferroelectric polarization in (001) oriented BFO films (Fig. 2.5a) is observed to be $\sim \frac{100}{2} = 50\mu m/cm^2$ (recall that pulsed measurements measure twice the remanent polarization value), even though the spontaneous polarization magnitude in BFO is a $\sim 90 - 100\mu C/cm^2$, *i.e.*, $90\mu C/cm^2 \times ((0,0,1) \cdot \frac{1}{\sqrt{3}}(1,1,1)) \approx 52\mu C/cm^2$. However, BFO is believed to switch via a 2-step ferroelastic switching pathway (Fig. 1.8). Such two-step switching has been observed via time-resolved PFM studies [9], though the time resolution of the technique use

[1]See ref [232] for an example of how THz emission can be used to probe the polarization state in BFO

there, was limited to 40μs, significantly slower than the timescales observed in our measurements. As such, I seek a new technique, capable of resolving in-plane (71° in BFO) switching on the timescale of ns or below. The technique I turn to is second harmonic generation.

Second harmonic generation: Second harmonic generation (SHG) is a process that combines two incident photons at frequency ω into a single photon of frequency 2ω, and can occur in materials that do not possess inversion symmetry (*e.g.*, ferroelectrics)[8, 233]. The review by Denev *et. al.* [233] serves as an excellent reference for the details of SHG in general, and as they relate to ferroelectric materials, but for the purposes of this thesis, it is not especially insightful to restate those details here. In terms of dynamics, SHG can be a valuable tool, for example, in detecting ferroelectric polarization reversal at ultrafast timescales[231], owing to the time-resolution of pulsed optical based setups (100s of fs). Further, by performing SHG measurements with linearly polarized photons, the technique can act as a directional probe, sensitive to symmetry changes along the electric field polarization direction. As such, by tuning the electric-field polarization, and angle of incidence of the incident photons one can resolve symmetry changes in a variety of directions. In particular, operating a near normal incidence (Fig. 6.1a.), the electric field lies in the plane of the sample, offering a probe of in-plane symmetry changes, which 71° switching, for example, will induce. SHG, therefore, gives us the ability to probe in-plane switching in BFO, and my colleagues and I devised a scheme to both measure the OOP ferroelectric switching (through collection of displacement current) while simultaneously monitoring the in-plane switching via time-resolved second harmonic generation (Fig. 6.1).

We use 800nm incident light and collect the 400nm light produced via SHG. We perform electric-field-pump, time-resolved (TR) SHG-probe experiments, with a variable time delay, t_d, between the onset of the applied electric field and 800nm pulse (Fig. 6.1d.) providing time resolution. At each time delay, we perform many trials to improve the signal to noise ratio, and I use a preset electric field pulse to ensure that the ferroelectric state is the same for each trial. I fabricate devices from SRO/BFO/SRO heterostructures (Fig. 6.1a,b,c), which are designed to allow for optical access and *in-situ* electric field control (via wirebonding). I show the results of the displacement current for both preset and switching pulses as well as the change in SHG counts, defined as the change in SHG signal from time ~ -1500, for the switching pulse (Fig. 6.1e). The preset electric-field pulse is lower in magnitude than the switching pulse in order to reduce degradation of the film. As observed (Fig. 6.1e), there is a correlation between the ferroelectric switching displacement current and the P-polarized-in, S-polarized-out ΔSHG (Green arrow in Fig. 6.1. This is evidence that supports the two-step (*i.e.*, 71°, and 109°) switching process, where the displacement current is sensitive to the 109° and the change in SHG signal is sensitive to the 71° switching. It appears that the two processes occur at similar timescales, which is potentially the result of an ensemble average of many domains, where some domains follow 71° →109° switching, while others follow the opposite order. Following the initial transient, which correlates with the observed ferroelectric switching displacement current, there is a sustained ΔSHG observed. This is most likely from electric field induced second harmonic generation[234], and is most likely not from long-time in-plane dynamics of the ferroelectric order.

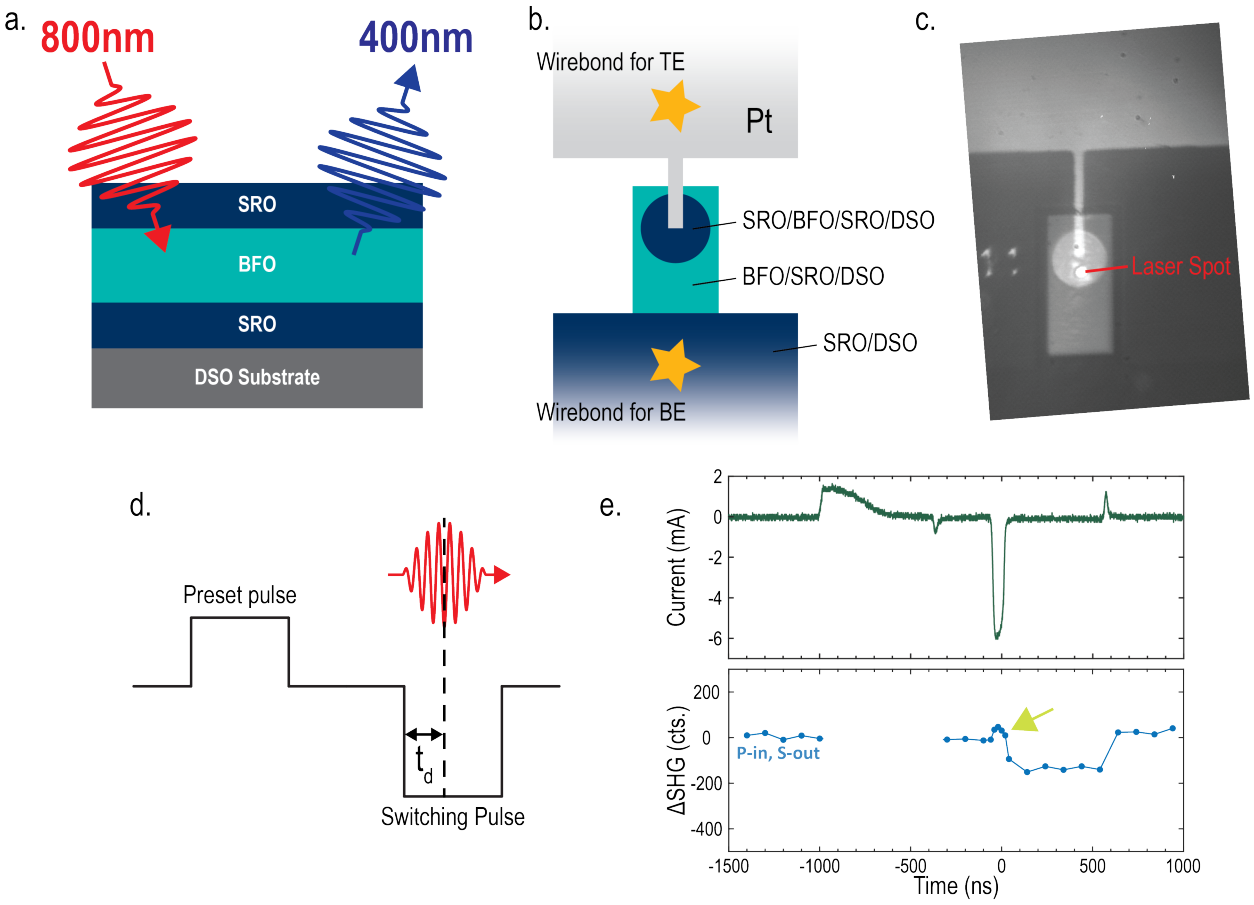

Figure 6.1: Time-resolved second harmonic generation studies of ferroelectric switching. **a.** Schematic of near normal incidence SHG in BFO. **b.** Schematic of device for making electrical contact to top and bottom electrode, and performing *in-operando* SHG. **c.** Optical image of fabricated device under study. **d.** Schematic of electric field pulse/SHG pulse timing. **e.** Displacement current (OOP) and change in SHG counts during ferroelectric switching. Yellow regions indicate times when electric field pulses are applied. Green arrow highlights transient feature in P-in, S-out signal during FE switching.

These studies offer some of the first experimental data apparently verifying real-time two-step ferroelastic switching pathways in BFO at these timescales, and provide a basis for future work. In particular, as discussed in detail in Chapter 3, Section 3.3, freestanding membranes of BTO, have been shown to exhibit enhanced switching dynamics, possibly owing to the emergence of a ferroelastic switching pathway upon removal of the mechanical constraints imposed by the substrate. TR-SHG, as described here can resolve the emergence of such pathways. Furthermore, TR-SHG could help settle the debates, more broadly in ferroelectrics, about the fast-timescale mechanisms of switching, for example, whether or not ferroelectric switching proceeds through the high symmetry phase, or instead by rotation of

the ferroelectric dipoles.

6.2.1.3 Switching of coupled (magnetic) order

Coupled ferroelectric and antiferromagnetic dynamics What follows is a proposal to study ultrafast time-resolved ferroelectric and antiferromagnetic dynamics in BFO using a free-electron laser (FEL). Specifically, the following is a proposal for the MagneDyn beamline at Elettra Sincrotrone Trieste.[2]

As I hope you have learned from this dissertation, from both technological and fundamental perspectives, key research in the field of multiferroics studies the dynamics of coupled magnetic and ferroelectric order. As such, I am interested in the fundamental limits that govern the out-of-equilibrium dynamical response (on the natural femtosecond timescales) of spin and charge degrees of freedom. To answer this question, I propose to study the ultrafast ferroelectric (FE) and antiferromagnetic (AFM) dynamics in the prototypical multiferroic, $BiFeO_3$. I present a multi-modal approach that will utilize the sensitivity of x-ray magnetic linear dichroism (XMLD) at the iron M-edge to AFM ordering with element-specificity and the polarization selectivity of second harmonic generation (SHG) to deconvolute the ultrafast response of the relevant order parameters to an optical excitation. Harnessing full x-ray polarization control with ultrafast time resolution, this first-of-its-kind measurement will elucidate key timescales and dynamical coupling mechanisms that will advance strongly correlated materials theory and set benchmarks on the ultimate speed limits of next-generation magnetoelectric-based logic devices.

FE and AFM ordering in BFO are coupled in equilibrium, enabling deterministic switching of the magnetic state via application of applied electric fields [9, 47]. Transport measurements [26] have studied FE dynamics as fast as ns timescales relevant for device applications and time-resolved x-ray diffraction has been used to study the ps-to-ns lattice relaxation after an optical pump pulse [235, 236], though sub-ps measurements of coupled magnetic and FE order parameters remain elusive. Investigations of sub-ps dynamics have been an extensive area of research in materials possessing either dominant spin- or charge-ordering, but a systematic study of the ultrafast non-equilibrium response in a material possessing strong magnetoelectric coupling is lacking, in part owing to the few experimental approaches capable of deconvoluting the response.

The goal is to characterize the sub-ps response of BFO to an ultrashort optical pulse with specificity to both AFM and FE order parameters. Fundamentally, it is still an open question as to whether the magnetoelectric coupling observed in equilibrium remains one-to-one coupled in the time-domain, particularly on the natural timescales of the charge- and spin-dynamics. Previous studies of sub-ns dynamics in BFO have studied the photo-induced lattice response on ps timescales. Transient x-ray diffraction in combination with optical transient absorption revealed a fast lattice expansion occurring within tens of ps, attributed to photoexcited carrier screening of the FE depolarization field, followed by a slower thermal

[2]This proposal was accepted, though unfortunately later cancelled. I hope that by including it here, a future scientist will pursue this direction.

relaxation [235, 236]. Time resolved optical SHG measurements in ref. [237] showed that an above band gap (∼3 eV) [238] optical pump pulse can collapse the FE ordering within 150 fs, which fails to recover completely within tens of ps. This phenomenon is attributed to photoexcited carriers modifying the ferroelectric state. As such, owing to magnetoelectric coupling, one would expect a corresponding change in AFM ordering, thereby offering a means to study magneto-electric dynamics on ultrafast timescales. However, missing from both of the aforementioned studies is the sub-ps temporal resolution and specificity to AFM ordering necessary to deconvolute the spin and charge response. While traditional probes of magnetic dynamics utilize the magneto-optical Kerr effect (MOKE) that can be used in conjunction with optical SHG, the former is nontrivial to perform in multiferroic materials, particularly those with AFM ordering, where the FE ordering gives rise to a significant electro-optical effect and since MOKE requires a nonvanishing magnetic moment.

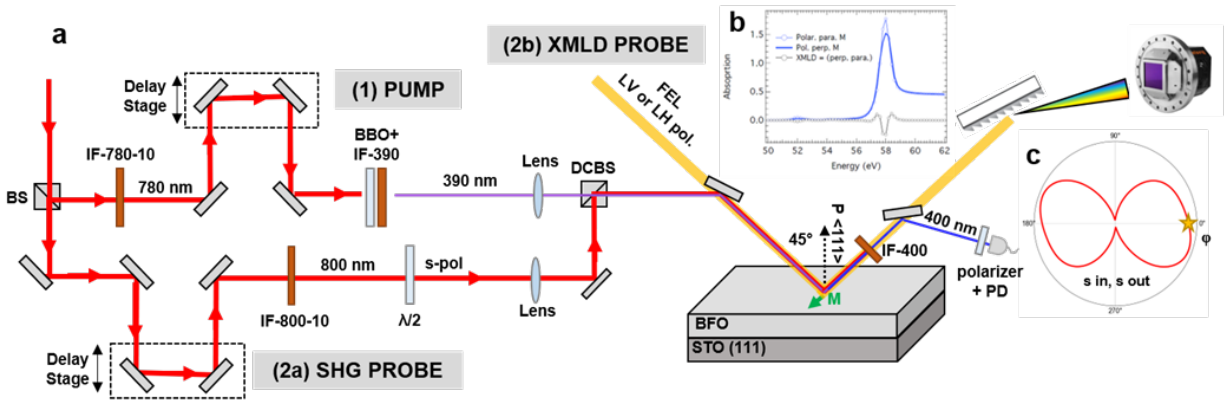

Figure 6.2: Experimental scheme. **a.** The three color experiment consists of a pump at 390 nm generated from the SLU (800nm seed laser) using a 780 nm interference filter and a BBO crystal, an s-polarized optical SHG probe at 800 nm, and an XUV pulse at the Fe M-edge with either LV or LH polarization. All three beams are incident at 45° onto the sample. The STO (111)-BFO sample has the FE axis out-of-plane and the AFM ordering in-plane. **b.** Preliminary calculations of the expected XMLD signal at above the Fe M-edge with ∼10% contrast expected around 58 eV. c) Preliminary calculations of optical SHG intensity estimate the strongest signal in the s-polarization channel with an in-plane rotational angle of ∼0°, denoted by a star. (BS = beamsplitter, IF = interference filter, DCBS = dichroic beamsplitter, PD = photodiode).

To address these issues, we will perform XMLD above the Fe $M_{2,3}$ edge (∼52.7 eV) and optical SHG in a simultaneous fashion to uncover the ultrafast non-equilibrium response with spin-, charge- and elemental specificity (Fig. 6.2). This multi-modal scheme avoids the added challenge of changing experimental conditions that all-too-often renders the combined interpretation of different ultrafast probes difficult. The XMLD signal measures the absorption or reflectivity when the x-ray polarization is parallel and perpendicular to the

AFM ordering axis. XMLD theory shows that this difference depends on $\langle M^2 \rangle$, rather than $\langle M \rangle$, and exhibits a $\cos^2 \theta_M$ dependence, where θ_M denotes the angle between the magnetic axis and the x-ray polarization, thus making XMLD sensitive to anti-ferroic ordering [239, 240, 241]. On the other hand, optical SHG will assist in decoupling the FE response since it is a measure of the nonlinear susceptibility, $\chi^{(2)}(2\omega)$, which is only nonzero when inversion symmetry is broken [242]. By varying the sample orientation with respect to the incoming light polarizations, we expect to observe anisotropic dynamical fluctuations in the spin- and charge- degrees of freedom.

We will be characterizing the coupled spin-charge dynamics that ensue following an out-of-equilibrium perturbation by performing fluence, temperature-, and time-resolved measurements where the SHG and XMLD probe signals are captured simultaneously. This is a three-color experiment consisting of 1 pump pulse and 2 time-delayed probes that will travel collinearly into the sample chamber in a reflection geometry. The angle of incidence will be 45° for all three beams.

1. Pump: Above band-gap pump at 390 nm. This will be generated from a portion of the broadband SLU (800nm seed laser) centered at 785 cm using a 780 nm interference filter frequency-doubled with BBO to 390 nm. This pump beam will be focused to a variable spot size that ensures a fluence ranging from 0.1-5 mJ/cm^2 where we expect a significant population of excited carriers to screen the depolarization field [235] and a 10-30% decrease in SHG intensity within 1 ps [237].

2. Probe 1: Fully compressed FEL tuned around the Fe $M_{2,3}$ edge with either LH and LV polarizations for measuring XMLD. Our preliminary calculations estimate a 10% modulation in XMLD response at ∼58 eV. The exact energy above the M-edge should be confirmed with static synchrotron XMLD measurements.

3. Probe 2: 800 nm probe for SHG at 400 nm upon interacting with the sample. The 800 nm probe will be generated from the SLU using an 800 nm interference filter, time-delayed using a delay stage, and recombined with the 390 nm pump beam using a dichroic beam splitter. An on-target fluence of 1 mJ/cm^2 will be sufficient for SHG. The resulting 400 nm beam after SHG from the sample will be isolated using a 400 nm interference filter that will sufficiently block out both the 800 nm and 390 nm incident beams.

We will perform three sets of experiments using all three beams. All experiments will involve 30 pump-probe delay combinations ranging from -0.1 to 20 ps with steps in the tens to hundreds of femtoseconds.

1. Sample Orientation Dependence - At room temperature, the 390 nm pump/FEL probe/SHG probe experiment will be performed with LH and LV FEL polarizations to capture the XMLD signal and at two different in-plane sample orientations (ϕ = 0° and ϕ = 71° AFM ordering vector with respect to the x-ray LH polarization) to characterize anisotropies (= 4 time scans).

2. Fluence Dependence - Next, LH and LV scans will be performed at room temperature, $\phi = 0°$ AFM orientation, and at three different pump fluences (0.1, 1, 3 mJ/cm^2) to follow dynamics as a function of photo-excited carrier concentration (= 6 time scans). Here, we are curious how screening of the depolarization field affects magnetic dynamics.

3. Temperature Dependence - Finally, LH and LV scans will be performed at a single pump fluence, chosen based on the results of the previous measurement, but at the maximum available temperature (∼200 °C) where we expect the spin dynamics to be partially suppressed, given that $T_{Nèel}$ = 370 °C (= 2 time scans).

Through this set of measurements, we will gain valuable insight into the coupled FE and AFM dynamics in BFO at ultrafast timescales.

Giant magnetoresistance of BFO-based heterostructures Here, I will discuss future and ongoing giant magnetoresistance studies on BFO-based heterostructures. Motivated by earlier studies [9, 10, 51, 52] that explored quasi-static switching of an adjacent ferromagnetic overlay to BFO, I am interested in the dynamics of such processes. As discussed in Chapter 1 the coupling between charge and magnetic degrees of freedom is, in some ways, surprising, where magnetism inherently carries angular momentum and ferroelectricity does not. This begs the obvious question, can we observe transient decoupling, or other dynamic processes as a result? For applications, specifically magnetoelectric spin orbit logic devices, one is interested in the timescales accessible for switching, which sets the processing speed of future devices.

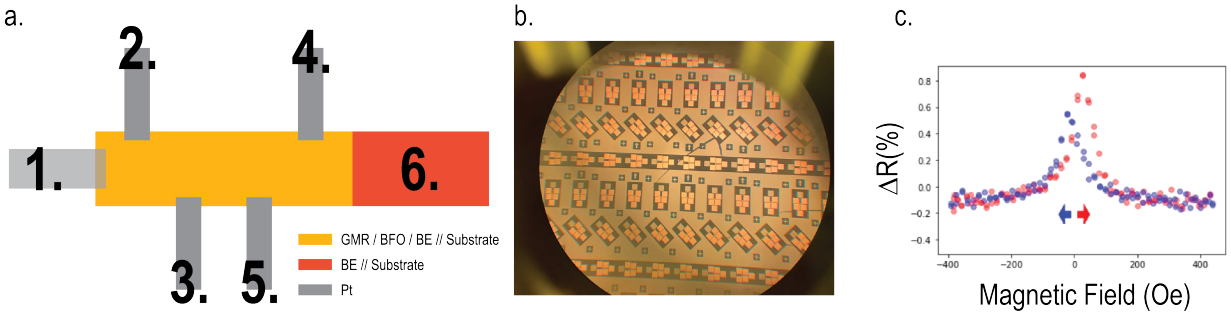

Figure 6.3: GMR device used for studying timescales of ferroelectric-switching-induced ferromagnetic switching. **a.** Schematic, **b.** optical image of many devices, **c.** magnetic field sweeps, showing split loops.

To study the timescales of both ferromagnetic and ferroelectric switching, I fabricate devices using the "wirebonding" process, as described in Appendix B. Fig. 6.3a. shows a schematic of the 6-terminal device used here. Pads 1 and 6 are used to switch the BFO with an applied electric field. Using pulsed voltages, we can collect the ferroelectric switching displacement current as a means of measuring the timescales of ferroelectric switching. Pads

2-5 are used to measure the 4-point resistance of the GMR stack, where changes in the resistance upon electric field poling can be attributed to switching of the ferromagnetic layer adjacent (coupled to) the BFO. Fig. 6.3b. shows and optical microscope image of many such devices. Fig 6.3c. shows the resistance of the GMR spin valve as a function of applied magnetic field sweeps, showing characteristic hysteretic loops, and proving the quality of my devices.

In order to access the timescales of switching, one can, in principle use precise control of the pulsewidth and magnitude of the applied voltage for ferroelectric switching, with theoretical work predicting decoupling between ferroelectric and ferromagnetic degrees of freedom below a critical ferroelectric switching time [133]. By applying a sufficiently large voltage between pads 1 and 6, for example, one can expect to induce ferroelectric switching fast enough to decouple the two order parameters. To measure the induced change in the ferromagnetic order (which will be apparent in the resistance of the GMR stack), one simply measures the 4-point resistance at any time after switching. Of course, this method of probing the resistance is reliant on changes induced being stable and remnant over the time period ($\sim$ seconds) that the resistance measurement takes place. In principle this is no problem, however, in practice, the asymmetry of the electrodes (GMR stack : CoFe/Cu/CoFe as top electrode, and SRO as bottom electrode)[3] can introduce "imprint" into the ferroelectric hysteresis loop, making the switched state, metastable, unstable, or transient (as in Fig. 4.3). The issues of imprint are more substantial in the thin films studied in this thesis as opposed to thicker films studied in the literature previously [9]. Issues of imprint can be made better by adding a thin $La_{0.7}Sr_{0.3}MnO_3$ layer between the bottom SRO and BFO layer [51].

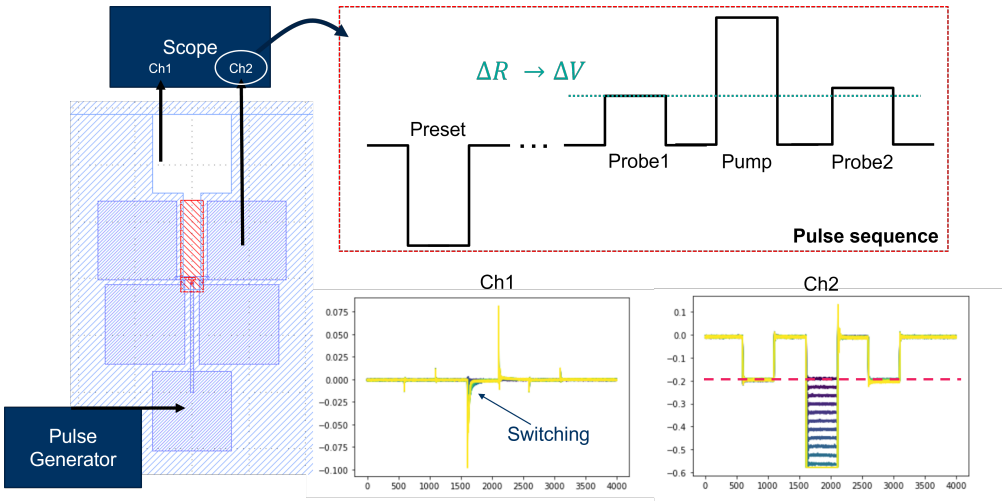

Figure 6.4: Scheme for measuring transient GMR using a set of four voltage pulses.

[3]Which is required in order to have interfacial coupling between the BFO and the CoFe

To handle the issues of imprint, if they persist, I devised a scheme to monitor transient changes in resistance, using a series of three pulses (Fig. 6.4). We use two channels on the oscilloscope for this measurement scheme. Channel 1 is set to 50Ω impedance and collects the ferroelectric switching displacement current. As observed (Fig. 6.4), probe pulses 1 and 2 correspond to only capacitive responses (*i.e.*, no ferroelectric switching). Channel 2 is set to high impedance (to match that of the ferroelectric capacitor) and is used to measure the voltage amplitude through the GMR stack (pads 1→5, Fig. 6.3a), as a proxy for resistance. Changes in observed voltage amplitude for probe pulses 1 and 2 correspond to changes in resistance of the GMR stack. The pump pulse induces ferroelectric switching. This measurement scheme allows one to deal with imprint, since the GMR measurement occurs immediately following switching. One should compare GMR responses in both the switching and non-switching directions (Fig. 4.3). Such studies have so far proven inconclusive and are on-going. I include these notes here in hopes that someone in the future will find the idea behind the measurement scheme helpful.

6.2.1.4 Depolarization

There are several pathways to mitigating the effects of depolarization fields. A significant reduction in the screening length (λ) is possible by changing electrode material, though growth quality must be maintained. A potential choice is yttrium barium copper oxide (YBCO) which is superconducting at liquid nitrogen temperatures. In the superconducting phase, the YBCO will, in principle have a vanishingly small screening length. In this limit, the depolarization field should also vanish. Another option is to address the reduction in activation energy presently observed. This can be achieved through defect implantation[159] though will also coincide with increased coercivity. In the drive toward 100mV operation of ferroelectric materials, one must not lose sight of the stability of the polar state, and must find a delicate balance of effects.

There exists, however, a new opportunity for polar materials with inherent instability. Recent progress in probabilistic computing, where logical bits populate "on" and "off" states subject to a (electric-field-dependent, for example) probability distribution, has shown promise for a number of use-cases[156, 157, 158]. While implementations so far have been limited to ferromagnetic tunnel junctions, such as in ref [157], work studying a parallel implementation using ferroelectrics with inherent instabilities, such as those presented here, is on-going. The very same mechanisms, of low coercivity and high depoling fields, which contribute to depolarization in my ultra-low coercivity BTO films, for example, can cause dipolar fluctuations whose timescale and probability of occurrence will be strongly influenced by an external DC bias. To study polar fluctuations I have proposed to use noise electrometry with nitrogen-vacancy centers in diamond [155] in addition to using fabricated devices and measuring the electrical noise spectrum. The latter technique would consist of an isolated (including Faraday cage[4]) ferroelectric capacitor which is electrically contacted with a

[4]One must take care to remove erroneous signals such as WiFi in the building

wirebond. If the polarization fluctuates with characteristic time-scales, I can observe such fluctuations in the noise spectrum (as measured with a network or spectrum analyzer) of the current in the circuit. By applying a DC bias, I expect to be able to tune the probability distribution (biasing one state over the other) of the polarization in the film, which will be observed as a change in the noise spectrum.

6.2.2 Magnon spin transport

There exist a number of open questions and extensions concerning my magnon work in BFO. In this section, I will classify two sets of directions that I believe could be fruitful pathways. The first class addresses fundamental questions pertaining to spin transport and the ways I believe BFO provides a unique opportunity to gain new understanding both of spin transport, and of BFO. The second class (as discussed in section 5.2.6) concerns applications to computing technology and pathways to creating viable magnon-based technology.

Fundamental In the iron oxide (a parent compound of BFO) literature there exists a discrepancy between SAM and thermal magnons, where SAM magnons are believed to traverse the Néel vector, $\vec{L}$, while thermal magnons are believed to be transmitted along $\vec{M}$[185, 198], which is consistent with my findings (Fig. 5.4, 5.5). Of course, $\vec{M}$ and $\vec{L}$ are conventions that I have adopted to succinctly summarize the magnetic order in a material, and, as such, can overly simplify the picture of magnon spin transport in the system. A proper treatment of magnonic spin transport (see [35, 194, 224]) must consider the dispersion relation of the system which consists of many modes with different magnon spin polarizations. I direct the interested reader to Dr. Hoogeboom's doctoral dissertation[224], Chapter 2, Figure 2.18, which shows the many different types of possible magnon modes in antiferromagnetic NiO (also see the final paragraph of Chapter 2). The population of each of these modes (via thermal excitation or other means), as well as the magnon-spin polarization relative to the interfacial spin in the detector SOC metal ultimately determines the non-local voltage observed. In an effort to better understand magnon mode occupation and experimentally verify spin polarization of different modes, it would be useful to be able to use the geometry of the system to your advantage. As a simple illustration of this point, consider, as a thought experiment, an out-of-plane ferromagnet. Non-local spin transport as I have described in this chapter (in-plane), would be insensitive to changes in the magnetic order in the out-of-plane direction. However, if I were to take the system and force the magnetization in-plane, I would now be able to measure a nonlocal signal. BFO offers a unique system to do just this type of study, albeit with significantly more complex magnetic structure than a simple ferromagnet. Via expitaxy, electrostatic boundary conditions (recall that ferroelectricity sets the dominant energy scale) and device geometry, I can build out a toolbox for experimentally probing magnon occupation and spin polarization.

The detection mechanism, via the ISHE, acts as a directional detector, only sensitive to magnon spin polarization orthogonal to the length of the channel. In the case of the first harmonic signal, the injector also acts directionally. By tuning the orientation of the BFO film, by growing on $DyScO_3$, $SrTiO_{3(111)}$, or $SrTiO_{3(110)}$ oriented substrates, for example, I

can modify the relative orientation between the detector/injector directionality and relevant magnon modes in the BFO with different spin polarization. As an example, in ⟨111⟩ oriented BFO the polarization points purely OOP, while the magnetic order lies in the plane of the sample. This control via epitaxy potentially allows us to interrogate specific eigen modes. Importantly, however, by modifying the film orientation, one will also modify the domain structure [45], and must take care to properly account for this (perhaps by using e-beam lithography to always operate within a single domain). Future measurements can be supplemented by first-principles calculations, or micromagnetic simulations, to better understand the excitation and detection mechanisms as well as provide a holistic (experimentally verifiable) map of the magnon dispersion in BFO, which includes sensitivity to mode-specific magnon spin polarization.

Finally, non-local spin transport also allows us access to additional information about the nature of magnetic ordering in BFO itself. My results are consistent with the canted moment pointing along $\langle 11-2\rangle$ (Fig. 5.5), consistent with that reported in much of the thin-film literature on BFO[9, 10, 133]. In bulk BFO, however, the magnetic ordering is known to exhibit the so-call spin cycloid [226, 227, 228] where the magnetic Néel vector and canted moment rotate with a propagation vector along one of three directions, $[-211]$, $[1-21]$, $[11-2]$. The spin cycloid is typically thought to be destroyed in thin-films, owing to expitaxial constraints [229], though recent work using nitrogen-vacancy (NV) centers in diamond as sensitive magnetometers has suggested that the spin cycloid can persist even in thin films [214, 230]. If this is the case, the spin cycloid's existence will certainly modify the magnon modes and dispersion in BFO, something that will hopefully be studied by a combination of NV magnetometry and non-local spin transport in the future.

Applied As discussed in section 5.2.6, my work on magnons in BFO has laid a strong foundation for using magnon-based technology for computing applications. Here I will discuss on-going work aimed at maturing such technology. A key barrier to using magnon-based BFO devices is the low, 100s of nV, voltages measured on the detector wire. In Table 5.1, I outline several characteristics that determine the magnitude of the detected voltage, intrinsic and extrinsic factors which impact these characteristics, and outline potential pathways for improving each.

Spin transport in magnetic insulators has been shown to follow a 1D spin diffusion model[192], where the nonlocal voltage is given by:

$$V_{nl} = \frac{C}{\lambda}\frac{e^{x/\lambda}}{1-e^{2x/\lambda}} \tag{6.1}$$

with x the channel spacing, λ the characteristic diffusion length, and C a fitting parameter including the diffusion coefficient, spin conductance and spin-charge conversion efficiency. As observed in Fig. 5.15a., my data (although additional data is required to confirm such scaling) can be fit to Eq. 6.1, allowing us to *roughly* estimate the voltage scaling I can expect by going to smaller channel spacings, as in [185]. Owing to the mechanism of magnon scattering at domain walls, I am interested in using domain engineering via epitaxy, in conjunction with channel spacing series, to ideally reveal a family of curves (in addition to

that presented in Fig. 5.15a). The emergence of such a family of curves may be possible, if, for example, one is able to tune the average domain size (reducing scattering per length), transition to ballistic transport, or manipulate which magnon modes are occupied as different modes may have different scattering characteristics.

The results presented here offer a pathway for improving the measured nonlocal voltage by decreasing the channel spacing. However, even more importantly, by moving to an alternate (out-of-plane) device geometry, as in Fig. 5.15b, I expect to see dramatic improvements in the measured voltage as well as the emergence of the first harmonic signal. In an OOP geometry, I can get the benefits of exceptionally thin propagation distances, where PLD grown thin-films can reliably be made less than 10nm thick. Eq. 6.1 scales as $1/x$ to leading order, meaning that as the magnon propagation length is made ever smaller, I expect to see a larger signal. Additionally, in the OOP configuration, I expect minimal scattering at domain walls (Fig. 5.15, likely resulting in significantly higher signals, and the appearance a first harmonic (SAM) signal. The OOP geometry in BFO is made possible by the fact that BFO can be grown epitaxially on $SrIrO_3$ (SIO), which is already known to have a high spin Hall angle (good spin-to charge conversion) [220]. The SIO/BFO epitaxial interface will also help with improved spin conductance. By using a combination of epitaxy, device geometry, thickness scaling, and alternative SOC metals, I believe nonlocal voltages of at least 100s of μV are obtainable.

6.3 Concluding Notes

This thesis presents a body of work dedicated to ferroic dynamics in BFO and related materials. I first interrogated fundamental limits on ferroelectric switching and the implications for multiferroic switching. To that end, I discussed both extrinsic and intrinsic limits, with the tuning of the free-energy double-well landscape being a recurring theme. By manipulating chemical composition, lattice dynamics and dipolar dynamics I observe changes in the switching process, both as driven by an externally applied field and by internal depolarization fields. I have addressed low energy dynamic excitations of magnetic order in BFO and shown how one can manipulate thermal magnons with an applied electric field and domain walls. The culmination of this work is a holistic picture of various types of ferroic order, their couplings and most importantly their (coupled) dynamics in the BFO system.

The work presented here comes at an exciting, though challenging time. From an applied viewpoint, the slowing of Moore's law, and the ever increasing demand for computing power in today's world, means that paradigmatic shifts in computing technology, such as using the collective nature of the ferroelectric order parameter for logic or memory, are required. Much of the work in this thesis is directly applicable to such efforts.

While future device applications provide important context and direction, I am personally more excited, not by the implications of my findings, but simply the findings themselves. The interplay between free- and bound-charge dynamics, and the model I created, for example, is an important step in understanding the fundamental limits on ferroelectric switching. It

is remarkable that humanity has known about ferroelectricity for so long, and that, while a ferroelectric is characterized by its ability to switch from one remnant state to another, we still have much to learn about the precise details of how that switching process occurs. I attempted to look at the problem holistically, and study both intrinsic and extrinsic factors impacting polarization switching (and depolarization), simply because it is an exciting and challenging problem to try to discover the minute details of the process. There is always more work to be done.

I believe magnonics (particularly in the BFO system) has the potential to revolutionize the future of computing. BFO is uniquely positioned to take a front seat in the field of magnonics owing to its unique capability to bridge charge-based devices and magnon-based devices through its intrinsic multiferroic nature. Further, non-local studies of spin transport in BFO can provide a means of answering unanswered (or un-asked) questions in BFO. For example, magnon studies can help us gain new understanding of coherent versus diffusive magnon transport, and, perhaps most interestingly, a holistic, 3-dimensional map of the magnon dispersion relation including $k \neq 0$ modes, and their spin polarization.

I hope you, whether you are a brand-new researcher or veteran, use this thesis, as well as the references and appendices that follow, as a reference for measurement techniques, analysis, and insight. I hope you challenge my results and help continue to expand upon the world's understanding of ferroic materials and their dynamics.

Bibliography

[1] M E Lines and A M Glass. "Principles and Applications of Ferroelectrics and Related Materials". In: (2001). DOI: 10.1093/acprof:oso/9780198507789.001.0001.

[2] Sasikanth Manipatruni, Dmitri E. Nikonov, and Ian A. Young. "Beyond CMOS computing with spin and polarization". In: *Nature Physics* 14.4 (2018), pp. 338–343. ISSN: 1745-2473. DOI: 10.1038/s41567-018-0101-4.

[3] Sasikanth Manipatruni et al. "Scalable energy-efficient magnetoelectric spin–orbit logic". In: *Nature* 565.7737 (2019), pp. 35–42. ISSN: 0028-0836. DOI: 10.1038/s41586-018-0770-2.

[4] Karin M. Rabe et al. "Modern Physics of Ferroelectrics: Essential Background". In: Berlin, Heidelberg: Springer Berlin Heidelberg, pp. 1–30. ISBN: 978-3-540-34591-6. DOI: 10.1007/978-3-540-34591-6_1. URL: https://doi.org/10.1007/978-3-540-34591-6%5C_1.

[5] N. A. Spaldin and R. Ramesh. "Advances in magnetoelectric multiferroics". In: *Nature Materials* 18.3 (2019), pp. 203–212. ISSN: 1476-1122. DOI: 10.1038/s41563-018-0275-2.

[6] R. Ramesh and Nicola A. Spaldin. "Multiferroics: progress and prospects in thin films". In: *Nature Materials* 6.1 (2007), pp. 21–29. ISSN: 1476-1122. DOI: 10.1038/nmat1805.

[7] Hans Schmid. "Multi-ferroic magnetoelectrics". In: *Ferroelectrics* 162.1 (1994), pp. 317–338. ISSN: 0015-0193. DOI: 10.1080/00150199408245120.

[8] Manfred Fiebig. "Revival of the magnetoelectric effect". In: *Journal of Physics D: Applied Physics* 38.8 (2005), R123. ISSN: 0022-3727. DOI: 10.1088/0022-3727/38/8/r01.

[9] J. T. Heron et al. "Deterministic switching of ferromagnetism at room temperature using an electric field". In: *Nature* 516.7531 (2014), pp. 370–373. ISSN: 0028-0836. DOI: 10.1038/nature14004.

[10] J. T. Heron et al. "Electric-Field-Induced Magnetization Reversal in a Ferromagnet-Multiferroic Heterostructure". In: *Physical Review Letters* 107.21 (2011), p. 217202. ISSN: 0031-9007. DOI: 10.1103/physrevlett.107.217202.

[11] S. W. Lovesey and G. van der Laan. "Resonant x-ray diffraction from chiral electric-polarization structures". In: *Physical Review B* 98.15 (2018), p. 155410. ISSN: 2469-9950. DOI: 10.1103/physrevb.98.155410. eprint: 1808.04204.

[12] J. M. Wesselinowa and St. Kovachev. "Hardening and softening of soft phonon modes in ferroelectric thin films". In: *Physical Review B* 75.4 (2007), p. 045411. ISSN: 1098-0121. DOI: 10.1103/physrevb.75.045411.

[13] R. Haumont et al. "Phonon anomalies and the ferroelectric phase transition in multiferroic BiFeO3". In: *Physical Review B* 73.13 (2006), p. 132101. ISSN: 1098-0121. DOI: 10.1103/physrevb.73.132101. eprint: cond-mat/0507291.

[14] Sverre M. Selbach et al. "The Ferroic Phase Transitions of BiFeO3". In: *Advanced Materials* 20.19 (2008), pp. 3692–3696. ISSN: 1521-4095. DOI: 10.1002/adma.200800218.

[15] F. Zavaliche et al. "Multiferroic BiFeO3 films: domain structure and polarization dynamics". In: *Phase Transitions* 79.12 (2006), pp. 991–1017. ISSN: 0141-1594. DOI: 10.1080/01411590601067144.

[16] Qiwu Shi et al. "The role of lattice dynamics in ferroelectric switching". In: *Nature Communications* 13.1 (2022), p. 1110. DOI: 10.1038/s41467-022-28622-z.

[17] Lev Landau. *Collected Papers of L.D. Landau*. Ed. by Dirk ter Haar. Pergamon Press Ltd., Gordon, and Breach, Science Publishers Inc., 1965. ISBN: 9781483152707.

[18] J M Ziman. *Electrons and Phonons*. 2001. ISBN: 9780198507796. DOI: 10.1093/acprof:oso/9780198507796.001.0001.

[19] Satadeep Bhattacharjee et al. "Ultrafast Switching of the Electric Polarization and Magnetic Chirality in BiFeO3 by an Electric Field". In: *Physical Review Letters* 112.14 (2014), p. 147601. ISSN: 0031-9007. DOI: 10.1103/physrevlett.112.147601. eprint: 1403.0671.

[20] Takeshi Nishimatsu et al. "Fast molecular-dynamics simulation for ferroelectric thin-film capacitors using a first-principles effective Hamiltonian". In: *Physical Review B* 78.10 (2008), p. 104104. ISSN: 1098-0121. DOI: 10.1103/physrevb.78.104104. eprint: 0804.1853.

[21] Fang-Yin Lin et al. "Strain effects on domain structures in ferroelectric thin films from phase-field simulations". In: *Journal of the American Ceramic Society* 101.10 (2018), pp. 4783–4790. ISSN: 0002-7820. DOI: 10.1111/jace.15705.

[22] Y.L. Li et al. "Effect of substrate constraint on the stability and evolution of ferroelectric domain structures in thin films". In: *Acta Materialia* 50.2 (2002), pp. 395–411. ISSN: 1359-6454. DOI: 10.1016/s1359-6454(01)00360-3.

[23] Sou-Chi Chang et al. "Physical Origin of Transient Negative Capacitance in a Ferroelectric Capacitor". In: *Physical Review Applied* 9.1 (2018), p. 014010. DOI: 10.1103/physrevapplied.9.014010. eprint: 1709.03255.

[24] Yoshihiro Ishibashi and Yutaka Takagi. "Note on Ferroelectric Domain Switching". In: *Journal of the Physical Society of Japan* 31.2 (1971), pp. 506–510. ISSN: 0031-9015. DOI: 10.1143/jpsj.31.506.

[25] Yoshihiro Ishibashi and Hiroshi Orihara. "A theory of D-E hysteresis loop". In: *Integrated Ferroelectrics* 9.1-3 (1995), pp. 57–61. ISSN: 1058-4587. DOI: 10.1080/10584589508012906.

[26] Eric Parsonnet et al. "Toward Intrinsic Ferroelectric Switching in Multiferroic $BiFeO_3$". In: *Physical Review Letters* 125.6 (2020), p. 067601. ISSN: 0031-9007. DOI: 10.1103/physrevlett.125.067601.

[27] I. Dzyaloshinsky. "A thermodynamic theory of "weak" ferromagnetism of antiferromagnetics". In: *Journal of Physics and Chemistry of Solids* 4.4 (1958), pp. 241–255. ISSN: 0022-3697. DOI: 10.1016/0022-3697(58)90076-3.

[28] Tôru Moriya. "Anisotropic Superexchange Interaction and Weak Ferromagnetism". In: *Physical Review* 120.1 (1960), pp. 91–98. DOI: 10.1103/physrev.120.91.

[29] M. A. Gilleo. "Superexchange Interaction Energy for Fe3+-O2–Fe3+ Linkages". In: *Physical Review* 109.3 (1958), pp. 777–781. ISSN: 0031-899X. DOI: 10.1103/physrev.109.777.

[30] I. A. Sergienko and E. Dagotto. "Role of the Dzyaloshinskii-Moriya interaction in multiferroic perovskites". In: *Physical Review B* 73.9 (2006), p. 094434. ISSN: 1098-0121. DOI: 10.1103/physrevb.73.094434. eprint: cond-mat/0508075.

[31] M. Lakshmanan. "The fascinating world of the LandauLifshitzGilbert equation: an overview". In: *Philosophical Transactions of the Royal Society A: Mathematical, Physical and Engineering Sciences* 369.1939 (2011), pp. 1280–1300. ISSN: 1364-503X. DOI: 10.1098/rsta.2010.0319. eprint: 1101.1005.

[32] Mark D. Stiles and Jacques Miltat. "Spin Dynamics in Confined Magnetic Structures III". In: *Topics in Applied Physics* (2006), pp. 225–308. DOI: 10.1007/10938171_7.

[33] Daniel C. Mattis. *The Theory of Magnetism I*. Ed. by Manuel Cardona et al. 1988. ISBN: 978-3-540-18425-6.

[34] F Keffer, H Kaplan, and Y Yafet. "Spin Waves in Ferromagnetic and Antiferromagnetic Materials". In: *American Journal of Physics* 21.4 (1953), pp. 250–257. ISSN: 0002-9505. DOI: 10.1119/1.1933416.

[35] Sergio M. Rezende, Antonio Azevedo, and Roberto L. Rodríguez-Suárez. "Introduction to antiferromagnetic magnons". In: *Journal of Applied Physics* 126.15 (2019), p. 151101. ISSN: 0021-8979. DOI: 10.1063/1.5109132.

[36] A. V. Chumak et al. "Magnon spintronics". In: *Nature Physics* 11.6 (2015), pp. 453–461. ISSN: 1745-2473. DOI: 10.1038/nphys3347.

[37] Dmitri E. Nikonov and Ian A. Young. "Benchmarking of Beyond-CMOS Exploratory Devices for Logic Integrated Circuits". In: *IEEE Journal on Exploratory Solid-State Computational Devices and Circuits* 1 (2015), pp. 3–11. DOI: 10.1109/jxcdc.2015.2418033.

[38] Claude Chappert, Albert Fert, and Frédéric Nguyen Van Dau. "The emergence of spin electronics in data storage". In: *Nature Materials* 6.11 (2007), pp. 813–823. ISSN: 1476-1122. DOI: 10.1038/nmat2024.

[39] Nicola A. Hill. "Why Are There so Few Magnetic Ferroelectrics?" In: *The Journal of Physical Chemistry B* 104.29 (2000), pp. 6694–6709. ISSN: 1520-6106. DOI: 10.1021/jp000114x.

[40] J. Wang et al. "Epitaxial BiFeO3 Multiferroic Thin Film Heterostructures". In: *Science* 299.5613 (2003), pp. 1719–1722. ISSN: 0036-8075. DOI: 10.1126/science.1080615.

[41] J. B. Neaton et al. "First-principles study of spontaneous polarization in multiferroic BiFeO3". In: *Physical Review B* 71.1 (2005), p. 014113. ISSN: 1098-0121. DOI: 10.1103/physrevb.71.014113. eprint: cond-mat/0407679.

[42] Claude Ederer and Nicola A. Spaldin. "Weak ferromagnetism and magnetoelectric coupling in bismuth ferrite". In: *Physical Review B* 71.6 (2005), p. 060401. ISSN: 1098-0121. DOI: 10.1103/physrevb.71.060401. eprint: cond-mat/0407003.

[43] Ram Seshadri and Nicola A. Hill. "Visualizing the Role of Bi 6s "Lone Pairs" in the Off-Center Distortion in Ferromagnetic BiMnO3". In: *Chemistry of Materials* 13.9 (2001), pp. 2892–2899. ISSN: 0897-4756. DOI: 10.1021/cm010090m.

[44] P. Ravindran et al. "Theoretical investigation of magnetoelectric behavior in BiFeO3". In: *Physical Review B* 74.22 (2006), p. 224412. ISSN: 1098-0121. DOI: 10.1103/physrevb.74.224412. eprint: 0705.0460.

[45] Lane Wyatt Martin. "Engineering Multiferroic Materials and New Functionalities in Materials". PhD thesis. 2008.

[46] L W Martin et al. "Multiferroics and magnetoelectrics: thin?films and nanostructures". In: *Journal of Physics: Condensed Matter* 20.43 (2008), p. 434220. ISSN: 0953-8984. DOI: 10.1088/0953-8984/20/43/434220.

[47] T. Zhao et al. "Electrical control of antiferromagnetic domains in multiferroic BiFeO3 films at room temperature". In: *Nature Materials* 5.10 (2006), pp. 823–829. ISSN: 1476-1122. DOI: 10.1038/nmat1731.

[48] Satoshi Kokado and Masakiyo Tsunoda. *Intuitive explanation of Anisotropic Magnetoresistance (AMR) effect and necessary condition for half-metallic ferromagnet "negative AMR"*. San Diego, California, United States, 2018. URL: https://doi.org/10.1117/12.2320021.

[49] G. Binasch et al. "Enhanced magnetoresistance in layered magnetic structures with antiferromagnetic interlayer exchange". In: *Physical Review B* 39.7 (1989), pp. 4828–4830. ISSN: 1098-0121. DOI: 10.1103/physrevb.39.4828.

[50] M N Baibich et al. "Giant Magnetoresistance of (001)Fe/(001)Cr Magnetic Superlattices". In: *Physical Review Letters* 61.21 (1988), pp. 2472–2475. ISSN: 0031-9007. DOI: 10.1103/physrevlett.61.2472.

[51] Bhagwati Prasad et al. "Ultralow Voltage Manipulation of Ferromagnetism". In: *Advanced Materials* 32.28 (2020), p. 2001943. ISSN: 0935-9648. DOI: 10.1002/adma.202001943.

[52] Yen-Lin Huang et al. "Manipulating magnetoelectric energy landscape in multiferroics". In: *Nature Communications* 11.1 (2020), p. 2836. DOI: 10.1038/s41467-020-16727-2.

[53] Walter J. Merz. "Domain formation and domain wall motions in ferroelectric BaTiO3 single crystals". In: *Physical Review* 95.3 (1954), pp. 690–698. ISSN: 0031899X. DOI: 10.1103/PhysRev.95.690.

[54] Shigeharu Hashimoto, Hiroshi Orihara, and Yoshihiro Ishibashi. "Study on D-E Hysteresis Loop of TGS Based on the Avrami-Type Model". In: *Journal of the Physical Society of Japan* 63.4 (1994), pp. 1601–1610. ISSN: 0031-9015. DOI: 10.1143/jpsj.63.1601.

[55] Young-Han Shin et al. "Nucleation and growth mechanism of ferroelectric domain-wall motion". In: *Nature* 449.7164 (2007), pp. 881–884. ISSN: 0028-0836. DOI: 10.1038/nature06165.

[56] B. Meyer and David Vanderbilt. "Ab initio study of ferroelectric domain walls in PbTiO3". In: *Physical Review B* 65.10 (2002), p. 104111. ISSN: 1098-0121. DOI: 10.1103/physrevb.65.104111. eprint: cond-mat/0109257.

[57] Pesquera D et al. "Elastic anomalies associated with domain switching in BaTiO3 single crystals under in situ electrical cycling". In: *APL Materials* 7.5 (2019), p. 051109. DOI: 10.1063/1.5088749.

[58] J. Li et al. "Ultrafast polarization switching in thin-film ferroelectrics". In: *Applied Physics Letters* 84.7 (2004), pp. 1174–1176. ISSN: 0003-6951. DOI: 10.1063/1.1644917.

[59] Alexei Grigoriev, Mandana Meisami Azad, and John McCampbell. "Ultrafast electrical measurements of polarization dynamics in ferroelectric thin-film capacitors". In: *Review of Scientific Instruments* 82.12 (2011). ISSN: 00346748.

[60] P. K. Larsen et al. "Nanosecond switching of thin ferroelectric films". In: *Applied Physics Letters* 59.5 (1991), pp. 611–613. DOI: 10.1063/1.105402.

[61] Mengwei Si et al. "Ultrafast measurements of polarization switching dynamics on ferroelectric and anti-ferroelectric hafnium zirconium oxide". In: *Applied Physics Letters* 115.7 (2019), p. 072107. DOI: 10.1063/1.5098786.

[62] E. Miranda et al. "Modeling of hysteretic Schottky diode-like conduction in Pt / $BiFeO_3$ / $SrRuO_3$ switches". In: *Appl. Phys. Lett.* 105.8 (2014), p. 082904. DOI: 10.1063/1.4894116.

[63] Gary W. Pabst et al. "Leakage mechanisms in BiFeO3 thin films". In: *Applied Physics Letters* 90.7 (2007), p. 072902. DOI: 10.1063/1.2535663.

[64] S. Y. Yang et al. "Photovoltaic effects in BiFeO3". In: *Applied Physics Letters* 95.6 (2009), p. 062909. DOI: 10.1063/1.3204695.

[65] Sahwan Hong et al. "Large Resistive Switching in Ferroelectric BiFeO3 Nano-Island Based Switchable Diodes". In: *Advanced Materials* 25.16 (2013), pp. 2339–2343. DOI: 10.1002/adma.201204839.

[66] Dongxia Chen, Aidong Li, and Di Wu. "Resistive switching in BiFeO3-based heterostructures due to ferroelectric modulation on interface Schottky barriers". In: *Journal of Materials Science: Materials in Electronics* 25.8 (2014), pp. 3251–3256. ISSN: 0957-4522. DOI: 10.1007/s10854-014-2010-3.

[67] M. Trassin et al. "Interfacial coupling in multiferroic/ferromagnet heterostructures". In: *Phys. Rev. B* 87 (13 Apr. 2013), p. 134426. DOI: 10.1103/PhysRevB.87.134426. URL: https://link.aps.org/doi/10.1103/PhysRevB.87.134426.

[68] Vishal Boddu, Florian Endres, and Paul Steinmann. "Molecular dynamics study of ferroelectric domain nucleation and domain switching dynamics". In: *Scientific Reports* 7.1 (Apr. 2017), p. 806. ISSN: 2045-2322. DOI: 10.1038/s41598-017-01002-0. URL: https://doi.org/10.1038/s41598-017-01002-0.

[69] Walter J Merz. "Switching Time in Ferroelectric BaTiO 3 and Its Dependence on Crystal Thickness". In: *Journal of Applied Physics* 27.8 (1956), pp. 938–943. ISSN: 0021-8979. DOI: 10.1063/1.1722518.

[70] G. Vizdrik et al. "Kinetics of ferroelectric switching in ultrathin films". In: *Phys. Rev. B* 68 (9 Sept. 2003), p. 094113. DOI: 10.1103/PhysRevB.68.094113. URL: https://link.aps.org/doi/10.1103/PhysRevB.68.094113.

[71] J. Y. Jo et al. "Domain Switching Kinetics in Disordered Ferroelectric Thin Films". In: *Phys. Rev. Lett.* 99 (26 Dec. 2007), p. 267602. DOI: 10.1103/PhysRevLett.99.267602. URL: https://link.aps.org/doi/10.1103/PhysRevLett.99.267602.

[72] R. Gaynutdinov et al. "Polarization switching kinetics in ultrathin ferroelectric barium titanate film". In: *Physica B: Condensed Matter* 424 (2013), pp. 8–12. ISSN: 0921-4526. DOI: https://doi.org/10.1016/j.physb.2013.04.056. URL: http://www.sciencedirect.com/science/article/pii/S0921452613002901.

[73] J. Y. Jo et al. "Polarization Switching Dynamics Governed by the Thermodynamic Nucleation Process in Ultrathin Ferroelectric Films". In: *Phys. Rev. Lett.* 97 (24 Dec. 2006), p. 247602. DOI: 10.1103/PhysRevLett.97.247602. URL: https://link.aps.org/doi/10.1103/PhysRevLett.97.247602.

[74] Hyejung Chang et al. "Watching domains grow: In-situ studies of polarization switching by combined scanning probe and scanning transmission electron microscopy". In: *Journal of Applied Physics* 110.5 (2011), p. 052014. DOI: 10.1063/1.3623779.

[75] C. Alessandri et al. "Switching Dynamics of Ferroelectric Zr-Doped HfO2". In: *IEEE Electron Device Letters* 39.11 (2018), pp. 1780–1783.

[76] Lei Zhang et al. "Enhanced pyroelectric properties of $Bi_{1-x}La_xFeO_3$ thin films". In: *APL Materials* 7.11 (2019), p. 111111. DOI: 10.1063/1.5128413.

[77] Jinjin Li. "Studies of Ultrafast processes in thin film high temperature superconductor and ferroelectric material". PhD thesis. University of Maryland at College Park, 2004.

[78] Can Wang et al. "Switchable diode effect and ferroelectric resistive switching in epitaxial BiFeO3 thin films". In: *Appl. Phys. Lett.* 98.19 (2011), p. 192901. DOI: 10.1063/1.3589814.

[79] Adenilson J Chiquito et al. "Back-to-back Schottky diodes: the generalization of the diode theory in analysis and extraction of electrical parameters of nanodevices". In: *Journal of Physics: Condensed Matter* 24.22 (May 2012), p. 225303. DOI: 10.1088/0953-8984/24/22/225303.

[80] Jozef Osvald. "Back-to-back connected asymmetric Schottky diodes with series resistance as a single diode". In: *physica status solidi (a)* 212.12 (2015), pp. 2754–2758. DOI: 10.1002/pssa.201532374.

[81] Ryo Nouchi. "Extraction of the Schottky parameters in metal-semiconductor-metal diodes from a single current-voltage measurement". In: *J. Appl. Phys.* 116.18 (2014), p. 184505. DOI: 10.1063/1.4901467.

[82] AN Kolmogorov. "On the Statistical Theory of Metal Crystallization". In: *Izv. Akad. Nauk SSSR, Ser. Math* 1 (1937), pp. 335–360.

[83] Melvin Avrami. "Kinetics of phase change. II Transformation-time relations for random distribution of nuclei". In: *The Journal of Chemical Physics* 8.2 (1940), pp. 212–224. ISSN: 00219606. DOI: 10.1063/1.1750631.

[84] T. K. Song et al. "Activation field of ferroelectric (Pb,La)(Zr,Ti)O3 thin film capacitors". In: *Appl. Phys. Lett.* 71.15 (1997), pp. 2211–2213. DOI: 10.1063/1.119383.

[85] Asif Islam Khan et al. "Negative capacitance in a ferroelectric capacitor". In: *Nature Materials* 14.2 (Feb. 2015), pp. 182–186. ISSN: 1476-4660. DOI: 10.1038/nmat4148. URL: https://doi.org/10.1038/nmat4148.

[86] Yu Jin Kim et al. "Voltage Drop in a Ferroelectric Single Layer Capacitor by Retarded Domain Nucleation". In: *Nano Letters* 17.12 (Dec. 2017), pp. 7796–7802. ISSN: 1530-6984. DOI: 10.1021/acs.nanolett.7b04008. URL: https://doi.org/10.1021/acs.nanolett.7b04008.

[87] S. Smith, K. Chatterjee, and S. Salahuddin. "Multidomain Phase-Field Modeling of Negative Capacitance Switching Transients". In: *IEEE Transactions on Electron Devices* 65.1 (2018), pp. 295–298.

[88] K. J. Choi et al. "Enhancement of Ferroelectricity in Strained BaTiO3 Thin Films". In: *Science* 306.5698 (2004), pp. 1005–1009. ISSN: 0036-8075. DOI: 10.1126/science.1103218.

[89] Takaaki Yasumoto et al. "Epitaxial Growth of BaTiO3 Thin Films by High Gas Pressure Sputtering". In: *Japanese Journal of Applied Physics* 39.9S (2014), p. 5369. ISSN: 1347-4065. DOI: 10.1143/jjap.39.5369.

[90] Anoop R. Damodaran et al. "Enhancement of Ferroelectric Curie Temperature in BaTiO3 Films via Strain-Induced Defect Dipole Alignment". In: *Advanced Materials* 26.36 (2014), pp. 6341–6347. ISSN: 1521-4095. DOI: 10.1002/adma.201400254.

[91] Wei Peng et al. "Constructing Polymorphic Nanodomains in BaTiO3 Films via Epitaxial Symmetry Engineering". In: *Advanced Functional Materials* 30.16 (2020). ISSN: 1616-301X. DOI: 10.1002/adfm.201910569.

[92] Catherine Dubourdieu et al. "Switching of ferroelectric polarization in epitaxial BaTiO3 films on silicon without a conducting bottom electrode". In: *Nature Nanotechnology* 8.10 (2013), pp. 748–754. ISSN: 1748-3387. DOI: 10.1038/nnano.2013.192.

[93] Aidong Li et al. "Fabrication and electrical properties of sol-gel derived BaTiO3 films with metallic LaNiO3 electrode". In: *Applied Physics Letters* 70.12 (1997), pp. 1616–1618. ISSN: 0003-6951. DOI: 10.1063/1.118633.

[94] E. J. H. Lee et al. "Preparation and properties of ferroelectric BaTiO3 thin films produced by the polymeric precursor method". In: *Journal of Materials Science Letters* 19.16 (2000), pp. 1457–1459. ISSN: 0261-8028. DOI: 10.1023/a:1011027624446.

[95] Zhi Zhou et al. "Hydrothermal growth of highly textured BaTiO3 films composed of nanowires". In: *Nanotechnology* 24.9 (2013), p. 095602. ISSN: 0957-4484. DOI: 10.1088/0957-4484/24/9/095602.

[96] K Iijima et al. "Preparation of ferroelectric BaTiO 3 thin films by activated reactive evaporation". In: *Applied Physics Letters* 56.6 (1990), pp. 527–529. ISSN: 0003-6951. DOI: 10.1063/1.103300.

[97] Hanfei Zhu et al. "Increasing energy storage capabilities of space-charge dominated ferroelectric thin films using interlayer coupling". In: *Acta Materialia* 122 (2017), pp. 252–258. ISSN: 1359-6454. DOI: 10.1016/j.actamat.2016.09.051.

[98] Bikram Bhatia et al. "High Power Density Pyroelectric Energy Conversion in Nanometer - Thick BaTiO3 Films". In: *Nanoscale and Microscale Thermophysical Engineering* 20.3-4 (2016), pp. 137–146. ISSN: 1556-7265. DOI: 10.1080/15567265.2016.1252820.

[99] Yizhe Jiang et al. "Enabling ultralow voltage switching in $BaTiO_3$". In: *Nature Materials* (2022).

[100] Zibin Chen et al. "Giant tuning of ferroelectricity in single crystals by thickness engineering". In: *Science Advances* 6.42 (2020). DOI: 10.1126/sciadv.abc7156.

[101] Zibin Chen et al. "Facilitation of Ferroelectric Switching via Mechanical Manipulation of Hierarchical Nanoscale Domain Structures". In: *Physical Review Letters* 118.1 (2017), p. 017601. ISSN: 0031-9007. DOI: 10.1103/physrevlett.118.017601.

[102] R. Xu et al. "Kinetic control of tunable multi-state switching in ferroelectric thin films". In: *Nature Communications* 10.1 (2019), p. 1282. DOI: 10.1038/s41467-019-09207-9.

[103] Ruijuan Xu et al. "Ferroelectric polarization reversal via successive ferroelastic transitions". In: *Nature Materials* 14.1 (2015), pp. 79–86. ISSN: 1476-1122. DOI: 10.1038/nmat4119.

[104] Jason M. Munro et al. "Discovering minimum energy pathways via distortion symmetry groups". In: *Physical Review B* 98.8 (2018), p. 085107. ISSN: 2469-9950. DOI: 10.1103/physrevb.98.085107. eprint: 1804.06798.

[105] Igor A. Kornev et al. "Finite-Temperature Properties of Multiferroic BiFeO3". In: *Physical Review Letters* 99.22 (2007), p. 227602. ISSN: 0031-9007. DOI: 10.1103/physrevlett.99.227602.

[106] P. Marton et al. "First-principles-based Landau-Devonshire potential for BiFeO3". In: *Physical Review B* 96.17 (2017), p. 174110. ISSN: 2469-9950. DOI: 10.1103/physrevb.96.174110. eprint: 1705.08235.

[107] D. Pesquera et al. "Large magnetoelectric coupling in multiferroic oxide heterostructures assembled via epitaxial lift-off". In: *Nature Communications* 11.1 (2020). DOI: 10.1038/s41467-020-16942-x. eprint: 2006.00034.

[108] G W Burr et al. "Overview of candidate device technologies for storage-class memory". In: *IBM Journal of Research and Development* 52.4.5 (2008), pp. 449–464. ISSN: 0018-8646. DOI: 10.1147/rd.524.0449.

[109] Dianxiang Ji et al. "Freestanding crystalline oxide perovskites down to the monolayer limit". In: *Nature* 570.7759 (2019), pp. 87–90. ISSN: 0028-0836. DOI: 10.1038/s41586-019-1255-7.

[110] W. L. Zhong et al. "Phenomenological study of the size effect on phase transitions in ferroelectric particles". In: *Physical Review B* 50.2 (1994), pp. 698–703. ISSN: 1098-0121. DOI: 10.1103/physrevb.50.698.

[111] N. A. Pertsev, A. G. Zembilgotov, and A. K. Tagantsev. "Effect of Mechanical Boundary Conditions on Phase Diagrams of Epitaxial Ferroelectric Thin Films". In: *Physical Review Letters* 80.9 (1998), pp. 1988–1991. ISSN: 0031-9007. DOI: 10.1103/physrevlett.80.1988.

[112] Fei Xue et al. "Orientations of low-energy domain walls in perovskites with oxygen octahedral tilts". In: *Physical Review B* 90.22 (2014), p. 220101. ISSN: 1098-0121. DOI: 10.1103/physrevb.90.220101.

[113] J. X. Zhang et al. "Microscopic Origin of the Giant Ferroelectric Polarization in Tetragonal-like BiFeO3". In: *Physical Review Letters* 107.14 (2011), p. 147602. ISSN: 0031-9007. DOI: 10.1103/physrevlett.107.147602.

[114] Alexander Umantsev. *Field Theoretic Method in Phase Transformations*. New York: Springer-Verlag, 2012. DOI: 10.1007/978-1-4614-1487-2.

[115] Saidur R. Bakaul et al. "Ferroelectric Domain Wall Motion in Freestanding Single-Crystal Complex Oxide Thin Film". In: *Advanced Materials* 32.4 (2019), p. 1907036. ISSN: 0935-9648. DOI: 10.1002/adma.201907036.

[116] Di Lu et al. "Synthesis of freestanding single-crystal perovskite films and heterostructures by etching of sacrificial water-soluble layers". In: *Nature Materials* 15.12 (2016), pp. 1255–1260. ISSN: 1476-1122. DOI: 10.1038/nmat4749.

[117] Seung Sae Hong et al. "Two-dimensional limit of crystalline order in perovskite membrane films". In: *Science Advances* 3.11 (2017), eaao5173. DOI: 10.1126/sciadv.aao5173.

[118] Hyun S. Kum et al. "Heterogeneous integration of single-crystalline complex-oxide membranes". In: *Nature* 578.7793 (2020), pp. 75–81. ISSN: 0028-0836. DOI: 10.1038/s41586-020-1939-z.

[119] Rui Guo et al. "Continuously controllable photoconductance in freestanding BiFeO3 by the macroscopic flexoelectric effect". In: *Nature Communications* 11.1 (2020), p. 2571. DOI: 10.1038/s41467-020-16465-5.

[120] V. Nagarajan et al. "Dynamics of ferroelastic domains in ferroelectric thin films". In: *Nature Materials* 2.1 (2003), pp. 43–47. ISSN: 1476-1122. DOI: 10.1038/nmat800.

[121] Ren-Ci Peng et al. "Understanding and predicting geometrical constraint ferroelectric charged domain walls in a BiFeO3 island via phase-field simulations". In: *Applied Physics Letters* 113.22 (2018), p. 222902. ISSN: 0003-6951. DOI: 10.1063/1.5050802.

[122] Y. L. Li et al. "Effect of electrical boundary conditions on ferroelectric domain structures in thin films". In: *Applied Physics Letters* 81.3 (2002), pp. 427–429. ISSN: 0003-6951. DOI: 10.1063/1.1492025.

[123] Shinji Nambu and Djuniadi A. Sagala. "Domain formation and elastic long-range interaction in ferroelectric perovskites". In: *Physical Review B* 50.9 (1994), pp. 5838–5847. ISSN: 1098-0121. DOI: 10.1103/physrevb.50.5838.

[124] Hong-Liang Hu and Long-Qing Chen. "Three-Dimensional Computer Simulation of Ferroelectric Domain Formation". In: *Journal of the American Ceramic Society* 81.3 (1998), pp. 492–500. ISSN: 1551-2916. DOI: 10.1111/j.1151-2916.1998.tb02367.x.

[125] Charles Kittel. "Theory of the Structure of Ferromagnetic Domains in Films and Small Particles". In: *Physical Review* 70.11-12 (1946), pp. 965–971. ISSN: 0031-899X. DOI: 10.1103/physrev.70.965.

[126] Dong Su et al. "Origin of 90° domain wall pinning in Pb(Zr0.2Ti0.8)O3 heteroepitaxial thin films". In: *Applied Physics Letters* 99.10 (2011), p. 102902. ISSN: 0003-6951. DOI: 10.1063/1.3634028.

[127] James F. Scott and Carlos A. Paz de Araujo. "Ferroelectric Memories". In: *Science* 246.4936 (1989), pp. 1400–1405. ISSN: 0036-8075. DOI: 10.1126/science.246.4936.1400.

[128] André Chanthbouala et al. "Solid-state memories based on ferroelectric tunnel junctions". In: *Nature Nanotechnology* 7.2 (2012), pp. 101–104. ISSN: 1748-3387. DOI: 10.1038/nnano.2011.213.

[129] Jiankun Li et al. "Reproducible Ultrathin Ferroelectric Domain Switching for High-Performance Neuromorphic Computing". In: *Advanced Materials* 32.7 (2020). ISSN: 0935-9648. DOI: 10.1002/adma.201905764.

[130] S. M. Yang et al. "ac dynamics of ferroelectric domains from an investigation of the frequency dependence of hysteresis loops". In: *Physical Review B* 82.17 (2010), p. 174125. ISSN: 1098-0121. DOI: 10.1103/physrevb.82.174125. eprint: 1001.5195.

[131] Y. J. Shin et al. "Suppression of creep-regime dynamics in epitaxial ferroelectric BiFeO3 films". In: *Scientific Reports* 5.1 (2015), p. 10485. DOI: 10.1038/srep10485.

[132] Van Tuong Pham et al. "Spin–orbit magnetic state readout in scaled ferromagnetic/heavy metal nanostructures". In: *Nature Electronics* 3.6 (2020), pp. 309–315. DOI: 10.1038/s41928-020-0395-y. eprint: 2002.10581.

[133] Yu-Ching Liao et al. "Understanding the Switching Mechanisms of the Antiferromagnet/Ferromagnet Heterojunction". In: *Nano Letters* 20.11 (2020), pp. 7919–7926. ISSN: 1530-6984. DOI: 10.1021/acs.nanolett.0c01852.

[134] Asif Islam Khan, Ali Keshavarzi, and Suman Datta. "The future of ferroelectric field-effect transistor technology". In: *Nature Electronics* 3.10 (2020), pp. 588–597. DOI: 10.1038/s41928-020-00492-7.

[135] H. Lu et al. "Enhancement of Ferroelectric Polarization Stability by Interface Engineering". In: *Advanced Materials* 24.9 (2012), pp. 1209–1216. ISSN: 1521-4095. DOI: 10.1002/adma.201104398.

[136] James J. Steffes et al. "Thickness scaling of ferroelectricity in BiFeO3 by tomographic atomic force microscopy". In: *Proceedings of the National Academy of Sciences of the United States of America* 116.7 (2019), pp. 2413–2418. ISSN: 0027-8424. DOI: 10.1073/pnas.1806074116.

[137] V. I. Yukalov and E. P. Yukalova. "Ultrafast polarization switching in ferroelectrics". In: *Physical Review Research* 1.3 (2019), p. 033136. DOI: 10.1103/physrevresearch.1.033136.

[138] Javier Junquera and Philippe Ghosez. "Critical thickness for ferroelectricity in perovskite ultrathin films". In: *Nature* 422.6931 (2003), pp. 506–509. ISSN: 0028-0836. DOI: 10.1038/nature01501.

[139] Suraj S. Cheema et al. "Enhanced ferroelectricity in ultrathin films grown directly on silicon". In: *Nature* 580.7804 (2020), pp. 478–482. ISSN: 0028-0836. DOI: 10.1038/s41586-020-2208-x.

[140] D. J. Kim et al. "Polarization Relaxation Induced by a Depolarization Field in Ultrathin Ferroelectric BaTiO3 Capacitors". In: *Physical Review Letters* 95.23 (2005), p. 237602. ISSN: 0031-9007. DOI: 10.1103/physrevlett.95.237602. eprint: cond-mat/0506480.

[141] R R Mehta, B D Silverman, and J T Jacobs. "Depolarization fields in thin ferroelectric films". In: *Journal of Applied Physics* 44.8 (1973), pp. 3379–3385. ISSN: 0021-8979. DOI: 10.1063/1.1662770.

[142] J. J. Wang et al. "Temperature-pressure phase diagram and ferroelectric properties of BaTiO3 single crystal based on a modified Landau potential". In: *Journal of Applied Physics* 108.11 (2010), p. 114105. ISSN: 0021-8979. DOI: 10.1063/1.3504194.

[143] Y. L. Li, L. E. Cross, and L. Q. Chen. "A phenomenological thermodynamic potential for BaTiO3 single crystals". In: *Journal of Applied Physics* 98.6 (2005), p. 064101. ISSN: 0021-8979. DOI: 10.1063/1.2042528.

[144] P. Wurfel and I. P. Batra. "Depolarization effects in thin ferroelectric films". In: *Ferroelectrics* 12.1 (1976), pp. 55–61. ISSN: 0015-0193. DOI: 10.1080/00150197608241393.

[145] Dong Zhao et al. "Depolarization of multidomain ferroelectric materials". In: *Nature Communications* 10.1 (2019), p. 2547. DOI: 10.1038/s41467-019-10530-4.

[146] A. Gruverman et al. "Direct studies of domain switching dynamics in thin film ferroelectric capacitors". In: *Applied Physics Letters* 87.8 (2005), p. 082902. ISSN: 0003-6951. DOI: 10.1063/1.2010605.

[147] Alexander K. Tagantsev et al. "Non-Kolmogorov-Avrami switching kinetics in ferroelectric thin films". In: *Physical Review B* 66.21 (2002), p. 214109. ISSN: 1098-0121. DOI: 10.1103/physrevb.66.214109.

[148] Biao Wang and C. H. Woo. "Curie temperature and critical thickness of ferroelectric thin films". In: *Journal of Applied Physics* 97.8 (2005), p. 084109. ISSN: 0021-8979. DOI: 10.1063/1.1861517.

[149] Emad Almahmoud, Igor Kornev, and L. Bellaiche. "Dependence of Curie temperature on the thickness of an ultrathin ferroelectric film". In: *Physical Review B* 81.6 (2010), p. 064105. ISSN: 1098-0121. DOI: 10.1103/physrevb.81.064105.

[150] T K Song et al. "Activation field of ferroelectric (Pb,La)(Zr,Ti)O3 thin film capacitors". In: *Applied Physics Letters* 71.15 (1997), pp. 2211–2213. ISSN: 0003-6951. DOI: 10.1063/1.119383.

[151] Hiroyuki Takenaka et al. "Slush-like polar structures in single-crystal relaxors". In: *Nature* 546.7658 (2017), pp. 391–395. ISSN: 0028-0836. DOI: 10.1038/nature22068.

[152] George A Samara. "The relaxational properties of compositionally disordered ABO3 perovskites". In: *Journal of Physics: Condensed Matter* 15.9 (2003), R367. ISSN: 0953-8984. DOI: 10.1088/0953-8984/15/9/202.

[153] L. Eric Cross. "Relaxor ferroelectrics". In: *Ferroelectrics* 76.1 (1987), pp. 241–267. ISSN: 0015-0193. DOI: 10.1080/00150198708016945.

[154] Jieun Kim et al. "Ultrahigh capacitive energy density in ion-bombarded relaxor ferroelectric films". In: *Science* 369.6499 (2020), pp. 81–84. ISSN: 0036-8075. DOI: 10.1126/science.abb0631.

[155] Rahul Sahay et al. "Noise Electrometry of Polar and Dielectric Materials". In: *arXiv* (2021). eprint: 2111.09315.

[156] Kerem Y. Camsari, Brian M. Sutton, and Supriyo Datta. "p-bits for probabilistic spin logic". In: *Applied Physics Reviews* 6.1 (2019), p. 011305. DOI: 10.1063/1.5055860. eprint: 1809.04028.

[157] William A. Borders et al. "Integer factorization using stochastic magnetic tunnel junctions". In: *Nature* 573.7774 (2019), pp. 390–393. ISSN: 0028-0836. DOI: 10.1038/s41586-019-1557-9.

[158] Jan Kaiser and Supriyo Datta. "Probabilistic computing with p-bits". In: *Applied Physics Letters* 119.15 (2021), p. 150503. ISSN: 0003-6951. DOI: 10.1063/5.0067927. eprint: 2108.09836.

[159] Sahar Saremi et al. "Enhanced Electrical Resistivity and Properties via Ion Bombardment of Ferroelectric Thin Films". In: *Advanced Materials* 28.48 (2016), pp. 10750–10756. ISSN: 1521-4095. DOI: 10.1002/adma.201603968.

[160] Anjan Barman et al. "The 2021 Magnonics Roadmap". In: *Journal of Physics: Condensed Matter* 33.41 (2021), p. 413001. ISSN: 0953-8984. DOI: 10.1088/1361-648x/abec1a.

[161] Sergio M. Rezende. "Fundamentals of Magnonics". In: *Lecture Notes in Physics* (2020). ISSN: 0075-8450. DOI: 10.1007/978-3-030-41317-0.

[162] Sergej and Andrei N. Slavin. *Magnonics, From Fundamentals to Applications*. Topics in Applied Physics. 2013. ISBN: 978-3-642-30246-6. DOI: 10.1007/978-3-642-30247-3.

[163] Robin R. Jones et al. "Raman Techniques: Fundamentals and Frontiers". In: *Nanoscale Research Letters* 14.1 (2019), p. 231. ISSN: 1931-7573. DOI: 10.1186/s11671-019-3039-2.

[164] T.P. Martin et al. "Resonant two magnon Raman scattering in α-Fe_2O_3". In: *Solid State Communications* 22.9 (1977), pp. 565–567. ISSN: 0038-1098. DOI: 10.1016/0038-1098(77)90137-5.

[165] R. E. Dietz, G. I. Parisot, and A. E. Meixner. "Infrared Absorption and Raman Scattering by Two-Magnon Processes in NiO". In: *Physical Review B* 4.7 (1971), pp. 2302–2310. ISSN: 1098-0121. DOI: 10.1103/physrevb.4.2302.

[166] Manoj K Singh, Ram S Katiyar, and J F Scott. "New magnetic phase transitions in BiFeO3". In: *Journal of Physics: Condensed Matter* 20.25 (2008), p. 252203. ISSN: 0953-8984. DOI: 10.1088/0953-8984/20/25/252203.

[167] B.K. Das et al. "Emergence of two-magnon modes below spin-reorientation transition and phonon-magnon coupling in bulk BiFeO3: An infrared spectroscopic study". In: *Journal of Alloys and Compounds* 832 (2020), p. 154754. ISSN: 0925-8388. DOI: 10.1016/j.jallcom.2020.154754.

[168] G. Khabiri et al. "Phonon and magnon excitations in Raman spectra of an epitaxial bismuth ferrite film". In: *Physics of the Solid State* 56.12 (2014), pp. 2507–2513. ISSN: 1063-7834. DOI: 10.1134/s1063783414120154.

[169] P. Rovillain et al. "Electric-field control of spin waves at room temperature in multiferroic BiFeO3". In: *Nature Materials* 9.12 (2010), pp. 975–979. ISSN: 1476-1122. DOI: 10.1038/nmat2899. eprint: 1010.2678.

[170] Rogerio de Sousa and Joel E. Moore. "Electrical control of magnon propagation in multiferroic BiFeO3 films". In: *Applied Physics Letters* 92.2 (2008), p. 022514. ISSN: 0003-6951. DOI: 10.1063/1.2835704. eprint: 0801.3012.

[171] M Cazayous et al. "Possible Observation of Cycloidal Electromagnons in BiFeO3". In: *Physical Review Letters* 101.3 (2008), p. 037601. ISSN: 0031-9007. DOI: 10.1103/physrevlett.101.037601. eprint: 0712.3044.

[172] M. Cazayous et al. "Possible interplay between a two phonon mode and high energy magnetic excitations in BiFeO3". In: *The European Physical Journal B* 67.2 (2009), pp. 209–212. ISSN: 1434-6028. DOI: 10.1140/epjb/e2009-00033-7. eprint: 0803.3015.

[173] Ashok Kumar, J. F. Scott, and R. S. Katiyar. "Electric control of magnon frequencies and magnetic moment of bismuth ferrite thin films at room temperature". In: *Applied Physics Letters* 99.6 (2011), p. 062504. ISSN: 0003-6951. DOI: 10.1063/1.3624845.

[174] J. H. Van Vleck. "Concerning the Theory of Ferromagnetic Resonance Absorption". In: *Physical Review* 78.3 (1950), pp. 266–274. ISSN: 0031-899X. DOI: 10.1103/physrev.78.266.

[175] F. Keffer and C. Kittel. "Theory of Antiferromagnetic Resonance". In: *Physical Review* 85.2 (1951), pp. 329–337. ISSN: 0031-899X. DOI: 10.1103/physrev.85.329.

[176] C. Kittel. "Theory of Antiferromagnetic Resonance". In: *Physical Review* 82.4 (1951), pp. 565–565. ISSN: 0031-899X. DOI: 10.1103/physrev.82.565.

[177] S.D. Bader and S.S.P. Parkin. "Spintronics". In: *Annual Review of Condensed Matter Physics* 1.1 (2010), pp. 71–88. ISSN: 1947-5454. DOI: 10.1146/annurev-conmatphys-070909-104123.

[178] Vinod Kumar Joshi. "Spintronics: A contemporary review of emerging electronics devices". In: *Engineering Science and Technology, an International Journal* 19.3 (2016), pp. 1503–1513. ISSN: 2215-0986. DOI: 10.1016/j.jestch.2016.05.002.

[179] Atsufumi Hirohata et al. "Review on spintronics: Principles and device applications". In: *Journal of Magnetism and Magnetic Materials* 509 (2020), p. 166711. ISSN: 0304-8853. DOI: 10.1016/j.jmmm.2020.166711.

[180] Satoshi Iihama et al. "Spin-transfer torque induced by the spin anomalous Hall effect". In: *Nature Electronics* 1.2 (2018), pp. 120–123. DOI: 10.1038/s41928-018-0026-z.

[181] A. Kumar et al. "Spin transfer torque ferromagnetic resonance induced spin pumping in the Fe/Pd bilayer system". In: *Physical Review B* 95.6 (2017), p. 064406. ISSN: 2469-9950. DOI: 10.1103/physrevb.95.064406.

[182] Yi Wang, Rajagopalan Ramaswamy, and Hyunsoo Yang. "FMR-related phenomena in spintronic devices". In: *Journal of Physics D: Applied Physics* 51.27 (2018), p. 273002. ISSN: 0022-3727. DOI: 10.1088/1361-6463/aac7b5. eprint: 1805.08496.

[183] Jairo Sinova et al. "Spin Hall effects". In: *Reviews of Modern Physics* 87.4 (2015), pp. 1213–1260. ISSN: 0034-6861. DOI: 10.1103/revmodphys.87.1213.

[184] Tomas Jungwirth, Jörg Wunderlich, and Kamil Olejník. "Spin Hall effect devices". In: *Nature Materials* 11.5 (2012), pp. 382–390. ISSN: 1476-1122. DOI: 10.1038/nmat3279.

[185] R. Lebrun et al. "Tunable long-distance spin transport in a crystalline antiferromagnetic iron oxide". In: *Nature* 561.7722 (2018), pp. 222–225. ISSN: 14764687. DOI: 10.1038/s41586-018-0490-7. eprint: 1805.02451.

[186] Abdulqader Mahmoud et al. "Introduction to spin wave computing". In: *Journal of Applied Physics* 128.16 (2020), p. 161101. ISSN: 0021-8979. DOI: 10.1063/5.0019328. eprint: 2006.12905.

[187] Alexander Khitun, Mingqiang Bao, and Kang L Wang. "Magnonic logic circuits". In: *Journal of Physics D: Applied Physics* 43.26 (2010), p. 264005. ISSN: 0022-3727. DOI: 10.1088/0022-3727/43/26/264005.

[188] György Csaba, Ádám Papp, and Wolfgang Porod. "Perspectives of using spin waves for computing and signal processing". In: *Physics Letters A* 381.17 (2017), pp. 1471–1476. ISSN: 0375-9601. DOI: 10.1016/j.physleta.2017.02.042.

[189] Andrii V. Chumak, Alexander A. Serga, and Burkard Hillebrands. "Magnon transistor for all-magnon data processing". In: *Nature Communications* 5.May 2013 (2014), pp. 1–8. DOI: 10.1038/ncomms5700.

[190] Jin Lan et al. "Spin-Wave Diode". In: *Physical Review X* 5.4 (2015), p. 041049. DOI: 10.1103/physrevx.5.041049.

[191] Ran Cheng et al. "Antiferromagnetic spin wave field-effect transistor". In: *Scientific Reports* 6.April (2016), pp. 2–7. ISSN: 20452322. DOI: 10.1038/srep24223. eprint: 1509.05295.

[192] L. J. Cornelissen et al. "Long-distance transport of magnon spin information in a magnetic insulator at room temperature". In: *Nature Physics* 11.12 (2015), pp. 1022–1026. ISSN: 17452481. DOI: 10.1038/nphys3465. eprint: 1505.06325.

[193] L. J. Cornelissen et al. "Magnon spin transport driven by the magnon chemical potential in a magnetic insulator". In: *Physical Review B* 94.1 (2016), p. 014412. ISSN: 2469-9950. DOI: 10.1103/physrevb.94.014412. eprint: 1604.03706.

[194] Geert R. Hoogeboom and Bart J. van Wees. "Nonlocal spin Seebeck effect in the bulk easy-plane antiferromagnet NiO". In: *Physical Review B* 102.21 (2020), p. 214415. ISSN: 2469-9950. DOI: 10.1103/physrevb.102.214415. eprint: 2009.01160.

[195] L. Baldrati et al. "Mechanism of Néel Order Switching in Antiferromagnetic Thin Films Revealed by Magnetotransport and Direct Imaging". In: *Physical Review Letters* 123.17 (2019), p. 177201. ISSN: 0031-9007. DOI: 10.1103/physrevlett.123.177201. eprint: 1810.11326.

[196] Andrew Ross et al. "Propagation Length of Antiferromagnetic Magnons Governed by Domain Configurations". In: *Nano Letters* 20.1 (2020), pp. 306–313. ISSN: 1530-6984. DOI: 10.1021/acs.nanolett.9b03837. eprint: 1907.02751.

[197] Wei Yuan et al. "Experimental signatures of spin superfluid ground state in canted antiferromagnet Cr2O3 via nonlocal spin transport". In: *Science Advances* 4.4 (2018), eaat1098. DOI: 10.1126/sciadv.aat1098. eprint: 1804.07966.

[198] Jiahao Han et al. "Birefringence-like spin transport via linearly polarized antiferromagnetic magnons". In: *Nature Nanotechnology* 15.7 (2020), pp. 563–568. ISSN: 1748-3387. DOI: 10.1038/s41565-020-0703-8.

[199] Kamsul Abraha and David R. Tilley. "Theory of far infrared properties of magnetic surfaces, films and superlattices". In: *Surface Science Reports* 24.5-6 (1996), pp. 129–222. ISSN: 0167-5729. DOI: 10.1016/0167-5729(96)00003-9.

[200] G.T. Rado and J.R. Weertman. "Spin-wave resonance in a ferromagnetic metal". In: *Journal of Physics and Chemistry of Solids* 11.3-4 (1959), pp. 315–333. ISSN: 0022-3697. DOI: 10.1016/0022-3697(59)90233-1.

[201] K. Uchida et al. "Observation of the spin Seebeck effect". In: *Nature* 455.7214 (2008), pp. 778–781. ISSN: 0028-0836. DOI: 10.1038/nature07321.

[202] Matthew W Daniels et al. "Spin-transfer torque induced spin waves in antiferromagnetic insulators". In: *New Journal of Physics* 17.10 (2015), p. 103039. ISSN: 1367-2630. DOI: 10.1088/1367-2630/17/10/103039. eprint: 1409.5460.

[203] Changjiang Liu et al. "Electric field control of magnon spin currents in an antiferromagnetic insulator". In: *Science Advances* 7.40 (2021), eabg1669. DOI: 10.1126/sciadv.abg1669. eprint: 2007.12774.

[204] J. E. Hirsch. "Spin Hall Effect". In: *Physical Review Letters* 83.9 (1999), pp. 1834–1837. ISSN: 0031-9007. DOI: 10.1103/physrevlett.83.1834. eprint: cond-mat/9906160.

[205] N. Vlietstra et al. "Simultaneous detection of the spin-Hall magnetoresistance and the spin-Seebeck effect in platinum and tantalum on yttrium iron garnet". In: *Physical Review B* 90.17 (2014), p. 174436. ISSN: 1098-0121. DOI: 10.1103/physrevb.90.174436. eprint: 1410.0551.

[206] R. Lebrun et al. "Long-distance spin-transport across the Morin phase transition up to room temperature in ultra-low damping single crystals of the antiferromagnet α-Fe2O3". In: *Nature Communications* 11.1 (2020), p. 6332. DOI: 10.1038/s41467-020-20155-7. eprint: 2005.14414.

[207] F Volmer et al. "Charge-induced artifacts in non-local spin transport measurements: How to prevent spurious voltage signals". In: *arXiv* (2021). eprint: 2112.02047.

[208] Brandon L. Giles et al. "Long-range pure magnon spin diffusion observed in a nonlocal spin-Seebeck geometry". In: *Physical Review B* 92.22 (2015), p. 224415. ISSN: 1098-0121. DOI: 10.1103/physrevb.92.224415. eprint: 1504.02808.

[209] Sebastian T. B. Goennenwein et al. "Non-local magnetoresistance in YIG/Pt nanostructures". In: *Applied Physics Letters* 107.17 (2015), p. 172405. ISSN: 0003-6951. DOI: 10.1063/1.4935074.

[210] L. J. Cornelissen, J. Shan, and B. J. van Wees. "Temperature dependence of the magnon spin diffusion length and magnon spin conductivity in the magnetic insulator yttrium iron garnet". In: *Physical Review B* 94.18 (2016), p. 180402. ISSN: 2469-9950. DOI: 10.1103/physrevb.94.180402. eprint: 1607.01506.

[211] Wenyu Xing et al. "Magnon Transport in Quasi-Two-Dimensional van der Waals Antiferromagnets". In: *Physical Review X* 9.1 (2019), p. 011026. DOI: 10.1103/physrevx.9.011026. eprint: 1902.04719.

[212] Can Onur Avci et al. "Nonlocal Detection of Out-of-Plane Magnetization in a Magnetic Insulator by Thermal Spin Drag". In: *Physical Review Letters* 124.2 (2020), p. 027701. ISSN: 0031-9007. DOI: 10.1103/physrevlett.124.027701.

[213] J. Shan et al. "Criteria for accurate determination of the magnon relaxation length from the nonlocal spin Seebeck effect". In: *Physical Review B* 96.18 (2017), p. 184427. ISSN: 2469-9950. DOI: 10.1103/physrevb.96.184427. eprint: 1709.06321.

[214] A. Haykal et al. "Antiferromagnetic textures in BiFeO3 controlled by strain and electric field". In: *Nature Communications* 11.1 (2020), pp. 1–7. ISSN: 20411723. DOI: 10.1038/s41467-020-15501-8.

[215] A. V. Chumak et al. "Direct detection of magnon spin transport by the inverse spin Hall effect". In: *Applied Physics Letters* 100.8 (2012), p. 082405. ISSN: 0003-6951. DOI: 10.1063/1.3689787. eprint: 1112.4969.

[216] Steven S.-L. Zhang and Shufeng Zhang. "Spin convertance at magnetic interfaces". In: *Physical Review B* 86.21 (2012), p. 214424. ISSN: 1098-0121. DOI: 10.1103/physrevb.86.214424. eprint: 1210.2735.

[217] Jin Lan, Weichao Yu, and Jiang Xiao. "Antiferromagnetic domain wall as spin wave polarizer and retarder". In: *Nature Communications* 8.1 (2017), pp. 1–7. DOI: 10.1038/s41467-017-00265-5. eprint: 1706.01617.

[218] Weichao Yu, Jin Lan, and Jiang Xiao. "Polarization-selective spin wave driven domain - wall motion in antiferromagnets". In: *Physical Review B* 98.14 (2018), p. 144422. ISSN: 2469-9950. DOI: 10.1103/physrevb.98.144422. eprint: 1711.08929.

[219] Juan Shan et al. "Influence of yttrium iron garnet thickness and heater opacity on the nonlocal transport of electrically and thermally excited magnons". In: *Physical Review B* 94.17 (2016), p. 174437. ISSN: 2469-9950. DOI: 10.1103/physrevb.94.174437. eprint: 1608.01178.

[220] Xiaoxi Huang et al. "Novel Spin–Orbit Torque Generation at Room Temperature in an All-Oxide Epitaxial La0.7Sr0.3MnO3/SrIrO3 System". In: *Advanced Materials* 33.24 (2021), p. 2008269. ISSN: 0935-9648. DOI: 10.1002/adma.202008269.

[221] Sha Huang et al. "Multiferroic behavior from synergetic response of multiple ordering parameters in BiFeO3 single crystal under high magnetic field up to 50 Tesla". In: *Journal of Applied Physics* 127.4 (2020), p. 044101. ISSN: 0021-8979. DOI: 10.1063/1.5131411.

[222] Fida Mohmed et al. "Magnetic and thermal properties of ferromagnetic insulator: Yttrium Iron Garnet". In: *Ceramics International* 45.2 (2019), pp. 2418–2424. ISSN: 0272-8842. DOI: 10.1016/j.ceramint.2018.10.161.

[223] Shuai Ning et al. "Dependence of the Thermal Conductivity of BiFeO3 Thin Films on Polarization and Structure". In: *Physical Review Applied* 8.5 (2017), p. 054049. DOI: 10.1103/physrevapplied.8.054049.

[224] Geert Hoogeboom. "Spin transport and spin dynamics in antiferromagnets". English. PhD thesis. University of Groningen, 2021. DOI: 10.33612/diss.157444391.

[225] Zuhuang Chen et al. "Complex strain evolution of polar and magnetic order in multiferroic BiFeO3 thin films". In: *Nature Communications* 9.1 (2018), p. 3764. DOI: 10.1038/s41467-018-06190-5.

[226] Je-Geun Park et al. "Structure and spin dynamics of multiferroic BiFeO3". In: *Journal of Physics: Condensed Matter* 26.43 (2014), p. 433202. ISSN: 0953-8984. DOI: 10.1088/0953-8984/26/43/433202. eprint: 1409.0301.

[227] Stuart R. Burns et al. "The Experimentalist's Guide to the Cycloid, or Noncollinear Antiferromagnetism in Epitaxial BiFeO3". In: *Advanced Materials* 32.45 (2020). ISSN: 0935-9648. DOI: 10.1002/adma.202003711.

[228] Gustau Catalan and James F. Scott. "Physics and Applications of Bismuth Ferrite". In: *Advanced Materials* 21.24 (2009), pp. 2463–2485. ISSN: 1521-4095. DOI: 10.1002/adma.200802849.

[229] Feiming Bai et al. "Destruction of spin cycloid in (111)c-oriented BiFeO3 thin films by epitiaxial constraint: Enhanced polarization and release of latent magnetization". In: *Applied Physics Letters* 86.3 (2005), p. 032511. ISSN: 0003-6951. DOI: 10.1063/1.1851612.

[230] I. Gross et al. "Real-space imaging of non-collinear antiferromagnetic order with a single-spin magnetometer". In: *Nature* 549.7671 (2017), pp. 252–256. ISSN: 0028-0836. DOI: 10.1038/nature23656. eprint: 2011.12399.

[231] R. Mankowsky et al. "Ultrafast Reversal of the Ferroelectric Polarization". In: *Physical Review Letters* 118.19 (2017). DOI: 10.1103/physrevlett.118.197601. eprint: 1701.06312.

[232] Kouhei Takahashi, Noriaki Kida, and Masayoshi Tonouchi. "Terahertz Radiation by an Ultrafast Spontaneous Polarization Modulation of Multiferroic BiFeO3 Thin Films". In: *Physical Review Letters* 96.11 (2005), p. 117402. ISSN: 0031-9007. DOI: 10.1103/physrevlett.96.117402. eprint: cond-mat/0510132.

[233] Sava A. Denev et al. "Probing Ferroelectrics Using Optical Second Harmonic Generation". In: *Journal of the American Ceramic Society* 94.9 (2011), pp. 2699–2727. ISSN: 0002-7820. DOI: 10.1111/j.1551-2916.2011.04740.x.

[234] P Godefroy et al. "Electric field induced second harmonic generation spectroscopy on a metal-oxide-silicon structure". In: *Applied Physics Letters* 68.14 (1996), pp. 1981–1983. ISSN: 0003-6951. DOI: 10.1063/1.115646.

[235] Haidan Wen et al. "Electronic Origin of Ultrafast Photoinduced Strain in BiFeO3". In: *Physical Review Letters* 110.3 (2013), p. 037601. ISSN: 0031-9007. DOI: 10.1103/physrevlett.110.037601.

[236] Daniel Schick et al. "Localized Excited Charge Carriers Generate Ultrafast Inhomogeneous Strain in the Multiferroic BiFeO3". In: *Physical Review Letters* 112.9 (2014), p. 097602. ISSN: 0031-9007. DOI: 10.1103/physrevlett.112.097602. eprint: 1311.1634.

[237] Hongwu Yu et al. "Ultrafast Nonlinear Spectroscopy in (111) Oriented Bismuth Ferrite Oxide". In: *Journal of the Physical Society of Japan* 89.6 (2020), p. 063401. ISSN: 0031-9015. DOI: 10.7566/jpsj.89.063401.

[238] X. S. Xu et al. "Optical properties and magnetochromism in multiferroic BiFeO3". In: *Physical Review B* 79.13 (2009), p. 134425. ISSN: 1098-0121. DOI: 10.1103/physrevb.79.134425.

[239] B. T. Thole, G. van der Laan, and G. A. Sawatzky. "Strong Magnetic Dichroism Predicted in the M4,5 X-Ray Absorption Spectra of Magnetic Rare-Earth Materials". In: *Physical Review Letters* 55.19 (1985), pp. 2086–2088. ISSN: 0031-9007. DOI: 10.1103/physrevlett.55.2086.

[240] Gerrit van der Laan et al. "Experimental proof of magnetic x-ray dichroism". In: *Physical Review B* 34.9 (1986), pp. 6529–6531. ISSN: 1098-0121. DOI: 10.1103/physrevb.34.6529.

[241] M. B. Holcomb et al. "Probing the evolution of antiferromagnetism in multiferroics". In: *Physical Review B* 81.13 (2010), p. 134406. ISSN: 1098-0121. DOI: 10.1103/physrevb.81.134406.

[242] Morgan Trassin et al. "Probing Ferroelectric Domain Engineering in BiFeO3 Thin Films by Second Harmonic Generation". In: *Advanced Materials* 27.33 (2015), pp. 4871–4876. ISSN: 1521-4095. DOI: 10.1002/adma.201501636.

[243] S. Das et al. "Observation of room-temperature polar skyrmions". In: *Nature* 568.7752 (2019), pp. 368–372. ISSN: 0028-0836. DOI: 10.1038/s41586-019-1092-8.

[244] Ajay K. Yadav et al. "Spatially resolved steady-state negative capacitance". In: *Nature* 565.7740 (2019), pp. 468–471. ISSN: 0028-0836. DOI: 10.1038/s41586-018-0855-y.

[245] J M Kosterlitz and D J Thouless. "Ordering, metastability and phase transitions in two-dimensional systems". In: *Journal of Physics C: Solid State Physics* 6 (1973), p. 1181. ISSN: 0022-3719. DOI: 10.1088/0022-3719/6/7/010.

[246] Naoto Nagaosa and Yoshinori Tokura. "Topological properties and dynamics of magnetic skyrmions". In: *Nature Nanotechnology* 8.12 (2013), pp. 899–911. ISSN: 1748-3387. DOI: 10.1038/nnano.2013.243.

[247] U. K. Rößler, A. N. Bogdanov, and C. Pfleiderer. "Spontaneous skyrmion ground states in magnetic metals". In: *Nature* 442.7104 (2006), pp. 797–801. ISSN: 0028-0836. DOI: 10.1038/nature05056. eprint: cond-mat/0603103.

[248] S. Mühlbauer et al. "Skyrmion Lattice in a Chiral Magnet". In: *Science* 323.5916 (2009), pp. 915–919. ISSN: 0036-8075. DOI: 10.1126/science.1166767. eprint: 0902.1968.

[249] Y. Nahas et al. "Discovery of stable skyrmionic state in ferroelectric nanocomposites". In: *Nature Communications* 6.1 (2015), p. 8542. DOI: 10.1038/ncomms9542.

[250] Qi Zhang et al. "Nanoscale Bubble Domains and Topological Transitions in Ultrathin Ferroelectric Films". In: *Advanced Materials* 29.46 (2017), p. 1702375. ISSN: 0935-9648. DOI: 10.1002/adma.201702375.

[251] J. M. Gregg. "Exotic Domain States in Ferroelectrics: Searching for Vortices and Skyrmions". In: *Ferroelectrics* 433.1 (2012), pp. 74–87. ISSN: 0015-0193. DOI: 10.1080/00150193.2012.678131.

[252] Ivan I. Naumov, L. Bellaiche, and Huaxiang Fu. "Unusual phase transitions in ferroelectric nanodisks and nanorods". In: *Nature* 432.7018 (2004), pp. 737–740. ISSN: 0028-0836. DOI: 10.1038/nature03107.

[253] Sayeef Salahuddin and Supriyo Datta. "Use of Negative Capacitance to Provide Voltage Amplification for Low Power Nanoscale Devices". In: *Nano Letters* 8.2 (2008), pp. 405–410. ISSN: 1530-6984. DOI: 10.1021/nl071804g.

[254] Sayeef Salahuddin and Supriyo Datta. "Can the subthreshold swing in a classical FET be lowered below 60 mV/decade?" In: *2008 IEEE International Electron Devices Meeting* (2008), pp. 1–4. DOI: 10.1109/iedm.2008.4796789.

[255] Thomas N. Theis and Paul M. Solomon. "It's Time to Reinvent the Transistor!" In: *Science* 327.5973 (2010), pp. 1600–1601. ISSN: 0036-8075. DOI: 10.1126/science.1187597.

[256] Pavlo Zubko et al. "Negative capacitance in multidomain ferroelectric superlattices". In: *Nature* 534.7608 (2016), pp. 524–528. DOI: 10.1038/nature17659.

[257] Daniel J. R. Appleby et al. "Experimental Observation of Negative Capacitance in Ferroelectrics at Room Temperature". In: *Nano Letters* 14.7 (2014), pp. 3864–3868. ISSN: 1530-6984. DOI: 10.1021/nl5017255.

[258] Jorge Íñiguez et al. "Ferroelectric negative capacitance". In: *Nature Reviews Materials* 4.4 (2019), pp. 243–256. DOI: 10.1038/s41578-019-0089-0.

[259] Michael Hoffmann et al. "Unveiling the double-well energy landscape in a ferroelectric layer". In: *Nature* 565.7740 (2019), pp. 464–467. ISSN: 0028-0836. DOI: 10.1038/s41586-018-0854-z.

[260] A. M. Bratkovsky and A. P. Levanyuk. "Depolarizing field and "real" hysteresis loops in nanometer-scale ferroelectric films". In: *Applied Physics Letters* 89.25 (2006), p. 253108. ISSN: 0003-6951. DOI: 10.1063/1.2408650. eprint: cond-mat/0608283.

[261] Xiaowei Wang et al. "Van der Waals negative capacitance transistors". In: *Nature Communications* 10.1 (2019), p. 3037. DOI: 10.1038/s41467-019-10738-4.

[262] S. Das et al. "Local negative permittivity and topological phase transition in polar skyrmions". In: *Nature Materials* 20.2 (2021), pp. 194–201. ISSN: 1476-1122. DOI: 10.1038/s41563-020-00818-y.

[263] Shang-Lin Hsu et al. "Emergence of the Vortex State in Confined Ferroelectric Heterostructures". In: *Advanced Materials* 31.36 (2019), p. 1901014. ISSN: 0935-9648. DOI: 10.1002/adma.201901014.

[264] Piush Behera et al. "Electric field control of chirality". In: *Science Advances* 8.1 (2022), eabj8030. DOI: 10.1126/sciadv.abj8030.

[265] Sina Hashemizadeh and Dragan Damjanovic. "Nonlinear dynamics of polar regions in paraelectric phase of (Ba1-x,Srx)TiO3 ceramics". In: *Applied Physics Letters* 110.19 (2017), p. 192905. ISSN: 0003-6951. DOI: 10.1063/1.4983366. eprint: 1705.04002.

[266] Abel Fernandez et al. "Finite-size effects in lead scandium tantalate relaxor thin films". In: *Physical Review B* 101.9 (2020), p. 094102. ISSN: 2469-9950. DOI: 10.1103/physrevb.101.094102.

[267] Dragan Damjanovic and Marlyse Demartin. "The Rayleigh law in piezoelectric ceramics". In: *Journal of Physics D: Applied Physics* 29.7 (1996), p. 2057. ISSN: 0022-3727. DOI: 10.1088/0022-3727/29/7/046.

[268] Jieun Kim et al. "Frequency-dependent suppression of field-induced polarization rotation in relaxor ferroelectric thin films". In: *Matter* 4.7 (2021), pp. 2367–2377. ISSN: 2590-2385. DOI: 10.1016/j.matt.2021.04.017.

Appendix A

Extended Data

A.1 Electric field control of thermal magnons

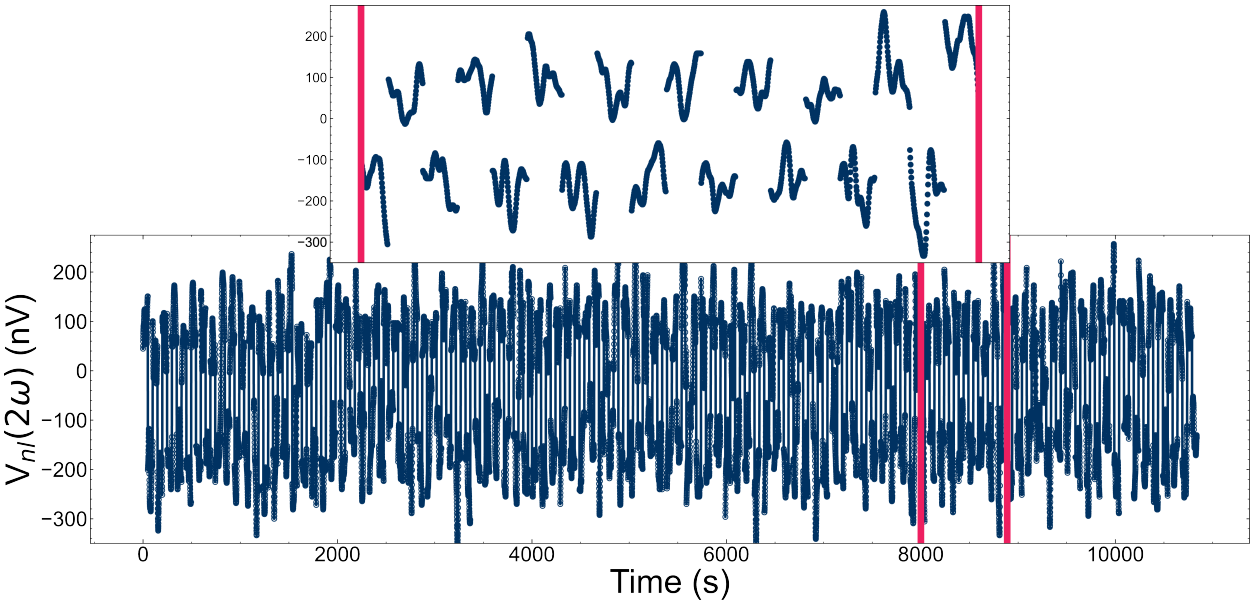

Figure A.1: Repeatability of magnon current switching. Extension of Fig. 5.4 showing data for ∼100 bipolar poling events, showing robust electric field manipulation of magnon current.

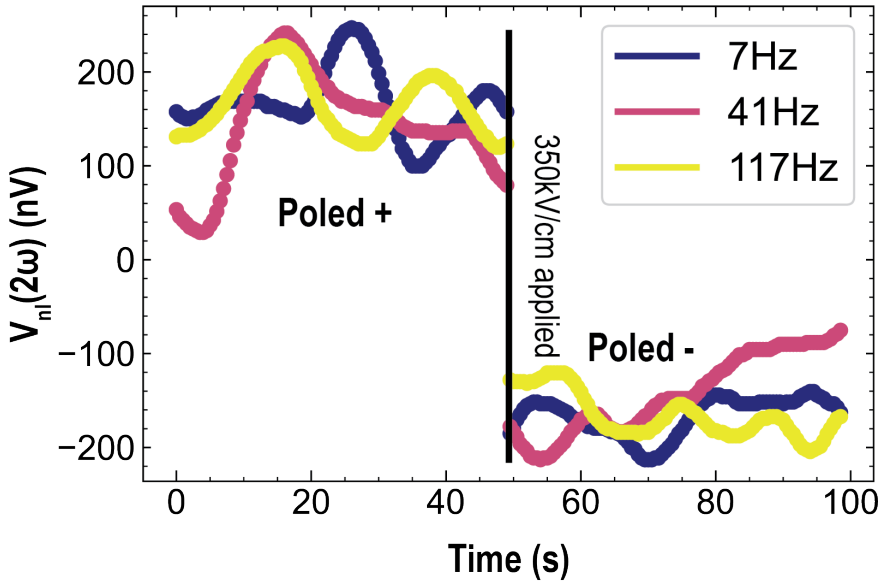

Figure A.2: Independence of magnon current on lock-in frequency. Results of electric field control of magnon current as measured with various lock-in frequencies. The data is independent of the frequency used, as expected in the (low) frequency regime studied.

A.2 Polar skyrmion recombination

In this and the following section, I describe dynamic studies of complex polar textures, such as polar skyrmions and polar vortices.

Spatially complex, real-space topological configurations and their phase transitions have recently emerged as a fertile playground in condensed matter physics[243, 244, 245, 246]. Although the focus has been on spin textures in magnets [246, 247, 248], leading to the formation of skyrmions and related topologically protected states, in recent years there has been renewed efforts to discover analogous charge textures in, for example, ferroelectrics[249, 250, 251, 252]. With the discovery of such polar textures (for example, vortices and skyrmions), it is of both fundamental and practical interest to understand the microscopic and macroscopic nature of their dielectric response and explore the possibility of a field-driven topological phase transition[243, 244].

In parallel, the possibility of capturing "negative permittivity" states in ferroelectrics, either in the temporal (that is, dynamical, see Chapter 2) or spatial (that is, in equilibrium) domain, has drawn the attention of scientists and engineers alike [253, 254, 255, 256, 257, 258, 259, 260, 261]. The concept of negative capacitance was developed for monodomain ferroelectric capacitors by considering double well potential (Fig. 1.1 that appears upon transitioning from a paraelectric to a ferroelectric state. The minima of these wells represent the equilibrium state of the material and the curvature of the energy landscape near these equilibria dictates that small electric field perturbations should give rise to a classical

positive capacitive response (that is, positive permittivity). It was proposed, however, that if one could place the material in the region between these two states (that is, in a region of negative curvature of the energy landscape), it could give rise to a negative capacitive response (that is, negative permittivity) under electric field excitation[1, 244]. In a capacitor heterostructure comprising an ideal ferroelectric capacitor (capacitance C_F) in series with a regular dielectric capacitor (capacitance C_D), the overall capacitance $C = \left(C_F^{-1} + C_D^{-1}\right)^{-1}$ has to be positive for thermodynamic stability. But if $C_F < 0$, the total capacitance, C, will be larger than either of the two constituent capacitors taken independently. Accessing this regime, where the ferroelectric is stabilized in the region of negative free energy curvature, however, remains a challenge in the static sense[256, 258, 260]: if the capacitor is driven by a voltage, the region of negative curvature is unstable, and indeed only transiently occupied. Researchers have explored approaches wherein the capacitor is driven by a charge that can be simply controlled in an electrostatically coupled ferroelectric/dielectric series capacitor[255]. If it is a dielectrically stiff material, it will effectively suppress the spontaneous polarization of the ferroelectric and thus stabilize the paraelectric state even if the ferroelectric is below its nominal transition temperature[260]. Recent work has further demonstrated that in multidomain ferroelectric polar structures, such as the vortices found in $(PbTiO_3)_n/(SrTiO_3)_n$ superlattices, the complex polar order, while producing an overall positive dielectric permittivity, exhibits regions of varying dielectric susceptibility, including areas of local negative capacitive response in the $PbTiO_3$ layers[244].

The recent discovery of chiral polar skyrmions in $(PbTiO_3)_n/(SrTiO_3)_n$ superlattices stemming from the interplay of elastic, electrostatic and gradient energies, with a topological number of +1 raises a fundamentally important question: do such skyrmions also exhibit a spatial distribution of varying dielectric susceptibility?[243] In our work [262], we demonstrate a strong enhancement of the out-of-plane dielectric permittivity and that this is a direct consequence of a negative permittivity region that forms at the periphery of each skyrmion. Under the influence of an applied electric field, we find that we can tune the system from having arrays of polar skyrmions, to a uniformly polarized state, whereby the skyrmion diameter shrinks as the field increases in magnitude (Fig. A.3). When the field is taken away, the skyrmions reform.

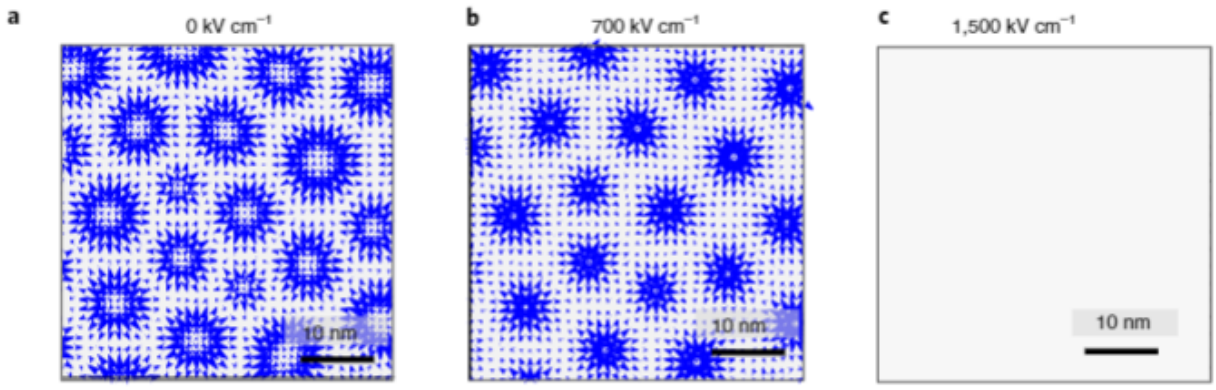

Figure A.3: Used with permission from [262]. Electric field control of the topological phase transition of the polar skyrmion of the $[(SrTiO_3)_{16}$ / $(PbTiO_3)_{16}]_8$ superlattice. **a**–**c**, Phase-field simulations show the shrinkage of the diameters of the skyrmions when an electric field is applied, from zero field (**a**) to 700 kV cm^{-1} (**b**), and ultimately the entire sample becomes uniformly ferroelectric at ∼1500 kV cm^{-1} (**c**)

In the context of this thesis, then, one is naturally inclined to ask, can we study the dynamics of the "popping" (where the skyrmions are annihilated by the applied field) and recombining process? And what do any finding means in terms of capacitance of the system? To further understand the reversible evolution of these structures under applied electric fields, the temporal evolution of the skyrmion ground state can be probed by perturbing it with electric field pulses that drive the system to a uniform polar state, and then measuring the time-dependent evolution back to the skyrmion state (Fig. A.4, A.5). Here, we performed two sets of measurements. The first focused on applying strong, unipolar pulses (U_1 and U_2) with varying lengths of delay time (t_d) between the pulses. We measured the current that flows in the capacitor during the application of U_1 (that is, I_1), then allowed possible relaxation to occur during t_d and finally measured the current that flows during the application of U_2 (that is, I_2). Taking the difference I_1 – I_2 for various t_d provides a time-dependent measure of the amount of relaxation after the poling process. For short delay times ($t_d \leq$10 μs, Fig. A.4a), for the parent 50-nm-thick $PbTiO_3$ film (here, with t_d= 200 ns, Fig. A.4b,c), a flat, zero response corresponding to stable, poled ferroelectric behav-iour was observed. On the other hand, similar experiments on the superlattices with skyrmions (here, with t_d= 200 ns, Fig. A.4d) revealed a transient peak, suggesting that there is a relaxation process different from that observed in a classical ferroelectric based on the same material (data for other short t_d values are also provided in Fig. A.5).

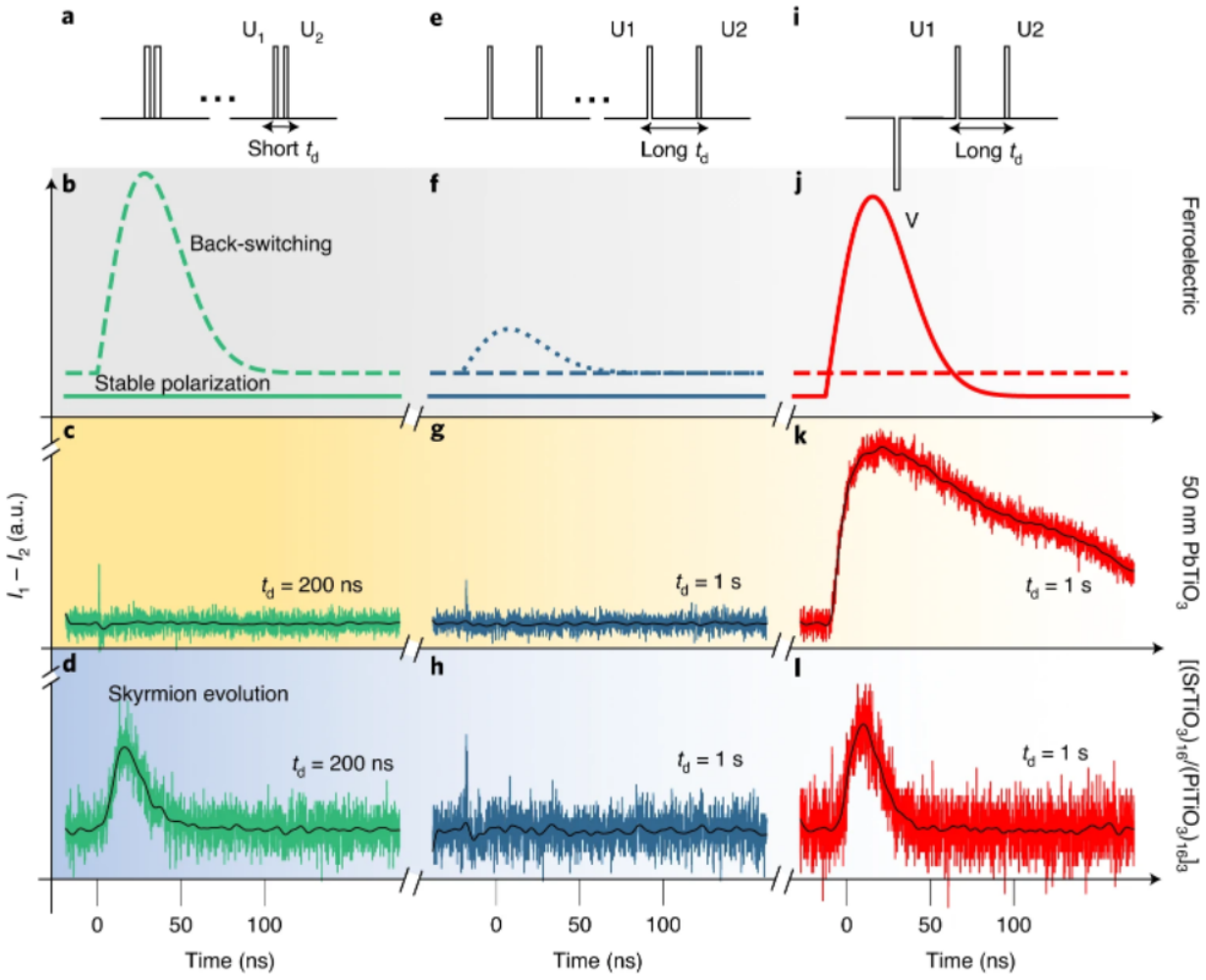
a
U1 U2
Short t_d
e
U1 U2
Long t_d
i
U1 U2
Long t_d
b
Back-switching
Stable polarization
f
j
V
Ferroelectric
c
t_d = 200 ns
g
t_d = 1 s
k
t_d = 1 s
50 nm $PbTiO_3$
$I_1 - I_2$ (a.u.)
d
Skyrmion evolution
t_d = 200 ns
h
t_d = 1 s
l
t_d = 1 s
$[(SrTiO_3)_{16}/(PTiO_3)_{16}]_3$
0 50 100
Time (ns)
0 50 100
Time (ns)
0 50 100
Time (ns)

Figure A.4 *(previous page)*: Used with permission from [262]. Generation of a transient state with time-dependent capacitance under out-of-plane measurement of the skyrmion. **a**, Schematic of two unipolar pulses (U_1 and U_2) applied to a sample with a short delay time (t_d) between pulses. Application of unipolar pulse U_1 poles the sample to the uniform polarization state. Zero field was applied for time t_d, during which the system relaxes. We monitored the difference in current response to U_1 and U_2 ($I_1 - I_2$) to reveal a transient state after initial poling. **b**, Expected difference in the current response ($I_1 - I_2$) for a ferroelectric with (dashed green line) and without (solid green line) back-switching. **c**, $I_1 - I_2$ for the parent ferroelectric (50 nm $PbTiO_3$ layer), indicating stable polarization. **d**, $I_1 - I_2$ for the superlattice shows a notable peak, suggesting the occurrence of a relaxation process. **e**, To probe the relaxation timescale, we performed the same experiment with a long time delay. **f**, Expected behaviour for a classical ferroelectric with complete back-switching (dashed line), partial back-switching (dotted line) and stable ferroelectric polarization (solid line). **g**, As expected, the parent 50 nm $PbTiO_3$ layer shows a flat line for $I_1 - I_2$, that is, stability. **h**, Notably, the superlattice also shows a flat line for $I_1 - I_2$, indicating that relaxation is complete on this timescale ($t_d = 1$s shown). **i**, Finally, we performed an experiment in which we also included a preset pulse-down pulse (V) and monitored $I_1 - I_2$ for long t_d. **j**, The ferroelectric back switching is represented by the dashed line and the expected behaviour from a ferroelectric, a switchable, stable polarization (solid line). **k**, The parent 50 nm $PbTiO_3$ layer shows a strong signal coming from the switchable remnant polarization. **l**, The difference in the current response ($I_1 - I_2$) for the skyrmion sample, which importantly shows a distinguishable signal. This, in conjunction with the data in d and h, indicates that the origin of the relaxation seen in the skyrmion sample is not derived from back-switching of the small remnant polarization, but rather a new mechanism originating in the polar skyrmion structure.

To further understand the relaxation processes and, in par-ticular, reveal the timescales over which these processes persist, we carried out similar experiments with progressively longer t_d. Upon transitioning to long delay times (10 μs $\leq t_d \leq$1s, Fig. A.4e), for the parent 50-nm-thick $PbTiO_3$ film (here, with t_d= 1s, Fig. A.4f,g), a flat, zero response corresponding to stable, poled ferroelectric behaviour was once again observed. Likewise, similar experiments for the superlattices exhibiting sky-rmion structures revealed a flat, zero response, suggesting the relaxation process has been completed within 1s (here, with t_d= 1s, Fig. A.4h and Fig. A.5).Thus far, the observations suggest that (not surprisingly) the single-layer parent ferroelectric film remains stable in whatever state it is electrically poled into, whereas the superlattices exhibit-ing skyrmion structures exhibit relaxation processes. This could correspond to classical back-switching (that is, the applied bias pushes the skyrmion into a uniform polar state, which then relaxes back to a classical up-and-down-poled domain structure) or indi-cate an exotic relaxation back towards the skyrmion structure. To distinguish between these two cases, we performed a second set of experiments in which we applied a

preset pulse V opposite to U_1 and U_2 with a long t_d (Fig. A.4i). When this experiment was performed on the parent 50-nm-thick $PbTiO_3$ film (here, with t_d= 1s, Fig. A.4j,k), a non-zero response, corresponding to what is expected for stable, poled ferroelectric behaviour, was observed. This contrasts with the long delay time study without the preset pulse, which showed no peak (Fig. A.4g). On the other hand, similar experiments on the superlattices exhibiting sky-rmions (here, with t_d= 1s, Fig. A.4l) revealed a small transient peak, suggesting that the small remnant polarization of the superlattice can be switched. From other experiments (Fig. A.4d,g), it appears that these superlattices relax or back-switch within ∼1s; however, if this was true, we should have seen no peak in this preset pulse experiment (Fig. A.4l). Thus, this is indicative of a totally different relaxation process, that is, it cannot be explained simply by the classical back-switching of a ferroelectric, but instead suggests there is an exotic, time-dependent evolution of the emergent polarization state that we can unravel and then re-establish reversibly.

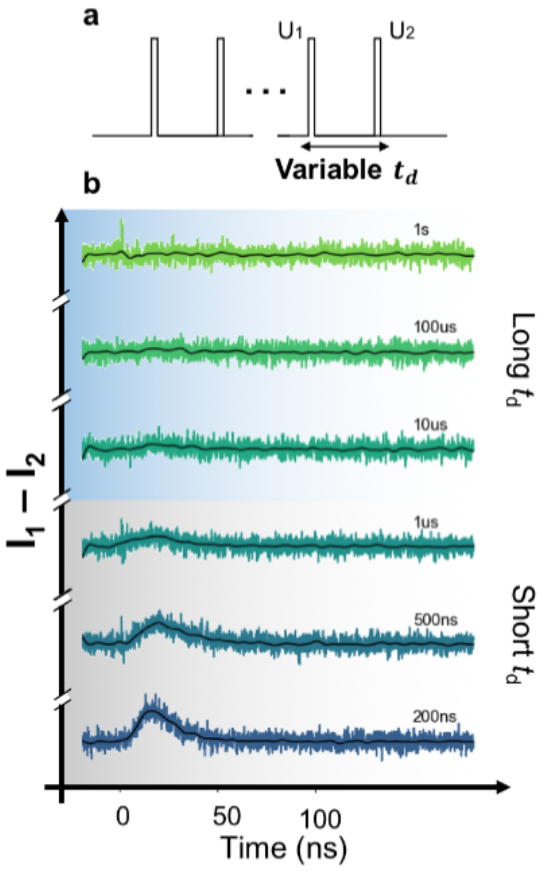

Figure A.5 *(previous page)*: Used with permission from [262]. Time dependence transient capacitance state of out-of-plane device geometry of skyrmion. In order to understand how the transient state decays, we apply unipolar pulses as in **a**, with variable delay time. The data in **b**, shows the difference in current response of the sample to U_1 and to U_2 (I_1-I_2) for various delay times. On "short" timescales (200 ns$\leq t_d \leq$10 μs) there is a significant difference I_1–I_2attributed to the transient capacitance state in the superlattice structure. For "long" delay times (10 μs $\leq t_d \leq$1 s) little to no difference is observed, indicating the complete decay of the transient state at those timescales.

A.3 Polar vortices

Topological phases in polar materials (like the polar skyrmion in section A.2) arise as a result of electrostatic and mechanical boundary conditions. One can tune the electrostatic boundary conditions by inserting dielectric layers within the ferroelectric (creating a superlattice), thereby modifying screening at the ferroelectric/dielectric surface. Epitaxial strain resulting from choice of growth substrate sets the mechanical boundary conditions. For example, the tensile strain imposed by $DyScO_3$ (DSO) on $PbTiO_3$ (PTO) favors an a/c domain structure; however, by sandwiching the $PbTiO_3$ layer between layers of $SrTiO_3$ (STO), the dielectric $SrTiO_3$ inhibits screening of the ferroelectric order, forcing in-plane polarization at the $PbTiO_3$ / $SrTiO_3$ interface and results in the emergence of flux-closure domains. By shrinking the number of unit cells in the $PbTiO_3$ and $SrTiO_3$ layers, the system evolves from flux closure domains to a vortex state (Fig. A.6a), characterized by continuous rotation of the polar order[244, 263].

Polar vortices[1] are 3-dimensional objects, where the polar order rotates, either clockwise or counterclockwise, in a plane (with the rotating region having radius ∼2-5nm). This rotating region extends (∼100nm) along the direction normal to the plane of rotation, thereby creating a "tube"-like structure[263, 264]. In PTO/STO superlattices grown on DSO, the anisotropy of the substrate forces the tube direction to be along the $[010]_{\mathrm{pc}}$ direction (Fig. A.6). Within a single PTO layer, many vortices exist, with neighboring vortices rotating opposite (*i.e.*, alternating clockwise and counter-clockwise rotation). Under tensile strain, like that imposed by DSO, there exists a "buckling" structure, whereby adjacent vortices also exhibit alternating "up" and "down" off-centering (along the out-of-plane direction), (Fig. A.6). This buckling results in a net in-plane polarization pointing along $[100]_{\mathrm{pc}}$ direction[2]. Thus, in a simplified, though useful, picture, the vortex system can be thought of,

[1] Typically, vortices form in PTO_n/STO_n when the number of unit cells, $n \approx 12 - 20$

[2] The formation of the buckled phase can be understood as a freezing of a "vortexon" mode at a critical strain ϵ_c, analogous to the freezing of a soft phonon mode at a critical temperature, for soft-mode phase transitions in ferroelectric (see chapter 1)

macroscopically, as an in-plane ferroelectric that forms 180° domains (domains of opposite buckling).

Just like a classical ferroelectric, when one applies an electric field with component antiparallel to the the direction of net polarization, the system will undergo polarization reversal, albeit here, accompanied by (or progressing via) switching of the buckling pattern[264]. This leads to the observation of a ferroelectric-like hysteresis loop (Fig. A.6c), as measured on in-plane capacitors (Fig. A.6b). We can think of this "large" field switching event akin to a classical ferroelectric. There exists, however, a second switching event (Fig. A.6d), at lower field, where we observe minor hysteresis loops akin to an anti-ferroelectric. To understand how this arises, first imagine a simplified system where the vortices are all aligned (*i.e.*, no buckling), and there is no net polarization. If we apply an in-plane field perpendicular to the vortex tubes (along $[100]_{\mathrm{pc}}$), the vortices will eventually be destroyed, favoring the formation of a single domain ferroelectric state. While this is not surprising, the nature of the system, whereby neighboring vortices alternate rotation direction, results in nuanced behavior for the transition to a mono-domain state. Consider a vortex, V_1 rotating in the x-y plane, where the polarization rotates counter-clockwise, *i.e.* the top polarization points along $-\hat{x}$. Its neighboring vortex, V_2, will have clockwise roation, *i.e.*, bottom polarization along $-\hat{x}$. Upon application of an electric field $\vec{E} \propto -\hat{x}$, the core of V_1 will move along $-\hat{y}$, as the region (top region) of polarization aligned with the field grows and the region (bottom region) aligned anti-parallel shrinks. For V_2, the opposite will occur, with the core moving in $+\hat{y}$. Neighboring vortices move in opposite directions, and in a manner *orthogonal* to the applied field. At low field, the system acts similar to a relaxor ferroelectric, where there is continuous deformation of the vortices until they are destroyed. When the field is removed, the vortices reform. In the simple case of no buckling, one can understand the system as possessing a single-welled free energy landscape, which, in principle, should not show hysteresis. However, due to polar correlations and/or size constraints (the face of the vortex is $\sim$10 unit-cells tall and has only $\sim$20 unit-cells in which to move), there may be "ripples" in the single well, *i.e.*, small, local minima in the free energy. These minima result in the minor hysteresis, observed.

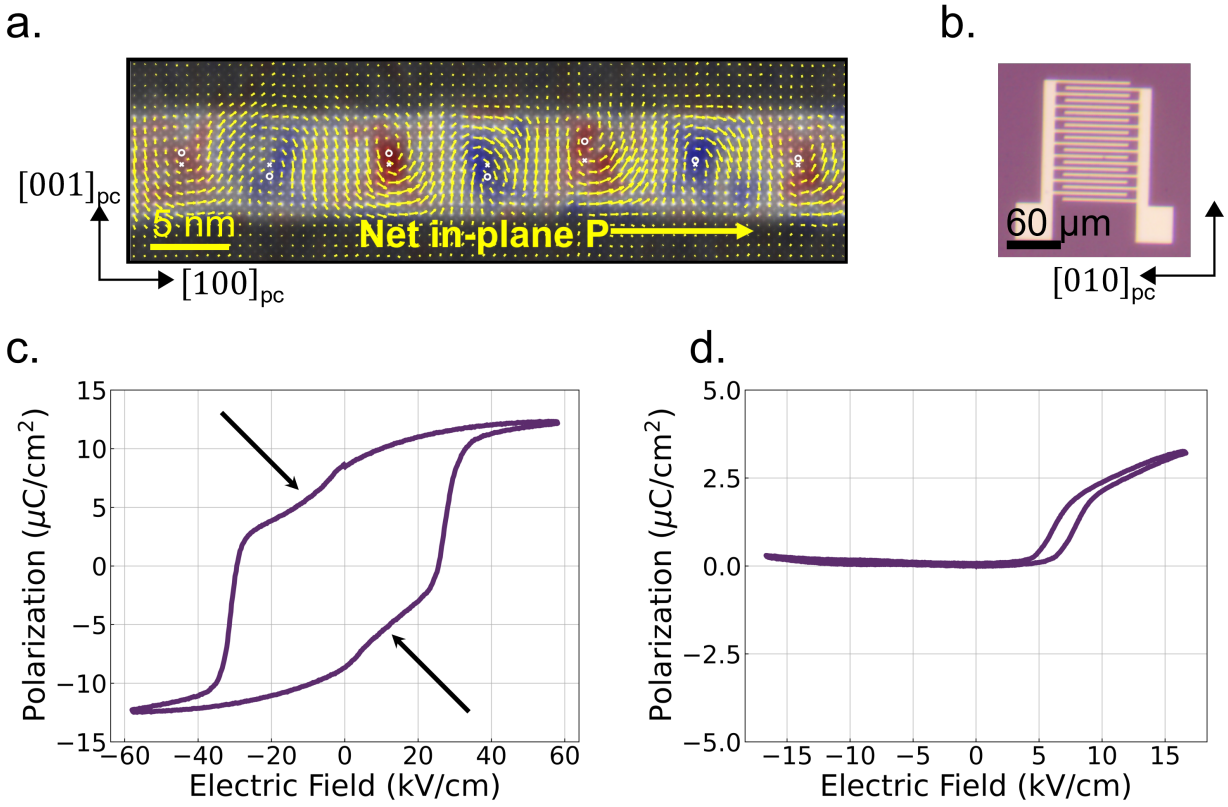

Figure A.6: Polar vortices. **a.** Polar vortex structure (imaged via transmission electron microscopy). **b.** Optical image of interdigitaded electrode device used to study electric field switching. **c.** "Large" field ferroelectric-like hysteresis loop, corresponding to reversal of in-plane polarization and buckling configuration. Arrows indicate loop "pinching". **d.** Minor hystersis loop corresponding to relaxor-like behavior of vortices at low field.

Now, we return to the buckled vortex system, which has a net in-plane polarization in the ground state. With application of a sufficiently strong electric field anti-parallel to the net polarization, the system can be poled to a uniform polarization state with the polarization direction reversed. When the vortices reform, the buckling, following the new polarization direction, will be switched as well. The existence of net in-plane polarization in the buckled system requires a double-well free energy landscape. The convolution of the this double well and the single, "rippled", well, detailed above, results in the observed behavior (Fig. A.6). Given the complexity of switching in this system, we turn to dynamic studies of switching in a effort to gain more insight.

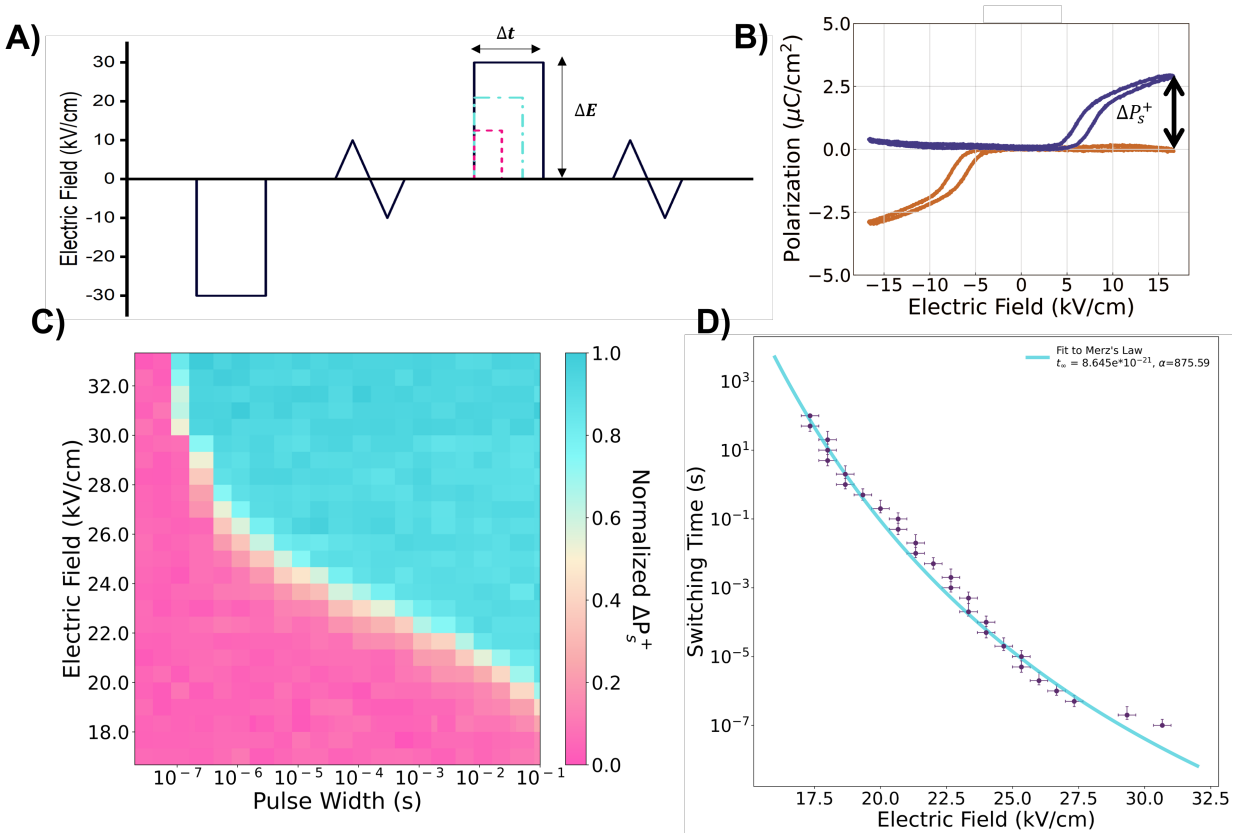

Figure A.7: Switching dynamics of polar vortices. **a.** Experimental protocol. Pulses of variable pulsewidth and electric field magnitude are used to preset and drive switching of the polar vortex state. Single bipolar hysteresis loops are used as non-destructive readouts of initial and final states. **b.** Prototypical minor (non-destructive) single bipolar hysteresis loops of the system poled up (orange) and down (purple). By analyzing the difference between the first and second hysteresis loop measured (**a.**) we can determine the extent to which the system has switched. **c.** Heat map of extent of switching for various applied fields and pulsewidths. Blue indicates complete switching, while pink indicates no switching. **d.** Switching time as a function of applied field and fit to Merz' law (Eq. 2.8).

We begin by studying the timescales and electric field dependence of switching in the polar vortex samples. We do this following the protocol outlined in Fig. A.7a using in-plane fields as applied via the interdigitated electrode device (Fig. A.6b). We first preset the system with a large negative pulse (30kV/cm^2), then take a minor hysteresis loop, then apply a "switching" pulse of variable pulsewidth and electric field amplitude, followed by a final, minor hysteresis loop. The first minor loop acts as a reference (purple loop in Fig. A.7b), whereby we are able to confirm the initial state (following preset) in a non-destructive fashion. Following the switching pulse, the second minor loop serves as a non-desctructive readout of the final state. In the case that the system has switched, we observe a hysteresis loop similar

to that shown (orange) in Fig. A.7b. In the case of no switching, we observe an identical loop to the first, reference, minor loop. By taking the aggregate difference between minor loops 1 and 2 we are thus able to provide a metric for switching completeness, with 1 being fully switched (corresponding to the aggregate difference for a switching pulse of maximum pulsewidth and electric field amplitude), and 0 being the case of no switching. We show the results of such an experiment in Fig. A.7c for various switching pulse pulsewidths and amplitudes. As observed to induce switching at longer pulsewidths, lower field is required. This is reminiscent of similar observations in BFO and BTO (chapter 2), and indicates that switching of the net in-plane polarization may proceed via nucleation and growth. We can define a switching time for a given electric field amplitude to be pulsewidth at which the switching metric is ≥ 0.5. Indeed (Fig. A.7d), a plot of switching time versus electric field can be fit by Merz' law (Eq. 2.8), further evidencing that the process may occur via and nucleation and growth. This analysis is only valid for the "large" switching event, and not the relaxor-like behavior at low field. To better understand the behavior at low field, and and further investigate the mechanism of switching at high field ("large" switching event) we turn to dielectric harmonic measurements.

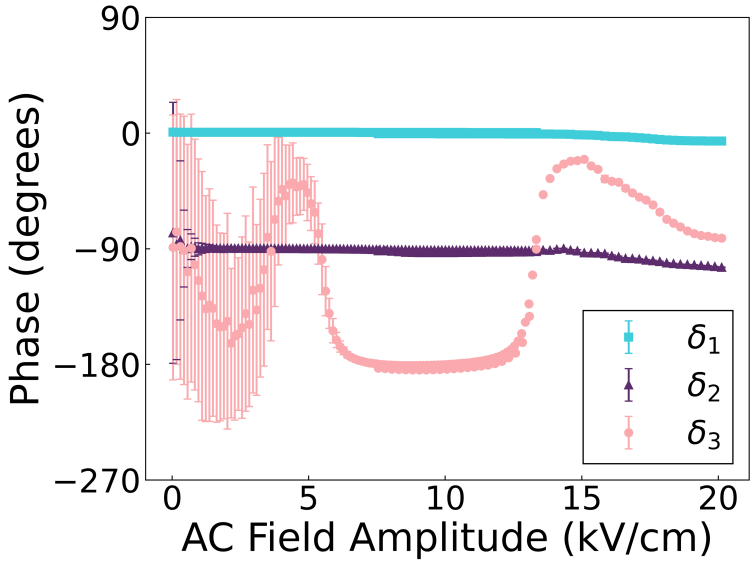

Figure A.8: Rayleigh harmonic measurements. First, second, and third harmonic Rayleigh measurements on polar vortex samples.

Harmonic dielectric measurements [265, 266, 267] consist of using a lock-in amplifier to measure the first, second, and third harmonic (particularly phase) response of the system to an applied AC voltage of varying amplitude. Fig. A.8 shows the results of such measurements. The third harmonic is especially crucial, as two important regimes are known to exist [265, 266]. The first is the case of the phase of the third harmonic $\approx 180°$. This is what is referred to as "reversible" motion, or non-hysteretic motion. In essence, the polar

regions in the sample move, under the influence of the AC voltage, but do so in a locally symmetric energy well, where all motion is reversible. Relaxor ferroelectrics, for example exhibit a third harmonic response at $\approx 180°$. The second regime is when the third harmonic phase is $\approx 90°$, as is the case for a prototypical ferroelectric. In this regime, the dynamics are understood to be governed by irreversible, hysteretic domain wall motion. Our data in Fig. A.8, exhibits both regimes, and each can be perfectly correlated to the two mechanisms of switching, explained above. At low field $\sim 5 \rightarrow 15$kV/cm, the phase of third harmonic is close to 180°, consistent with relaxor-like behavior, and reversible motion of the up and down. Once we reach fields > 15kV/cm, the third harmonic transitions to a phase of 90°, consistent with irreversible domain wall motion. These two mechanisms perfectly align with the fields at which the minor and major hysteresis loops occur (Fig. A.7), and further evidence two different regimes, and two different mechanisms of polar dynamics in the system!

Appendix B

Fabrication details and recipes

Here, I will motivate and explain a number of device fabrication designs, including tips for working with small (< 5mm x 5mm) chips and recipes for a variety of fabrication processes.

B.1 Wirebond process

The "wirebond" process described in this section is desirable for a variety of devices, including the GMR devices (Appendix A, section 6.2.1.3), the TR-SHG devices (Section 6.2.1.2), the devices use for *in-operando* X-ray diffraction [268] and also for non-local devices (Chapter 5) where one grows a bottom electrode in the material stack. The same process can also be used to make ferroelectric capacitors with areas so small that one cannot land on them with a probe tip. In many of these cases, wirebonds are required, in lieu of probe tips. However, when using wirebonds on thin films, the penetration depth of the bond itself is sufficiently deep that one will inevitably "punch-through" to the bottom electrode when attempting to bond to pads on the top surface, thereby shorting the device. Even without wirebonding, if the bottom electrode is not removed below a large ($\sim 100\mu$m pad) the chance of pinholes or other defects causing sufficient leakage to short the entire device to the bottom electrode is high. In order to avoid this, one must remove the bottom electrode (via ion milling, or other means) wherever top electrode (large contact) pads will eventually be placed, and leave the film only in a small, active, region. Here, I outline the process for doing this. I will use as an example the case of fabricating a GMR device for studying switching of magnetic order via applied electric fields, as follows. The process consists of several steps:

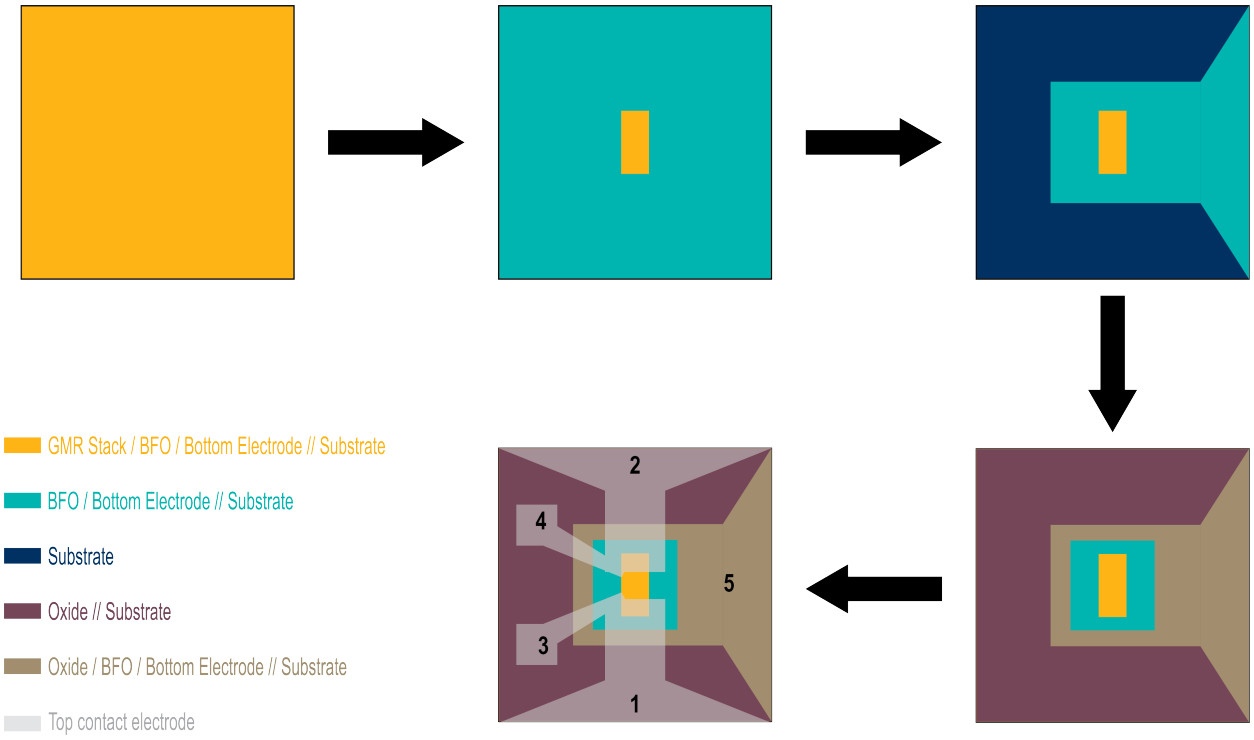

Figure B.1: Process for making GMR devices. End result is a 5-terminal device where ferroelectric switching can be driven between pads 1 and 5, and a 4-point resistance measurement (*i.e.*, GMR) can be performed using pads 1,2,3,4. All pads can be wirebonded without fear of shorting the device.

1. (Etch) Shallow mill/etch[1] (into the BFO) of active region
2. (Etch) Deep mill/etch (to substrate) of bottom electrode structure. This step removes all undesired bottom electrode to avoid shorting.
3. (Liftoff) Insulating oxide deposition (often MgO, grown via PLD). This step protects the exposed bottom electrode on the sidewall of the milled BE structure defined in the previous step. If no oxide layer is deposited, the (typically conformal) deposition of the top contact layer in the next step will short to the BE
4. (Liftoff) Top contact deposition (typically sputtering of Pt)

in principle, steps 1 and 2 can be reversed, though in my experience it is best to do the most crucial lithography step (*i.e.*, the active region) as early as possible. The more you process a sample, the worse it gets. It is best to have the oxide layer have overlap (as in Fig. B.1)

[1]Typically I use ion milling, though material specific means, such as SRO wet etching can be preferred for precise control.

with the film, so that imperfect alignment and/or sidewall re-deposition during ion-milling does not short your device. If using PLD to grow the oxide layer, ensure it is thick enough, because PLD is line-of-sight growth, not conformal growth.
A few considerations:

- If working with $SrTiO_3$ substrates, ensure you do not over mill. This will cause the STO to conduct.
- Mill steps should be performed at 45 degrees. A sidewall clean at > 75 degrees (90 degrees being parallel to the sample surface), can be used for 20-30% of the 45 degree mill time to assist with any sidewall re-deposition. I normally do not use sidewall cleans as I rarely mill from the top electrode to the bottom electrode directly.

B.2 Working with Chips

Many of the tools you will be working with are designed for wafers, so working with chips can be a bit difficult. In general, its advised to use carrier wafers for everything from spin coating, to lithography, to ion milling or sputtering. If the process requires vacuum, double-sided kapton tape should be used. Otherwise, double-sided scotch, or double-sided carbon tape can be used. Always try to get the chip as flat as possible in whatever tool you are using.

Spin coating: because of the small size of the chips, it can be hard to get uniform distribution of PR during spin coating. To help with this, ensure your chip is as flat as possible on the carrier wafer (by pushing on each of the corners, perhaps), and spinning at slightly higher rpms than that suggested for wafers. For example, for MiR 701 resist, I spin chips at 7500 rpm, where as wafers can be spun at 6000 rpm.

B.3 Recipes

B.3.1 Liftoff

The process listed here is for small features. For larger features you do not need to be as careful.

1. Soak in NMP at 85°C overnight
2. Spray (with handheld spray bottle) with Acetone then IPA, blow dry. Check optically or AFM to see if you need to continue
3. The following steps are increasing aggressiveness, start low and proceed to more aggressive, as needed.
    a) Spray with Acetone and IPA

b) Use a Kimwipe, with a bit of NMP on it, to very gently wipe the surface of the sample

c) Use a cuetip, with a bit of NMP on it, to very gently wipe the surface of the sample

d) Sonicate in NMP for short periods (∼5s) of time, spray with IPA immediately after

B.3.2 Heidelberg MLA150 Maskless Aligner

1. Resist: MiR701
2. Spin Coating
   a) 500 rpm, 5 seconds (dispense resist, *e.g.*, a single drop for a chip)
   b) 7500 rpm, 60 seconds
3. Pre-bake: 90°C, 90 seconds
4. Expose: 375nm light, dose: 180
5. Post-bake: 110°C, 60 seconds
6. Develop: MF26A, 60 seconds, water 10 seconds, blow dry

B.3.3 Wirebonding

For aluminum bonder: power 350, time 40ms, force 25g
Tips and tricks:

1. Always do a dummy bond before hand
2. Leave yourself as much space as possible on the bonding pad for every bond (in case you have to try again)
3. When you bond to a chip carrier, shake the wire before making the second bond. This will help ensure the bond is good.
4. After bonds are complete, very carefully nudge the wire with a fine nose tweezers, it should bend in the middle, the bond ends should not move.

Appendix C

Data Acquisition and Analysis: ekpy

In this appendix, I will briefly introduce my data analysis and data acquisition package, ekpy. For up-to-date documentation visit https://github.com/eparsonnet93/ekpmeasure.

ekpy is a set of control and analysis code designed to help streamline experiments. The basic idea is that in experimental work we often take data from many different sources, store it in different places, have varying degrees meta data associated with the data (even for a single type of data) and somehow(!) we are supposed to make sense of it all. We like to compare across trials, days, experimental conditions, *etc.* and it is very difficult to keep track of what data is where, and quickly access it when we need it. Often I find that folks end up copying and pasting raw data between excel spreadsheets and if you're not careful you will quickly lose track of which data came from where. This package's goal is to make this all easier.

At the heart of the analysis module is the Dataset class which is a means of manipulating meta data alone in order to locate which actual data you want to analyze. Datasets don't care about what the real data looks like, and they keep track of where different data is stored so it is easy to select which data you want to look at - only then do you retrieve the data. The real data is returned in a Data class which allows you to group by parameters, perform calculations on all data corresponding to the same meta data configuration (Data.apply), build workflows and much more.

The control module is based on the Experiment class, which handles coordinating instruments, naming conventions, file saving, and most importantly meta data creation. You can define any number of inputs or outputs to your experiment, and easily perform a scan over any or all of them, using experiment.n_param_scan. For example, say you wanted to run a switching experiment (Chapter 2), and wanted to scan both pulsewidth and voltage amplitude while keeping everything else the same. ekpy makes this effortless. See https://github.com/eparsonnet93/ekpmeasure for more.

Index